

**Solar Selective Performance, Opto-dielectric and Mechanical  
Characteristics of Vacuum Fabricated Metal Nitride Thin Film  
Coatings**

**Khalil Ibrahim, BSc (Engineering), MEng**



Thesis Submitted for the Degree of Doctor of Philosophy in the  
School of Engineering & Information Technology at Murdoch  
University

2018

## **Declaration**

*I hereby declare that this thesis is my own account of research and contains as its main content work which has not been previously submitted elsewhere for the award of a degree at any tertiary education institution.*

.....

**(Khalil Ibrahim)**

**Copyright**



Copyright by  
Murdoch University, Australia

2018

## Abstract

In the present study, metal nitride based sputtered thin film coatings such as Mo/Si, CrN/Si, and Mo:CrN/Si were investigated for their solar selective surface and mechanical applications. Despite a large number of literature is available in the area of solar selective applications of metal nitride based thin film coatings, these materials are still to be commercialized for their practical device applications. In view of this, we chose metal nitride based thin film coatings *e.g.*, Mo, CrN and Mo:CrN to realize their structural, morphological, elemental compositions, optical, dielectric and mechanical properties in as-deposited, and annealed conditions. Detail analyses of these features were carried out using X-ray diffraction (XRD), field emission scanning electron microscopy (FESEM), energy dispersive X-Ray spectroscopy (EDS), X-ray photoelectron spectroscopy (XPS), UV-Vis spectroscopy and FTIR, nanoindentation and finite element modeling (FEM). In addition to these, the first principle based density functional theory (DFT) integrated with the B3LYP hybrid functional plus LANL2DZ basis sets based infrared (IR), Raman and ultraviolet-visible (UV-Vis) analysis were also carried out to probe the electronic structural and optical properties of pristine and Mo-doped CrN clusters in the non-crystalline phase.

Optical analysis showed that in the visible range of the solar spectrum, the CrN coatings exhibit the highest solar absorptance of 66% while the lowest thermal emittance value of 5.67 was recorded for the CrN coating doped with Mo. As a result, the highest solar selectivity of 9.6, and the energy band-gap of 2.88 eV were achieved with the Mo-doped CrN coatings. On the other hand, optical studies of the annealed coatings showed that with the rise in annealing temperature up to 700 °C, the solar absorptance of CrN coatings increased from 61% to 89% and slightly decreased at 800 °C, while the optical band-gap energy dropped from 2.62 to 1.38 eV but slightly increased to 1.48 eV at 800 °C. Nanoindentation results indicated that as the annealing progresses, the hardness and elastic modulus values of CrN coatings are lowered. Further optical studies of Mo-doped CrN coatings showed that as the annealing temperature increased up to 700 °C, the solar absorptance is increased from 55% to its maximum value of 86%, and the optical band-gaps were dropped from 2.48 to 1.14 eV. Nanoindentation and finite element modeling studies of Mo-doped CrN coatings indicated that as the annealing progresses, both the hardness and elastic modulus values of these coatings reduced. A first principle based DFT simulation on Cr<sub>4</sub>N<sub>4</sub>, Cr<sub>4</sub>MoN<sub>3</sub>, Cr<sub>4</sub>Mo<sub>2</sub>N<sub>2</sub>, Cr<sub>3</sub>MoN<sub>4</sub>, Cr<sub>3</sub>Mo<sub>2</sub>N<sub>3</sub>, and Cr<sub>2</sub>Mo<sub>2</sub>N<sub>4</sub>

clusters indicated that the  $\text{Cr}_4\text{Mo}_2\text{N}_2$  structure was chemically and energetically the most stable species among the six clusters considered. The DFT based electronic analysis revealed that  $\text{Cr}_4\text{MoN}_3$  and  $\text{Cr}_3\text{Mo}_2\text{N}_3$  clusters possess magnetic susceptibility while the infrared (IR), Raman and ultraviolet-visible (UV-Vis) studies indicated that the clusters formed by  $\text{Cr}_4\text{N}_4$  and  $\text{Cr}_4\text{Mo}_2\text{N}_2$  are naturally stable and able to function as light harnessing materials to be used in solar selective surfaces.

## **Dedication**

*This thesis has been dedicated to the memory of my parents Mrs Hajj Ghaniah,  
and Mr Hajj Ibrahim, and my brothers Abdul Karim and Ismail.*

## Table of Contents

<b>Title.....</b>	<b>i</b>
<b>Declaration.....</b>	<b>i</b>
<b>Copyright .....</b>	<b>ii</b>
<b>Abstract.....</b>	<b>iii</b>
<b>Dedication .....</b>	<b>v</b>
<b>Table of Contents .....</b>	<b>vi</b>
<b>Acknowledgements.....</b>	<b>xii</b>
<b>List of Publications.....</b>	<b>xiv</b>
Journal Papers.....	xiv
Conference Papers.....	xvi
<b>Statement of Contributions .....</b>	<b>1</b>
<b>CHAPTER ONE.....</b>	<b>8</b>
<b>Introduction.....</b>	<b>8</b>
1.1    General Introduction .....	8
1.2    Background of the Present Study .....	8
1.3    Review of Earlier Work .....	11
1.4    Objectives of the Present Study .....	14
1.5    Layout of the Thesis.....	15
References .....	16
<b>CHAPTER TWO.....</b>	<b>29</b>
<b>Paper I: Solar Selective Performance of Metal Nitride and Metal Oxynitride Based Sputtered Coatings: A Comprehensive Review .....</b>	<b>29</b>
Abstract .....	29
2.1    General Introduction .....	29
2.2    Optical Properties of Materials .....	31
2.2.1    Optical Parameters .....	32
2.2.1.1    Optical Reflection.....	32
2.2.1.2    Optical Refraction and Refractive Index .....	33

2.2.1.3	Optical Scattering .....	34
2.2.1.4	Solar Absorptance .....	34
2.2.1.5	Thermal Emittance .....	36
2.2.1.6	Solar Selectivity.....	36
2.3	Other Optical Properties.....	41
2.4	Solar Selective Surfaces .....	45
2.5	Selective Solar Absorber Designs .....	47
2.5.1	Intrinsic Solar Absorber Materials .....	47
2.5.2	Semiconductor-metal Tandem Surfaces.....	47
2.5.3	Textured Surface Coatings .....	48
2.5.4	Metal-dielectric based Composite Selective Coatings .....	48
2.5.5	Painted Solar Selective Coatings.....	49
2.6	Real-life Applications of Transition Metal Nitride/oxynitride based Coatings: Spectral Selectivity Data of Recently Developed Materials.....	50
2.7	Other Applications of Metal Nitride-based Thin Film Coatings.....	58
2.8	Summary and Conclusions.....	60
	References .....	61

**CHAPTER THREE .....** **76**

**Paper II: Structural, Morphological and Optical Characterizations of Mo, CrN and Mo:CrN Sputtered Coatings for Potential Solar Selective Applications .....** **76**

	Abstract .....	76
3.1	Introduction.....	76
3.2	Materials and Methods .....	79
3.2.1	Film Preparation Technique .....	79
3.2.2	Characterization of the Thin Film Coatings .....	79
3.2.2.1	XRD analysis.....	79
3.2.2.2	FESEM analysis .....	79
3.2.2.3	UV-Vis studies .....	80
3.2.2.4	FTIR studies .....	80
3.2.2.5	Solar selectivity .....	80



3.3	Results and Discussion.....	81
3.3.1	XRD analysis of Mo, CrN and CrMoN films .....	81
3.3.2	Morphological features of Mo, CrN and CrMoN films via FESEM studies.....	83
3.3.3	Optical Characterizations of Mo, CrN and CrMoN Films .....	86
3.3.3.1	UV-Vis Investigations .....	86
3.3.3.2	FTIR results .....	86
3.3.3.3	Solar selectivity results.....	87
3.3.3.4	Optical band-gap analysis.....	88
3.3.3.5	Refractive index and extinction coefficient analysis .....	91
3.3.6	Dielectric characterizations.....	93
3.3.3.7	Energy loss analysis .....	94
3.4	Conclusions .....	97
	References .....	97

**CHAPTER FOUR.....104**

**Paper III: Annealing Impacts on Microstructural, Optical and Mechanical Studies of Sputtered CrN Thin Film Coatings: Experimental Studies and FEM Modeling.....104**

	Abstract .....	104
4.1	Introduction.....	104
4.2	Experimental Technique .....	106
4.2.1	Film Preparation Technique .....	106
4.2.2	XRD Experiments .....	107
4.2.3	FESEM Experiments.....	108
4.2.4	XPS Experiments .....	108
4.2.5	UV-Vis Experiments .....	108
4.2.6	Nanoindentation Experiments .....	108
4.3	Results and Discussion.....	109
4.3.1	XRD Analysis of as-deposited and Annealed CrN Films .....	109
4.3.2	Morphological Features of CrN Films via FESEM Studies.....	113
4.3.3	X-ray Photoelectron Spectroscopy (XPS) Characterizations of CrN Films before and after Annealing .....	114

4.3.4	Optical Characterizations of CrN Films before and after Annealing .....	115
4.3.4.1	UV-Vis Characterizations.....	115
4.3.4.2	Optical Band-gap Analysis.....	116
4.3.4.3	Refractive Index and Extinction Coefficient Analysis .....	119
4.3.4.4	Dielectric Characterizations .....	121
4.3.5	Mechanical Characterizations of CrN Films: Nanoindentation and FEM Modeling .....	122
4.3.5.1	Nanoindentation Results.....	122
4.3.5.2	FEM Modeling .....	125
4.4	Conclusions .....	131
	References .....	131

**CHAPTER FIVE.....137**

**Paper IV: Tailoring the Annealing Impacts on Structural, Morphological, Opto-dielectric and Mechanical Behaviors of Mo:CrN Coatings: Experimental Studies and Finite Element Modeling.....137**

	Abstract .....	137
5.1	Introduction.....	137
5.2	Experimental Section .....	139
5.2.1	Film preparation methodology .....	139
5.2.2	XRD analysis .....	139
5.2.3	FESEM Imaging.....	139
5.2.4	UV-Vis Studies .....	139
5.2.5	Nanoindentation and Finite Element Modelling FEM Tests.....	140
5.3	Results and Discussion.....	140
5.3.1	XRD Analysis of the as-deposited and Annealed Mo:CrN Coatings.....	140
5.3.2	Morphological Features of Mo:CrN Films via FESEM Studies .....	144
5.3.3	Opto-dielectric Characterizations of Mo:CrN Films.....	146
5.3.3.1	UV-Vis Investigations.....	146
5.3.3.2	Optical Band-gap Analysis.....	148
5.3.3.3	Dielectric Characterizations .....	149
5.3.3.4	Urbach Energy and Steepness Parameters.....	150

5.3.4	Mechanical Characterizations of Mo:CrN Films: Nanoindentation and Finite Element Modeling .....	153
5.3.4.1	Nanoindentation Results .....	153
5.3.4.2	Finite Element Modeling (FEM).....	154
5.4	Conclusions .....	161
	References .....	162
<b>CHAPTER SIX.....</b>		<b>167</b>
<b>Paper V: Understanding the Electronic Structural and Optical Properties of CrN and Mo:CrN Clusters: A DFT based First Principle Study .....</b>		<b>167</b>
	Abstract .....	167
6.1	Introduction.....	167
6.2	Computational Details.....	169
6.3	Results and Discussion.....	171
6.3.1	Structural simulations.....	171
6.3.2	Electronic Properties .....	178
6.3.3	Optical Properties.....	180
6.4	Conclusions .....	182
	References .....	182
<b>CHAPTER SEVEN.....</b>		<b>187</b>
<b>Conclusions .....</b>		<b>187</b>
<b>APPENDIX 1 .....</b>		<b>192</b>
<b>Sample Preparation Methodology .....</b>		<b>192</b>
<b>APPENDIX 2 .....</b>		<b>195</b>
<b>Experimental Theory and Techniques .....</b>		<b>195</b>
1.	General Introduction .....	195
2.	X-ray Diffraction Measurements.....	195
2.1	Analyzing the X-ray Diffraction Data.....	197
3.	Emission Scanning Electron Microscopy (FESEM) and Energy Dispersive X-ray (EDX) Experiments .....	198
4.	X-ray Photoelectron Spectroscopy (XPS) Measurements.....	200

5.	Optical Characterisations via UV-Vis-NIR and FTIR Reflectance Spectra.....	201
6.	Mechanical Properties of Thin Film Coatings: Nanoindentation and Finite Element Modeling (FEM) Studies.....	206
6.1	Nanoindentation Measurements.....	206
6.2	Finite Element Modeling (FEM).....	208
7.	Density Function Theory.....	210
	References.....	211

## **Acknowledgements**

I would like to acknowledge my deepest sense of sincere thanks to my principal supervisor, Dr Zhong-Tao Jiang, and to my co-supervisors Dr Aleks Nicoloski in the School of Engineering & Information Technology at Murdoch University, and Dr M Mahbubur Rahman, Associate Professor in the Department of Physics at Jahangirnagar University and Honorary Research Fellow in the School of Engineering & Information Technology at Murdoch University. I am very much indebted with them for their mentoring, guidance and kind support over the entire period of my PhD studies at Murdoch. I highly appreciate the commitment and motivation that they have instilled in me.

The research work presented in this thesis has been carried out with the help and support of large number people around me, however, only some of the following persons, whose friendship, experience, and assistance has meant so much to me are:

- Dr Xiaoli Zhao, Edith Cowan University;
- Dr Chun-Yang Yin, Newcastle University in Singapore;
- Dr Zhi-feng Zhao, City University of Hong Kong;
- Dr Jean-Pierre Veder, Curtin University;
- Dr Juita Juita, Murdoch University;
- Dr Hantarto Widajaja, Murdoch University;
- Dr Amun Amri, Riau University in Indonesia;
- Mr Kris Parker, School of Engineering & Information Technology, Murdoch University;
- Dr Marc Hampton and Mr David Zeelenberg, School of Chemical & Analytical Sciences, Murdoch University;
- Dr Kane O'Donnell, Curtin University;
- Mr Nase Alamery, Curtin University;
- Dr Hossain Abid, Curtin University; and
- Dr Md Mominul Islam, Hatem Taha, Ehsan Mohammadpour, Oday Ahmed, Hussein Miran, Zainab Jaf, & Nick Mondinos, School of Engineering & Information Technology, Murdoch University.

I am most grateful to Murdoch University for offering the facilities and logistic supports, thereby giving me the ability to carry out my research comfortably.

I am highly privileged to receive the financial support from Iraqi Government through the Ministry of Education, Republic of Iraq.

I am immensely grateful to the members of my family: my wife Haj Aliya; sisters: Haj Radhia, Haj Karyma, and Haj Ameera; my sons: Ali, and Mohammed Hussein; and son-in-law Dr Moayed Moghbel, my daughters: Zharaa, Haj Ayat and Ghadeer, my granddaughters and my grandsons for their unconditional love, inspiration and support.

I would also like express my deepest gratitude and sincere thanks to the Iraqi community living in Australia especially around Perth for their kind supports, hospitality and friendships especially to Jabar Awad and Haj Adil Al-Hayani and Riyadh Abdul-Sahib from Baghdad, for their deep engorgement and helps.

Finally, all thanks to almighty Allah (swt) whose command has made all the aforementioned facilities available to me.

**Khalil Ibrahim**

**Murdoch University**

## List of Publications

### Journal Papers

**1. (Paper I): Khalil Ibrahim, Hatem Taha, M. Mahbubur Rahman, Humayun Kabir, Zhong-Tao Jiang. *Solar Selective Performance of Metal Nitride/oxynitride based Magnetron Sputtered Thin Film Coatings: A Comprehensive Review. Journal of Optics, 20 (2018) 033001.***

<https://doi.org/10.1088/2040-8986/aaa2c5>

**2. (Paper II): Khalil Ibrahim, M. Mahbubur Rahman, E. Mohammadpour, Hatem Taha, Zhifeng Zhou, Chun-Yang Yin, Aleksandar N. Nikoloski, Zhong-Tao Jiang. *Structural, Morphological, and Optical Characterizations of Mo, CrN and Mo:CrN Sputtered Coatings for Potential Solar Selective Applications. Applied Surface Science, 440 (2018) 1001-1110.***

<https://doi.org/10.1016/j.apsusc.2018.01.267>

**3. (Paper III): Khalil Ibrahim, M. Mahbubur Rahman, Xiaoli Zhao, Jean-Pierre Veder, Zhi-feng Zhou, Ehsan Mohammadpour, Ridha Hameed Majeed, Aleksandar N. Nikoloski, Zhong-Tao Jiang. *Annealing Impacts on Microstructural, Optical, Mechanical Properties of Sputtered CrN Thin Film Coatings: Experimental Studies and Finite Element Modeling. Journal of Alloys and Compounds, 750 (2018) 451-464.***

<https://doi.org/10.1016/j.jallcom.2018.04.012>

**4. (Paper IV): Khalil Ibrahim, M. Mahbubur Rahman, Xiaoli Zhao, Hatam Taha, Zhong-Tao Jiang. *Tailoring the annealing impact on structural, morphological, opto-dielectric and mechanical behaviours of Mo:CrN coatings: Experimental studies and finite element modeling. Under Review: Thin Solid Films (2018). Date of Submission: 15/05/2018***

**5. (Paper V): Khalil Ibrahim, M. Mahbubur Rahman, Syed Mahedi Hasan, Hatem Taha, Muna S. Kassim, Chun-Yang Yin, Zhong-Tao Jiang. *Understanding the electronic structural and optical behaviours of CrN and Mo:CrN clusters: A DFT based first principle study. Submitted: Materials Research Bulletin (2018). Submitted on 12/07/2018***

Manuscript No. MRB\_2018\_2139

6. M. Mahbubur Rahman, Zhong-Tao Jiang, Paul Munroe, Lee Siang Chuah, Zhi-feng Zhou, Zonghan Xie, Chun Yang Yin, **Khalil Ibrahim**, Amun Amri, Humayun Kabir, Md Mahbubul Haque, Nicholas Mondinos, Mohammednoor Altarawneh, Bogdan Z. Dlugogorski. *Chemical Bonding States and Solar Selective Characteristics of Unbalanced Magnetron Sputtered  $T_xM_{1-x}N_y$  Coatings*. *RSC Advances*, **6** (2016) 36373-36383.

**DOI:** 10.1039/c6ra02550a

7. Tapos Kumar Bromho, **Khalil Ibrahim**, Humayun Kabir, M. Mahbubur Rahman, Kamrul Hasan, Tahmina Ferdous, Hatem Taha, Mohammednoor Altarawneh, Zhong-Tao Jiang. *Understanding the Impacts of  $Al^{+3}$ -substitutions on the Enhancement of Magnetic, Dielectric and Electrical behaviors of Ceramic Processed Nickel-zinc Mixed Ferrites: FTIR Assisted Studies*. *Materials Research Bulletin*, **97** (2018) 444-451.

**DOI:** 10.1016/j.materresbull.2017.09.013



## Conference Papers




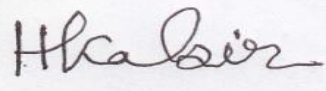

1. M. Mahbubur Rahman, Zhong-Tao Jiang, Chun Yang Yin, **Khalil Ibrahim**, Zhonghan Xie, Zhi-feng Zhou, Amun Amri, Nicholas Mondinos. *Spectral Selectivity of Unbalanced Magnetron Sputtered TiN, TiAlN and TiAlSiN Coatings: XRD, SEM and optical analyses*. International Conference on Smart Materials and Surfaces (ICSMS 2014), Bangkok, Thailand. August 26-28, 2014.
2. M. Mahbubur Rahman, Zhong-Tao Jiang, **Khalil Ibrahim**, Ehsan Mohammadpour, Hantarto Widjaja, Nicholas Mondinos, Amun Amri. *Development of Solar Selective Surfaces for Photothermal Applications*. Royal Society of Western Australia Centenary Postgraduate Symposium, University of Western Australia, Perth, Western Australia 6009, Australia. October 3, 2014.
3. Ehsan Mohammadpour, M. Mahbubur Rahman, Zhong-Tao Jiang, **Khalil Ibrahim**, Hantarto Widjaja, Nicholas Mondinos. *Phase Transition in  $Cr_xAl_{(1-x)}N$  Coating at High Temperatures*. Royal Society of Western Australia Centenary Postgraduate Symposium, University of Western Australia, Perth, Western Australia 6009, Australia. October 3, 2014.
4. **Khalil Ibrahim**, M Mahbubur Rahman, Nick Mondinos, Zhao Zhifeng, Zhong-Tao Jiang. *Understanding the structural, morphological and optical features of Mo, CrN and CrMoN sputtered films*. Australian Institute of Physics (AIP) WA 2016 Postgraduate Conference, University of Western Australia, Western Australia 6009, Australia. October 13, 2016.

# Statement of Contributions

## Journal Publication

1. **Khalil Ibrahim**, Hatem Taha, M. Mahbubur Rahman, Humayun Kabir, Zhong-Tao Jiang. *Solar Selective Performance of Metal Nitride/oxynitride based Magnetron Sputtered Thin Film Coatings: A Comprehensive Review*. **Journal of Optics, 20 (2018) 033001**.

<https://doi.org/10.1088/2040-8986/aaa2c5>





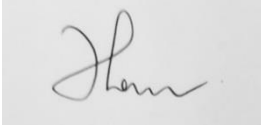


Author's Name	Contribution	Overall Percentage (%)	Signature
<b>Khalil Ibrahim</b>	Literature review, interpretation of the results, writing up the manuscript and preparation of related documents to complete the manuscript	70	
Hatem Taha	Literature review, analysis of the results	30	
M. Mahbubur Rahman	Data analysis and disucssion, refining and structuring the manuscript, submitting the manuscript to the journal and the corresponding author for this paper Corresponding author		
Humayun Kabir	Contributed in literature review and writing up the introduction and methodology section		
Zhong-Tao Jiang	Project leader Result discussion and manuscript preparation, revision and overall follow up		


## Statement of Contribution

### Journal Publication

2. **Khalil Ibrahim**, M. Mahbubur Rahman, E. Mohammadpour, Hatem Taha, Zhifeng Zhou, Chun-Yang Yin, Aleksandar N. Nikoloski, Zhong-Tao Jiang. *Structural, Morphological, and Optical Characterizations of Mo, CrN and Mo:CrN Sputtered Coatings for Potential Solar Selective Applications. Applied Surface Science, 440 (2018) 1001-1110.*

<https://doi.org/10.1016/j.apsusc.2018.01.267>

Author's Name	Contribution	Overall Percentage (%)	Signature
<b>Khalil Ibrahim</b>	Sample preparation for the experiments, and conducted various experimental procedures, data analysis, and writing up the manuscript	70	
M. Mahbubur Rahman	Data analysis and disucssion Manuscript preparation and submission to the journal for publication Corresponding author	30	
Ehsan Mohammadpour	Result discussion and manuscript preparation		
Hatem Taha	Result discussion and manuscript preparation		
Zhifeng Zhou	Preperation and synthesis of Mo, CrN and Mo:CrN coatings		
Chun-Yang Yin	Manuscript preparation and refining the writings		
Aleksandar N. Nikoloski	Refining the manuscript		




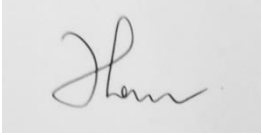



Zhong-Tao Jiang	Project leader Data analysis and disucssion Manuscript preparation and refining and revising the manuscript	
--------------------	---	---


## Statement of Contribution

### Journal Publication

**3. Khalil Ibrahim, M. Mahbubur Rahman, Xiaoli Zhao, Jean-Pierre Veder, Zhi-feng Zhou, Ehsan Mohammadpour, Ridha Hameed Majeed, Aleksandar N. Nikoloski, Zhong-Tao Jiang. *Annealing Impacts on Microstructural, Optical, Mechanical Properties of Sputtered CrN Thin Film Coatings: Experimental Studies and Finite Element Modeling. Journal of Alloys and Compounds, 750 (2018) 451-464.***

Manuscript No. JALCOM-D-18-00259

Author's Name	Contribution	Overall Percentage (%)	Signature
<b>Khalil Ibrahim</b>	Sample preparation, experiments, analysis and interpretation of the results, writing up the manuscript	70	
M. Mahbubur Rahman	Data analysis and disucssion Manuscript preparation and submission Corresponding author	30	
Xiaoli Zhao	Machanical chrarakterizations via nanoindentation and FEM studies, and the related data analysis		X
Jean-Pierre Veder	XPS characterisations		
Zhi-feng Zhou	Fabrication and synthesis of the CrN thin films		
Ehsan Mohammadpour	Analysis of XRD and related data		
Ridha Hameed Majeed	Manuscript prepartion and refining the article		
Aleksandar N. Nikoloski	Experimental help, data analysis and refining the article		

Zhong-Tao Jiang	Project leader Data analysis and disucssion, revising the manuscript	
--------------------	--	---




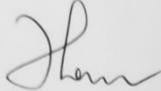


## Statement of Contribution

### Journal Publication

**4. Khalil Ibrahim, M Mahbubur Rahman, Xiaoli Zhao, Hatam Taha, Zhi-feng Zhou, Aleksandar N. Nikoloski, Zhong-Tao Jiang. *Tailoring the Structural, Morphological, Opto-dielectric and Mechanical behaviors of Mo-doped CrN Coatings: Experimental Studies and Finite Element Modeling. Submitted: Thin Solid Films (2018).***

**Submitted on 15/05/2018**

Manuscript No. TSF-S-18-00833-2




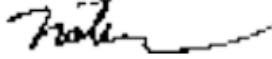



Author's Name	Contribution	Overall Percentage (%)	Signature
<b>Khalil Ibrahim</b>	Sample preparation and get them ready for the analysis, Data interpretation, writing up the manuscript	70	
M. Mahbubur Rahman	Data analysis, results and disucssion, manuscript preparation, refining the writings and submission to the journal Corresponding author	30	
Hatem Taha	Data analysis, literature review		
Zhi-feng Zhou	Synthesis the Mo:CrN coatings using the sputtering system, writing up the manuscript		
Aleksandar N. Nikoloski	Data analysis, and writing up the manuscript		
Xiaoli Zhao	Machenical chraracterizations via nanoindentation and FEM studies, and the related data analysis		X
Zhong-Tao Jiang	Project leader Data analysis and disucssion Manuscript preparation		

## Statement of Contribution

### Journal Publication

**5. Khalil Ibrahim, M Mahbubur Rahman, Syed Mahedi Hasan, Hatem Taha, Muna S. Kassim, Chun-Yang Yin, Zhong-Tao Jiang. *A First-principle Study of Electronic Structural and Optical Properties of CrN and Mo:CrN Clusters. Submitted: Materials Research Bulletin (2018). Submitted on 12/07/2018.***

Manuscript No. MRB\_2018\_2139

Author's Name	Contribution	Overall Percentage (%)	Signature
<b>Khalil Ibrahim</b>	Data preparation and get them ready for the (DFT) computational analysis, Data interpretation, writing up the manuscript	70	
Syed Mahedi Hasan	DFT simulation, literature review, computational analysis, data interpretation, writing up the manuscript	30	
M. Mahbubur Rahman	Literature review, data analysis, manuscript preparation, refining the writings and submission to the journal Corresponding author		
Hatem Taha	Literature review, data analysis, and revising the paper		
Muna S. Kassim	Manuscript preparation, results and discussion writings		
Chun-Yang Yin	Data analysis and discussion writing, refining the manuscript		
Zhong-Tao Jiang	Project leader Manuscript preparation, data analysis, and refining the manuscript		



# CHAPTER ONE

---

## Introduction

---

### 1.1 General Introduction

Transition metal and transition metal nitride based vacuum deposited thin film coatings such as Mo, CrN and Mo:CrN which have been synthesized onto the Si(100) substrates were thoroughly investigated for their potential use in solar selective absorbing surfaces and in mechanical applications. These materials constitute a new approach in maximizing power conversion efficiency with a mechanical steadiness in mid to high temperature exposures. The subsequent sections of this chapter present brief background information on the present study, a comprehensive literature review, notes on the relevance and importance of the study, a detailed outline of its objectives, and lastly, information regarding the layout of the thesis.

### 1.2 Background of the Present Study

The sun is an unlimited, environmentally friendly, sustainable and renewable source of energy. Solar energy can be effectively converted into usable forms through different methods [1, 2]. Atmospheric mass flow is used in the generation of wind power, using solar energy through the non-uniform heating of the earth's surface resulting in the formation of moving air. Hydro-mechanical power generation uses solar energy through water circulation in the earth's surface which is driven by the sun. For all kinds of biosphere, the power generated from biomass and biogas, are sourced from solar energy through energy crops. These examples are indirect uses of solar energy.

Solar radiation can be directly converted to electricity by means of photovoltaic (PV) technology while solar-thermal conversion devices help with the transformation of solar energy into heat [3, 4]. Solar thermal conversion devices belong in the category of technology in which solar selective absorbing materials play the key role. Nowadays, there is much research into the development of solar-thermal systems because of the cost effectiveness of solar power with consumers all over the world having flat plate solar collectors installed for domestic hot water and space heating. Meanwhile, solar-thermal technology in power generation for in solar air-conditioning, swimming pool filtration systems, solar process heating, and solar thermal power plants [5].

Photovoltaic solar generation techniques that have been studied since 1839, and are considered to be the simplest and most promising for achieving the direct conversion of solar energy to electrical power. In PV systems, sunlight is absorbed by a semiconductor material which has suitable energy band-gaps and which generates electrons and holes [6, 7]. In a PV cell, only photons having energy which is equal to or greater than the band gap of the cell material can free an electron for an electric circuit. In such cases, the semiconductor diode junction separates the charge carriers and creates a voltage difference leading to the flow of electricity [7, 8]. In general, the conversion process involves three major steps: (i) solar radiation absorption and forming locally constrained excitons, (ii) the transportation of excitons to the donor-acceptor interface followed by subsequent dissociations to form free electrons and holes, and (iii) the movement of charged particles towards the electrodes producing an electric output [6, 9]. Only 5-30% of the incident solar radiation can be converted to electricity by PV systems and the remaining solar energy is wasted as heat. An excessive amount of heat energy increased the temperature of the PV panels and leads to an undesirable drop in the efficiency of the PV cells and structural damage to the PV device [10].

Solar photothermal devices are commonly used for domestic and industrial water heating or space heating purposes. The photothermal collector is one of the most essential modules of a solar thermal device. The most important part of the solar thermal collector is the solar selectivity of the absorbing surface which strongly affects the efficiency of the solar thermal conversion system [11, 12]. Photothermal devices require high performance and low-cost solar selective materials for the surface of solar energy converters. A good solar selective surface exhibits high spectral absorptance in the visible range and low thermal emittance in the infrared to far-infrared range of the solar spectrum. Nowadays, 3d transition metal oxide and metal nitride based thin film coatings are considered as being very important materials due to their widespread application in electrical and optical devices. They possess high solar selectivity which makes them ideal for being used as solar selective coatings in solar energy harvesting devices. An ideal solar selective surface absorbs 100% of the incident solar radiation in the ultraviolet to visible range of the solar spectra and emits all the incoming radiation in the infrared range of the solar spectra. However, in reality no such single material exists that will meet these criteria. A practical selective surface possesses high solar absorptance,  $\alpha$  (0.3 to 2.5  $\mu\text{m}$ ) and low thermal emittance,  $\varepsilon$  ( $\geq 2.5 \mu\text{m}$ ) at the operating temperatures [13, 14]. A brief summary of the spectral selective features of an ideal solar selective surface and real selective absorber for

Hemispherical solar irradiance for air mass 1.5 (ISO standard 9845-1, 1992) and blackbody-like spectral emittance at 100, 200, and 300 °C are presented in section 2.2.1.6, Chapter 2 of this thesis. Nowadays, thin film coatings based solar selective surfaces are made which consist of novel metallic nanostructures embedded in metallic oxides and/or metallic nitrides and/or metallic oxinitrides [15-19]. More recently, there have been many studies in which transition metal nitride based thin film coating have been used in mid and high temperature solar selective surface applications [13, 20-36].

Generally, spectral selective surfaces can be classified into six different categories: intrinsic absorber, two and three dimensional quantum size effects, multilayer absorbers, absorber-reflector solar selective tandems, textured surfaces and heat mirrors. Detailed descriptions of different solar selective absorbing surfaces together with their deposition mechanisms can be found elsewhere [37-40]. Among these six categories, absorber-reflector tandem is the most common which consists of two surfaces: a highly absorbing surface in the visible wavelength and a highly reflective surface in the thermal infrared wavelength range. This absorber-reflector tandem system can be of two types: a semiconductor-metal tandem, and composite coatings. Our studies were undertaken using the semiconductor-metal tandem absorbing surface which was achieved by placing a low band-gap semiconducting surface (a thin film coating) onto the top of a highly infrared reflecting metal surface. The semiconducting thin film coating layer absorbs the solar radiation which has energy greater than the band-gap and thereby releasing the valance electrons into the conduction bands while photons with energy less than the band-gaps are transmitted through the surface of the coatings. Since the semiconducting surfaces offer higher refractive indices, a higher degree of solar absorption can be attained by placing an anti-reflection layer (such as  $\text{Al}_2\text{O}_3$ ,  $\text{SiO}_2$ ,  $\text{Si}_3\text{N}_4$ ) onto the top of the coatings to reduce the reflection of light at the air/semiconductor interface. This kind of semiconductor-metal tandem solar selective surface can be useful in low to mid temperature applications [41, 42]. There are several design options and physical mechanisms available when developing a solar selective absorbing surface. The efficiency of a photothermal energy conversion system can be enhanced by the development of new selective absorber materials with the desired properties [43, 44]. Several factors are to be taken into consideration in the production of photothermal absorbers: simplicity in fabrication, cost-effectiveness, long-term thermal and mechanical durability, and minimal environmental impact in the production process. The optical performance of a solar selective absorbing surface depends upon the

composition of the thin film coating, surface morphology and nanostructure, the surface design, surface roughness, film thickness and optical constants of the constituent materials.

Metal nitride based hard protective coatings such as CrN and Mo:CrN are used in the manufacture of high-speed/dry cutting and metal forming tools and require high hardness, good oxidation, wear, and corrosion resistance, as well as high physical, thermal, and chemical stability. All these properties are dependent on the microstructure, synthesis mechanisms, and stoichiometry. High hardness, good tribological characteristics and superior oxidation resistance behaviours of AlCrN coatings have been reported in several studies [45-50]. The toughening and hardening mechanisms of nanosized coating materials have been described in an earlier study [51]. Metal nitride based hard coatings can be synthesized *via* unbalanced magnetron sputtering [52-54], beam plasma-assisted physical vapour deposition method [55], cathodic arc ion plating [56-58], and other methods [59-62]. Nanostructured superhard coatings can also be produced by a combination of hard transition metal-nitrides such TiN, W<sub>2</sub>N, and VN; and a covalent nitride such as Si<sub>3</sub>N<sub>4</sub>, and BN [63]. These coatings are thermodynamically stable, possess strong spinodal segregation [64], and demonstrate superhardness at high temperature exposures [65].

The hardness of CrN coatings is governed by grain size and the grain boundary structure [66, 67]. The hardness of a material is increased with the decrease in grain size and vice versa [68]. The incorporation of suitable dopants such as Mo, Si, Al or Ti into the CrN structure, results in the refining of the grain size thus enhancing the hardness of the CrN phase [69]. In nanostructures, the hardness of the Cr<sub>1-x</sub>M<sub>x</sub>N coatings is believed to be governed by the grain boundaries [51, 70]. The oxidation resistance behaviours of thin film coatings at high temperatures, is controlled by its surface chemistry and grain boundary assemblies [71]. The natural oxide layers formed onto the surface of metal nitride coatings leads to an increase their heat tolerance [72]. The introduction of appropriate doping obstructs the further penetration of surface oxide layers onto the grain boundary regions and thereby modifies the hardness of the coatings.

### **1.3 Review of Earlier Work**

Metal nitride based sputtered coatings well known as being hard protective and decorative coatings and they are widely used in high-speed/dry cutting and metal forming tools. The high hardness, oxidation, wear corrosion resistance, as well as tribological behaviors of these coatings depend on the microstructural features and chemical compositions of their

constituting elements. Nowadays, various new dopants are employed to initiate defects in the metal nitride structures in order to develop new phenomena, improve the films' quality and to utilize them in new applications. Because of this, over the years, research interests on metal and metal nitride based thin film coatings (for solar selective surface and mechanical applications) have been accelerated due to their large number of favorable properties such as; large band-gap, high surface acoustic velocity, wear, oxidation, corrosion, and erosion resistance, higher thermal and chemical stability, and mechanical toughness [73, 74]. As a result, these materials have widespread industrial and commercial applications in solar absorbing and solar selective surfaces [16, 18, 75, 76], microelectronic devices [77], ultraviolet and visible light emitters and detectors [78], high temperature structural materials [79, 80], for absorption optimizations and industrial applications [1, 2, 81], pollution controls [82], batteries and memory devices [83, 84], and semiconductor industry for optoelectronic devices at high power and high temperatures [85]. Because of their high hardness, good adhesion to substrate, excellent wear resistance, low friction coefficient, high corrosion-, and oxidation resistance, superior elastic modulus values, high melting point and superior chemical stabilities, large optical energy band-gaps, physico-chemical, optical, electronic, mechanical and thermal characteristics, and scalability metal nitrides based thin film coating materials also have a varied range of technological and industrial applications. For instance, these materials have secured their applications in high-speed cutting and machining [86], moulding dies and cold forming [87], combustion engine moving parts and rocket nozzles [88], non-volatile storage devices [89-91], superhard coatings [70, 92, 93], anti-reflective coatings [94-97], and optical storage devices [98].

Among various metal nitride compounds CrN based coatings show significant superiority over TiN-based coatings due to their extremely high hardness, higher melting point, corrosion and wear resistance, and anti-oxidative nature at high temperature environments [99-102]. In recent years, MoCrN coating are being considered as the potential substitute for CrN matrix as they exhibit structural evolution and superior hardness within the range of 28–31 GPa after an appropriate Mo-doping [103]. Klimashin *et al.*, performed theoretical and experimental analysis on MoCrN and MoCrAlN systems and found their mechanical hardness to be more pronounced than that of CrN films [103, 104]. Therefore, it can be seen that Mo can enhance the properties of CrN films.

Al-, and Si-doped CrN films were studied by means of cross-sectional bright field transmission electron microscope (XTEM), high resolution XPS, nanoindentation and

finite element modeling methods [105, 106]. The XTEM method was used to investigate the factors influencing the mechanical properties of CrSiN coatings while the nanoindentation technique was used to estimate the hardness, elastic modulus and residual stress of CrSiN sputtered coatings [105]. Various surface analysis methods aided by the finite element analysis, were used to observe the effect of Al-dopants in determining the microstructural and mechanical features of CrAlN coatings [106]. Grazing incidence X-ray diffraction (GIXRD) studies of Al-doped (with low, medium and high amount of Al-content) CrN coatings confirmed the alternations of preferred orientations with the subsequent Al-substitutions [106]. The (200) preferred orientation in CrN coatings was gradually reduced with the increase in Al-content while subsequent increase of intensity in (111) and (220) diffraction planes were detected. The influence of Si-content on ZrN and WN matrices showed remarkable enhancements of their physical hardness, toughness and oxidation resistance properties [107]. As the amount of Si-addition is enhanced, these structures lost their degree of crystallinity by significant broadening of their intensity peaks. Near edge X-ray absorption fine structure (NEXAFS) spectroscopy has been also widely used in solving complex systems and to identify the coexistence of different crystalline and amorphous phases of CrN matrices [70, 92, 93]. Deposition methods, characterizations, oxidation behaviors and hardness mechanisms of CrN,  $\text{Cr}_{1-x}\text{Al}_x\text{N}$ , and CrAlON thin film coatings have been extensively studied by Hirai *et al.* in a series of research articles [45, 108-110]. The mechanical properties of nanostructured coatings are very dependent on grain boundary structure, grain boundary angle, grain boundary sliding and movement of dislocations. Another reason for there being higher hardness in nanosized coatings is the plastic deformation and the leading role of dislocations. Furthermore, the cohesive forces between atoms, and compression macrostresses originated during the synthesis process is also believed to be involved in hardening the coating structures [111].

A good combination of reasonably high hardness and high toughness is very important from an application viewpoint of hard coating materials. The introduction of Si, Al, and Y can considerably increase the high temperature features of CrZr-based nitride coatings [112-114]. High hardness, high temperature wear and oxidation resistance behaviours were discerned in CrZr(Si/Al)N coatings [112, 114]. The impressive oxidation resistance nature of CrN coatings arise by the formation of  $\text{Cr}_2\text{O}_3$  solid and a protective layer around the CrN coatings' surface at high temperature applications [115]. The high hardness, and oxidation resistance properties of a large number of other metal nitride coatings have been reported [116-120]. At high temperatures, CrN coatings are not well-suited for hot forming dies and

high speed machining applications [121]. In order to overcome these limitations; zirconium, silicon, and/or aluminium was successfully integrated into the CrN structure [122-125]. In another study, the CrZrN coatings were evaluated as a good candidate for high temperature applications [126]. To date, many metal nitrides and metal oxynitrides based thin film coatings have been developed for solar selective and mechanical applications [13, 16, 18, 21-23, 70, 92, 93, 127-133]. The power conversion efficiency and mechanical performance of a thin film coating based material depends upon the selection of the coating material, coating design, microstructural features, chemical bonding states, hardness, toughness, adhesion, phase structure and other physical properties.

#### **1.4 Objectives of the Present Study**

There have been many developments and efforts made in investigating metal nitride based selective solar surfaces, however, these materials are yet to be commercialized for practical solar energy device applications [134-136]. Thus, in order to develop efficient solar selective absorptive surfaces, it is important to identify suitable product materials, fabricating techniques, and analytical tools. Prior to commercial production, research and development work on the material and coating selection, performance testing, system optimization, quality control and reliability, and ease of delivery and installation are necessary. This study was focused on the basic research question: Can novel solar absorptive surface with high optical and dielectric performance, mechanically superior and mechanically durable be fabricated by means of closed field unbalanced magnetron sputtering methodology onto a Si(100) substrate for mid and high temperature applications?

In view of the above facts,

- (1) A comprehensive study has been conducted to investigate the magnetron sputtering deposited on Mo/Si, CrN/Si, and Mo:CrN/Si coatings, in as-deposited and annealed states, for their structural, microstructural, morphological, and opto-dielectric properties and providing a detailed mechanical analysis *via* experimental procedure and fine element modeling (FEM) techniques.
- (2) The nanoindentation method was used to probe the mechanical parameters of these coatings. The intrinsic hardness of the coatings was estimated both *via* experiment and by modeling the substrate effect and was found to relate to the microstructural features of the coatings.

- (3) Correlation between their mechanical properties, residual stress level, and levels of stress induced at the coating-substrate interface was also examined.
- (4) A density functional theory (DFT) analysis was carried out to investigate the electronic-structural, density of states, and the optical properties of the CrN phase and the different Mo:CrN complexes in a non-crystalline phase. The overall DFT analysis was conducted *via* structural optimization of the clusters through density of states (DOS) studies, IR analysis, Raman analysis, and ultraviolet-visible (UV-Vis) spectra simulations for CrN and Mo:CrN phases.

## 1.5 Layout of the Thesis

This thesis consists of seven chapters in total. Chapter 1 illustrates the background information, a brief literature review and objectives of the study. Chapter 2 presents a comprehensive review of the recent advances in the solar selective performance of metal nitride based magnetron sputtered thin-film coatings which has been published in the *Journal of Optics (Paper I)*.

The structural features, surface morphology, optical and dielectric properties of Mo, CrN and Mo:CrN thin film coatings are discussed in Chapter 3 which has been published in *Applied Surface Science (Paper II)*.

Chapter 4 deals with the impact of the annealing temperatures on structural, surface morphological, mechanical, surface chemical bonding states and the solar absorption properties of magnetron sputtered CrN thin film coatings. The contents of Chapter 4 has been published in *Journal of Alloys and Compounds (Paper III)*.

Chapter 5 covers the novel insights of temperature dependent structural, opto-dielectric, mechanical studies, and finite element modeling (FEM) of Mo:CrN sputtered coatings. The results presented in Chapter 5, have been under review with the *Thin Solid Films (Paper IV)*.

Chapter 6 covers the first principle of electronic structural and optical studies of CrN and Mo:CrN clusters in noncrystalline phases *via* density function theory (DFT). The results presented in Chapter 6, has been submitted in the *Materials Research Bulletin (Paper V)*.

The concluding remarks of the thesis, suggestions, the further scope of relevant studies, and the need for the future developments are discussed in Chapter 7 as Conclusions. A brief



explanation of the preparation methodology, experimental theory and experimental techniques used in this thesis have been described in the appendices.

## References

- [1] S. Berrhazi, O. Ahmed, R. Benchrif, D. Zejli, Optimal design with materials selection for thermal energy storages in high temperature concentrating solar power, *IET Renewable Power Generation*, 12 (2018) 37-44.
- [2] Z. Wang, Z.M. Zhang, X. Quan, P. Cheng, A perfect absorber design using a natural hyperbolic material for harvesting solar energy, *Solar Energy*, 159 (2018) 329-336.
- [3] E. Dijkgraaf, T.P. Van Dorp, E. Maasland, On the effectiveness of feed-in tariffs in the development of solar photovoltaics, *Energy Journal*, 39 (2018) 81-99.
- [4] A.A. Bayod-Rújula, A. Burgio, Z. Leonowicz, D. Menniti, A. Pinnarelli, N. Sorrentino, Recent Developments of Photovoltaics Integrated with Battery Storage Systems and Related Feed-In Tariff Policies: A Review, *International Journal of Photoenergy*, 2017 (2017).
- [5] Q. Li, C. Zheng, A. Shirazi, O. Bany Mousa, F. Moscia, J.A. Scott, R.A. Taylor, Design and analysis of a medium-temperature, concentrated solar thermal collector for air-conditioning applications, *Applied Energy*, 190 (2017) 1159-1173.
- [6] B.J. Huang, T.H. Lin, W.C. Hung, F.S. Sun, Performance evaluation of solar photovoltaic/thermal systems, *Solar Energy*, 70 (2001) 443-448.
- [7] I.P. Koronaki, M.T. Nitsas, Experimental and theoretical performance investigation of asymmetric photovoltaic/thermal hybrid solar collectors connected in series, *Renewable Energy*, 118 (2018) 654-672.
- [8] S. Lo Piano, K. Mayumi, Toward an integrated assessment of the performance of photovoltaic power stations for electricity generation, *Applied Energy*, 186 (2017) 167-174.
- [9] S. Bhattarai, G.K. Kafle, S.-H. Euh, J.-H. Oh, D.H. Kim, Comparative study of photovoltaic and thermal solar systems with different storage capacities: Performance evaluation and economic analysis, *Energy*, 61 (2013) 272-282.
- [10] X. Ju, C. Xu, X. Han, X. Du, G. Wei, Y. Yang, A review of the concentrated photovoltaic/thermal (CPVT) hybrid solar systems based on the spectral beam splitting technology, *Applied Energy*, 187 (2017) 534-563.
- [11] M. Ghazouani, M. Bouya, M. Benaissa, A new methodology to select the thermal solar collectors by localizations and applications, *Proceedings of 2015 IEEE International Renewable and Sustainable Energy Conference, IRSEC 2015*, 2016.

- [12] J. Freeman, K. Hellgardt, C.N. Markides, An Assessment of Solar-Thermal Collector Designs for Small-Scale Combined Heating and Power Applications in the United Kingdom, *Heat Transfer Engineering*, 36 (2015) 1332-1347.
- [13] H.C. Barshilia, N. Selvakumar, K.S. Rajam, A. Biswas, Spectrally selective NbAlN/NbAlON/Si<sub>3</sub>N<sub>4</sub> tandem absorber for high-temperature solar applications, *Solar Energy Materials and Solar Cells*, 92 (2008) 495-504.
- [14] W.E.J. Neal, An introduction to selective surfaces for solar applications, *Surface Technology*, 20 (1983) 295-299.
- [15] A. Millar, M.M. Rahman, Z.-T. Jiang, Review of Sol-Gel Derived Mixed Metal Oxide Thin Film Coatings with the Addition of Carbon Materials for Selective Surface Applications, *Journal of Advanced Physics*, 3 (2014) 179-193.
- [16] M.M. Rahman, Z.-T. Jiang, P. Munroe, L.S. Chuah, Z.-f. Zhou, Z. Xie, C.Y. Yin, K. Ibrahim, A. Amri, H. Kabir, M.M. Haque, N. Mondinos, M. Altarawneh, B.Z. Dlugogorski, Chemical bonding states and solar selective characteristics of unbalanced magnetron sputtered Ti<sub>x</sub>M<sub>1-x-y</sub>N<sub>y</sub> films, *RSC Advances*, 6 (2016) 36373-36383.
- [17] M.M. Rahman, Z.-T. Jiang, C.-Y. Yin, L.S. Chuah, H.-L. Lee, A. Amri, B.-M. Goh, B.J. Wood, C. Creagh, N. Mondinos, M. Altarawneh, B.Z. Dlugogorski, Structural Thermal Stability of Graphene Oxide-Doped Copper–Cobalt Oxide Coatings as a Solar Selective Surface, *Journal of Materials Science & Technology*, 32 (2016) 1179-1191.
- [18] M.M. Rahman, Z.-T. Jiang, Z.-f. Zhou, Z. Xie, C.Y. Yin, H. Kabir, M.M. Haque, A. Amri, N. Mondinos, M. Altarawneh, Effects of annealing temperatures on the morphological, mechanical, surface chemical bonding, and solar selectivity properties of sputtered TiAlSiN thin films, *Journal of Alloys and Compounds*, 671 (2016) 254-266.
- [19] H.C. Barshilia, N. Selvakumar, K.S. Rajam, D.V. Sridhara Rao, K. Muraleedharan, Deposition and characterization of TiAlN/TiAlON/Si<sub>3</sub>N<sub>4</sub> tandem absorbers prepared using reactive direct current magnetron sputtering, *Thin Solid Films*, 516 (2008) 6071-6078.
- [20] C.G. Granqvist, Transparent conductors as solar energy materials: A panoramic review, *Solar Energy Materials and Solar Cells*, 91 (2007) 1529-1598.
- [21] N. Selvakumar, H.C. Barshilia, Review of physical vapor deposited (PVD) spectrally selective coatings for mid- and high-temperature solar thermal applications, *Solar Energy Materials and Solar Cells*, 98 (2012) 1-23.
- [22] H.C. Barshilia, N. Selvakumar, K.S. Rajam, A. Biswas, Optical properties and thermal stability of TiAlN/AlON tandem absorber prepared by reactive DC/RF magnetron sputtering, *Sol Energ Mater Sol Cells*, 92 (2008) 1425-1433.

- [23] M. Du, L. Hao, J. Mi, F. Lv, X. Liu, L. Jiang, S. Wang, Optimization design of  $\text{Ti}_{0.5}\text{Al}_{0.5}\text{N}/\text{Ti}_{0.25}\text{Al}_{0.75}\text{N}/\text{AlN}$  coating used for solar selective applications, *Solar Energy Materials and Solar Cells*, 95 (2011) 1193-1196.
- [24] S.A. Kalogirou, Solar thermal collectors and applications, *Progress in Energy and Combustion Science*, 30 (2004) 231-295.
- [25] C.E. Kennedy, H. Price, Progress in development of high-temperature solarselective coating, *Proceedings of ISEC 2005*, 520 (2005).
- [26] Y. Liu, C. Wang, Y. Xue, The spectral properties and thermal stability of NbTiON solar selective absorbing coating, *Solar Energy Materials and Solar Cells*, 96 (2012) 131-136.
- [27] C. Nunes, V. Teixeira, M.L. Prates, N.P. Barradas, A.D. Sequeira, Graded selective coatings based on chromium and titanium oxynitride, *Thin Solid Films*, 442 (2003) 173-178.
- [28] S. Yue, S. Yueyan, W. Fengchun, High-temperature optical properties and stability of  $\text{Al}_x\text{O}_y\text{-AlN}_x\text{-Al}$  solar selective absorbing surface prepared by DC magnetron reactive sputtering, *Solar Energy Materials and Solar Cells*, 77 (2003) 393-403.
- [29] A. Amri, Z.T. Jiang, T. Pryor, C.Y. Yin, Z. Xie, N. Mondinos, Optical and mechanical characterization of novel cobalt-based metal oxide thin films synthesized using sol-gel dip-coating method, *Surface and Coatings Technology*, 207 (2012) 367-374.
- [30] A. Amri, Z.-T. Jiang, X. Zhao, Z. Xie, C.-Y. Yin, N. Ali, N. Mondinos, M.M. Rahman, D. Habibi, Tailoring the physicochemical and mechanical properties of optical copper–cobalt oxide thin films through annealing treatment, *Surface and Coatings Technology*, 239 (2014) 212-221.
- [31] H.C. Barshilia, N. Selvakumar, K.S. Rajam, D.V. Sridhara Rao, K. Muraleedharan, A. Biswas,  $\text{TiAlN}/\text{TiAlON}/\text{Si}_3\text{N}_4$  tandem absorber for high temperature solar selective applications, *Applied Physics Letters*, 89 (2006) 191909.
- [32] N. Selvakumar, N.T. Manikandanath, A. Biswas, H.C. Barshilia, Design and fabrication of highly thermally stable  $\text{HfMoN}/\text{HfON}/\text{Al}_2\text{O}_3$  tandem absorber for solar thermal power generation applications, *Sol Energ Mater Sol Cells*, 102 (2012) 86-92.
- [33] A. Amri, Z.-T. Jiang, P.A. Bahri, C.-Y. Yin, X. Zhao, Z. Xie, X. Duan, H. Widjaja, M.M. Rahman, T. Pryor, Surface Electronic Structure and Mechanical Characteristics of Copper–Cobalt Oxide Thin Film Coatings: Soft X-ray Synchrotron Radiation Spectroscopic Analyses and Modeling, *The Journal of Physical Chemistry C*, 117 (2013) 16457-16467.

- [34] A. Amri, A. Fadli, Z.-T. Jiang, C.-Y. Yin, M.M. Rahman, H. Widjaja, S. Herman, S.R. Yenti, M.M. Munir, G. Priyotomo, M. Iqbal, N. Frimayanti, Surface structural and solar absorptance features of nitrate-based copper-cobalt oxides composite coatings: Experimental studies and molecular dynamic simulation, *Ceramics International*, DOI [https://doi.org/10.1016/j.ceramint.2018.05.171\(2018\)](https://doi.org/10.1016/j.ceramint.2018.05.171(2018)).
- [35] A. Amri, X. Duan, C.-Y. Yin, Z.-T. Jiang, M.M. Rahman, T. Pryor, Solar absorptance of copper–cobalt oxide thin film coatings with nano-size, grain-like morphology: Optimization and synchrotron radiation XPS studies, *Applied Surface Science*, 275 (2013) 127-135.
- [36] A. Amri, Z.-T. Jiang, N. Wyatt, C.-Y. Yin, N. Mondinos, T. Pryor, M.M. Rahman, Optical properties and thermal durability of copper cobalt oxide thin film coatings with integrated silica antireflection layer, *Ceramics International*, 40 (2014) 16569-16575.
- [37] O.T. Inal, A. Scherer, Optimization and microstructural analysis of electrochemically deposited selective solar absorber coatings, *Journal of Materials Science*, 21 (1986) 729-736.
- [38] C.G. Granqvist, V. Wittwer, Materials for solar energy conversion: An overview, *Solar Energy Materials and Solar Cells*, 54 (1998) 39-48.
- [39] W.F. Bogaerts, C.M. Lampert, Materials for photothermal solar energy conversion, *Journal of Materials Science*, 18 (1983) 2847-2875.
- [40] C.E. Kennedy, Review of Mid- to High-Temperature Solar Selective Absorber Materials, ; National Renewable Energy Lab., Golden, CO. (US), 2002, pp. Medium: ED; Size: 58 pages.
- [41] B. Seraphin, Topics in Applied Physics/ Solar Energy Conversion, Springer-Verlag, Berlin, Germany, 1979.
- [42] F. Zaversky, L. Aldaz, M. Sánchez, A.L. Ávila-Marín, M.I. Roldán, J. Fernández-Reche, A. Füssel, W. Beckert, J. Adler, Numerical and experimental evaluation and optimization of ceramic foam as solar absorber – Single-layer vs multi-layer configurations, *Applied Energy*, 210 (2018) 351-375.
- [43] Y. Okuhara, T. Kuroyama, D. Yokoe, T. Kato, M. Takata, T. Tsutsui, K. Noritake, High-temperature solar-thermal conversion by semiconducting  $\beta$ -FeSi<sub>2</sub> absorbers with thermally stabilized silver layers, *Solar Energy Materials and Solar Cells*, 174 (2018) 351-358.
- [44] Z. Crnjak Orel, M. Klanjšek Gunde, A. Lenčec, N. Benz, The preparation and testing of spectrally selective paints on different substrates for solar absorbers, *Solar Energy*, 69 (2001) 131-135.

- [45] M. Hirai, Y. Ueno, T. Suzuki, W. Jiang, C. Grigoriu, K. Yatsui, Characteristics of  $(\text{Cr}_{1-x}, \text{Al}_x)\text{N}$  films prepared by pulsed laser deposition, *Japanese Journal of Applied Physics, Part 1: Regular Papers and Short Notes and Review Papers*, 40 (2001) 1056-1060.
- [46] Y. Ide, T. Nakamura, K. Kishitake, M. Okumiya, M. Griepentrog, Mechanical properties and tribological behavior of TiN-CrAlN and CrN-CrAlN multilayer coatings, *Second International Conference on Processing Materials for Properties*. San Francisco, CA, 112 (2000) 291-128.
- [47] E. Lugscheider, K. Bobzin, S. Bärwulf, T. Hornig, Oxidation characteristics and surface energy of chromium-based hardcoatings for use in semisolid forming tools, *Surface and Coatings Technology*, 133-134 (2000) 540-547.
- [48] R.J. Smith, C. Tripp, A. Knospe, C.V. Ramana, A. Kayani, V. Gorokhovskiy, V. Shutthanandan, D.S. Gelles, Using CrAlN multilayer coatings to improve oxidation resistance of steel interconnects for solid oxide fuel cell stacks, *Journal of Materials Engineering and Performance*, 13 (2004) 295-302.
- [49] J. Vetter, E. Lugscheider, S.S. Guerreiro, (Cr:Al)N coatings deposited by the cathodic vacuum arc evaporation, *Surface and Coatings Technology*, 98 (1998) 1233-1239.
- [50] M. Okumiya, M. Griepentrog, Mechanical properties and tribological behavior of TiN-CrAlN and CrN-CrAlN multilayer coatings, *Surface and Coatings Technology*, 112 (1999) 123-128.
- [51] S. Zhang, H.L. Wang, S.E. Ong, D. Sun, X.L. Bui, Hard yet tough nanocomposite coatings - Present status and future trends, *Plasma Processes and Polymers*, 4 (2007) 219-228.
- [52] O. Banakh, P.E. Schmid, R. Sanjinés, F. Lévy, J.C. Sánchez-López, D. Martínez-Martínez, C. López-Cartes, A. Fernández, M. Brizuela, A. García-Luis, J.I. Oñate, Mechanical behavior and oxidation resistance of Cr(Al)N coatings, *Surf. Coat. Technol.*, 23 (2003) 681-686.
- [53] S. Ulrich, H. Holleck, J. Ye, H. Leiste, R. Loos, M. Stüber, P. Pesch, S. Sattel, Influence of low energy ion implantation on mechanical properties of magnetron sputtered metastable (Cr,Al)N thin films, *Thin Solid Films*, 437 (2003) 164-169.
- [54] J.C. Sánchez-López, D. Martínez-Martínez, C. López-Cartes, A. Fernández, M. Brizuela, A. García-Luis, J.I. Oñate, Mechanical behavior and oxidation resistance of Cr(Al)N coatings, *Journal of Vacuum Science and Technology A: Vacuum, Surfaces and Films*, 23 (2005) 681-686.
- [55] G.S. Kim, S.Y. Lee, Microstructure and mechanical properties of AlCrN films deposited by CFUBMS, *Surface and Coatings Technology*, 201 (2006) 4361-4366.

- [56] A.E. Reiter, V.H. Derflinger, B. Hanselmann, T. Bachmann, B. Sartory, Investigation of the properties of  $Al_{1-x}Cr_xN$  coatings prepared by cathodic arc evaporation, *Surface and Coatings Technology*, 200 (2005) 2114-2122.
- [57] M. Uchida, N. Nihira, A. Mitsuo, K. Toyoda, K. Kubota, T. Aizawa, E. Le Bourhis, P. Goudeau, M.H. Staia, E. Carrasquero, E.S. Puchi-Cabrera, Mechanical properties of hard AlCrN-based coated substrates, *Surf. Coat. Technol.*, 203 (2004) 2961-2968.
- [58] E. Le Bourhis, P. Goudeau, M.H. Staia, E. Carrasquero, E.S. Puchi-Cabrera, Mechanical properties of hard AlCrN-based coated substrates, *Surface and Coatings Technology*, 203 (2009) 2961-2968.
- [59] J. Musil, Hard and superhard nanocomposite coatings, *Surface and Coatings Technology*, 125 (2000) 322-330.
- [60] J. Musil, P. Karvánková, J. Kasl, Hard and superhard Zr-Ni-N nanocomposite films, *Surface and Coatings Technology*, 139 (2001) 101-109.
- [61] J. Musil, I. Leipner, M. Kolega, Nanocrystalline and nanocomposite CrCu and CrCu-N films prepared by magnetron sputtering, *Surface and Coatings Technology*, 115 (1999) 32-37.
- [62] J. Musil, P. Zeman, H. Hrubý, P.H. Mayrhofer, ZrN/Cu nanocomposite film - A novel superhard material, *Surface and Coatings Technology*, 120-121 (1999) 179-183.
- [63] P. Karvánková, H.D. Männling, C. Eggs, S. Vepřek, Thermal stability of ZrN-Ni and CrN-Ni superhard nanocomposite coatings, *Surface and Coatings Technology*, 146-147 (2001) 280-285.
- [64] S. Vepřek, S. Reiprich, L. Shizhi, Superhard nanocrystalline composite materials: The TiN/Si<sub>3</sub>N<sub>4</sub> system, *Applied Physics Letters*, DOI (1995) 2640.
- [65] S. Vepřek, The search for novel, superhard materials, *Journal of Vacuum Science and Technology A: Vacuum, Surfaces and Films*, 17 (1999) 2401-2420.
- [66] J. Lin, B. Mishra, J.J. Moore, W.D. Sproul, Microstructure, mechanical and tribological properties of  $Cr_{1-x}Al_xN$  films deposited by pulsed-closed field unbalanced magnetron sputtering (P-CFUBMS), *Surface and Coatings Technology*, 201 (2006) 4329-4334.
- [67] M. Zhou, Y. Makino, M. Nose, K. Nogi, Phase transition and properties of Ti-Al-N thin films prepared by r.f.-plasma assisted magnetron sputtering, *Thin Solid Films*, 339 (1999) 203-208.
- [68] W.D. Callister Jr, J. Lin, J.J. Moore, B. Mishra, M. Pinkas, W.D. Sproul, J.A. Rees, Effect of asynchronous pulsing parameters on the structure and properties of CrAlN films

- deposited by pulsed closed field unbalanced magnetron sputtering (P-CFUBMS), *Fundamentals of Materials Science and Engineering*, 202 (2001) 1418-1436.
- [69] J. Lin, J.J. Moore, B. Mishra, M. Pinkas, W.D. Sproul, J.A. Rees, Effect of asynchronous pulsing parameters on the structure and properties of CrAlN films deposited by pulsed closed field unbalanced magnetron sputtering (P-CFUBMS), *Surface and Coatings Technology*, 202 (2008) 1418-1436.
- [70] M. Mahbubur Rahman, A. Duan, Z.-T. Jiang, Z. Xie, A. Wu, A. Amri, B. Cowie, C.-Y. Yin, Near-edge X-ray absorption fine structure studies of Cr<sub>1-x</sub>M<sub>x</sub>N coatings, *Journal of Alloys and Compounds*, 578 (2013) 362-368.
- [71] D.P. Whittle, J. Stringer, *Phil. Trans. R. Soc. London*, 295 (1980) 309-329.
- [72] M.S. Ahmed, X. Zhao, Z.F. Zhou, P. Munroe, N. Chen-Tan, L.K.Y. Li, Z. Xie, Effect of thermal annealing upon residual stress and mechanical properties of nanostructured TiSiN coatings on steel substrates, *Journal of the American Ceramic Society*, 94 (2011) 1546-1551.
- [73] P. Eklund, S. Kerdsonpanya, B. Alling, Transition-metal-nitride-based thin films as novel energy harvesting materials, *Journal of Materials Chemistry C*, 4 (2016) 3905-3914.
- [74] G. Greczynski, L. Hultman, In-situ observation of self-cleansing phenomena during ultra-high vacuum anneal of transition metal nitride thin films: Prospects for non-destructive photoelectron spectroscopy, *Applied Physics Letters*, 109 (2016).
- [75] B.S. Yilbas, H. Ali, A. Al-Sharafi, N. Al-Aqeeli, N. Abu-Dheir, F. Al-Sulaiman, M. Khaled, Characteristics of a solar selective absorber surface subjected to environmental dust in humid air ambient, *Solar Energy Materials and Solar Cells*, 172 (2017) 186-194.
- [76] N. Selvakumar, S. Santhoshkumar, S. Basu, A. Biswas, H.C. Barshilia, Spectrally selective CrMoN/CrON tandem absorber for mid-temperature solar thermal applications, *Solar Energy Materials and Solar Cells*, 109 (2013) 97-103.
- [77] B.D. Beake, V.M. Vishnyakov, R. Valizadeh, J.S. Colligon, Influence of mechanical properties on the nanoscratch behaviour of hard nanocomposite TiN/Si<sub>3</sub>N<sub>4</sub> coatings on Si, *Journal of Physics D: Applied Physics*, 39 (2006) 1392.
- [78] X. Fang, Y. Bando, U.K. Gautam, T. Zhai, H. Zeng, X. Xu, M. Liao, D. Golberg, ZnO and ZnS Nanostructures: Ultraviolet-Light Emitters, Lasers, and Sensors, *Critical Reviews in Solid State and Materials Sciences*, 34 (2009) 190-223.
- [79] Z. Li, W.F. Ding, C.Y. Ma, J.H. Xu, Grinding temperature and wheel wear of porous metal-bonded cubic boron nitride superabrasive wheels in high-efficiency deep grinding, *Proceedings of the Institution of Mechanical Engineers, Part B: Journal of Engineering Manufacture*, 231 (2017) 1961-1971.

- [80] M.M.H. Bhuiyan, J. Wang, L.H. Li, P. Hodgson, A. Agarwal, M. Qian, Y. Chen, Boron nitride nanotube reinforced titanium metal matrix composites with excellent high-temperature performance, *Journal of Materials Research*, 32 (2017) 3744-3752.
- [81] E. Ríos, S. Abarca, P. Daccarett, H. Nguyen Cong, D. Martel, J.F. Marco, J.R. Gancedo, J.L. Gautier, Electrocatalysis of oxygen reduction on  $\text{Cu}_x\text{Mn}_{3-x}\text{O}_4$  ( $1.0 \leq x \leq 1.4$ ) spinel particles/polypyrrole composite electrodes, *International Journal of Hydrogen Energy*, 33 (2008) 4945-4954.
- [82] E. Szabados, A. Jobbágy, A.J. Tóth, P. Mizsey, G. Tardy, C. Pulgarin, S. Giannakis, E. Takács, L. Wojnárovits, M. Makó, Z. Trócsányi, A. Tungler, Complex treatment for the disposal and utilization of process wastewaters of the pharmaceutical industry, *Periodica Polytechnica Chemical Engineering*, 62 (2018) 76-90.
- [83] K. Song, D.A. Agyeman, M. Park, J. Yang, Y.M. Kang, High-Energy-Density Metal–Oxygen Batteries: Lithium–Oxygen Batteries vs Sodium–Oxygen Batteries, *Advanced Materials*, 29 (2017).
- [84] M. Islam, M.G. Jeong, J.Y. Hwang, I.H. Oh, Y.K. Sun, H.G. Jung, Self-assembled nickel-cobalt oxide microspheres from rods with enhanced electrochemical performance for sodium ion battery, *Electrochimica Acta*, 258 (2017) 220-227.
- [85] B.J. Arnold, S. Krishnamurthy, B. Kennedy, D. Cockburn, D. McNally, J.G. Lunney, R. Gunning, M. Venkatesan, J. Alaria, J. Michael, D. Coey, C. McGuinnessy, J.H. Guo, Growth and characterisation of  $\text{Al}_{1-x}\text{Cr}_x\text{N}$  thin films by RF plasma assisted pulsed laser deposition, *e-Journal of Surface Science and Nanotechnology*, 7 (2009) 497-502.
- [86] J.Y. Cheong, X.Z. Ding, B.K. Tay, X.T. Zeng, Thermal stability and oxidation resistance of CrAlSiN nano-structured coatings deposited by lateral rotating cathode arc, *Key Engineering Materials*, 2010, pp. 725-729.
- [87] S.R. Pulugurtha, D.G. Bhat, M.H. Gordon, J. Shultz, M. Staia, S.V. Joshi, S. Govindarajan, Mechanical and tribological properties of compositionally graded CrAlN films deposited by AC reactive magnetron sputtering, *Surface and Coatings Technology*, 202 (2007) 1160-1166.
- [88] J. Musil, Hard nanocomposite coatings: Thermal stability, oxidation resistance and toughness, *Surface and Coatings Technology*, 207 (2012) 50-65.
- [89] A. Mycielski, L. Kowalczyk, R.R. Gałazka, R. Sobolewski, D. Wang, A. Burger, M. Sowińska, M. Groza, P. Siffert, A. Szadkowski, B. Witkowska, W. Kaliszek, Applications of II-VI semimagnetic semiconductors, *Journal of Alloys and Compounds*, 423 (2006) 163-168.



- [90] F. Pan, C. Song, X.J. Liu, Y.C. Yang, F. Zeng, Ferromagnetism and possible application in spintronics of transition-metal-doped ZnO films, *Materials Science and Engineering R: Reports*, 62 (2008) 1-35.
- [91] Y.C. Yang, F. Pan, Q. Liu, M. Liu, F. Zeng, Fully room-temperature-fabricated nonvolatile resistive memory for ultrafast and high-density memory application, *Nano Letters*, 9 (2009) 1636-1643.
- [92] M.M. Rahman, Z.-T. Jiang, X. Duan, Z. Xie, A. Tadich, Z.-f. Zhou, N. Mondinos, C.-Y. Yin, M. Altarawneh, B.Z. Dlugogorski, NEXAFS N K-edge study of the bonding structure on Al/Si doped sputtered CrN coatings, *Journal of Alloys and Compounds*, 661 (2016) 268-273.
- [93] M.M. Rahman, Z.-T. Jiang, Z. Xie, X. Duan, Z.-f. Zhou, P.C. Wo, C.-Y. Yin, N. Mondinos, Q. Gu, H. Widjaja, K. Jack, A. Yago, A. Amri, Understanding Local Bonding Structures of Ni-Doped Chromium Nitride Coatings through Synchrotron Radiation NEXAFS Spectroscopy, *The Journal of Physical Chemistry C*, 118 (2014) 18573-18579.
- [94] D. Barbier, X. Orignac, X.M. Du, R.M. Almeida, X. Orignac, D. Barbier, X.M. Du, R.M. Almeida, Fabrication and characterization of sol-gel planar waveguides doped with rare-earth ions, *Proc. of Topical Symp. VII on Advanced Materials in Optics, Electro-Optics and Communication Technologies*, 69 (1995) 33-897.
- [95] X. Orignac, D. Barbier, X.M. Du, R.M. Almeida, Fabrication and characterization of sol-gel planar waveguides doped with rare-earth ions, *Applied Physics Letters*, 69 (1996) 895-897.
- [96] R.M. Almeida, X. Orignac, D. Barbier, Silica-based sol-gel films doped with active elements - Code: E4, *Journal of Sol-Gel Science and Technology*, 2 (1994) 465-467.
- [97] Y. Sorek, R. Reisfeld, I. Finkelstein, S. Ruschin, Sol-gel glass waveguides prepared at low temperature, *Applied Physics Letters*, 63 (1993) 3256-3258.
- [98] H. Morkoc, S. Strite, G.S. Gao, M.E. Lin, B. Sverdlov, M. Burns, M.L. Reed, N.A. El-Masry, H.H. Stadelmaier, M.K. Ritums, M.J. Reed, C.A. Parker, J.C. Roberts, S.M. Bedair, Room temperature ferromagnetic properties of (Ga, Mn)N, *J. Appl. Phys.*, 73 (1994) 3473-3475.
- [99] L. Cunha, M. Andritschky, K. Pischow, Z. Wang, Microstructure of CrN coatings produced by PVD techniques, *Thin Solid Films*, 355-356 (1999) 465-471.
- [100] C. Nouveau, M.A. Djouadi, O. Banakh, R. Sanjinés, F. Lévy, Stress and structure profiles for chromium nitride coatings deposited by r.f. magnetron sputtering, *Thin Solid Films*, 398-399 (2001) 490-495.

- [101] X. Guan, Y. Wang, G. Zhang, J. Xin, L. Wang, Q. Xue, A novel duplex PDMS/CrN coating with superior corrosion resistance for marine applications, *RSC Advances*, 6 (2016) 87003-87012.
- [102] P.Z. Shi, J. Wang, C.X. Tian, Z.G. Li, G.D. Zhang, D.J. Fu, B. Yang, Structure, mechanical and tribological properties of CrN thick coatings deposited by circular combined tubular arc ion plating, *Surface and Coatings Technology*, 228 (2013) S534-S537.
- [103] F.F. Klimashin, H. Riedl, D. Primetzhofer, J. Paulitsch, P.H. Mayrhofer, Composition driven phase evolution and mechanical properties of Mo–Cr–N hard coatings, *Journal of Applied Physics*, 118 (2015) 025305.
- [104] F.F. Klimashin, P.H. Mayrhofer, Ab initio-guided development of super-hard Mo–Al–Cr–N coatings, *Scripta Materialia*, 140 (2017) 27-30.
- [105] P.C. Wo, P.R. Munroe, Z. Li, Z.T. Jiang, Z.H. Xie, Z.F. Zhou, K.Y. Li, Factors governing the mechanical behaviour of CrSiN coatings: Combined nanoindentation testing and transmission electron microscopy, *Materials Science and Engineering: A*, 534 (2012) 297-308.
- [106] Z. Li, P. Munroe, Z.-t. Jiang, X. Zhao, J. Xu, Z.-f. Zhou, J.-q. Jiang, F. Fang, Z.-h. Xie, Designing superhard, self-toughening CrAlN coatings through grain boundary engineering, *Acta Materialia*, 60 (2012) 5735-5744.
- [107] P. Zeman, J. Musil, Difference in high-temperature oxidation resistance of amorphous Zr-Si-N and W-Si-N films with a high Si content, *Applied Surface Science*, 252 (2006) 8319-8325.
- [108] M. Hirai, Y. Ueno, T. Suzuki, W. Jiang, C. Grigoriu, K. Yatsui, Characteristics of CrN films prepared by pulsed laser deposition, *Japanese Journal of Applied Physics, Part 1: Regular Papers and Short Notes and Review Papers*, 40 (2001) 1052-1055.
- [109] M. Hirai, H. Saito, T. Suzuki, H. Suematsu, W. Jiang, K. Yatsui, Oxidation behavior of Cr-Al-N-O thin films prepared by pulsed laser deposition, *Thin Solid Films*, 407 (2002) 122-125.
- [110] M. Hirai, T. Suzuki, H. Suematsu, W. Jiang, K. Yatsui, Mechanism of hardening in Cr-Al-N-O thin films prepared by pulsed laser deposition, *Journal of Vacuum Science and Technology A: Vacuum, Surfaces and Films*, 21 (2003) 947-954.
- [111] A.D. Pogrebnjak, A.P. Shpak, N.A. Azarenkov, V.M. Beresnev, Structures and properties of hard and superhard nanocomposite coatings, *Physics-Uspekhi*, 52 (2009) 29-54.

- [112] Y.J. Kim, H.Y. Lee, Y.M. Kim, K.S. Shin, W.S. Jung, J.G. Han, Structure and mechanical properties of ZrCrAlN nanostructured thin films by closed-field unbalanced magnetron sputtering, *Surface and Coatings Technology*, 201 (2007) 5547-5551.
- [113] J.W. Lee, S.T. Chang, H.W. Chen, C.H. Chien, J.G. Duh, C.J. Wang, Microstructure, mechanical and electrochemical properties evaluation of pulsed DC reactive magnetron sputtered nanostructured Cr-Zr-N and Cr-Zr-Si-N thin films, *Surface and Coatings Technology*, 205 (2010) 1331-1338.
- [114] S.Y. Lee, Y.S. Kim, G.S. Kim, Thermal stability and tribological properties of CrZr-Si-N films synthesized by closed field unbalanced magnetron sputtering, *Journal of Vacuum Science and Technology A: Vacuum, Surfaces and Films*, 27 (2009) 867-872.
- [115] P.H. Mayrhofer, H. Willmann, C. Mitterer, Oxidation kinetics of sputtered Cr-N hard coatings, *Surface and Coatings Technology*, 146-147 (2001) 222-228.
- [116] M. Cekada, P. Panjan, M. Maček, P. Šmíd, Comparison of structural and chemical properties of Cr-based hard coatings, *Surface and Coatings Technology*, 151-152 (2002) 31-35.
- [117] P.E. Gannon, C.T. Tripp, A.K. Knospe, C.V. Ramana, M. Deibert, R.J. Smith, V.I. Gorokhovskiy, V. Shutthanandan, D. Gelles, High-temperature oxidation resistance and surface electrical conductivity of stainless steels with filtered arc Cr-Al-N multilayer and/or superlattice coatings, *Surface and Coatings Technology*, 188-189 (2004) 55-61.
- [118] J.H. Hsieh, C. Li, A.L.K. Tan, C.K. Poh, N.J. Tan, Study of oxidation and wear behaviors of (Nb,Cr)N thin films using Raman spectroscopy, *Surface and Coatings Technology*, 177-178 (2004) 299-305.
- [119] J.H. Hsieh, W.H. Zhang, C. Li, C.Q. Sun, Characterization of  $(\text{Ti}_x \text{Cr}_{0.6-x}) \text{N}_{0.4}$  coatings and their tribological behaviors against an epoxy molding compound, *Surface and Coatings Technology*, 146-147 (2001) 331-337.
- [120] K. Yamamoto, T. Sato, K. Takahara, K. Hanaguri, Properties of (Ti,Cr,Al)N coatings with high Al content deposited by new plasma enhanced arc-cathode, *Surface and Coatings Technology*, 174-175 (2003) 620-626.
- [121] W.Z. Li, M. Evaristo, A. Cavaleiro, Influence of Al on the microstructure and mechanical properties of Cr-Zr-(Al)-N coatings with low and high Zr content, *Surface and Coatings Technology*, 206 (2012) 3764-3771.
- [122] G. Kim, B. Kim, S. Lee, J. Hahn, Structure and mechanical properties of Cr-Zr-N films synthesized by closed field unbalanced magnetron sputtering with vertical magnetron sources, *Surface and Coatings Technology*, 200 (2005) 1669-1675.

- [123] R. Lamni, R. Sanjińs, M. Parlinska-Wojtan, A. Karimi, F. lvy, Microstructure and nanohardness properties of Zr-Al-N and Zr-Cr-N thin films, *Journal of Vacuum Science and Technology A: Vacuum, Surfaces and Films*, 23 (2005) 593-598.
- [124] I.W. Park, D.S. Kang, J.J. Moore, S.C. Kwon, J.J. Rha, K.H. Kim, Microstructures, mechanical properties, and tribological behaviors of Cr-Al-N, Cr-Si-N, and Cr-Al-Si-N coatings by a hybrid coating system, *Surface and Coatings Technology*, 201 (2007) 5223-5227.
- [125] Q.M. Wang, K.H. Kim, Microstructural control of Cr-Si-N films by a hybrid arc ion plating and magnetron sputtering process, *Acta Materialia*, 57 (2009) 4974-4987.
- [126] T. Polcar, R. Martinez, T. Vítu, L. Kopecky, R. Rodriguez, A. Cavaleiro, High temperature tribology of CrN and multilayered Cr/CrN coatings, *Surface and Coatings Technology*, 203 (2009) 3254-3259.
- [127] H.C. Barshilia, N. Selvakumar, K.S. Rajam, D.V. Sridhara Rao, K. Muraleedharan, A. Biswas, TiAlN/TiAlON/Si<sub>3</sub>N<sub>4</sub> tandem absorber for high temperature solar selective applications, *Applied Physics Letters*, 89 (2006) 1919-191911.
- [128] A. Satta, G. Beyer, K. Maex, K. Elers, S. Haukka, A. Vantomme, Properties of TiN thin films deposited by ALCVD as barrier for CU metallization, *Materials Research Society Symposium - Proceedings*, 612 (2000) D651-D656.
- [129] N. Selvakumar, N.T. Manikandanath, A. Biswas, H.C. Barshilia, Design and fabrication of highly thermally stable HfMoN/HfON/Al<sub>2</sub>O<sub>3</sub> tandem absorber for solar thermal power generation applications, *Solar Energy Materials and Solar Cells*, 102 (2012) 86-92.
- [130] A. Schuler, V. Thommen, P. Reimann, P. Oelhafen, G. Francz, T. Zehnder, M. Duggelin, D. Mathys, R. Guggenheim, Structural and optical properties of titanium aluminum nitride films (Ti<sub>1-x</sub>Al<sub>x</sub>N), *Journal of Vacuum Science and Technology A*, 19 (2001) 922-929.
- [131] K. Ibrahim, M. Mahbubur Rahman, H. Taha, E. Mohammadpour, Z. Zhou, C.-Y. Yin, A. Nikoloski, Z.-T. Jiang, Structural, morphological, and optical characterizations of Mo, CrN and Mo:CrN sputtered coatings for potential solar selective applications, *Applied Surface Science*, 440 (2018) 1001-1010.
- [132] K. Ibrahim, M.M. Rahman, X. Zhao, J.-P. Veder, Z.-f. Zhou, E. Mohammadpour, R.H. Majeed, A.N. Nikoloski, Z.-T. Jiang, Annealing effects on microstructural, optical, and mechanical properties of sputtered CrN thin film coatings: Experimental studies and finite element modeling, *Journal of Alloys and Compounds*, 750 (2018) 451-464.

- [133] I. Khalil, T. Hatem, M.M. Rahman, K. Humayun, J. Zhong-Tao, Solar selective performance of metal nitride/oxynitride based magnetron sputtered thin film coatings: a comprehensive review, *Journal of Optics*, 20 (2018) 033001.
- [134] M.S. Prasad, B. Mallikarjun, M. Ramakrishna, J. Joarder, B. Sobha, S. Sakthivel, Zirconia nanoparticles embedded spinel selective absorber coating for high performance in open atmospheric condition, *Solar Energy Materials and Solar Cells*, 174 (2018) 423-432.
- [135] K. Zhang, M. Du, L. Hao, J. Meng, J. Wang, J. Mi, X. Liu, Highly Corrosion Resistant and Sandwich-like  $\text{Si}_3\text{N}_4/\text{Cr-CrN}_x/\text{Si}_3\text{N}_4$  Coatings Used for Solar Selective Absorbing Applications, *ACS Applied Materials and Interfaces*, 8 (2016) 34008-34018.
- [136] I. Heras, E. Guillén, F. Lungwitz, G. Rincón-Llorente, F. Munnik, E. Schumann, I. Azkona, M. Krause, R. Escobar-Galindo, Design of high-temperature solar-selective coatings based on aluminium titanium oxynitrides  $\text{Al}_y\text{Ti}_{1-y}(\text{O}_x\text{N}_{1-x})$ . Part 1: Advanced microstructural characterization and optical simulation, *Solar Energy Materials and Solar Cells*, 176 (2018) 81-92.

## CHAPTER TWO

---

### **Paper I: Solar Selective Performance of Metal Nitride and Metal Oxynitride Based Sputtered Coatings: A Comprehensive Review**

---

#### **Abstract**

Since solar thermal collectors are considered to be the most direct way of converting the solar energy into the usable form, in the last few years growing attention has been paid to the development of transition metal nitride and metal oxynitride based thin film selective surfaces for solar-thermal collectors in order to harvest more solar energy. A solar-thermal energy system, generally, shows very high solar absorption of incident solar radiation from the solar-thermal collectors in the visible range (0.3 to 2.5  $\mu\text{m}$ ) and extremely low thermal losses through emission (or high reflection) in the infrared region ( $\geq 2.5 \mu\text{m}$ ). The efficiency of a solar-thermal energy conversion system can be improved by the use of solar selective surfaces consisting of novel metallic nanoparticles surrounded in metal nitride/oxynitrides systems. In order to enhance the effectiveness of solar thermal devices, solar selective surfaces with high thermal stability are a prerequisite. Over the years, substantial efforts have been made in the field of solar selective surfaces to attain higher solar absorptance and lower thermal emittance at high temperature (above 400  $^{\circ}\text{C}$ ) applications. In this article, we review the present state-of-the-art transition metal nitride and/or oxynitrides based vacuum sputtered nanostructured thin film coatings with respect to their optical and solar selective surface applications. We have also summarized the solar selectivity data from recent published literature investigations, including discussion on some potential applications for these materials.

#### **2.1 General Introduction**

Over the years, scientists and technologists around the world have been showing enormous research interest in investigating the transition metal nitride thin films based large band-gap semiconductors in their pure state and with various dopants, because of their widespread applications in spintronics and nonvolatile storage devices [1-3]. Binary nitride films such as AlN, GaN and InN have been extensively used in light emitters and detectors (in ultraviolet and visible range), and optical storage devices [4]. Each of these materials has a wide band-gap. Due to their exceptional thermal and chemical stability and higher physical hardness, GaN and AlN are also very popular in microelectronic applications [5]. Silicon and silicon-titanium based nitride thin films are largely used in many optical

devices such as active and passive optical planar waveguides, and antireflecting coatings [6, 7]. Due to their enhanced mechanical and functional features such as superelasticity and shape memory effects, TiNi-based nitride alloys are widely used in the design of instruments, aerospace technologies and medicine [8, 9]. The incorporation of an appropriate amount of additive can remarkably improve the properties of such materials by inducing various defects such as vacancy, atom substitution, deformation, and cluster formation [10]. In a recent report, C-doping on CrAlN carried out by Zeng *et al.* [10] confirmed that C-doped dispersed clusters results in superior resistivity at low frequency. Structural, optical and electrical properties of Mn- and Cr-added GaN diluted magnetic semiconductors (DMSs) were inspected for their potential applications in electronic and spin-dependent photonics [11-13]. Endrino *et al.* [14] studied the effect of Si on the TiN and AlCrN thin films *via* XRD and NEXAFS methods. The addition of Si to the transition metal nitride matrix can remarkably improve their physical hardness, toughness and oxidation resistance [15, 16]. However, a higher amount of Si-content results in lowering the crystallinity by forming the amorphous silicon nitride ( $\text{Ni}_3\text{N}_4$ ) phase [14].

The transition metal nitride based coatings are considered as potential candidates to be used in solar selective surface applications due to a good combination of chemical-, corrosion-, oxidation-, and wear resistance behaviours, extraordinary thermal stability and tunable optical properties *e.g.*, refractive index, absorptance, reflectance and transmittance [17-20]. Despite their technological importance, thus far there have been a very limited number of investigations on optical selectivity in the presence of various dopants. For the selective surface applications, these coatings must possess high solar absorption in the visible range and low thermal emittance in the infrared range of the solar spectra. Widespread applications and steadily increasing scientific interests in transition metal nitrides have been dedicated to the development of new thin film composites with superior properties. Properties of nanocomposite transition metal nitrides can be controlled by the type and level of elemental dopant and fabrication procedure. Nanocrystalline transition metal nitrides, carbides and carbonitrides are investigated due to their interesting optical and decorative properties [21-25]. Correlations between chemical structure and optical properties [21, 22, 25], and structural morphology and optical behaviours of CrN, ZrN, TiN systems have been established [21]. Interrelationships among the mechanical properties, chemical composition, optical properties, and crystal structure of DC magnetron sputtered metal nitride thin film coatings was investigated by Zeman *et al.* [26]. Nanocrystalline titanium nitride thin films have applications in different areas of semiconductor device

technology *e.g.*, gate electrodes in field-effect transistors, Al diffusion barriers, and ultra-large scale integrated circuits [27-29]. The electronic properties of titanium nitrides and carbides have been extensively studied under different experimental and theoretical approaches [30-34], however optical studies of these materials has not received significant concentration either experimentally or theoretically [30, 35, 36], especially the solar selectivity studies are quite rare [37-43].

The optical analysis of solid materials is very important in order to understand their fundamental characteristics, find their preferable device applications, and identifying other potential zones in which they would demonstrate higher competence. Furthermore, from the simple dispersion relation of refractive index of a solid material, the oscillator energy  $E_0$ , dispersion energy parameter  $E_d$ , the refractive index at zero photon energy  $n_0$ , dielectric constant at high frequency  $\epsilon_\infty$ , the oscillator position  $\lambda_0$ , the oscillator strength  $S_0$ , and loss tangent, volume and surface energy losses are calculated. To date, there has been much scientific articles that have expounded the correspondence between electronic structure and phase stability of metal nitride based films [44, 45]. Transition metal nitride based thin film coatings also have been found their prospective applications as high temperature structural materials and gate dielectrics in microstructural devices [46]. Meanwhile, attempts at producing new doping materials and research on improving their unique properties are still ongoing [47]. To the best of our knowledge, comprehensive studies on optical and dispersion analysis of transition metal nitride based thin film materials have not been carried out. In view of these issues, this paper intends to build up a systematic theoretical background in studying the optical, electronic and dielectric behaviors of transition metal nitride based thin film coating together with a focus onto the recent development of such thin film composites for the applications of solar selective surfaces. Thus, it is believed that this review work would provide substantial theoretical aspects and some recent experimental data on the solar selectivity values of transition metal nitride based thin film coatings and assist researchers to carry out research in this field.

## **2.2 Optical Properties of Materials**

The optical properties of a material mean its response after being exposed to the electromagnetic spectrum of solar radiation. When a solar radiation is incident upon a material's surface, electromagnetic radiation may be reflected back, refracted through the material, absorbed by the material, transmitted through the materials, scattered by atoms and molecules, and so on. Interactions of light with matters predominantly depend upon



the frequency of the incident radiation and the characteristics of the atoms in the materials. In the subsequent sections, we introduce some fundamental optical parameters, theories, principles and concepts associating with the behaviors of electromagnetic radiation and their interactions with materials.

### 2.2.1 Optical Parameters

Upon the incidence and interactions of solar (or electromagnetic) radiation onto the surface of an object, depending on the energy of the incident photon and nature of the atoms of the material, a large number of various phenomena could arise. In the following sections, we discuss some of the specific optical parameters within the scope of this study.

#### 2.2.1.1 Optical Reflection

As the light is incident on a surface at a certain specific angle, it changes the direction at the interface of two media and returns back into the medium from which it has originated. Reflection of light depends on the nature of the interface. Generally, reflection of light arises whenever light passes through the interface of two media having two different refractive indices and surface roughness. It is to be noted that a small fraction of the incident light is reflected from the interface while the rest is refracted through the surface. Reflection of light obeys the following rules:

- a. The incident beam, reflected beam and the normal to the reflection surface all lie in the plane of incidence.
- b. The angle of incidence must be equal to the angle of reflection.

Reflectivity or reflectance is also defined as the fraction of the incident light that is reflected at the interface. In mathematical form it is expressed as,

$$R = \frac{I_R}{I_0} \quad (1)$$

where  $I_R$  and  $I_0$  are the intensities of the incident and reflected light respectively. In the case of normal incidence the reflectivity is measured by Fresnel's equation

$$R = \frac{(n_2 - n_1)^2}{(n_2 + n_1)^2} \quad (2)$$

where  $n_1$  and  $n_2$  are the indices of refraction of two media. However, if the incident beam is not perpendicular to the interface,  $R$  will be a function of the angle of incidence. Since the index of reflection of air is near about unity, hence when light travels from air into a solid medium the reflectivity is given as,

$$R = \frac{(n_1 - 1)^2}{(n_s + 1)^2} \quad (3)$$

Accordingly, the higher the index of refraction of the solid medium, the lower the reflectivity is. The refractive index of a solid material depends on the incident beam's wavelength, thereby the reflectivity also varies with the wavelength.

### 2.2.1.2 Optical Refraction and Refractive Index

Two optical constants: refractive index ( $n$ ) and the extinction coefficient ( $k$ ) are conveniently used to represent the propagation of electromagnetic waves and the dissipation of energy in the medium of propagation. Assuming the material to extend indefinitely, the complex refractive index can be defined by the following function,

$$\begin{aligned}\tilde{N} = n + ik &= \left[ \epsilon\mu + i \frac{4\pi\mu\sigma}{\omega} \right]^{\frac{1}{2}} \\ &= \left[ \mu \left( \epsilon + i \frac{4\pi\sigma}{\omega} \right) \right]^{\frac{1}{2}} \\ &= [\mu\tilde{\epsilon}]^{\frac{1}{2}}\end{aligned}\quad (4)$$

Complex wave vector,

$$\bar{q} = \frac{\omega}{c} \tilde{N} = \frac{n\omega}{c} + i \frac{k\omega}{c} \quad (5)$$

where the refractive index  $n$  and the extinction coefficient  $k$  are defined in terms of by the conductivity ( $\sigma_1$ ), the permeability ( $\mu_1$ ), and the dielectric constant ( $\epsilon_1$ ):

$$n^2 = \frac{\mu}{2} \left[ \left\{ \epsilon^2 + \left( \frac{4\pi\sigma}{\omega} \right)^2 \right\}^{1/2} + \epsilon \right] \quad (6)$$

$$k^2 = \frac{\mu}{2} \left[ \left\{ \epsilon^2 + \left( \frac{4\pi\sigma}{\omega} \right)^2 \right\}^{1/2} - \epsilon \right] \quad (7)$$

Equations (6) and (7) relate to the propagation of the electromagnetic waves in the matter. The quantities  $\epsilon$ ,  $\sigma$  and  $\mu$  are defined only when  $\omega = 0$ . Thus, in terms of  $n$  and  $k$  the dielectric constant, permeability and conductivity are expressed:

$$n^2 - k^2 = \epsilon\mu \quad (8)$$

$$2nk = \frac{4\pi\mu\sigma}{\omega} \quad (9)$$

Thus, Eq. (4) can be rearranged as,

$$\tilde{N}^2 = \left[ \mu \left( \epsilon + i \frac{4\pi\sigma}{\omega} \right) \right] = \mu\tilde{\epsilon} \approx \frac{4\pi i \mu \tilde{\sigma}}{\omega} \quad (10)$$

The absolute value of  $\tilde{N}$  and the phase difference  $\phi$  between the magnetic and dielectric field vectors are given by,

$$|\tilde{N}| = (n^2 + k^2)^{\frac{1}{2}} \quad (11)$$

$$\tan\phi = \frac{k}{n} \quad (12)$$

In an ideal insulator or in free space, the electric and magnetic fields are in phase because  $k = 0$ . However in a metal at low frequencies,  $n \approx k$  and phase difference  $\phi = 45^\circ$ .

### 2.2.1.3 Optical Scattering

Scattering is a physical process where various types of waves (light, sound etc) or particles are deviated from their straight trajectory due to some localized irregularities in the medium which they pass through or at the interface between two media. Scattering may arise as a result of the physical collision between electrons, protons, atoms, molecules, photon or other kinds of particles. Absorption and scattering are two major physical processes that contribute to the visible appearance of most objects. The visual appearance of an object which is described as white is caused by the multiple scattering of light by internal or surface inhomogeneity. A highly scattering surface of an object appears dusty or dull whereas in the absence of scattering the object exhibits a refined and glossy appearance. Scattering in light can be caused via two mechanisms: surface scattering and volume scattering. Surface scattering emerges from the interaction of photons of light with the surface of a material, while volume scattering occurs only in the bulk of the material and is completely independent of the surfaces of the material. Surface scattering of light is a consequence of the interaction of light photons with the electric field of a particle or molecule of a material. The incident photons induce oscillating dipoles around the electron cloud and radiate energy in all possible directions. This radiated energy is known as the scattering of light. Scattering of light by individual particles depends on the particle's size, refractive index and wavelength of the incident light.

### 2.2.1.4 Solar Absorptance

A material can absorb the solar radiation either *via* electronic polarization or valence band-conduction band electron transitions. The first kind of absorption arises at light frequencies around the relaxation frequency of the constituent atoms, while the second mechanism depends on the energy band-gap, and band structures of materials. When solar radiation is incident upon the surface of a material, it is absorbed by the excitation of an electron from the nearly filled valence band travels across the band gap, and into an empty state within the conduction band. Consequently, a free electron is created in the conduction band leaving a hole behind the valence band. Absorption of light obeys the following relationship,

$$h\nu \geq E_g \quad (13)$$

which can be written as,

$$\frac{hc}{\lambda} \geq E_g \quad (14)$$

The maximum and minimum energy band-gap at which light is absorbed are expressed as,

$$E_g(\text{max}) = \frac{hc}{\lambda_{\min}} \quad (15)$$

$$E_g(\text{min}) = \frac{hc}{\lambda_{\max}} \quad (16)$$

However, the intensity of the absorbed solar radiation depends on the nature of the medium and exponentially decreases with distance traversed by the light according to the following relation,

$$I = I_0 e^{-\beta x} \quad (17)$$

where  $x$  is the intensity of the incident radiation and  $\beta$  is the absorption coefficient, characteristic of the particular material. Materials that possess large  $\beta$  are highly absorptive. Upon the incidence of solar radiation into the surface of a material, some part of the light is absorbed, some portion is reflected back to the medium while the rest being transmitted through the material

According to the principle of conservation of energy, the summation of the solar absorptance, reflectance and transmittance is unity.

$$\alpha(\lambda) + \rho(\lambda) + t(\lambda) = 1 \quad (18)$$

For a highly reflecting or opaque surface, the transmission coefficient is zero *i.e.*,  $t(\lambda) = 0$  and energy is absorbed or reflected from all directions. In thermodynamic equilibrium, for a certain specific wavelength the absorptance of an object is equal to the emittance. Hence, Eq. (18) can be written as,

$$\alpha(\lambda) = \varepsilon(\lambda) = 1 - \rho(\lambda) \quad (19)$$

The solar absorptance of a material's surface is defined as a fraction of the solar radiation incident on the surface of the material that is absorbed. According to Duffie and Beckman method, the solar absorptance of a material can be conveniently computed using following relationship [48],

$$\alpha = \frac{\int_0^{\infty} I_s(\lambda)(1-\rho(\lambda))d\lambda}{\int_0^{\infty} I_s(\lambda)d\lambda} \quad (20)$$

where  $\rho(\lambda)$  is the reflectance as a function of the wavelength,  $\lambda$  and  $I_s$  is the intensity distribution of the incoming photons.

In the solar absorption process of solar selective coatings, the valence electrons absorb energy from the sunlight and jump into the conduction bands. But the essential condition has to be satisfied is 'the energy of photons must be equal to greater less than the gap of

forbidden energy band as described in Eq. (13). Generally, the transition metals Cr, Mn, Ni, Mo, etc have excellent forbidden energy gaps, and after the introduction of various doping (oxide or nitride or oxynitride) they become outstanding absorbing materials.

#### 2.2.1.5 Thermal Emittance

The thermal emittance of an absorbing medium is defined as the weighted fraction of the emitted solar radiation and can be calculated using the intensity distribution of a blackbody spectrum within the operating temperature. According to Duffie and Beckman method, the thermal emittance of a material is defined as [48],

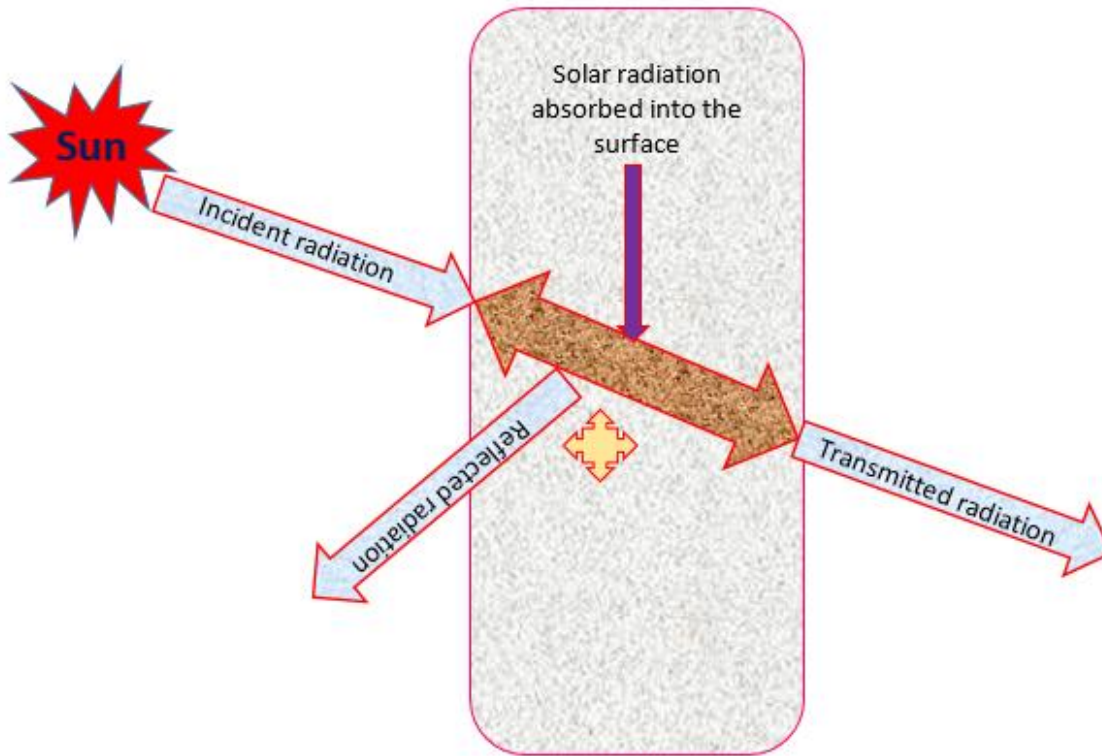
$$\varepsilon = \frac{\int_0^{\infty} I_p(\lambda)(1-\rho(\lambda))d\lambda}{\int_0^{\infty} I_p(\lambda)d\lambda} \quad (21)$$

where  $I_p$  is the intensity distribution of the Planck black-body.

The solar absorptance and thermal emittance are material-dependent parameters which can be calculated using the optical reflectance data of UV-Vis and FTIR measurements of materials within a certain wavelength range.

#### 2.2.1.6 Solar Selectivity

Generally, an ideal solar selective surface would have zero reflectance in the visible range of the solar spectrum and 100% reflectance in the infrared region of the solar spectrum which corresponds to the thermal radiation spectrum of a blackbody at the operating temperature of the absorbing surface. In real life, no such ideally selective surface exists that absorbs 100% of the incident solar radiation in the visible range and reflects 100% of the incident solar radiation in the IR range. However, in the laboratory we can fabricate solar selective materials that can maximize the solar absorption in the visible range and minimize the energy lost *via* thermal emittance. A very common way of preparing a solar selective surface is to apply a highly solar absorptive thin film onto a non-selective highly reflective metal substrate which is generally known as absorber–reflector tandem system. Absorption, transmission and emission from such an absorber–reflector tandem system are depicted in Figure 1.

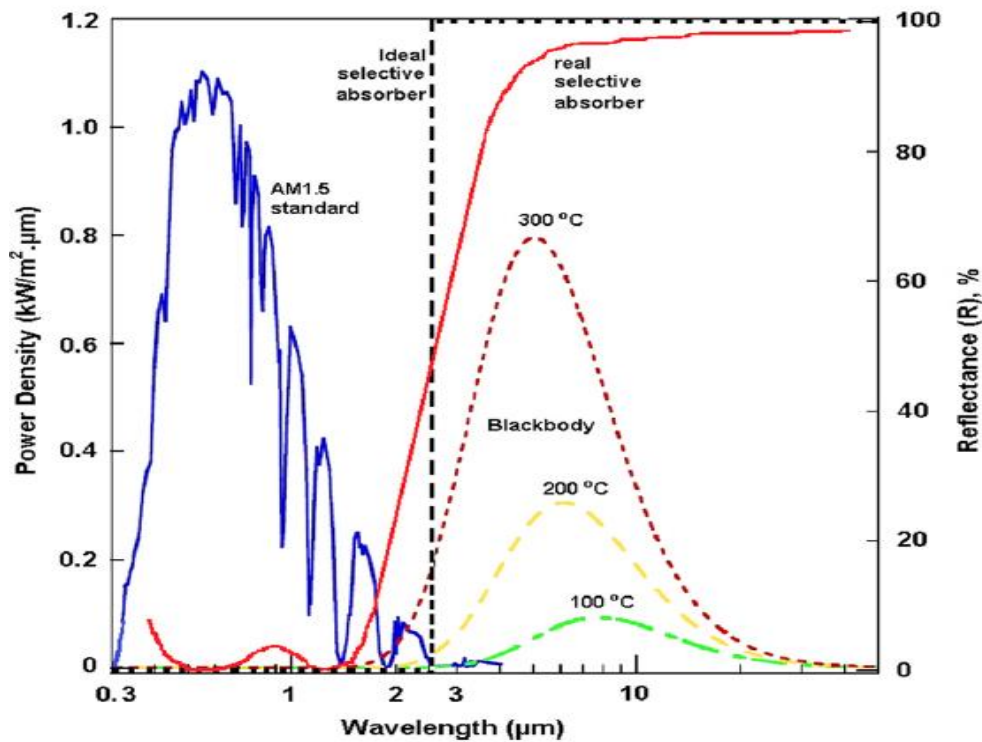


**Figure 1.** Phenomenon of absorption, reflection and transmission of solar radiation.

The spectral features of an ideal solar selective surface and the basis of a real solar selective surface are clearly demonstrated in Figure 2 [49]. At earth's surface, the incident solar flux is limited to the range between 0.3 and 2.5  $\mu\text{m}$  (in the UV-Vis-NIR wavelength range) with the maximum solar intensity at 0.55  $\mu\text{m}$ . In the infrared and far-infrared (IR-FIR) range of the solar spectrum, the optical response of a real material can be characterized by its thermal emission compared to an ideal blackbody at 100, 200 and 300  $^{\circ}\text{C}$ . Figure 2 indicates that as the temperature of the blackbody increases, energy emission is increased and the peak positions are moved towards the shorter wavelength sides of the spectrum. These features indicate the potential of patterning a material that absorbs the maximum amount of incident solar radiation and reemits a minimum amount of the absorbed radiation. This is the fundamental concept of forming an ideal solar selective surface. The performance criterion of a solar selective surface is, generally, evaluated by the ratio of the solar absorptance ( $\alpha$ ) to the thermal emittance ( $\varepsilon$ ) via following relation,

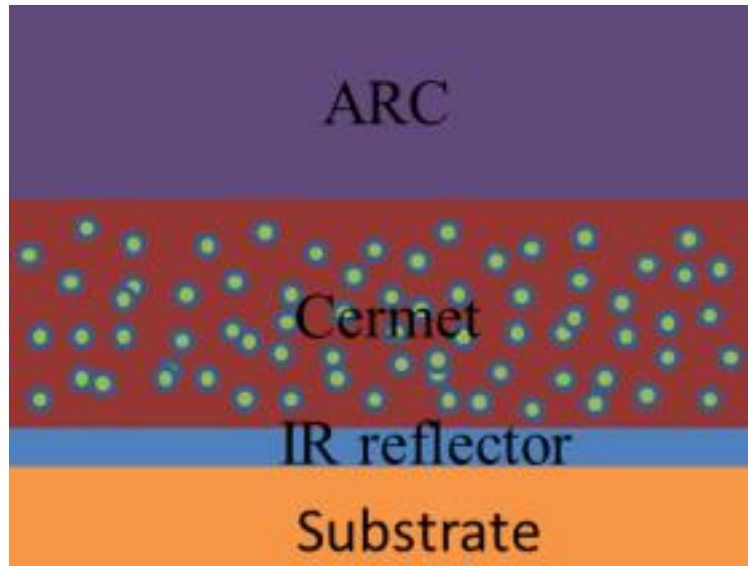
$$s = \frac{\alpha}{\varepsilon} \quad (22)$$

This important parameter,  $s$  is known as the solar selectivity of the solar selective surface.



**Figure 2.** Spectral features of an ideal and real solar selective surface, the solar spectrum at AM 1.5 (ISO standard 9845-1 (1992)) and the blackbody-like emission spectra at temperatures 100, 200 and 300 °C. Reprinted with permission from Ref. [49].

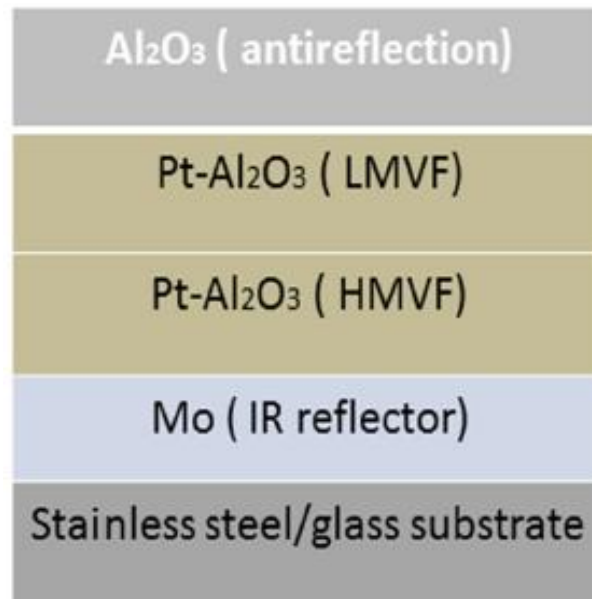
In a typical solar thermal conversion system, the sunlight is strongly absorbed as heat at the absorbing surface and a very little portion of the incident solar radiation is lost to the environment *via* convection and radiation. As already described, an absorbing surface, which absorbs the major portion of the incident photons and has very low infrared emittance, is known as the solar selective surface. A spectrally selective absorbing surface based on cermets are composed of ceramics and metal components. An effective spectrally selective surface can be formed by integrating with an antireflection coating (ARC) and an infrared-reflective base layer as depicted in the following Figure 3.



**Figure 3.** The anti-reflection coating (ARC) helps to reduce solar reflection off the surface; the cermet provides solar absorption; and the IR reflector (*e.g.*, Cu, Al, Mo, or other metal with low intrinsic emissivity) aids to decrease the radiation losses. The substrate can be either a metal or a glass. Reprinted with permission from Ref. [50].

Double cermets based selective solar coatings can be deposited onto metal (stainless steel, SS) or glass substrates using sputtering system. A multilayer film was deposited on flexible metal or glass substrates: from the bottom side, a Mo IR reflector layer, a high metal volume fraction (HMVF) metal oxide layer, a low metal volume fraction (LMVF) layer, and an antireflection coating on the top of film surface (see Figure 4) [51]. Another similar type of solar selective design has been proposed elsewhere [52]. Each layer deposited onto glass and stainless steel substrates in order to successive measure of the film thickness, reflectance, and transmittance, respectively.





**Figure 4.** Solar selective designs of cermet based solar selective surface. Reprinted with permission from Ref. [51].

In a cermet based solar selective coating, metal component is surrounded in the dielectric matrix by a metal oxide, metal nitride, or metal oxynitride constituents. A cermet shows ceramic behaviors in the visible range of the solar spectrum and metallic properties in the infrared spectrum. The film thickness, constituents, particle size, shape and orientation, and metal volume fraction in the matrix, strongly affect the ceramic and metallic properties exhibited across the visible and infrared spectra. Higher film thickness and reduced particle sizes are favorable for higher solar absorptance, while an increase in particle radius results in an alteration of the solar absorption and scattering, and thereby causing a lower absorption in the visible spectra. At the same time, the thermal emittance in the can be decreased by reducing the film thickness and increasing the metal volume fraction [53]. In general, smaller size particles are influenced by the interference phenomena and are more sensitive to thickness changes. Thus, the desired optical properties of the cermet based solar selective coatings can be achieved by optimizing the film thickness and particle diameter. The microstructure and spectral selectivity of a series of thin films based solar selective cermets coating integrated with  $\text{Al}_2\text{O}_3$  antireflection layer exhibited a high solar absorptance of 0.92 and a relatively low thermal emittance of 0.19 at 80 °C [54]. However, after the films being annealed at 800 °C for 2 hours in vacuum, the solar absorptance was dwindled to 0.91 and the thermal emittance attained to 0.27. It is suspected that after high temperature annealing, some defects such as widened the grain boundaries, cracks and

holes were initiated around the Al<sub>2</sub>O<sub>3</sub> layer, which induces the Mo diffusion, and worsen the spectral selectivity values of the deposited coatings. During the high temperature annealing, the microstructure of solar selective coatings is changed which also plays an important role in altering the solar selectivity behaviors because grain size of the coatings is diligently associated with the optical properties. As the grain size is decreased, the scattering of the ultraviolet light (within the range of 300-400 nm) gets stronger and thereby reduce the reflectance. The solar absorptance of AlCrON coatings was increased, while the grain size was decreased, after the samples being annealed at 500 °C in air [55]. In another study, Zheng *et al.* [56] reported that vacuum annealing at 600 °C causes the refinement of Mo grains, forming a denser and compact cermet layer. Consequently, the solar thermal conversion efficiency was increased by 0.6%, however 800 °C annealing resulted to the anomalous growth of Mo grains, and a decrement of the solar thermal conversion efficiency by 1.3%. This reveals the fact that the grain boundaries and interfaces have excess energy after synthesis of the films, and the minimization of the total energy delivers a driving force of the grain size refinements. It is also assumed that with the increase of heat treatment duration, the residual stress will release *via* boundary diffusions or atomic movements, and thus enables the grain size refinements. Apart from abnormal grain size refinements, there exist many other defects that intensely impact the various properties of solar selective coatings, such as widened interface, presence of water molecules, oxidations, presence of cavity, and cracks.

### 2.3 Other Optical Properties

Generally, optical studies of materials are predominantly based on the transmittance and/or the reflectance measurements in the UV-visible range of the solar spectra. Using the UV-visible transmittance and/or the reflectance spectra, a number of other optical parameters can be estimated which provide substantial information on structural, optical and electronic mechanisms occurring in these materials, and their fundamental characteristics [57]. The subsequent sections of this review article describes a large number of optical and dielectric properties of solid materials which will be useful for materials researchers.

The optical band structure and the types of electron transition involved in the absorption process of thin film coatings and other materials can be identified from the linear absorption coefficient [58, 59],

$$\beta = 2.3026 \frac{A}{d} \quad (23)$$

where  $\beta$  is the absorption coefficient,  $A$  is the solar absorptance assessed from the UV-Vis reflectance data, and  $d$  is the thickness of the films.

In the crystalline and other materials the optical energy gap,  $E_g$  and the electron transition type can be estimated from the absorption coefficient and optical absorption edge using Tauc relation [6-62],

$$\beta h\nu = C(h\nu - E_g)^x \quad (24)$$

where,  $\beta$  is the absorption coefficient,  $h\nu$  is the incident photon energy,  $h$  is Planck's constant,  $\nu$  is the frequency of incident light,  $C$  is an energy independent constant,  $E_g$  is the optical band-gap and  $x$  has a value of either  $\frac{1}{2}$  or 2 for the direct and indirect optical transitions, respectively. The direct energy band-gap is estimated by plotting  $h\nu$  vs  $(ah\nu)^2$  and extrapolating the linear portion of the curve to  $(ah\nu)^2 = 0$  along the  $x$ -axis while the indirect band-gap can be computed by plotting  $h\nu$  vs  $(ah\nu)^{1/2}$  and extrapolating the linear part of the curve to  $(ah\nu)^{1/2} = 0$  along  $h\nu$ -axis.

Since the solar absorption in a material depends on the existence of localized states in the forbidden energy band-gap, the solar absorption spectra can provide with the significant information about the localized states and the occurrence of disorderness in the material. Below the optical band-gap, the absorption coefficient shows an exponential decline by forming so-called Urbach tails, and is expressed as,

$$\beta(h\nu) = \beta_0 e^{\left(\frac{h\nu}{E_u}\right)} \quad (25)$$

where  $\beta_0$  is a constant and  $E_u$  is the Urbach energy indicates the widths of optical absorption edges. Equation (25) can be rearranged as,

$$\beta = \beta_0 \exp\left(\frac{\gamma h\nu}{k_B T}\right) \quad (26)$$

where  $\gamma$  is the steepness parameter denoting the broadening of absorption edges and expressed as,

$$\gamma = \frac{k_B T}{E_u} \quad (27)$$

The complex refractive index, used to interpret many other properties of thin film materials and their derivatives, is defined as,

$$n^* = n + ik \quad (28)$$

where  $n$  is real, and  $k$  is the imaginary part of the complex refractive index known as the extinction coefficient which can be directly estimated from the known value of  $\alpha$  via following relation,

$$k = \frac{\alpha\lambda}{4\pi} \quad (29)$$

The refractive index,  $n$  is defines as,

$$n = \left( \frac{1+R}{1-R} \right) + \sqrt{\frac{4R}{(1-R)^2} - k^2} \quad (30)$$

where  $R$  is the reflectance in percentages, and  $k$  is the well-known extinction coefficient.

The phenomenon of optical dispersion plays an important role in optical communication and in the design of optical devices. Using DiDomenico *et al.*'s single oscillator model [63], the relationship for the dispersion of refractive index below the energy band-gap of a material is represented as,

$$(n^2 - 1)^{-1} = \frac{E_0}{E_d} - \frac{1}{E_0 E_d} (h\nu)^2 \quad (31)$$

where  $E_d$  is the dispersion energy indicating the strength of optical transition and  $E_0$  is the single oscillator energy. The values of dispersion energy parameters can be calculated from the intercept of a straight line drawn between  $(\mu^2-1)^{-1}$  and  $(h\nu)^2$  to  $(\mu^2-1)^{-1}$  axis,  $(E_0/E_d)$  and the gradient/slope  $(E_0 E_d)^{-1}$ . The optical dispersion energy parameters  $E_0$  and  $E_d$  also depend on the optical transition moments  $M_{-1}$  and  $M_{-3}$  by the following equations [64],

$$E_0^2 = \frac{M_{-1}}{M_{-3}} \text{ and } E_d^2 = \frac{M_{-1}^3}{M_{-3}} \quad (32)$$

The strength of oscillator energy,  $E_0$  and dispersion energy,  $E_d$  values are also related to the crystalline structure and ionicity of ionic or covalent materials which reveals that in addition to the optical properties, the single oscillator model can be applied to gain the structural information of a material [65]. The oscillator strength,  $f$  is defined by Wemple and DiDomenico single oscillator model is given by [63],

$$f = E_0 E_d \quad (33)$$

The high frequency optical dielectric constant,  $\epsilon_\infty$  known as static dielectric constant, and the static refractive index,  $n_0$  is associated with the oscillator energy,  $E_0$  and dispersion energy,  $E_d$  by the following relation [64],

$$n_0^2 = \epsilon_\infty = 1 + \frac{E_d}{E_0} \quad (34)$$

In the longer wavelength regions, the dispersion of refractive index is expressed in terms of Sellmeier relation [64, 66, 67],

$$\frac{n_0^2-1}{n^2-1} = 1 - \left(\frac{\lambda_0}{\lambda}\right)^2 \quad (35)$$

where  $\lambda_0$  is the average inter-band oscillator wavelength and  $n_0$  is the refractive index at zero photon energy. Equation (35) can be re-ordered to,

$$n^2 - 1 = \frac{S_0 \lambda_0^2}{1 - \frac{\lambda_0^2}{\lambda^2}} \quad (36)$$

where  $S_0$  is the average oscillator strength related to the inter-band oscillator wavelength and static dielectric constant by the following relation [64, 66, 67],

$$S_0 = \frac{n_0^2-1}{\lambda_0^2} \quad (37)$$

The complex dielectric function of solid materials can be defined using the dispersion relation of the incident photon,

$$\varepsilon(\omega) = \varepsilon_1(\omega) + i\varepsilon_2(\omega) = (n(\omega) + ik(\omega))^2 \quad (38)$$

where  $\varepsilon_1$  and  $\varepsilon_2$  are the real and imaginary parts of the complex dielectric constant, respectively are correlated to the refractive index and extinction coefficient as [66],

$$\varepsilon_1 = n^2 - k^2 \text{ and } \varepsilon_2 = 2nk \quad (39)$$

Since below the optical band-gap energy, the free carrier absorption play a significant role in the absorption process thus, the real part of dielectric constant,  $\varepsilon_1$  must include the carrier contribution and take the following relation [68],

$$\varepsilon_1 = n^2 - k^2 = \varepsilon_\infty - \left(\frac{Ne^2}{4\pi^2 c^2 \varepsilon_0 m^*}\right) \lambda^2 \quad (40)$$

While the imaginary part of the dielectric constant,  $\varepsilon_2$  will be written as,

$$\varepsilon_2 = 2nk = \left(\frac{\varepsilon_\infty \omega_p^2}{8\pi^2 c^3 \tau}\right) \lambda^3 \quad (41)$$

where  $\varepsilon_\infty$  is the dielectric constant at high frequency,  $e$  is the electron's charge,  $c$  is the speed of light,  $\varepsilon_0$  is the permittivity of free space,  $N$  is the free carrier concentration,  $m^*$  is the effective mass,  $\omega_p$  is the plasma frequency,  $\tau$  is the relaxation time and  $k$  is the extinction coefficient. The  $\varepsilon_1$  and  $\varepsilon_2$  represent the quantity of energy deposited in dielectrics as polarization and energy loss, respectively. In solid materials, power loss in the form of heat is known as loss tangent, and is normally associated with the inelastic scattering in charge transfer and charge conduction processes during device operations. Mathematically, the loss tangent is defined as,

$$\tan\delta = \frac{\varepsilon_2}{\varepsilon_1} \quad (42)$$

It measures the loss-rate of power in a mechanical and oscillatory dissipative system. This power loss is related to the fact that dipole alignments become insignificant at lower temperatures however, at higher temperatures the orientations of dipoles are governed by the thermal excitements and thereby the power loss is enhanced.

In dielectric materials, the inelastic scattering of electrons is associated with energy loss functions known as volume energy loss function,  $V_{el}$  and surface energy loss function,  $S_{el}$  [66].

$$V_{el} = \text{Im} \left( -\frac{1}{\varepsilon(\omega)} \right) = \frac{\varepsilon_2}{\varepsilon_1^2 + \varepsilon_2^2} \quad (43)$$

$$S_{el} = \text{Im} \left( -\frac{1}{\varepsilon(\omega) + 1} \right) = \frac{\varepsilon_2}{(1 + \varepsilon_1)^2 + \varepsilon_2^2} \quad (44)$$

As seen from Equations (43) and (44), the energy loss functions are connected to the optical characteristics of a material by its real and imaginary parts of dielectric function.

The dielectric relaxation time,  $\tau$  is defined by the following relation [69],

$$\tau = \frac{\varepsilon_\infty - \varepsilon_1}{\omega \varepsilon_2} \quad (45)$$

where  $\varepsilon_\infty$  is the dielectric constant at high frequency, and  $\varepsilon_1$  and  $\varepsilon_2$  are the real and imaginary parts of the dielectric functions, respectively.

The optical absorption coefficient,  $\beta$  is used to estimate the optical conductivity of solid materials as follows,

$$\sigma_{opt} = \frac{\beta n c}{4\pi} \quad (46)$$

where  $n$  is the refractive index and  $c$  is the speed of light.

## 2.4 Solar Selective Surfaces

A spectrally selective solar surface has different spectral reflectance at different wavelengths. An ideal selective solar absorbing surface should have a zero reflectance in the visible range (between 0.3 and 3  $\mu\text{m}$ ) and unity in the IR region (between 3 and 50  $\mu\text{m}$ ) which does not exist in nature, and it is not possible to fabricate such a device either. Solar radiation at Earth's surface is in the wavelength range of 300 to 2500 nm with the maximum solar intensity at  $\sim 550$  nm, the selective characteristics of an object in the infrared range can be defined by its thermal spectrum similar to that of a blackbody. Figure 2 demonstrates

the thermal emission spectra of an ideal and practical selective surface and the solar spectrum at AM1.5 and the blackbody-like spectra at different temperatures. W. Wien interpreted these data in the following way: the wavelength at which the intensity of a material reaches to a peak is inversely proportional to the absolute temperature of that material- the well-known Wien's displacement law. The corresponding frequency of the emitted radiation by a blackbody can be estimated using the Wien's displacement law. Mathematically, Wien's law is expressed as,

$$\lambda_{\max} T = \frac{hc}{4.96k_B} = 2.898 \times 10^{-3} \text{ m} \cdot \text{K} \quad (47)$$

where  $\lambda_{\max}$  is the maximum wavelength and  $T$  is the absolute temperature of the black body. A hotter object emits the shorter the wavelengths radiation. Wien's displacement law indicates the peak shift towards the shorter wavelength sides with the increase in temperature and Stefan-Boltzmann law construes the height of spectra as the rise in temperature of a blackbody. According to Stefan's law: this growth is not continuous; rather it varies with the fourth power of the absolute temperature of the material.

Since the discovery of solar selective surfaces by Tabor [70] back in 1950's, a great deal of literature is now available on the detailed overview, design and fabrication of solar selective surfaces. For instance, intrinsic solar absorbers, coating/metal tandems, multilayer thin films, optical trapping absorbers, semiconductor/metal tandems, and transparent heat reflector/absorber tandems [71-74]. Among the existing solar selective surfaces, an absorber-reflector tandem formed by a combination of a highly absorbing surface in the visible range and a highly reflective surface in the infrared region of the solar spectra, is the most common type of commercially available selective absorbers [71, 75]. Absorber-reflector metal based tandem solar selective absorbers have been extensively studied by many research groups around the world [76-79]. Over the years, many different types of solar selective absorbing coatings have been studied and developed *via* numerous approaches [80]. For example, metal nitride based cermet solar selective coatings (MeAlN) deposited *via* magnetron sputtering system in which AlN worked as the ceramic component in the cermets and stainless steel [81]. In another study, electrochemical deposition method was successfully utilized for the growth of black chromium or black nickel thin film based solar selective surfaces for the effective transformation of solar energy into the thermal energy [82]. Various types of solar selective surface designs and their optical characteristics are extensively elucidated in earlier reports [83, 84]. A few solar selective surfaces and their design methodologies are briefly presented in the subsequent sections.

## **2.5 Selective Solar Absorber Designs**

Transition metal based compounds and semiconductors are known to work well as the intrinsic solar selective materials [78, 85]. Majority of the commercially manufactured solar selective surfaces are of absorber-reflector tandem type. Some of the commonly used solar selective designs are briefly discussed in the following sections.

### **2.5.1 Intrinsic Solar Absorber Materials**

First group includes materials have intrinsically absorbing selectivity in nature mass absorbers [86]. This type of solar selective surfaces have high structural stability than the multilayered stacks.  $ZrB_2$  is considered to be one of the best absorbers of this type known today [87], some of the other examples include  $SnO_2$  [88],  $MoO_3$ -doped Mo [89], Si doped with B, and  $CaF_2$  [90]. It is well known that none of the naturally occurring materials displays intrinsically ideal solar selective behaviors but roughly can be approximated to have some decent solar selective characteristics. Transition metals and semiconductor demonstrate solar selective properties to a certain degree but both of them needed to be modified to serve the purpose of an intrinsic solar selective absorbing material. Till date reports on the intrinsic absorber materials is very scant due to the fact that there are no ideal intrinsic materials. However, intrinsic materials are enjoying significant research interests to be used as a component in high-temperature multilayer solar selective materials and composite absorbing thin film based coatings.

### **2.5.2 Semiconductor-metal Tandem Surfaces**

Low band gap (0.5 to 1.26 eV) semiconducting materials (such as Si, Ge, and PbS) based solar selective coatings are, generally, deposited onto highly reflecting metal substrates so that it absorbs the short-wavelength solar radiation, and the metal substrates deliver low emittance to achieve a reasonably high selectivity value by the semiconductor-metal tandems. Upon the incidence of solar radiation, photons having energies larger than the band-gaps are absorbed and the photons with energy less than the band-gaps of the material are passed through the surface. In order to attain higher solar absorptance, the refractive index of the semiconductor-metal tandems must be kept to a minimum. But it is well-known that the semiconductor based coatings possess a high refractive index. A minimum value of the refractive index parameter can be attained by adjusting the thickness of the coatings or by using an antireflection layer on the top of the coating surface (examples of AR layers:  $SiO_2$ ,  $Si_3N_4$ , and Si) [91]. These AR layers are successfully used to obtain a



destructive interference effect. Sometime thin semiconductor films of high porosities are also used to reduce the refractive indices.

### **2.5.3 Textured Surface Coatings**

Solar selective surfaces are also synthesized by texturing the surfaces to a suitable scale on metal substrates to obtain the desired spectral selectivity by the optical trapping of solar energy. A properly textured surface appears rough and absorbs solar energy in the shorter wavelength regions and looks highly reflective and mirror-like to thermal energy in the infrared region of the solar spectra. The textured surface absorbs solar energy by capturing the solar radiation via multiple reflections and absorptions processes. Textured Cu, Ni, and stainless steel prepared by sputtering techniques are popularly used as textured metal surfaces [92, 93]. Microstructural morphology of the textured coatings can be shown as a top absorbing layer of air filled metal *i.e.*, rough surface backed by a highly reflecting metal substrate. The thermal emittance of a solar selective material can be also adjusted by altering the microstructure of the coatings *via* ion-beam treatments. A properly orientated textured surface can also improve the solar absorption and thermal emission of a solar selective absorber. Examples of such properly orientated flat-plate textured solar selective surfaces are available elsewhere [94].

### **2.5.4 Metal-dielectric based Composite Selective Coatings**

Composite based solar selective surfaces are usually transition metals embedded in an oxide matrix (dielectric) also known as cermets. Composite coatings are usually deposited on a highly infrared reflecting metal substrate. Composite coatings absorb solar radiation strongly and are almost transparent in the IR region and exhibit good optical properties appropriate for selective solar absorbing surfaces [95, 96]. Metal-dielectric based composite solar selective coatings or absorber-reflector tandems have highly absorbing black materials in the solar region which is very transparent in the longer wavelength region and are deposited onto highly reflective metal substrates. They are composed of fine metal particles in a dielectric or ceramic matrix, or a porous oxide impregnated with metal. The high transparency in the IR region and strongly absorbing in the solar region of these materials arise due to the fact of interband transitions in the metal and the small particle resonance. The high absorptance of these materials may be intrinsic, or geometrically enhanced, or the combination of both. Using a metal-dielectric assembly, the solar selectivity value can be significantly enhanced by proper choice of constituent elements, particle concentration, particle size and shape, and an appropriate coating thickness. The

solar absorptance of system can be improved with a suitable choice of substrates and adopting an anti-reflection layer. A large number of different techniques, such as electroplating, inorganic pigmentation of anodized aluminium, chemical vapour deposition, and physical vapour deposition are widely used to produce the metal-dielectric based composite solar selective surfaces.

For example, metal-dielectric composite coatings with thickness 0.5 to 1.0  $\mu\text{m}$ , and volume fraction of 0.3 to 0.4, have a solar absorptance of between 0.94 to 0.97 and a thermal emittance of  $\sim 0.10$  to 0.20 [95-98]. Metal-dielectric based selective solar surfaces *e.g.*, molybdenum-aluminium oxide ( $\text{Mo-Al}_2\text{O}_3$ ), and nickel/nickel oxide ( $\text{Ni-NiO}_x$ ), both produced by magnetron sputtering technique, nickel pigmented anodic aluminium oxide ( $\text{Ni-Al}_2\text{O}_3$ ), and electroplated black chrome ( $\text{Cr-Cr}_2\text{O}_3$ ) are commercially available for flat plate solar collectors [96, 97, 99, 100]. While a ceramic-metal absorber with an anti-reflection layer on the top could attain a solar absorptance of 0.91 to 0.97 and a thermal emittance of 0.02 to 0.07 [101]. In cermet coatings, higher degree of absorption is achieved due to the light scattering by the boundaries between the metallic and dielectric phases [102, 103], where the metallic particles work as modifiers for the optical response of the ceramic phase [104, 105].

### **2.5.5 Painted Solar Selective Coatings**

Solar selective absorbing paints are simple and cost-effective tandem type absorbing surfaces which are uniformly distributed in a matrix and can be produced on metal substrates [106-114]. Since the selective paints usually contain various types of polymers as binders that absorb infrared radiation, consequently having a higher thermal emittance and thereby a lower solar selectivity value. The optical performances of solar selective paints are, generally, governed by intrinsic optical constants, particle size-dependent scattering and absorption. In an experimental study on FeMnCu-oxide pigment with a silicone binder found to offer a solar absorptance of 0.92 and a thermal emittance of 0.13 [115]. The solar selectivity values of such pigmented surfaces depend on the distribution of particles in the matrix, particle volume fraction and coatings thickness. Sol-gel derived  $\text{CuCoMnO}_x$  pigmented solar selective coatings developed without binder have been well-known for lower thermal emittance values [116, 117]. Spinel or metal oxide type solar selective paints of less than three components of transition metal are reported by other groups [118-120]. CuMn spinel oxide solar selective paints are very popular for their smart

performances in industrial applications [120]. The Solarect-Z, and the SolkoteHI/SORB-II™ are the commercially used solar selective paints.

## **2.6 Real-life Applications of Transition Metal Nitride/oxynitride based Coatings: Spectral Selectivity Data of Recently Developed Materials**

A large number of work have been devoted for the development of transition metal nitride based thin film coatings to be used as solar selective surfaces [17-20, 62]. Due to the variation in their optical parameters from one application to another, wide range of applications and steadily increased scientific demands, transition metal nitride based thin film coatings have been significantly concerned with the development of new species with superior properties. Properties of such coatings can be tailored by choosing the elements and varying the process parameters. Correlation among the structural morphology, crystalline structure, chemical structure, mechanical properties, and optical properties of dc magnetron sputtered metal nitride thin film coatings been studied in an earlier report [26]. The optical applications of transition metal nitrides based selective solar coatings have been extensively discussed in a previous review study [121]. In Ref. [42], magnetron sputtered TiAlN/TiAlON coatings synthesized onto a metal substrate demonstrated high solar absorptance in the visible range and low thermal emittance in the infrared range. The solar absorptance of TiAlN/TiAlON coatings was substantially enhanced to 0.95 by coated with Si<sub>3</sub>N<sub>4</sub> antireflection layers on the top of these films. A high thermal stability in air up to 600 °C and high solar selectivity of  $0.95/0.07 = 13.57$  was achieved. Since, solar selective surfaces are the easiest and most direct way to enhance the solar energy harvesting of solar energy captors, in recent years, transition metal nitrides have received significant research interest for middle (up to 200 °C) and high temperature (Up to 600 °C) solar applications [18, 19, 42, 122-130]. The solar selectivity values of some recently published transition metal nitride/oxynitride based thin film coatings are listed in Table 1.

**Table 1.** Spectral selectivity values of transition metal nitride/oxy-nitride based thin film coatings as seen in the literature.

Sample compositions	Substrate	Absorptance ( $\alpha$ ) and emittance ( $\varepsilon$ ) calculation method	Solar selectivity, $s = \frac{\alpha}{\varepsilon}$
TiN	Stainless steel	UV-Vis and FTIR reflectivity	8.48 [62]
TiAlN	Stainless steel	UV-Vis and FTIR reflectivity	12.92 [62]
TiAlSiN	Stainless steel	UV-Vis and FTIR reflectivity	22.63 [62]
TiAlSiN	Stainless steel	UV-Vis and FTIR reflectivity	22.63-24.63 [131]
TiAlN	Copper	Solar spectrum reflectometer and emissometer	12.9 [132]
TiAlN/TiAlON	Copper	Solar spectrum reflectometer and emissometer	15.2 [132]
Ti <sub>1-x</sub> Al <sub>x</sub> N	Copper	UV-Vis and FTIR reflectivity	For $x = 0.21$ ; 5.4 [133]
	Copper	UV-Vis and FTIR reflectivity	For $x = 0.58$ ; 5.0 [133]
TiAlN/TiAlON/Si <sub>3</sub> N <sub>4</sub>	Copper	Solar spectrum reflectometer and emissometer	13.6 [42, 132, 134]
TiAlN/TiAlON/Si <sub>3</sub> N <sub>4</sub>	Glass	Solar spectrum reflectometer and emissometer	13.3 [132]
TiAlN/TiAlON/Si <sub>3</sub> N <sub>4</sub>	Stainless steel	Solar spectrum reflectometer and emissometer	7.4 [132]
TiAlN/TiAlON/Si <sub>3</sub> N <sub>4</sub>	Nickel	Solar spectrum reflectometer and emissometer	6.7 [132]
Ti <sub>1-x</sub> Al <sub>x</sub> N/Ag/ Ti <sub>1-x</sub> Al <sub>x</sub> N	Glass	UV-Vis and FTIR reflectivity	18.1 [135]
Ti <sub>0.5</sub> Al <sub>0.5</sub> N/ Ti <sub>0.25</sub> Al <sub>0.75</sub> N/AlN	Stainless steel	Spectroscopic phase modulated ellipsometer	23.5 [136]
Ti <sub>x</sub> Al <sub>1-x</sub> /(TiN-AlN) <sub>H</sub> /(TiN-AlN) <sub>L</sub> /AlN	Stainless steel	UV-Vis-NIR and emissometer	11.8 [137]
TiAl/TiAlN/TiAlON/TiAlO	Stainless steel and Copper	Spectrophotometer and FTIR	11.3 [138]

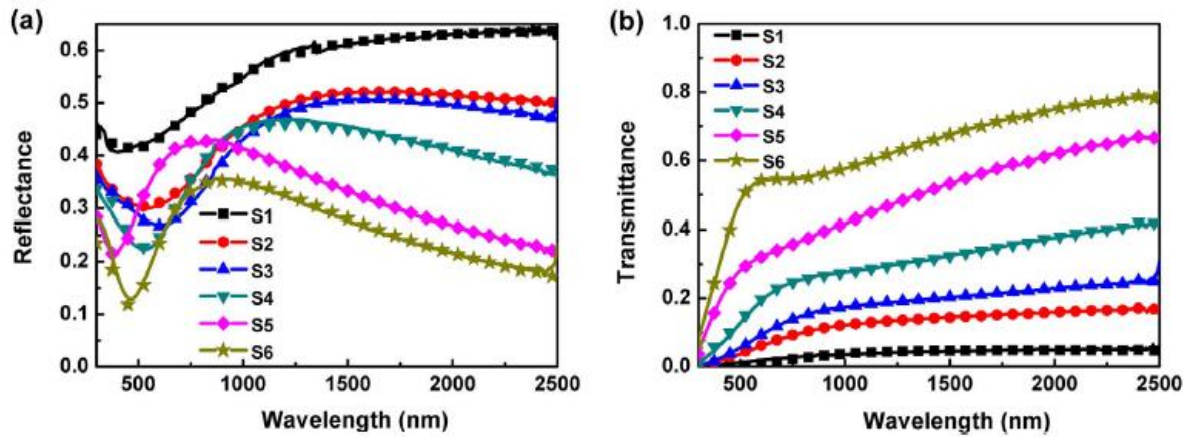
TiN/Al <sub>2</sub> O <sub>3</sub>	Stainless steel	UV-Vis-NIR and FTIR spectroscopies	8.36 [139]
Cu/Zr <sub>0.2</sub> AlN <sub>0.8</sub> /ZrN/AlN/ZrN/AlN/Al <sub>34</sub> O <sub>62</sub> N <sub>4</sub>	Si(1 11) and glass (soda lime glass)	UV-Vis-NIR and FTIR spectroscopies	7.85 [140]
TiAlN/SiO <sub>2</sub>	Copper and Silicon	UV-Vis-NIR and FTIR spectroscopies	15.33 [141]
TiAlC/TiAlCN/TiAlSiCN/TiAlSiCO/TiAlSiO	Stainless steel	UV-vis-NIR spectrophotometer	6.4 [142]
CrON/SnO <sub>2</sub>	Aluminium	UV-Vis-NIR and FTIR spectroscopies	19.00 [143]
CrN/Si <sub>3</sub> N <sub>4</sub>	Aluminium	UV-Vis-NIR and FTIR spectroscopies	15.49 [143]
CrN/SiO <sub>2</sub>	Aluminium	UV-Vis-NIR and FTIR spectroscopies	15.11 [143]
WAlN/WAlON/Al <sub>2</sub> O <sub>3</sub>	Stainless steel	UV-Vis-NIR and FTIR spectroscopies	11.98 [144]
CrN(H)/CrN(L)/CrON/Al <sub>2</sub> O <sub>3</sub>	Stainless steel	UV-Vis-NIR and FTIR spectroscopies	6.64 [145]
ZrO <sub>x</sub> /ZrC-ZrN/Zr	Stainless steel and Copper	UV-Vis-NIR and FTIR spectroscopies	22.00 [146]
HfMoN(H)/HfMoN(L)/HfON/Al <sub>2</sub> O <sub>3</sub>	Stainless steel	UV-Vis spectrometer and emissometer	6.79 [147]
CrAlN/CrAlON/Al <sub>2</sub> O <sub>3</sub>	Copper	Solar spectrum reflectometer and emissometer	14.06 [148]
CrAlN/CrAlON/Si <sub>3</sub> N <sub>4</sub>	Copper	Solar spectrum reflectometer and emissometer	11.5 [148]
TiAlN/TiAlON/Si <sub>3</sub> N <sub>4</sub>	Metal and non-metal	Phase modulated spectroscopic ellipsometry	11.5 [42]
Cu/NbAlN	Copper	Phase-modulated spectroscopic ellipsometer	15.68 [123]
Cu/NbAlN/NbAlON	Copper	Phase-modulated spectroscopic ellipsometer	15.50 [123]
Cu/NbAlN/NbAlON/Si <sub>3</sub> N <sub>4</sub>	Copper	Phase-modulated spectroscopic ellipsometer	13.66 [123]
Ti/AlTiN/AlTiON/AlTiO	Stainless steel	UV-Vis-NIR and FTIR spectroscopies	11.94 [149]

Al-AlN	Aluminium	UV-Vis-NIR and FTIR spectroscopies	14.27 [150]
TiAlSiN/TiAlSiON/SiO <sub>2</sub>	Copper	UV-Vis-NIR and FTIR spectroscopies	10.93 [151]
Al/NbMoN/NbMoON/SiO <sub>2</sub>	Stainless steel	UV-Vis-NIR and FTIR spectroscopies	8.62 [152]
TiAlC/TiAlCN/TiAlSiCN/TiAlSiCO/ TiAlSiO	Stainless steel	UV-Vis-NIR and FTIR spectroscopies	6.41 [153]
TiAlN <sub>x</sub> /TiAlN <sub>y</sub> /Al <sub>2</sub> O <sub>3</sub>	Stainless steel	UV-Vis-NIR and FTIR spectroscopies	4.23 [154]
Al/Si <sub>3</sub> N <sub>4</sub> /(Ti/Si <sub>3</sub> N <sub>4</sub> ) <sup>2</sup>	Silicon	UV-Vis and frontier spectroscopies	13.43 [155]
Mo/ZrSiN/ZrSiON/SiO <sub>2</sub>	Stainless steel	UV-Vis-NIR and FTIR spectroscopies	15.67 [156]
Al-AlN	Aluminum metal	A commercial optical software SCOUT	48.00 [157]
TiN <sub>x</sub> O <sub>y</sub>	Copper	UV-Vis-NIR and FT-NIR/MIR spectroscopies	15.94 [158]

Over the years, transition-metal nitrides and transition-metal oxynitrides based thin film coatings have gained substantial attention for use in mid to high temperature solar selective surfaces due to a good combination of their physical, chemical, optical and many other properties. The solar selective performance of a large number of recently developed transition-metal nitrides and transition-metal oxynitrides thin film based solar selective surfaces have been presented in Table 1. Higher values of solar selectivity of these thin film based solar selective coatings essentially indicating their high solar absorbance in the visible range and low thermal emittance in the infra-red range of the solar spectra. The solar selective performance of the transition-metal nitrides and transition-metal oxynitrides based coatings can be significantly modified by adjusting the films' stoichiometry that leads to changes in the density of free electrons in the *d*-bands. Some of the typical UV-Vis and FTIR spectra of the aforementioned solar selective surfaces are presented in the following section.

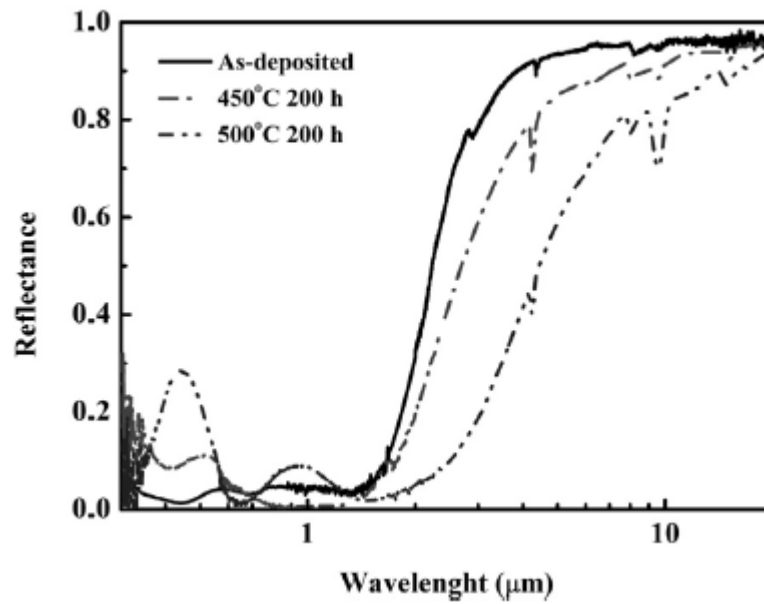
A number of ZrSiN and ZrSiON absorbing layers prepared *via* magnetron sputtering system in a multi-target assembly onto the glass substrates with different reactive gas flows

[156]. A high solar absorptance of 0.94 and a low thermal emittance of 0.06 at 25 °C were achieved [156]. As seen in Figure 5, a wide range of reflectance and transmittance values, for the various absorbing layers, was obtained. It was further noticed that with the subsequent increase in the reactive gas flows the reflectance values decrease and the transmittance values increase which arises due to a transition from metal-like behaviour to dielectric-like behaviour of the absorbing surfaces.



**Figure 5.** The UV-Vis (a) reflectance and (b) transmittance spectra of ZrSiN (S1, S2, S3) and ZrSiON (S4, S5, S6) solar selective coatings deposited onto glass substrates. Samples S1, S2, S3, S4, S5, and S6 differs in different amount of reactive gas flows and film thickness. Reprinted with permission from Ref. [156].

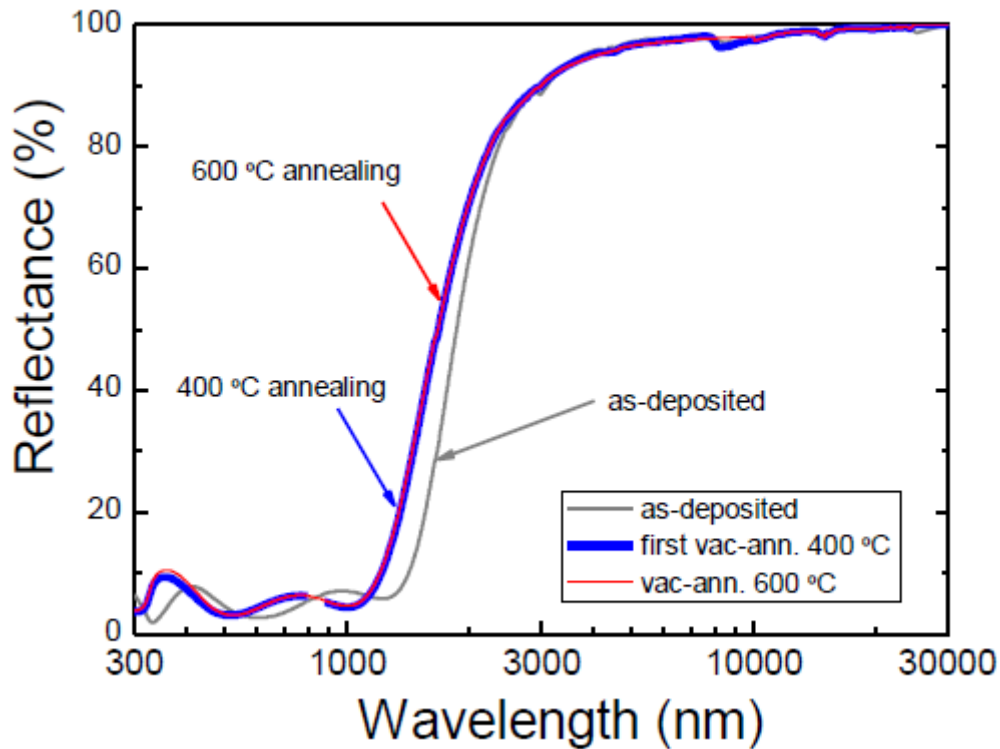
The Al/NbMoN/NbMoON/SiO<sub>2</sub> solar selective absorbing coatings (See Figure 6) developed for its potential applications in concentrated solar power (CSP) system were deposited onto the stainless steel substrates *via* magnetron sputtering method [152]. These coatings show a high value of solar absorptance and higher degree of thermal stability both in air and in vacuum up to 450 °C however, substantial degradation of the optical performance of these coatings was noticed at an annealing temperature of 500 °C.



**Figure 6.** The reflectance spectra of the Al/NbMoN/NbMoON/SiO<sub>2</sub> solar selective absorbing coating before and after being annealed at 450 °C and 500 °C for 200 h in air. Reprinted with permission from Ref. [152].

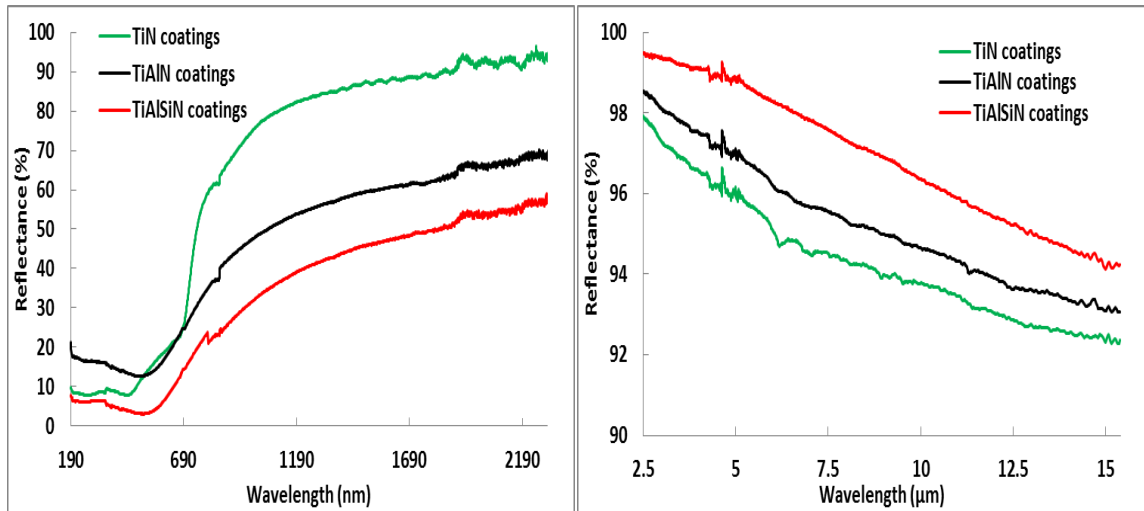
Figure 7 shows the UV-visible reflectance spectra of as-deposited, 400 °C and 600 °C vacuum annealed RF sputtered Mo-Si<sub>3</sub>N<sub>4</sub> solar selective coatings [159]. This first annealing was carried out to remove the inert sputtering gas remaining around the coating surfaces responsible to shrink the coating multilayers and modifying the optical interferences. As a result, a higher degree of optical stability was attained by the solar selective coatings after being vacuum annealed at 600 °C.





**Figure 7:** The UV-Vis reflectance spectra of Mo-Si<sub>3</sub>N<sub>4</sub> solar selective coatings deposited onto the stainless steel substrates annealed at 400 and 600 °C in vacuum. Reprinted with permission from Ref. [159].

The optical reflectance spectra ((See Figure 8(A)) of TiN, TiAlN and TiAlSiN thin film coatings deposited onto M2 steel substrates via magnetron sputtering technique were used to calculate the solar absorptance [62]. Figure 8 shows that these films show moderate absorptance to ultraviolet region, high absorptance in the visible region and very high reflectance in the near-infrared region of the solar radiation. This means that the highest value of the solar absorption is seen in the visible range of the solar spectrum and the lowest value of solar absorption is recorded in the near-infrared region. Due to this superior value of the solar absorptance, these films are considered efficient candidates to be used as solar selective absorbing surfaces. The FTIR reflectance spectra of these solar selective films shown in Figure 8(B) were used to estimate the thermal emittance values in the infrared range of the solar spectra [62]. The thermal emittance values of these films were decreased with the Al- and AlSi-doping to the TiN matrix. It is believed that as the Al and Si are added to the TiN system, the thermal emittance reduction was governed by the formation of the surface oxidation layers such as Al<sub>2</sub>O<sub>3</sub>, SiO<sub>2</sub> [62].



**Figure 8.** (A) UV-Vis and (B) FTIR reflectance spectra of the sputtered  $Ti_xM_{1-x-y}N_y$  films (TiN, TiAlN and TiAlSiN respectively stand for  $Ti_{0.5}N_{0.5}$ ,  $Ti_{0.25}Al_{0.25}N_{0.5}$  and  $Ti_{0.25}Al_{0.2}Si_{0.05}N_{0.5}$ ). Reprinted with permission from Ref. [62].

In order to harvest solar energy *via* solar thermal panels, researchers are persistently investigating for the developments of new materials to attain higher efficiencies by focusing on the constituent elements and structure features of the absorbing materials. Generally, a large number of materials have intrinsic absorption which is very low. For this reason, development of efficient solar selective materials by choosing appropriate materials and proper method is always in being in the hot spot. Typically, two phenomena can be successfully adopted to enhance the solar selective absorption: firstly, utilizing the interference effect of thin film coatings and optical trap to rise the solar absorptance and secondly, using an antireflective coating (ARC) on the top of the film surface to reduce thermal emittance and thereby increasing the absorptance [160-163]. In principle, the solar absorptance (in the visible range) and thermal emittance (in the infrared range) of a material depends on black coated layer, undercoating layer and substrates. The substrate and sublayer play very effective role to protect the solar selective absorbing layer against oxidation, diffusion, degradation, and corrosion at deleterious environmental conditions (mid to high temperature operations). Thus, a thermally stable diffusion barrier layer with superior optical properties can hinder diffusion of substrate into the solar selective absorbing surface. Generally, solar selective surfaces are coated onto a highly reflective metal substrate [164] is due to the fact that on such developed spectrally selective surfaces the output temperature from solar collectors can be enhanced. In order to produce highly efficient, robust and low-cost solar selective absorbers is adopting a highly reflective surface coated together with a highly absorbing spectrally selective surface which would

work as absorber–reflector tandem assembly [165, 166]. As a result, lower emittance of the coating in the infrared region is due to the highly reflecting substrate and coated sublayer [109].

## 2.7 Other Applications of Metal Nitride-based Thin Film Coatings

Impressive structural diversity and good combinations of physical, mechanical, chemical, and electrical properties of transition metal nitrides make them useful to a wide range of applications across many practical fields. Generally nitride materials fall into two main classes: transition-metal nitrides and ionic-covalent nitrides [167]. In metal nitride thin film coatings, the metal-metal bonds are predominant whereas nitrogen-(non)metal bonds are preeminent in ionic covalent nitrides. According to the crystal symmetry and characteristic nature of transition-metal nitrides, they are very similar to carbides while the ionic-covalent nitrides are close to oxides. The optical properties of metal oxynitride and ionic-covalent oxynitride materials, and the influences of synthesis conditions and chemical structures on the optical properties of such materials are reviewed by Xie *et al.* [167]. The optical properties of these materials can be modified by controlling the compositions that alters the density of free electrons in their *d*-bands [20, 43]. The optical properties can be also regulated by integrating different metal elements into the metal nitride framework through converting bonding nature from metallic to covalent one [43]. For example,  $\text{Ti}_{1-x}\text{Al}_x\text{N}$  coatings exhibit metallic characteristics with low Ti-content ( $x \leq 0.48$ ) and dielectric behavior with high Ti-content up to  $x = 0.77$  [43]. Gradual improvement in the optical transmittance was noticed with the subsequent increase in aluminum content to the  $\text{Ti}_{1-x}\text{Al}_x\text{N}$  coatings. Furthermore, coatings with  $x < 0.5$  showed a maximum transmission and a maximum reflection in the visible region together with a high reflectance and low absorptance in the infrared region. The applications of transition metal nitride and carbide class materials in low temperature fuel cell technology have been investigated by various research groups as mentioned in previous review and researches [168, 169]. Extensive overviews on various optical parameters such as band-gap, refractive index, reflectance, absorptance, emittance, transmittance and photoluminescence of different oxynitride materials and their applications as selective solar surfaces, antireflection coatings, visible-light-driven photocatalysts, phosphors for light-emitting diodes, ecological pigments, and smart windows have been previously documented [17-20, 167]. The requirement of optical parameters of transition metal nitride coatings vary from one application to another. In order to provide a better understanding, the property-structure (as well as associated efficiency for individual application) relationship the chemistry of different metal nitrides

and their corresponding crystal structures have been overviewed by many groups [170-173].

Due to good thermal and chemical stability and hardness, metal nitride thin film coatings based have large number of technological applications as hard and superhard protective coatings, oxidation-, wear-, corrosion-, and erosion resistance coatings [1-3], microelectronic devices [174], ultraviolet and visible light emitters and detectors, and optical storage devices, optical devices such as active and passive optical planar waveguides, and antireflecting coatings [37-41], electronics devices, and diffusion barriers [43, 175]. Because of their large band-gap, high surface acoustic velocity, excellent chemical and thermal stability and physical robustness, these materials have secured their places in many optical devices as well. They are also popularly used in the semiconductor industry for optoelectronic devices at high power and high temperatures [176], in high temperature structural materials and gate dielectrics in microstructural devices [177, 178], and in spin-dependent photonic devices [11, 13, 179]. Introduction of suitable amount of dopants to the binary nitrides or oxynitrides results in band-gap engineering and design of emitters and detectors operating in the ultraviolet region. In an experimental investigation, metal-like CrN and wide-band gap semiconducting Cr<sub>2</sub>O<sub>3</sub> was combined together by reactive dc magnetron sputtered system in Ar/N<sub>2</sub>/O<sub>2</sub>(N<sub>2</sub>O) atmospheres to deposit CrON and modify their band-gap and electronic properties for their optical and electronic applications [180]. Photothermal conversion of spectrally selective magnetron sputtered chromium oxynitride has been reported in a previous article [128]. Microstructural, electronic and optical characteristics of various chromium nitride coatings deposited by unbalanced reactive magnetron sputtering was performed by Logothetidis *et al.* [181]. The influence of nitrogen flow to the phase formation in Cr, Cr<sub>2</sub>N, CrN coatings was investigated *via* XRD studies. Using Drude-Lorentz model [182, 183] together with the electronic structure of Cr<sub>2</sub>N, CrN, the experimental results reckoned the metallic character of Cr<sub>2</sub>N phase and the semiconducting nature of CrN structure [184, 185]. Nanocrystalline titanium nitride thin films found applications in different areas of semiconductor technology such as gate electrodes in field-effect transistors, Al diffusion barriers, and ultra-large scale integrated circuits [27-29]. Mutual interactions with the electrons in Ti and N atoms and the electronic structure of the stoichiometric titanium nitride affect the optical, electronic, and electrical behaviours of these nanocomposite films [182]. The complex dielectric function of TiN films was analysed on the basis of intra-band absorption and inter-band transitions in terms of the free electron Drude model and the Lorentz oscillator

model respectively [182]. Furthermore, the combined Drude–Lorentz model was utilized to demonstrate the metallic nature of titanium nitride coatings and the origin of band structure modifications. In addition, the XRD and electron microscopy validated the spectroscopic ellipsometry results along with the insights on the atomistic mechanisms affecting the grains morphology and their correlation with the electronic and optical properties.

## **2.8 Summary and Conclusions**

We have reviewed the recent development of metal nitride and metal oxynitride thin film coatings, which are very prominent technological materials due to their outstanding physical properties and protective character, and for their optical and solar selectivity applications. Metal nitride based coatings *e.g.*, CrN, TiN, TiAlN, CrSiN, CrAlN, and NbN, have extensive industrial applications in cutting tools, in dry cutting, bearing spindles, metal forming, stamping dies, other mechanical machineries as well as automotive and aerospace applications because of their good wear resistance, thermal and corrosion resistance, good adhesion, high-temperature oxidation resistance, and a high level of hardness. These materials are also broadly used as optical, protective, and decorative coatings. Due to the combination of a large number of unique properties such as extraordinary thermal stability and superior optical properties, metal nitride based thin film coatings are considered to be one of the smartest aspirants in solar selective surface applications. Despite their technological importance, so far, there have been a very limited number of investigations on the solar selectivity features in the presence of various dopants. Optical responses of metal nitride based thin film coatings greatly vary from one application to another. As is mentioned previously, for the solar selective surface applications, these coatings must possess high solar absorptance to the visible light and low thermal emittance in the infrared region of the solar spectra. Until now, numerous binary, ternary and quaternary coatings *e.g.*, CrN, AlN, MoN, CrAlN, TiAlN, TiSiN, CrSiN, CrCN, CrMoN, CrON, CrWN, TiAlSiN, TiAlCrN, CrAlSiN, and CrMoSiN, have been extensively investigated. Among them TiAlN, TiAlSiN, CrON, ZrC-ZrN, NbAlN coatings have drawn more attention for their superior solar selectivity values (see Table 1) and thermal stability. Nevertheless, thorough research is still needed to further increase their mechanical properties, thermal and chemical stability and the oxidation resistance behaviours of these materials before their place in the commercial market for industrial productions is confirmed.

## References

- [1] A. Mycielski, L. Kowalczyk, R.R. Gałazka, R. Sobolewski, D. Wang, A. Burger, M. Sowińska, M. Groza, P. Siffert, A. Szadkowski, B. Witkowska, W. Kaliszek, Applications of II-VI semimagnetic semiconductors, *Journal of Alloys and Compounds*, 423 (2006) 163-168.
- [2] F. Pan, C. Song, X.J. Liu, Y.C. Yang, F. Zeng, Ferromagnetism and possible application in spintronics of transition-metal-doped ZnO films, *Materials Science and Engineering R: Reports*, 62 (2008) 1-35.
- [3] Y.C. Yang, F. Pan, Q. Liu, M. Liu, F. Zeng, Fully room-temperature-fabricated nonvolatile resistive memory for ultrafast and high-density memory application, *Nano Letters*, 9 (2009) 1636-1643.
- [4] H. Morkoç, S. Strite, G.B. Gao, M.E. Lin, B. Sverdlov, M. Burns, Large-band-gap SiC, III-V nitride, and II-VI ZnSe-based semiconductor device technologies, *Journal of Applied Physics*, 76 (1994) 1363-1398.
- [5] J.H. Edgar, *Properties of Group III Nitrides*, The Institution of Electrical Engineers, London, Wiley Online Library, UK (1994).
- [6] X. Orignac, D. Barbier, X.M. Du, R.M. Almeida, Fabrication and characterization of sol-gel planar waveguides doped with rare-earth ions, *Applied Physics Letters*, 69 (1996) 895-897.
- [7] R.M. Almeida, X. Orignac, D. Barbier, Silica-based sol-gel films doped with active elements, *J Sol-Gel Sci Technol*, 2 (1994) 465-467.
- [8] K. Otsuka, C.V. Wayman, *Shape Memory Materials*, Cambridge University Press, Cambridge, UK, 1998.
- [9] K. Otsuka, X. Ren, Physical metallurgy of Ti–Ni-based shape memory alloys, *Progress in Materials Science*, 50 (2005) 511-678.
- [10] F. Zeng, C. Chen, B. Fan, Y.C. Yang, P.Y. Yang, J.T. Luo, F. Pan, W.S. Yan, Effect of carbon doping on microstructure, electronic and magnetic properties of Cr:AlN films, *Journal of Alloys and Compounds*, 509 (2011) 440-446.
- [11] M. Hashimoto, Y.K. Zhou, M. Kanamura, H. Asahi, High temperature (>400 K) ferromagnetism in III-V-based diluted magnetic semiconductor GaCrN grown by ECR molecular-beam epitaxy, *Solid State Communications*, 122 (2002) 37-39.
- [12] M.S. Kim, Y.K. Zhou, M. Funakoshi, S. Emura, S. Hasegawa, H. Asahi, Tunnel magnetoresistance in GaCrN/AlN/GaCrN ferromagnetic semiconductor tunnel junctions, *Applied Physics Letters*, 89 (2006) 231511-232513.

- [13] M.L. Reed, N.A. El-Masry, H.H. Stadelmaier, M.K. Ritums, M.J. Reed, C.A. Parker, J.C. Roberts, S.M. Bedair, Room temperature ferromagnetic properties of (Ga, Mn)N, *Applied Physics Letters*, 79 (2001) 3473-3475.
- [14] J.L. Endrino, S. Palacín, A. Gutiérrez, F. Schäffers, J.E. Krzanowski, Low and increased solubility of silicon in metal nitrides: Evidence by X-ray absorption near edge structure, *Journal of Materials Science*, 42 (2007) 7607-7610.
- [15] B.D. Beake, V.M. Vishnyakov, R. Valizadeh, J.S. Colligon, Influence of mechanical properties on the nanoscratch behaviour of hard nanocomposite TiN/Si<sub>3</sub>N<sub>4</sub> coatings on Si, *Journal of Physics D: Applied Physics*, 39 (2006) 1392.
- [16] P. Zeman, J. Musil, Difference in high-temperature oxidation resistance of amorphous Zr-Si-N and W-Si-N films with a high Si content, *Applied Surface Science*, 252 (2006) 8319-8325.
- [17] K.E. Andersson, M. Veszelei, A. Roos, Zirconium nitride based transparent heat mirror coatings -preparation and characterisation, *Solar Energy Materials and Solar Cells*, 32 (1994) 199-212.
- [18] C.G. Granqvist, Transparent conductors as solar energy materials: A panoramic review, *Solar Energy Materials and Solar Cells*, 91 (2007) 1529-1598.
- [19] N. Selvakumar, H.C. Barshilia, Review of physical vapor deposited (PVD) spectrally selective coatings for mid- and high-temperature solar thermal applications, *Solar Energy Materials and Solar Cells*, 98 (2012) 1-23.
- [20] G.B. Smith, P.D. Swift, A. Bendavid, TiN<sub>x</sub> films with metallic behavior at high N/Ti ratios for better solar control windows, *Applied Physics Letters*, 75 (1999) 630-632.
- [21] C. Mitterer, P.H. Mayrhofer, W. Waldhauser, E. Kelesoglu, P. Losbichler, The influence of the ion bombardment on the optical properties of TiN<sub>x</sub> and ZrN<sub>x</sub> coatings, *Surface and Coatings Technology*, 108-109 (1998) 230-235.
- [22] P.E. Schmid, M.S. Sunaga, F. Lévy, Optical and electronic properties of sputtered TiN<sub>x</sub> thin films, *Journal of Vacuum Science and Technology A: Vacuum, Surfaces and Films*, 16 (1998) 2870-2875.
- [23] P. Hones, R. Sanjines, F. Lévy, Characterization of sputter-deposited chromium nitride thin films for hard coatings, *Surface and Coatings Technology*, 94-95 (1997) 398-402.
- [24] U. Beck, G. Reiners, I. Urban, K. Witt, Evaluation of optical properties of decorative coatings by spectroscopic ellipsometry, *Thin Solid Films*, 220 (1992) 234-240.
- [25] G. Reiners, H. Hantsche, H.A. Jehn, U. Kopacz, A. Rack, Decorative properties and chemical composition of hard coatings, *Surface and Coatings Technology*, 54-55 (1992) 273-278.

- [26] P. Zeman, R. Čerstvý, P.H. Mayrhofer, C. Mitterer, J. Musil, Structure and properties of hard and superhard Zr-Cu-N nanocomposite coatings, *Materials Science and Engineering A*, 289 (2000) 189-197.
- [27] C.A. Dimitriadis, J.I. Lee, P. Patsalas, S. Logothetidis, D.H. Tassis, J. Brini, G. Kamarinos, Characteristics of TiN<sub>x</sub>/n-Si Schottky diodes deposited by reactive magnetron sputtering, *Journal of Applied Physics*, 85 (1999) 4238-4242.
- [28] P. Patsalas, C. Charitidis, S. Logothetidis, C.A. Dimitriadis, O. Valassiades, Combined electrical and mechanical properties of titanium nitride thin films as metallization materials, *Journal of Applied Physics*, 86 (1999) 5296-5298.
- [29] A. Satta, G. Beyer, K. Maex, K. Elers, S. Haukka, A. Vantomme, Properties of TiN thin films deposited by ALCVD as barrier for CU metallization, *Materials Research Society Symposium - Proceedings*, 612 (2000) D651-D656.
- [30] G.G. Fuentes, E. Elizalde, J.M. Sanz, Optical and electronic properties of TiC<sub>x</sub>N<sub>y</sub> films, *Journal of Applied Physics*, 90 (2001) 2737-2743.
- [31] S.V. Didziulis, J.R. Lince, T.B. Stewart, E.A. Eklund, Photoelectron spectroscopic studies of the electronic structure and bonding in TiC and TiN, *Inorganic Chemistry*, 33 (1994) 1979-1991.
- [32] G.G. Fuentes, I.G. Mancheño, F. Balbás, C. Quirós, J.F. Trigo, F. Yubero, E. Elizalde, J.M. Sanz, Dielectric properties of Ti, TiO<sub>2</sub> and TiN from 1.5 to 60 eV determined by reflection electron energy loss spectroscopy (REELS) and ellipsometry, *Physica Status Solidi (A) Applied Research*, 175 (1999) 429-436.
- [33] L. Soriano, M. Abbate, H. Pen, P. Prieto, J.M. Sanz, The electronic structure of TiN and VN: X-ray and electron spectra compared to band structure calculations, *Solid State Communications*, 102 (1997) 291-296.
- [34] C.G.H. Walker, C.A. Anderson, A. McKinley, N.M.D. Brown, A.M. Joyce, A combined AES, resonant photoemission and EELS study of in-situ grown titanium nitride, *Surface Science*, 383 (1997) 248-260.
- [35] J.P.A.M. Driessen, A.D. Kuypers, J. Schoonman, Gas-phase chemistry in up-scaled plasma enhanced metal-organic chemical-vapor deposition of TiN and Ti(C, N) on tool steel, *Journal of Vacuum Science and Technology A: Vacuum, Surfaces and Films*, 18 (2000) 1971-1976.
- [36] M. Eizenberg, K. Littau, S. Ghanayem, M. Liao, R. Mosely, A.K. Sinha, Chemical vapor deposited TiCN: A new barrier metallization for submicron via and contact applications, *Journal of Vacuum Science and Technology A: Vacuum, Surfaces and Films*, 13 (1995) 590-595.



- [37] D. Barbier, X. Orignac, X.M. Du, R.M. Almeida, X. Orignac, D. Barbier, X.M. Du, R.M. Almeida, Fabrication and characterization of sol-gel planar waveguides doped with rare-earth ions, Proc. of Topical Symp. VII on Advanced Materials in Optics, Electro-Optics and Communication Technologies, 69 (1995) 33-897.
- [38] H. Schroeder, Physics of Thin Films, Academic, New York, USA (1969).
- [39] X. Orignac, D. Barbier, X.M. Du, R.M. Almeida, Fabrication and characterization of sol-gel planar waveguides doped with rare-earth ions, Applied Physics Letters, 69 (1996) 895-897.
- [40] R.M. Almeida, X. Orignac, D. Barbier, Silica-based sol-gel films doped with active elements - Code: E4, Journal of Sol-Gel Science and Technology, 2 (1994) 465-467.
- [41] Y. Sorek, R. Reisfeld, I. Finkelstein, S. Ruschin, Sol-gel glass waveguides prepared at low temperature, Applied Physics Letters, 63 (1993) 3256-3258.
- [42] H.C. Barshilia, N. Selvakumar, K.S. Rajam, D.V.S. Rao, K. Muraleedharan, A. Biswas, TiAlN/TiAlON/Si<sub>3</sub>N<sub>4</sub> tandem absorber for high temperature solar selective applications, Applied Physics Letters, 89 (2006) 191909.
- [43] A. Schüler, V. Thommen, P. Reimann, P. Oelhafen, G. Francz, T. Zehnder, M. Düggelin, D. Mathys, R. Guggenheim, Structural and optical properties of titanium aluminum nitride films (Ti<sub>1-x</sub>Al<sub>x</sub>N), Journal of Vacuum Science & Technology A: Vacuum, Surfaces, and Films, 19 (2001) 922-929.
- [44] N. Hatcher, O.Y. Kontsevoi, A.J. Freeman, Martensitic transformation path of NiTi, Physical Review B, 79 (2009) 020202.
- [45] J. Cai, D.S. Wang, S.J. Liu, S.Q. Duan, B.K. Ma, Electronic structure and B2 phase stability of Ti-based shape-memory alloys, Physical Review B, 60 (1999) 15691-15698.
- [46] G. Petzow, M. Herrmann, Silicon Nitride Ceramics, in: M. Jansen (Ed.) High Performance Non-Oxide Ceramics II, Springer Berlin Heidelberg, Berlin, Heidelberg, 2002, pp. 47-167.
- [47] P. Dev, Y. Xue, P. Zhang, Defect-induced intrinsic magnetism in wide-gap III nitrides, Physical Review Letters, 100 (2008) 117204.
- [48] J.A. Duffie, W.A. Beckman, Solar Engineering of Thermal Processes, 3rd ed., John Wiley & Sons, New Jersey, USA, 2006.
- [49] A. Amri, Z.T. Jiang, T. Pryor, C.-Y. Yin, S. Djordjevic, Developments in the synthesis of flat plate solar selective absorber materials via sol-gel methods: A review, Renewable and Sustainable Energy Reviews, 36 (2014) 316-328.
- [50] F. Cao, K. McEnaney, G. Chen, Z. Ren, A review of cermet-based spectrally selective solar absorbers, Energy & Environmental Science, 7 (2014) 1615-1627.

- [51] Z.Y. Nuru, D.E. Motaung, K. Kaviyarasu, M. Maaza, Optimization and preparation of Pt–Al<sub>2</sub>O<sub>3</sub> double cermet as selective solar absorber coatings, *Journal of Alloys and Compounds*, 664 (2016) 161-168.
- [52] S. Esposito, A. Antonaia, M.L. Addonizio, S. Aprea, Fabrication and optimisation of highly efficient cermet-based spectrally selective coatings for high operating temperature, *Thin Solid Films*, 517 (2009) 6000-6006.
- [53] C.A. Arancibia-Bulnes, C.A. Estrada, J.C. Ruiz-Suárez, Solar absorptance and thermal emittance of cermets with large particles, *Journal of Physics D: Applied Physics*, 33 (2000) 2489.
- [54] D. Xinkang, W. Cong, W. Tianmin, Z. Long, C. Buliang, R. Ning, Microstructure and spectral selectivity of Mo–Al<sub>2</sub>O<sub>3</sub> solar selective absorbing coatings after annealing, *Thin Solid Films*, 516 (2008) 3971-3977.
- [55] D. Gong, H. Liu, G. Luo, P. Zhang, X. Cheng, B. Yang, Y. Wang, J. Min, W. Wang, S. Chen, Z. Cui, L. Kewei, H. Lifang, Thermal aging test of AlCrNO-based solar selective absorbing coatings prepared by cathodic arc plating, *Sol Energ Mater Sol Cells*, 136 (2015) 167-171.
- [56] L. Zheng, F. Zhou, Z. Zhou, X. Song, G. Dong, M. Wang, X. Diao, Angular solar absorptance and thermal stability of Mo–SiO<sub>2</sub> double cermet solar selective absorber coating, *Solar Energy*, 115 (2015) 341-346.
- [57] M. Yıldırım, F. Özel, N. Tuğluoğlu, Ö.F. Yüksel, M. Kuş, Optical characterization of Cu<sub>2</sub>ZnSnSe<sub>4-x</sub>S<sub>x</sub> nanocrystals thin film, *Journal of Alloys and Compounds*, 666 (2016) 144-152.
- [58] G.D. Tang, Z.F. Shang, X.Y. Zhang, J. Xu, Z.Z. Li, C.M. Zhen, W.H. Qi, L.L. Lang, Evidence from infrared spectra for the magnetic moment directions of CR cations in the spinel ferrites, *Physica B: Condensed Matter*, 463 (2015) 26-29.
- [59] M.M. Rahman, H.A. Miran, Z.-T. Jiang, M. Altarawneh, L.S. Chuah, H.-L. Lee, A. Amri, N. Mondinos, B.Z. Dlugogorski, Investigation of the post-annealing electromagnetic response of Cu-Co oxide coatings via optical measurement and computational modelling, *RSC Advances*, 7 (2017) 16826-16835.
- [60] H. Kabir, M.M. Rahman, T.S. Roy, A.H. Bhuiyan, Structural and optical properties of plasma polymerized pyromucic aldehyde thin films, *International Journal of Mechanical & Mechatronics Engineering*, 12 (2012) 30-34.
- [61] A. Millar, M.M. Rahman, Z.-T. Jiang, Review of Sol-gel Derived Mixed Metal Oxide Thin Film Coatings with the Addition of Carbon Materials for Selective Surface Applications, *Journal of Advanced Physics*, 3 (2014) 179-193.

- [62] M.M. Rahman, Z.-T. Jiang, P. Munroe, L.S. Chuah, Z.-f. Zhou, Z. Xie, C.Y. Yin, K. Ibrahim, A. Amri, H. Kabir, M.M. Haque, N. Mondinos, M. Altarawneh, B.Z. Dlugogorski, Chemical bonding states and solar selective characteristics of unbalanced magnetron sputtered  $Ti_xM_{1-x-y}N_y$  films, *RSC Advances*, 6 (2016) 36373-36383.
- [63] S.H. Wemple, M. DiDomenico Jr, Theory of the elasto-optic effect in nonmetallic crystals, *Physical Review B*, 1 (1970) 193-202.
- [64] M. Yildirim, F. Özel, N. Tuğluoğlu, Ö.F. Yüksel, M. Kuş, Optical characterization of  $Cu_2ZnSnSe_{4-x}S_x$  nanocrystals thin film, *Journal of Alloys and Compounds*, 666 (2016) 144-152.
- [65] F. Yakuphanoglu, A. Cukurovali, I. Yilmaz, Single-oscillator model and determination of optical constants of some optical thin film materials, *Physica B: Condensed Matter*, 353 (2004) 210-216.
- [66] B. Barış, H.G. Özdemir, N. Tuğluoğlu, S. Karadeniz, O.F. Yüksel, Z. Kişnişci, Optical dispersion and dielectric properties of rubrene organic semiconductor thin film, *Journal of Materials Science: Materials in Electronics*, 25 (2014) 3586-3593.
- [67] A.A.M. Farag, M. Fadel, Optical absorption and dispersion analysis of nanocrystalline perylene-3,4,9,10-tetracarboxylic-3,4,9,10-dianhydride film prepared by dip coating and its optoelectronic application, *Opt Laser Technol*, 45 (2013) 356-363.
- [68] M.M. El-Nahass, A.M. Farid, A.A. Atta, Structural and optical properties of Tris(8-hydroxyquinoline) aluminum (III) ( $Alq_3$ ) thermal evaporated thin films, *Journal of Alloys and Compounds*, 507 (2010) 112-119.
- [69] M.Y. Han, W. Huang, C.H. Chew, L.M. Gan, X.J. Zhang, W. Ji, Large nonlinear absorption in coated  $Ag_2S/CdS$  nanoparticles by inverse microemulsion, *Journal of Physical Chemistry B*, 102 (1998) 1884-1887.
- [70] A. Einav, Solar Energy Research and Development Achievements in Israel and Their Practical Significance, *Journal of Solar Energy Engineering*, 126 (2004) 921-928.
- [71] J. Gordon, solar energy: the State of the Art: ISES position papers, Earthscan2001.
- [72] S. Chaudhuri, D. Bhattacharyya, A. Maity, A. Pal, Surface coatings for solar application, *Materials science forum*, Trans Tech Publ, 1997, pp. 181-206.
- [73] H.Z. Tabor, Selected Reprints of Papers by Harry Zvi Tabor: Solar Energy Pioneer, Balaban Publishers1999.
- [74] M. Farooq, Z.H. Lee, Computations of the optical properties of metal/insulator-composites for solar selective absorbers, *Renewable Energy*, 28 (2003) 1421-1431.
- [75] R.A. Buhrman, Physics of solar selective surfaces. In *Advances in Solar Energy*, ASES Plenum Press, New York, USA, 1986.

- [76] H. Tabor, Selective radiation-I. Wavelength discrimination, Bulletin of Research Council of Israel, 5A (1955) 119-128.
- [77] H. Tabor, Selective radiation-II. Wavefront discrimination, Bulletin of Research Council of Israel, 5A (1955) 129-134.
- [78] O. Agnihotri, B.K. Gupta, Solar selective surfaces, New York, Wiley-Interscience, 1 (1981) 232.
- [79] C.M. Lampert, Coatings for enhanced photothermal energy collection I. Selective absorbers, Solar Energy Materials, 1 (1979) 319-341.
- [80] T. Tesfamichael, Characterization of selective solar absorbers: Experimental and theoretical modeling, Faculty of Science and Technology, Uppsala University, Sweden, 2000.
- [81] Q.-C. Zhang, Metal-AlN cermet solar selective coatings deposited by direct current magnetron sputtering technology, Journal of Physics D: Applied Physics, 31 (1998) 355.
- [82] S. Süzer, F. Kadirgan, H.M. Söhmen, A.J. Wetherilt, I.E. Türe, Spectroscopic characterization of Al<sub>2</sub>O<sub>3</sub>-Ni selective absorbers for solar collectors, Solar Energy Materials and Solar Cells, 52 (1998) 55-60.
- [83] W.E.J. Neal, An introduction to selective surfaces for solar applications, Surface Technology, 20 (1983) 295-299.
- [84] P. Kontinen, Characterization and Aging Studies of Selective Solar C/Al<sub>2</sub>O<sub>3</sub>/Al Absorber Surfaces Department of Engineering Physics and Mathematics, Helsinki University of Technology, Espoo, Finland, 2004.
- [85] E. Randich, R.B. Pettit, Solar selective properties and high temperature stability of CVD ZrB<sub>2</sub>, Solar Energy Materials, 5 (1981) 425-435.
- [86] C.E. Kennedy, Review of mid-to high-temperature solar selective absorber materials, National Renewable Energy Laboratory Golden Colorado, USA (2002).
- [87] E. Randich, D. Allred, Chemically vapor-deposited ZrB<sub>2</sub> as a selective solar absorber, Thin Solid Films, 83 (1981) 393-398.
- [88] B.O. Seraphin, Optical properties of solids: new developments, North-Holland Publishing Co. Ltd. North Holland, 1976.
- [89] B.O. Seraphin, Spectrally selective surfaces and their impact on photothermal solar energy conversion, in: B. Seraphin (Ed.) Solar Energy Conversion, Springer Berlin Heidelberg, Germany, 1979.
- [90] G. Pellegrini, Experimental methods for the preparation of selectively absorbing textured surfaces for photothermal solar conversion, Solar Energy Materials, 3 (1980) 391-404.

- [91] B.O. Seraphin, Chemical vapor deposition of thin semiconductor films for solar energy conversion, *Thin Solid Films*, 39 (1976) 87-94.
- [92] G.L. Harding, M.R. Lake, Sputter etched metal solar selective absorbing surfaces for high temperature thermal collectors, *Solar Energy Materials*, 5 (1981) 445-464.
- [93] B.O. Seraphin, A.B. Meinel, *Optical Properties of Solids: New Developments*, North Holland Publishing Company, Amsterdam, Holland, 1976.
- [94] R.B. Bannerot, Moderately concentrating (not focusing) solar energy collectors," S. L. Sargent, ed., *Proceedings of the Workshop on Solar Collectors for Heating and Cooling of Buildings*, ASME, New York, USA, 1974.
- [95] R.A. Buhrman, H.G. Craighead, *Solar Materials Science*, Academic Press Inc., New York, USA, 1980.
- [96] G.A. Niklasson, C.G. Granqvist, *Materials science for solar energy conversion systems*, Pergamon Press, Oxford, UK, 1991.
- [97] E. Wäckelgård, T. Chibuye, B. Karlsson, Improved solar optical properties of a nickel pigmented anodized aluminum selective surface, *Energy Conservation in Buildings*, *Proceedings of NORTHSUN*, 90 (1990) 177-182.
- [98] H. Uchino, S. Aso, S. Hozumi, H. Tokumasu, Y. Yoshioka, Selective Surfaces of Color-Anodized Aluminum for Solar Collectors, *Natl. Tech. Rep.*, 25 (1979) 994-1004.
- [99] Å. Andersson, O. Hunderi, C.G. Granqvist, Nickel pigmented anodic aluminum oxide for selective absorption of solar energy, *Journal of Applied Physics*, 51 (1980) 754-764.
- [100] E. Wäckelgård, G. Hultmark, Industrially sputtered solar absorber surface, *Solar Energy Materials and Solar Cells*, 54 (1998) 165-170.
- [101] M.R. Nejati, V. Fathollahi, M. Khalaji Asadi, Computer simulation of the optical properties of high-temperature cermet solar selective coatings, *Solar Energy*, 78 (2005) 235-241.
- [102] Z. He, Z. Ji, S. Zhao, C. Wang, K. Liu, Z. Ye, Characterization and electrochromic properties of  $\text{Cu}_x\text{Ni}_{1-x}\text{O}$  films prepared by sol-gel dip-coating, *Solar Energy*, 80 (2006) 226-230.
- [103] Y.M. Lu, W.S. Hwang, J.S. Yang, H.C. Chuang, Properties of nickel oxide thin films deposited by RF reactive magnetron sputtering, *Thin Solid Films*, 420-421 (2002) 54-61.
- [104] G.A. Niklasson, C.G. Granqvist, Surfaces for selective absorption of solar energy: an annotated bibliography 1955-1981, *Journal of Materials Science*, 18 (1983) 3475-3534.
- [105] L. Kaluža, A. Šurca-Vuk, B. Orel, G. Dražič, P. Pelicon, Structural and IR Spectroscopic Analysis of Sol-Gel Processed  $\text{CuFeMnO}_4$  Spinel and  $\text{CuFeMnO}_4/\text{Silica}$  Films for Solar Absorbers, *Journal of Sol-Gel Science and Technology*, 20 (2001) 61-83.

- [106] M.K. Gunde, J.K. Logar, Z.C. Orel, B. OREL, Optimum thickness determination to maximise the spectral selectivity of black pigmented coatings for solar collectors, *Thin Solid Films*, 277 (1996) 185-191.
- [107] Z. Crnjak Orel, B. Orel, M. Klanjšek Gunde, Spectrally selective SnO<sub>2</sub>: F film on glass and black enamelled steel substrates: spray pyrolytical deposition and optical properties, *Solar Energy Materials and Solar Cells*, 26 (1992) 105-116.
- [108] Z. Crnjak Orel, B. Orel, Thermal stability and cross-linking studies of diisocyanate cured solar absorptance low-emittance paint coatings prepared via coil-coating process, *Solar Energy Materials and Solar Cells*, 36 (1995) 11-27.
- [109] Z. Crnjak Orel, N. Leskovšek, B. Orel, M.G. Hutchins, Spectrally selective silicon paint coatings: Influence of pigment volume concentration ratio on their optical properties, *Solar Energy Materials and Solar Cells*, 40 (1996) 197-204.
- [110] Z.C. Orel, M.K. Gunde, B. Orel, Application of the Kubelka-Munk theory for the determination of the optical properties of solar absorbing paints, *Progress in Organic Coatings*, 30 (1997) 59-66.
- [111] Z. Crnjak Orel, Characterisation of high-temperature-resistant spectrally selective paints for solar absorbers, *Solar Energy Materials and Solar Cells*, 57 (1999) 291-301.
- [112] Z. Crnjak Orel, M. Klanjšek Gunde, Spectrally selective paint coatings: Preparation and characterization, *Solar Energy Materials and Solar Cells*, 68 (2001) 337-353.
- [113] Z. Crnjak Orel, M. Klanjšek Gunde, A. Lenček, N. Benz, The preparation and testing of spectrally selective paints on different substrates for solar absorbers, *Solar Energy*, 69, Supplement 6 (2001) 131-135.
- [114] G.B. Smith, A. Gentle, P.D. Swift, A. Earp, N. Mronga, Coloured paints based on iron oxide and silicon oxide coated flakes of aluminium as the pigment, for energy efficient paint: optical and thermal experiments, *Solar Energy Materials and Solar Cells*, 79 (2003) 179-197.
- [115] R.J.H. Lin, P.B. Zimmer, Optimization of coatings for flat plate solar collectors, Report No. Coo/2930-4 to ERDA, 1977.
- [116] E. Barrera, A. Avila, J. Mena, V.H. Lara, M. Ruiz, J. Méndez-Vivar, Synthesis of cobalt-silicon oxide thin films, *Solar Energy Materials and Solar Cells*, 76 (2003) 387-398.
- [117] J. Vince, A. Šurca Vuk, U.O. Krašovec, B. Orel, M. Köhl, M. Heck, Solar absorber coatings based on CoCuMnOx spinels prepared via the sol-gel process: structural and optical properties, *Solar Energy Materials and Solar Cells*, 79 (2003) 313-330.

- [118] R. Bayón, G. San Vicente, C. Maffiotte, Á. Morales, Preparation of selective absorbers based on CuMn spinels by dip-coating method, *Renewable Energy*, 33 (2008) 348-353.
- [119] R. Bayón, G. San Vicente, C. Maffiotte, Á. Morales, Characterization of copper–manganese-oxide thin films deposited by dip-coating, *Solar Energy Materials and Solar Cells*, 92 (2008) 1211-1216.
- [120] R. Bayón, G. San Vicente, Á. Morales, Durability tests and up-scaling of selective absorbers based on copper–manganese oxide deposited by dip-coating, *Solar Energy Materials and Solar Cells*, 94 (2010) 998-1004.
- [121] C.G. Ribbing, A. Roos, Transition metal nitride films for optical applications, in: R.L. Hall (Ed.), San diego, CA, USA, 1997.
- [122] H.C. Barshilia, N. Selvakumar, K.S. Rajam, A. Biswas, Optical properties and thermal stability of TiAlN/AlON tandem absorber prepared by reactive DC/RF magnetron sputtering, *Sol Energ Mater Sol Cells*, 92 (2008) 1425-1433.
- [123] H.C. Barshilia, N. Selvakumar, K.S. Rajam, A. Biswas, Spectrally selective NbAlN/NbAlON/Si<sub>3</sub>N<sub>4</sub> tandem absorber for high-temperature solar applications, *Solar Energy Materials and Solar Cells*, 92 (2008) 495-504.
- [124] M. Du, L. Hao, J. Mi, F. Lv, X. Liu, L. Jiang, S. Wang, Optimization design of Ti<sub>0.5</sub>Al<sub>0.5</sub>N/Ti<sub>0.25</sub>Al<sub>0.75</sub>N/AlN coating used for solar selective applications, *Solar Energy Materials and Solar Cells*, 95 (2011) 1193-1196.
- [125] S.A. Kalogirou, Solar thermal collectors and applications, *Progress in Energy and Combustion Science*, 30 (2004) 231-295.
- [126] C.E. Kennedy, H. Price, Progress in development of high-temperature solarselective coating, *Proceedings of ISEC 2005*, 520 (2005).
- [127] Y. Liu, C. Wang, Y. Xue, The spectral properties and thermal stability of NbTiON solar selective absorbing coating, *Solar Energy Materials and Solar Cells*, 96 (2012) 131-136.
- [128] C. Nunes, V. Teixeira, M.L. Prates, N.P. Barradas, A.D. Sequeira, Graded selective coatings based on chromium and titanium oxynitride, *Thin Solid Films*, 442 (2003) 173-178.
- [129] N. Selvakumar, N.T. Manikandanath, A. Biswas, H.C. Barshilia, Design and fabrication of highly thermally stable HfMoN/HfON/Al<sub>2</sub>O<sub>3</sub> tandem absorber for solar thermal power generation applications, *Solar Energy Materials and Solar Cells*, 102 (2012) 86-92.

- [130] S. Yue, S. Yueyan, W. Fengchun, High-temperature optical properties and stability of  $\text{Al}_x\text{O}_y\text{-AlN}_x\text{-Al}$  solar selective absorbing surface prepared by DC magnetron reactive sputtering, *Solar Energy Materials and Solar Cells*, 77 (2003) 393-403.
- [131] M.M. Rahman, Z.-T. Jiang, Z.-F. Zhou, Z. Xie, C.Y. Yin, H. Kabir, M.M. Haque, A. Amri, N. Mondinos, M. Altarawneh, Effects of annealing temperatures on the morphological, mechanical, surface chemical bonding, and solar selectivity properties of sputtered  $\text{TiAlSiN}$  thin films, *Journal of Alloys and Compounds*, 671 (2016) 254-266.
- [132] H.C. Barshilia, N. Selvakumar, K.S. Rajam, D.V. Sridhara Rao, K. Muraleedharan, Deposition and characterization of  $\text{TiAlN/TiAlON/Si}_3\text{N}_4$  tandem absorbers prepared using reactive direct current magnetron sputtering, *Thin Solid Films*, 516 (2008) 6071-6078.
- [133] V. Godinho, D. Philippon, T.C. Rojas, N.N. Novikova, V.A. Yakovlev, E.A. Vinogradov, A. Fernandez, Characterization of  $\text{Ti}_{1-x}\text{Al}_x\text{N}$  coatings with selective IR reflectivity, *Solar Energy*, 84 (2010) 1397-1401.
- [134] H.C. Barshilia, N. Selvakumar, K.S. Rajam, Thermal stability of  $\text{TiAlN/TiAlON/Si}_3\text{N}_4$  tandem absorbers prepared by reactive direct current magnetron sputtering, *Journal of Vacuum Science & Technology A*, 25 (2007) 383-390.
- [135] J. Huang, C. Xiang, S. Li, X. Zhao, G. He, Preparation, characterization and performance of  $\text{Ti}_{1-x}\text{Al}_x\text{N/Ag/Ti}_{1-x}\text{Al}_x\text{N}$  low-emissivity films, *Applied Surface Science*, 293 (2014) 259-264.
- [136] M. Du, L. Hao, X. Liu, J. Mi, L. Jiang, S. Wang, Optimization design of  $\text{Ti}_{0.5}\text{Al}_{0.5}\text{N/Ti}_{0.25}\text{Al}_{0.75}\text{N/AlN}$  solar selective coating, *Procedia Engineering*, 27 (2012) 6-11.
- [137] L. Hao, M. Du, X. Liu, S. Wang, L. Jiang, F. Lü, Z. Li, J. Mi, Thermal stability of nitride solar selective absorbing coatings used in high temperature parabolic trough current, *Science China Technological Sciences*, 53 (2010) 1507-1512.
- [138] L. Hao, S. Wang, L. Jiang, X. Liu, H. Li, Z. Li, Preparation and thermal stability on non-vacuum high temperature solar selective absorbing coatings, *Chinese Science Bulletin*, 54 (2009) 1451-1454.
- [139] X.-H. Gao, Z.-M. Guo, Q.-F. Geng, P.-J. Ma, A.-Q. Wang, G. Liu, Enhanced optical properties of  $\text{TiN}$ -based spectrally selective solar absorbers deposited at a high substrate temperature, *Solar Energy Materials and Solar Cells*, 163 (2017) 91-97.
- [140] J.-p. Meng, X.-p. Liu, Z.-q. Fu, K. Zhang, Optical design of  $\text{Cu/Zr}_{0.2}\text{AlN}_{0.8}/\text{ZrN/AlN/ZrN/AlN/Al}_{34}\text{O}_{62}\text{N}_4$  solar selective absorbing coatings, *Solar Energy*, 146 (2017) 430-435.



- [141] A.G. Wattoo, C. Xu, L. Yang, C. Ni, C. Yu, X. Nie, M. Yan, S. Mao, Z. Song, Design, fabrication and thermal stability of spectrally selective TiAlN/SiO<sub>2</sub> tandem absorber, *Solar Energy*, 138 (2016) 1-9.
- [142] J. Jyothi, S. Latha, P. Bera, H.S. Nagaraja, H.C. Barshilia, Optimization of process parameters to achieve spectrally selective TiAlC/TiAlCN/TiAlSiCN/TiAlSiCO/TiAlSiO high temperature solar absorber coating, *Solar Energy*, 139 (2016) 58-67.
- [143] Z. Ke, D. Miao, H. Lei, M. Jianping, W. Jining, L. Xiaopeng, D. Zhejun, M. Jie, Z. Bo, Thermal stability test and ageing mechanisms study of different solar selective absorbing coatings, *Surface and Coatings Technology*, DOI <http://dx.doi.org/10.1016/j.surfcoat.2016.08.092>.
- [144] A. Dan, J. Jyothi, K. Chattopadhyay, H.C. Barshilia, B. Basu, Spectrally selective absorber coating of WAlN/WAlON/Al<sub>2</sub>O<sub>3</sub> for solar thermal applications, *Solar Energy Materials and Solar Cells*, 157 (2016) 716-726.
- [145] T.K. Tsai, Y.H. Li, J.S. Fang, Spectral properties and thermal stability of CrN/CrON/Al<sub>2</sub>O<sub>3</sub> spectrally selective coating, *Thin Solid Films*, 615 (2016) 91-96.
- [146] B. Usmani, A. Dixit, Spectrally selective response of ZrO<sub>x</sub>/ZrC-ZrN/Zr absorber-reflector tandem structures on stainless steel and copper substrates for high temperature solar thermal applications, *Solar Energy*, 134 (2016) 353-365.
- [147] N. Selvakumar, K. Prajith, A. Biswas, H.C. Barshilia, Optical simulation and fabrication of HfMoN/HfON/Al<sub>2</sub>O<sub>3</sub> spectrally selective coating, *Solar Energy Materials and Solar Cells*, 140 (2015) 328-334.
- [148] C. Zou, L. Huang, J. Wang, S. Xue, Effects of antireflection layers on the optical and thermal stability properties of a spectrally selective CrAlN-CrAlON based tandem absorber, *Solar Energy Materials and Solar Cells*, 137 (2015) 243-252.
- [149] H.C. Barshilia, Growth, characterization and performance evaluation of Ti/AlTiN/AlTiON/AlTiO high temperature spectrally selective coatings for solar thermal power applications, *Solar Energy Materials and Solar Cells*, 130 (2014) 322-330.
- [150] C. Wang, J. Shi, Z. Geng, X. Ling, Polychromic Al-AlN cermet solar absorber coating with high absorption efficiency and excellent durability, *Solar Energy Materials and Solar Cells*, 144 (2016) 14-22.
- [151] L. Rebouta, P. Capela, M. Andritschky, A. Matilainen, P. Santilli, K. Pischow, E. Alves, Characterization of TiAlSiN/TiAlSiON/SiO<sub>2</sub> optical stack designed by modelling calculations for solar selective applications, *Solar Energy Materials and Solar Cells*, 105 (2012) 202-207.

- [152] P. Song, Y. Wu, L. Wang, Y. Sun, Y. Ning, Y. Zhang, B. Dai, E. Tomasella, A. Bousquet, C. Wang, The investigation of thermal stability of Al/NbMoN/NbMoON/SiO<sub>2</sub> solar selective absorbing coating, *Solar Energy Materials and Solar Cells*, 171 (2017) 253-257.
- [153] J. Jyothi, A. Biswas, P. Sarkar, A. Soum-Glaude, H.S. Nagaraja, H.C. Barshilia, Optical properties of TiAlC/TiAlCN/TiAlSiCN/TiAlSiCO/TiAlSiO tandem absorber coatings by phase-modulated spectroscopic ellipsometry, *Applied Physics A*, 123 (2017) 496.
- [154] A. Soum-Glaude, A. Le Gal, M. Bichotte, C. Escape, L. Dubost, Optical characterization of TiAlN<sub>x</sub>/TiAlN<sub>y</sub>/Al<sub>2</sub>O<sub>3</sub> tandem solar selective absorber coatings, *Solar Energy Materials and Solar Cells*, 170 (2017) 254-262.
- [155] B. Li, D. Qi, X. Wang, F. Wang, Y. Nie, R. Gong, Enhanced spectra selectivity of solar absorber film with Ti/Si<sub>3</sub>N<sub>4</sub> photonic structures, *Materials Letters*, 201 (2017) 5-8.
- [156] Y. Ning, W. Wang, L. Wang, Y. Sun, P. Song, H. Man, Y. Zhang, B. Dai, J. Zhang, C. Wang, Y. Zhang, S. Zhao, E. Tomasella, A. Bousquet, J. Cellier, Optical simulation and preparation of novel Mo/ZrSiN/ZrSiON/SiO<sub>2</sub> solar selective absorbing coating, *Solar Energy Materials and Solar Cells*, 167 (2017) 178-183.
- [157] Y. Ning, W. Wang, Y. Sun, Y. Wu, H. Man, C. Wang, S. Zhao, E. Tomasella, A. Bousquet, Y. Zhang, Tuning of reflectance transition position of Al-AlN cermet solar selective absorbing coating by simulating, *Infrared Physics & Technology*, 80 (2017) 65-70.
- [158] J. Zhang, T.P. Chen, Y.C. Liu, Z. Liu, H.Y. Yang, Modeling of a selective solar absorber thin film structure based on double TiN<sub>x</sub>O<sub>y</sub> layers for concentrated solar power applications, *Solar Energy*, 142 (2017) 33-38.
- [159] C. Prieto, E. Céspedes, D. Hernández-Pinilla, A. Rodríguez-Palomo, O. Sánchez, F. Jiménez-Villacorta, E. Salas-Colera, Mo coordination and Thermal Stability of the Mo-Si<sub>3</sub>N<sub>4</sub> Absorbers for Solar Selective Coatings, *MRS Advances*, DOI 10.1557/adv.2017.408(2017) 1-8.
- [160] T.K. Boström, E. Wäckelgård, G. Westin, Anti-reflection coatings for solution-chemically derived nickel - Alumina solar absorbers, *Solar Energy Materials and Solar Cells*, 84 (2004) 183-191.
- [161] K. Forberich, G. Dennler, M.C. Scharber, K. Hingerl, T. Fromherz, C.J. Brabec, Performance improvement of organic solar cells with moth eye anti-reflection coating, *Thin Solid Films*, 516 (2008) 7167-7170.

- [162] C. Wang, J. Shi, Z. Geng, X. Ling, Polychromic Al-AlN cermet solar absorber coating with high absorption efficiency and excellent durability, *Solar Energy Materials and Solar Cells*, 144 (2016) 14-22.
- [163] A.D. Wilson, Reactively sputtered silicon oxy-nitride films for solar absorber anti-reflection coatings, *Solar Energy Materials*, 10 (1984) 9-24.
- [164] Z.C. Orel, Characterisation of high-temperature-resistant spectrally selective paints for solar absorbers, *Solar Energy Materials and Solar Cells*, 57 (1999) 291-301.
- [165] Z.C. Orel, M.K. Gunde, A. Lenček, N. Benz, The preparation and testing of spectrally selective paints on different substrates for solar absorbers, *Solar Energy*, 69 (2000) 131-135.
- [166] T. Tesfamichael, A. Hoel, E. Wäkelgård, G.A. Niklasson, M.K. Gunde, Z.C. Orel, Optical characterization and modeling of black pigments used in thickness-sensitive solar-selective absorbing paints, *Solar Energy*, 69 (2000) 35-43.
- [167] R.-J. Xie, H.T. Hintzen, Optical Properties of (Oxy)Nitride Materials: A Review, *Journal of the American Ceramic Society*, 96 (2013) 665-687.
- [168] D.J. Ham, J.S. Lee, Transition metal carbides and nitrides as electrode materials for low temperature fuel cells, *Energies*, 2 (2009) 873-899.
- [169] B. Avasarala, P. Haldar, On the stability of TiN-based electrocatalysts for fuel cell applications, *International Journal of Hydrogen Energy*, 36 (2011) 3965-3974.
- [170] D.H. Gregory, Nitride chemistry of the s-block elements, *Coordination Chemistry Reviews*, 215 (2001) 301-345.
- [171] E. Kroke, M. Schwarz, Novel group 14 nitrides, *Coordination Chemistry Reviews*, 248 (2004) 493-532.
- [172] R. Marchand, F. Tessier, A. Le Sauze, N. Diot, Typical features of nitrogen in nitride-type compounds, *International Journal of Inorganic Materials*, 3 (2001) 1143-1146.
- [173] M. Zeuner, S. Pagano, W. Schnick, Nitridosilicates and oxonitridosilicates: From ceramic materials to structural and functional diversity, *Angewandte Chemie - International Edition*, 50 (2011) 7754-7775.
- [174] B.D. Beake, V.M. Vishnyakov, R. Valizadeh, J.S. Colligon, Influence of mechanical properties on the nanoscratch behaviour of hard nanocomposite TiN/Si<sub>3</sub>N<sub>4</sub> coatings on Si, *Journal of Physics D: Applied Physics*, 39 (2006) 1392-1397.
- [175] H.C. Kim, T.L. Alford, Investigation on diffusion barrier properties of reactive sputter deposited TiAl<sub>x</sub>N<sub>y</sub>O<sub>z</sub> thin films for Cu metallization, *Thin Solid Films*, 449 (2004) 6-11.
- [176] B.J. Arnold, S. Krishnamurthy, B. Kennedy, D. Cockburn, D. McNally, J.G. Lunney, R. Gunning, M. Venkatesan, J. Alaria, J. Michael, D. Coey, C. McGuinnessy, J.H. Guo,

Growth and characterisation of  $\text{Al}_{1-x}\text{Cr}_x\text{N}$  thin films by RF plasma assisted pulsed laser deposition, *e-Journal of Surface Science and Nanotechnology*, 7 (2009) 497-502.

[177] V.I. Belyi, A. Vasil'evich, *Silicon Nitride in Electronics*, Materials Science Monographs, 34 (1988).

[178] M.H. G. Petzow, *Silicon Nitride Ceramics*, in: M. Jansen (Ed.) *High Performance Non-Oxide Ceramics II*, Springer Berlin Heidelberg, Berlin, Heidelberg, Germany, 2002.

[179] M.S. Kim, Y.K. Zhou, M. Funakoshi, S. Emura, S. Hasegawa, H. Asahi, S. Kimura, S. Emura, K. Tokuda, Y.K. Zhou, S. Hasegawa, H. Asahi, Structural properties of  $\text{AlCrN}$ ,  $\text{GaCrN}$  and  $\text{InCrN}$ , *Appl. Phys. Lett.*, 89 (2006) 232511-232048.

[180] R. Mientus, R. Grötschel, K. Ellmer, Optical and electronic properties of  $\text{CrO}_x\text{N}_y$  films, deposited by reactive DC magnetron sputtering in  $\text{Ar}/\text{N}_2/\text{O}_2(\text{N}_2\text{O})$  atmospheres, *Surface and Coatings Technology*, 200 (2005) 341-345.

[181] S. Logothetidis, P. Patsalas, K. Sarakinos, C. Charitidis, C. Metaxa, The effect of crystal structure and morphology on the optical properties of chromium nitride thin films, *Surface and Coatings Technology*, 180-181 (2004) 637-641.

[182] P. Patsalas, S. Logothetidis, Optical, electronic, and transport properties of nanocrystalline titanium nitride thin films, *Journal of Applied Physics*, 90 (2001) 4725-4734.

[183] P. Patsalas, S. Logothetidis, Interface properties and structural evolution of  $\text{TiN}/\text{Si}$  and  $\text{TiN}/\text{GaN}$  heterostructures, *Journal of Applied Physics*, 93 (2003) 989-998.

[184] D. Gall, C.S. Shin, R.T. Haasch, I. Petrov, J.E. Greene, Band gap in epitaxial  $\text{NaCl}$ -structure  $\text{CrN}(001)$  layers, *Journal of Applied Physics*, 91 (2002) 5882-5886.

[185] J. Häglund, G. Grimvall, T. Jarlborg, A.F. Guillermet, Band structure and cohesive properties of 3d-transition-metal carbides and nitrides with the  $\text{NaCl}$ -type structure, *Physical Review B*, 43 (1991) 14400-14408.

## CHAPTER THREE

---

### **Paper II: Structural, Morphological and Optical Characterizations of Mo, CrN and Mo:CrN Sputtered Coatings for Potential Solar Selective Applications**

---

#### **Abstract**

Mo, CrN, and Mo:CrN sputtered coatings synthesized onto silicon Si(100) substrates were investigated as solar selective surfaces and their potential applications in optical devices. These coatings were characterized using XRD, SEM, UV-Vis, and FTIR techniques. XRD investigation, showed a change in CrN thin film crystallite characteristic due to Mo doping. Compared to the CrN coatings, the Mo:CrN films has a higher lattice parameter and larger grain size than that of CrN phase owing to the formation of MoN phases. Larger grains sizes of Mo:CrN structures were also confirmed *via* FESEM imaging. Optical analysis showed that in the visible range of the solar spectrum, the CrN coatings exhibit the highest solar absorptance of 66% while the lowest thermal emittance value of 5.67 was recorded for the CrN coating doped with Mo. Consequently, the highest solar selectivity of 9.6, and the energy band-gap of 2.88 eV were achieved with the Mo-doped CrN coatings. Various optical coefficients such as optical absorption coefficient, refractive index, extinction coefficient, real and imaginary parts of dielectric constants, and energy loss functions of these coatings were also estimated from the optical reflectance data recorded in the wavelength range of 190 – 2300 nm.

#### **3.1 Introduction**

Metal nitride-based compounds have been widely used as ceramic coatings since the 1980's due to their superior hardness, excellent wear resistance, low friction coefficient, superior thermal stability, and corrosion resistance behaviors under detrimental environmental conditions [1-4]. Compared with other types of similar binary and ternary coatings, TiN or Ti-C-N, CrN ceramic coatings exhibit superior thermal stability [5]. In tribological applications, CrN coatings also demonstrate better performance than TiN coatings under dry and lubricated conditions. As such, CrN coatings are typically used as protective coatings for several tribological forming and casting applications, such as drawing dies, and moulds. Perovskite CrMeN coatings, where Me = Ti, Si, Al, Ta, Nb, Ni, B, and Mo have been explored to improve physical, mechanical and other characteristics of CrN matrix. The ternary CrMeN coatings usually form cation solid solution (Ti, Al, Ta, Nb, Ni, and Mo) or

anion solid solution (in cases of B or C). These solid solution-based coatings have received less attention than conventional coatings and as such, investigation of ternary Cr–Mo–N coatings would be timely [5].

Transition metal nitride-based coatings such as TiN, CrN, MoN, and ZrN have been previously characterized using XRD, and electron microscopy and hardness measurements via indentation method. The formation of cubic crystal lattice structures under non-equilibrium conditions was detected via XRD studies while greater hardness and superior resistance tolerance behaviours were acquired by those coatings [6]. Surface microstructures of Mo-based coatings studied via AFM technique indicated the grain size reduction with subsequent increase in acetylene flow rate [7]. Nanostructured Mo-based coatings deposited onto steel and hard metal substrates by magnetron sputtering technique exhibited a hardness of ~20 GPa together with very fine grains (~2 nm). Annealing in the range from 500 to 1000 °C significantly improved the hardness and elastic modulus of these coatings along with a higher resistance to plastic deformation ratio [8]. Higher ductility of these coatings was also recorded for the samples annealed up to 600 °C. Experimental and simulation based double cermet solar selective coatings has been reported in elsewhere [9]. The Mo-black solar selective coatings prepared by chemical methods from an aqueous solution of ammonium paramolybdate and nickel sulphate were studied for their optical band-gap and refractive index [10]. A high value of solar absorptance and lower value of thermal emittance were reported together with the suitable optical band-gap and refractive index values. Computer simulation was carried out to analyze the optical constants such as refractive index, dielectric constants and extinction coefficient of Mo/Al<sub>2</sub>O<sub>3</sub> solar selective coatings by means of Maxwell-Garnett effective medium theory in the wavelength range of 200-2500 nm [11]. An optimal coatings thickness of 200 nm for the absorption layer was proposed in the visible region of the solar spectra where the absorption was recorded to be invariant with the coating's thickness.

Surface-textured magnetron sputtered single-layer Mo coatings synthesised through the adjustment of deposition parameters onto the silicon Si(100) and stainless steel substrates characterized *via* XRD, SEM, AFM and optical studies exhibited a high solar absorptance and low emittance. It was reported that the controlled surface roughness and larger aspect ratio improves the solar absorption and reduces the thermal emittance values of this coating [12]. Tauc-Lorentz and Drude free-electron theories were used to model the optical constants and the dielectric nature of the coatings was reported. The annealing temperature

effect on the microstructure and spectral selectivity of single layer Mo solar selective coatings was carried out by Xinkang and co-workers [13] in order to establish the mechanism for the degradation of optical properties. After annealing, notable changes in microstructure and compositions were observed. However, the optical properties of the coatings and their thermal stability significantly improved.

Mo/Mo-SiO<sub>2</sub>/SiO<sub>2</sub> spectral selective absorbers deposited onto quartz substrate *via* co-sputtering method for high temperature applications showed high absorptance in the visible range and low thermal emittance in the infra-red range of the solar spectra [14]. After annealing at 800 °C, the thermal emittance of such absorber coatings was significantly reduced from 9.7% to 7.5%. However, the normal reflectance of the absorbers remained almost unchanged in the UV-Vis range of the solar spectrum and increased slightly in the IR region after being annealed at 800 °C in vacuum. Novel Mo/ZrSiN/ZrSiON/SiO<sub>2</sub> solar selective absorbers prepared through magnetron sputtering on the stainless steel substrates were investigated for their temperature dependent solar selective performance. Systematic reduction of the thicknesses of the ZrSiN, ZrSiON and SiO<sub>2</sub> layers, significantly reduced the thermal emittance at 500 °C while the solar absorptance was unaffected. On the other, the high thermal stability up to 500 °C in vacuum, indicated that these absorber coatings could be a viable candidate for high temperature concentrated solar power applications [15].

Experimental studies and computer simulation-based analysis of transition metal nitride based-coatings have been conducted to investigate their structural, microstructural, morphological, mechanical and general optical studies [11, 12, 16-20]. Recently, many researches have been reported on the effect of Mo-doping on CrN film coating in order to investigate their local electronic bonding states, mechanical, and tribological properties [5, 21-23]. Detailed optical analysis in conjunction with the structural and morphological features of these kinds of coatings are extensively discussed in earlier reports [24-29], though we find that a holistic approach integrating other pertinent analyses such as FESEM imaging, XRD analysis and band-gap calculations in tandem with single oscillator model optical dispersion analysis, dielectric characterizations, and energy loss mechanisms analysis are relatively lacking. This motivates to, therefore, incorporate these value-added analyses into the present study so that a clearer all-inclusive understanding of the crystallographic structures, morphological features and optical parameters could be established for Mo, CrN, and Mo:CrN thin film coatings.

## **3.2 Materials and Methods**

### **3.2.1 Film Preparation Technique**

The UDP650 closed field unbalanced magnetron sputtering ion plating system (Teer Coatings Ltd, UK) was employed to prepare Mo, CrN, and Mo:CrN thin film coatings. The silicon Si(100), with 50 mm diameter and 3.0 or 1.5 mm thick, were used as substrates. A rotating sample holder which could provide a uniform exposure for growing the film was surrounded by four vertically mounted pure metallic targets (Cr, Mo). Two chromium targets and one molybdenum target (Cr, Mo, purity 99.9 %, size 345 mm × 145 mm × 8 mm) were used. The background pressure and working pressure during sputtering were  $4 \times 10^{-4}$  Pa and  $15 \times 10^{-2}$  Pa, respectively. Mixed Ar (99.999 %; flow rate at 50 sccm, used as working gas for sputtering) and N<sub>2</sub> (99.999 %) was used as reactive gas to form nitrides. The optical emission monitor (OEM) was used to control the N<sub>2</sub> reactive gas injected near the substrate holder. The entire synthesis process was carried out without any external heating to maintain the target to a substrate distance of 17cm. Advanced Energy Pinnacle plus 5 kW, at a frequency of 250 kHz voltage mode was used to control the bias voltage while 6 kW DC current mode was used to control the target current supply. To coat the Mo:CrN films, 0.2 micron chromium adhesive layers was applied to promote the coating adhesion with a bias voltage of -80 V [30, 31].

### **3.2.2 Characterization of the Thin Film Coatings**

#### **3.2.2.1 XRD analysis**

The XRD measurements of the coatings were carried out using a Bruker AXS D8 Advance (Germany) with Cu- $K_{\alpha}$  radiation ( $\lambda = 1.54 \text{ \AA}$ ). The XRD machine was operated at 40 kV and 40 mA coupled with a Lynx-eyed detector. The scan parameters used were:  $2\theta$  scan range 30°-90°, step size (degree): 0.01°, time/step: 0.15 s and total scan time/sample was ~15 minutes. Phase identification of the films was confirmed by matching the diffraction peaks with those of JCPDS database. The lattice parameters of the defined structures were estimated from the XRD peaks using standard Cohen–Wagner’s plot for cubic crystal structure and Cohen procedure for hexagonal crystal structure [32].

#### **3.2.2.2 FESEM analysis**

The morphological analysis of the sputtered coatings was performed by a field-emission scanning electron microscope (FESEM) using Zeiss Neon 40EsB FIBSEM, an Oxford Instruments Inca X-act SDD X-ray detector. A secondary electron (SEI) detector was used to characterize the overall surface morphology of thin film structures. The SEM machine



was operated at 25 kV. The coatings were glued with double sided carbon tape affixed to the sample holders.

### 3.2.2.3 UV-Vis studies

The UV-Vis reflectance spectroscopy of the coatings was conducted to explore various optical parameters. A UV-Vis double beam spectrophotometer with 60 mm integrating sphere (Model: UV-670 UV-Vis spectrophotometer, JASCO, USA) was used to obtain UV-Vis reflectance spectra in the wavelength range from 190 to 2300 nm. For a given wavelength range, the solar absorptance ( $\alpha$ ) is defined as the weighted fraction between absorbed radiation and incoming solar radiation ( $I_{sol}$ ) (popularly known as the Beckman-Duffie method) [33-35]:

$$\alpha = \frac{\int_{0.19}^{2.5} I_{sol}(\lambda)(1-R(\lambda))d\lambda}{\int_{0.19}^{2.5} I_{sol}(\lambda)d\lambda} \quad (1)$$

The UV-Vis reflectance spectroscopic data was also used to calculate and determine the other optical constants, such as solar absorptance, band-gap, refractive index, dielectric constants and energy loss functions of Mo, CrN and Mo:CrN sputtered coatings.

### 3.2.2.4 FTIR studies

Infrared analysis of the coatings was conducted using FTIR spectrometer (Perkin Elmer Spectrum 100 FTIR Spectrometer, USA). The wavelength from 2.5 to 14.5  $\mu\text{m}$  was used to estimate their thermal emittance in the infrared ranges of the solar spectrum. The FTIR reflectance data collected in the range of 650–4000  $\text{cm}^{-1}$  was converted to the corresponding wavelengths. A bare glass substrate was used for baseline correction of the system before recording the FTIR spectra of the coatings [36]. The thermal emittance ( $\varepsilon$ ) is defined as the weighted fraction between emitted radiation and the Planck black-body distribution ( $I_p$ ) and can be calculated using Eq. (2) [33, 37]:

$$\varepsilon = \frac{\int_{2.5}^{15.36} I_p(\lambda)(1-R(\lambda))d\lambda}{\int_{2.5}^{15.36} I_p(\lambda)d\lambda} \quad (2)$$

### 3.2.2.5 Solar selectivity

The solar selectivity,  $s$  is the key parameter of a selective surface which is defined as a ratio of solar absorptance,  $\alpha$  to the thermal emittance,  $\varepsilon$  and can be expressed by the following Eq. (3) [38]:

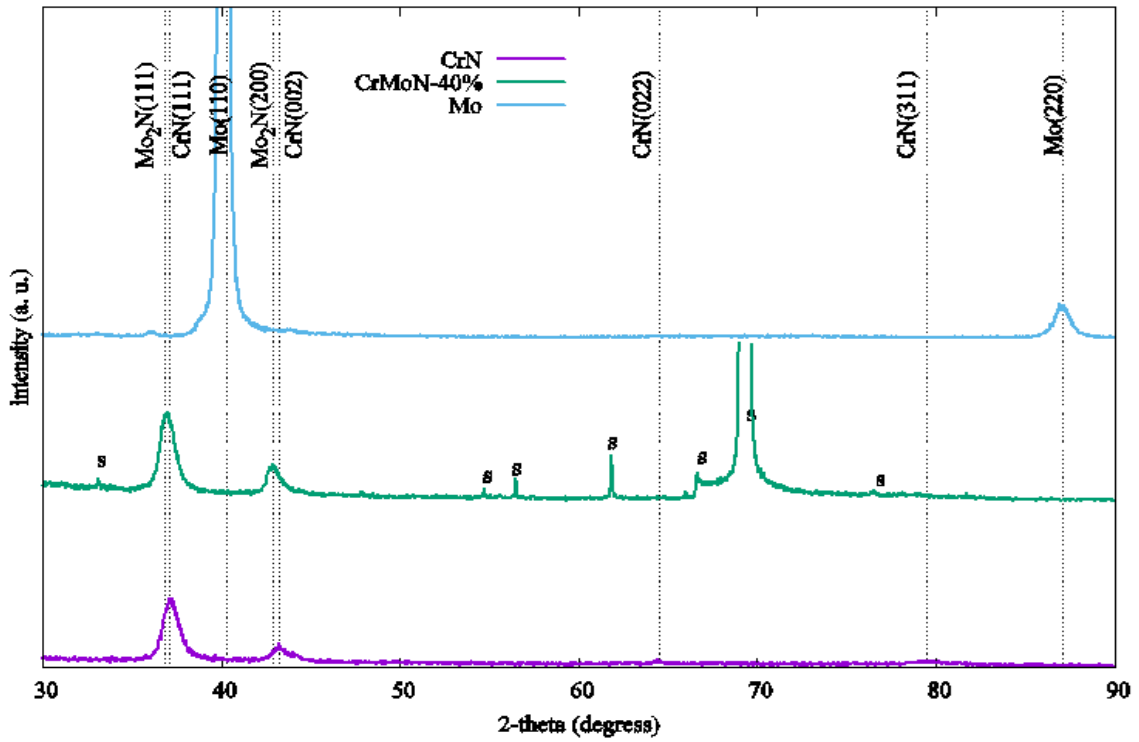
$$s = \frac{\alpha}{\varepsilon} \quad (3)$$

where  $\alpha$  is the solar absorptance of the coatings estimated in a wavelength range of 190 nm and 2300 nm while  $\varepsilon$  is the thermal emittance in the wavelength range between 2.5  $\mu\text{m}$  and 14.5  $\mu\text{m}$ . The air mass (AM) of solar spectrum,  $I_{sol}$  is 1.5 according to the ISO standard 9845-1 (1992).

### 3.3 Results and Discussion

#### 3.3.1 XRD analysis of Mo, CrN and CrMoN films

The XRD patterns of the Mo, CrN and Mo:CrN coatings sputtered on silicon Si (100) substrates are presented in Figure 1. From Figure 1, broadened peaks were observed at (111), (002), (022) and (311) reflection planes. CrN, and  $\gamma\text{-Mo}_2\text{N}$  phases were seen at (111), and (200) crystal planes while (110) reflection plane confirms the presence of Mo phase. The broadened peaks for Mo phases observed at (110) and (220) crystal planes are centred at approximately  $2\theta = 40.5^\circ$  and  $2\theta = 87.6^\circ$  and the strongest peak of Mo phase was observed at (110) crystal plane. The characteristic Mo thin film peaks were believed to be broadened as a result of the nano-sized agglomerations around the film surfaces [31, 39]. In the case of  $\text{Mo}_2\text{N}$  and CrN in the first two bottom graphs (see Figure 1), a strong peak centred at  $2\theta = 37.525^\circ$  corresponds to the (111) crystal planes in both graphs. The peaks centred at  $2\theta = 43.6^\circ$  were for CrN and  $\gamma\text{-Mo}_2\text{N}$  phases at (002) and (200) reflection planes, respectively, are less intense from the previously discussed peaks. Other two peaks assigned as (022) and (311) reflection planes are due to the presence of CrN phase. However, there is no clear indication of the occurrence of CrMoN phase that might be attributed to the very small crystallite size or amorphous state of the solid solution of CrMoN matrix [31]. The broadening and shifting nature of the diffraction peaks is believed to be associated with the development of internal stress and change of inter-planar spacing, which arise from the formation of a substitutional solid solution structure [40, 41]. In the case of Mo:CrN structure, its peaks are shifted towards the lower Bragg angle sides is due to the result of the substitution of Cr atoms by Mo atoms. It is believed that the Mo atom are dissolved into CrN matrix and larger Mo atoms (201  $\text{\AA}$ ) replaces the Cr atoms (185  $\text{\AA}$ ) [5]. Consequently, the lattice parameters, inter-planar spacing, and grain sizes were changed, as seen from Table 1.



**Figure 1.** XRD spectra of the as-deposited Mo, CrN, and Mo:CrN sputtered coatings synthesized on silicon substrates.

A similar effect was also observed by other studies [42-45]. This is in accordance with Bragg's equation  $2d\sin\theta = n\lambda$  (where  $\lambda$  and  $n$  are constants while  $2\theta$  is inversely proportional with lattice distance  $d$ ), the peaks end up with a certain peak shift [2]. In addition, the substrate negative bias voltage also can alter the preferred orientation of the growth plane of the coatings during the sputtering progression [46]. In sputtered coatings, the residual stress primarily arises from the working environment and elementary potentials of two sources: thermal and intrinsic stresses. Thermal discrepancy results in thermal stresses between the coating and substrate during final cooling from deposition to room temperature. The thermal effect becomes more exaggerated when multilayer films are coated *via* sputtering [47].

XRD data were used to estimate the average crystallite size of CrN, Mo, and Mo:CrN phases *via* Debye–Scherrer equation,

$$D = \frac{0.9 \lambda}{\beta \cos \theta} \quad (4)$$

where  $\lambda$  is the X-ray wavelength,  $\beta$  is the full width at half maximum (FWHM) and  $\theta$  is the diffraction angle. Estimated crystallite sizes are listed in Table 1. Table 1 shows that compared to the CrN matrix, the Mo:CrN films have higher lattice parameter and higher grain sizes. This is due to the formation of MoN phases *via* Mo interaction with N around the grain boundaries of CrN phase [31]. It is also assumed that the enlargement of both the lattice parameter and grain size of Mo-doped CrN coatings is due to the fact that the Mo atoms may not only replace the Cr on their sites, but they coalesce and agglomerate around the grain boundaries of the coating matrix. This supports the idea of the presence of the Mo phase in the coating structure.

**Table 1.** Lattice parameters and grain size of Mo, CrN and Mo:CrN sputtered coatings.

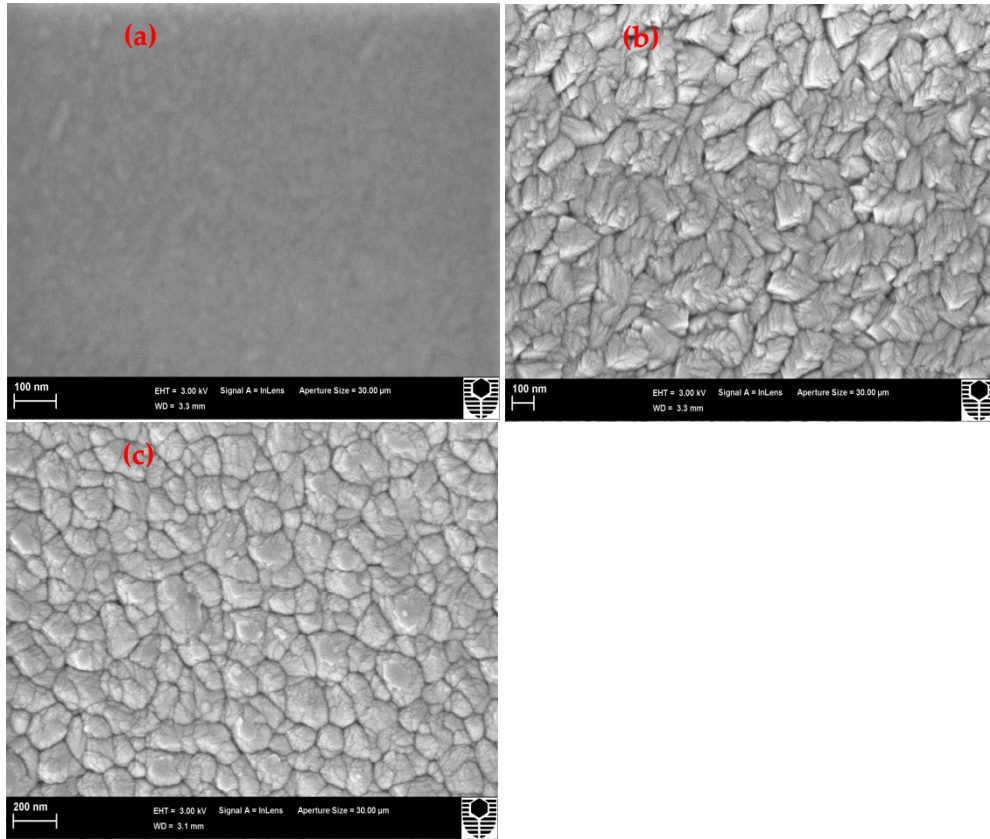
Coatings name	Lattice parameter, $a$ (Å)	Grain size ( $\pm 10\%$ ), $D$ (nm)
Mo	3.17	106.18
CrN	4.14	112.73
Mo:CrN	4.19	161.45

The development of intrinsic stresses and its magnitude depends on the deposition conditions, sputtering gases working pressures, substrate to target distance, reference potential on substrate, coating's thickness and stoichiometry [48, 49]. Mohammadpour *et al.* and Yousaf *et al.* have investigated the effect of metallic Al-doped TiN coatings on their physical and mechanical characteristics [50, 51]. CrN (111) phase observed at  $2\theta = 37.53^\circ$  has a lattice parameter of 4.14 Å is in good agreement with other literatures [41, 43, 52]. The lattice parameters of CrN and Mo:CrN phases were also found to be in good agreement with other reports [41, 43].

### 3.3.2 Morphological features of Mo, CrN and CrMoN films *via* FESEM studies

In order to investigate the surface morphology of Mo, CrN, and Mo:CrN coatings sputtered on silicon substrates, the samples were analysed using FESEM technique and results are shown in Figure 2. Figure 2(a) shows that the surface morphology of Mo/Si coating is markedly different from those of CrN and Mo:CrN. The Mo/Si coating displays uniform, fine, smooth, dense and compact surface structure the grain sizes seemed to be relatively smaller than the other two coatings. CrN/Si and Mo:CrN/Si coatings exhibit uniform structured films with larger grains and “loose” structures which are caused by a non-reactive nucleation. The CrN FESEM morphology indicates irregular, rougher grain with sharp edges. The Mo-dopant to the CrN system exhibited refined edged and slightly

increased grain sizes. This means that due to the Mo-doping, both the surface morphology and grain shapes are reformed with regular mould-like structures seen around the surface of the coatings. At the same time, surface roughness seems to dissipate in the Mo:CrN coatings. This may suggest that the Mo atoms are diffused around the CrN matrix during the sputtering processes and thereby stimulated grain growth is eventually acting as the nucleation site for lattice distortions. This is in good agreement with the XRD results that the substitution of Cr atoms by Mo atoms help to coalescence and agglomeration of the Mo particles to form larger grains. These features were supported in a previous study by Hones *et al.* [23]. They showed that CrN structures consist of a combination of larger elongated rhombohedral and small cubic crystallites while the Mo-doped CrN structure has grains with an average size of 100 nm. At a closer look, a substructure of these grains appears with a crystallite size of about 25 nm [23].



**Figure 2.** FESEM images of: (a) Mo, (b) CrN, and (c) Mo:CrN sputtered coatings.

The dense and closely packed structures of Mo:CrN morphology would exhibit more stability as a selective surface at high temperatures. On the other side, such coatings are more mechanically reliable than the CrN coatings without doping [31]. The surface roughness would produce a gradient in the optical constants rather than a sharp discontinuity at the interface. Kang and Kim [53] indicated that the gradient in the optical constants strengthen the optical behaviour of such kind of coatings.

EDS analysis gives the elemental chemical compositions, and the atomic concentrations Mo, CrN and Mo:CrN coatings. The EDS data collected at different surface areas of these coatings are tabulated in Table 2.

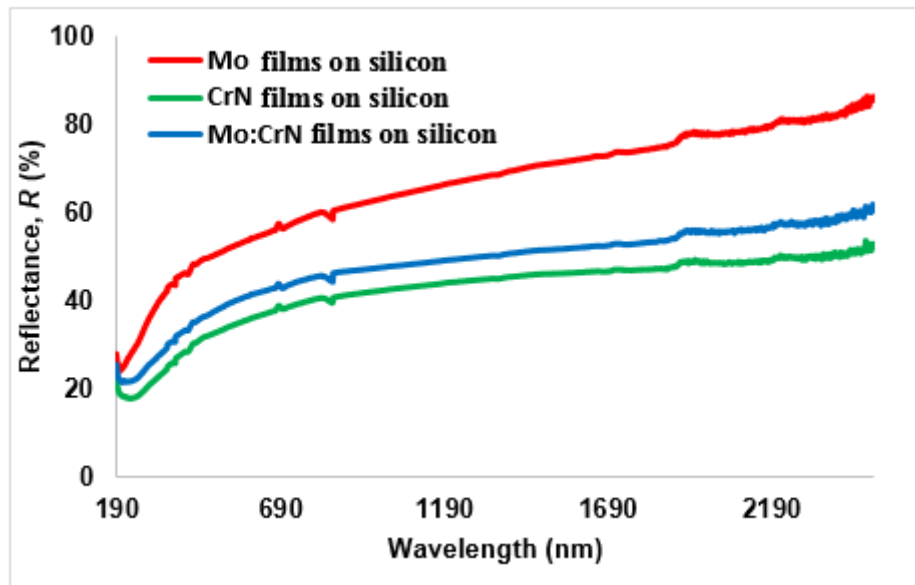
**Table 2.** EDS analysis of the as-deposited  $\text{Cr}_x\text{Mo}_{1-x-y}\text{N}_y$  magnetron sputtered films.

Coatings name	Mo (at.%)	Cr (at.%)	N (at.%)
Mo	100	-	-
CrN	-	92.42	7.58
Mo:CrN	24.35	70.12	5.53

### 3.3.3 Optical Characterizations of Mo, CrN and CrMoN Films

#### 3.3.3.1 UV-Vis Investigations

The solar absorptance of Mo, CrN and Mo:CrN coatings, measured from the UV-Vis reflectance data, as a function of wavelength within the range of 190-2300 nm, shown in Figure 3, is displayed in Table 3. Beckman-Duffie method described in equation (1) was used to calculate the solar absorptance values of these coatings [38, 54]. From Figure 3, it can be concluded that among the three coatings, in the visible range of solar spectrum, the CrN coating shows the lowest reflection of the solar radiation while Mo coating (being the sample with the highest Mo concentration) exhibits the highest reflection due to its metallic nature. On the other hand, Mo-doped CrN coating shows a reflectivity above CrN coating because Mo atoms agglomerate in the CrN structure and acting as scattering centres and traps for the incident light [55]. It is believed that Mo-doping in CrN matrix affects its band structure which clearly influences the solar selective characteristic of Mo:CrN system as seen in Figure 3. This behavior confirms that the solar absorptance of CrN coating has been slightly dropped while Mo was doped to form Mo:CrN system.

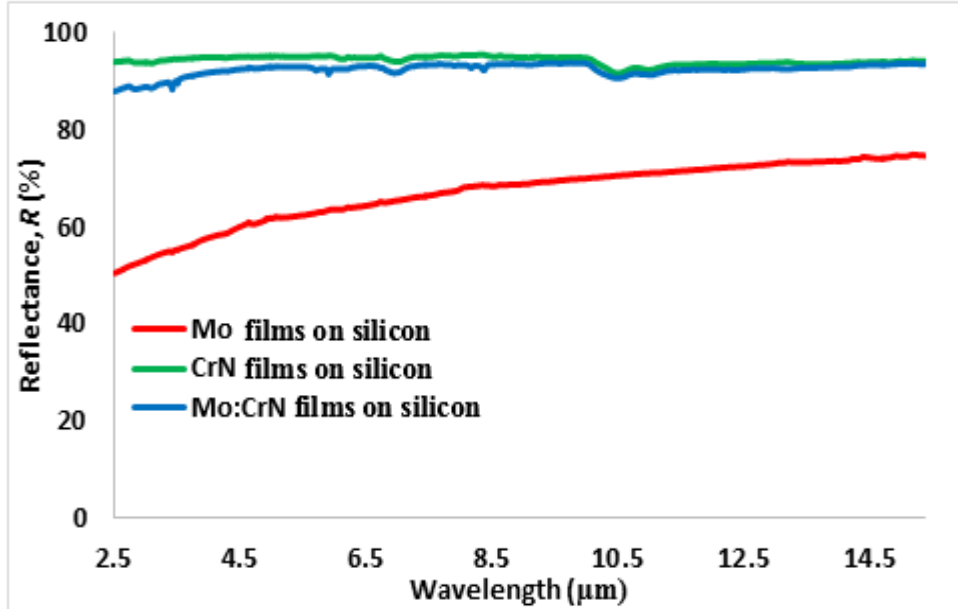


**Figure 3.** UV-Vis reflectance spectra of Mo, CrN, and Mo:CrN sputtered coatings deposited onto silicon substrates as a function of wavelength.

#### 3.3.3.2 FTIR results

Optical reflectance data measured *via* FTIR spectroscopy in the wavelength range from 2.5 to 14.5  $\mu\text{m}$  shown in the following Figure 4, was utilized to estimate the thermal emittance values of Mo, CrN, Mo:CrN coatings using the Beckmann-Duffie method described in Eq. (2) [38, 54]. The estimated thermal emittance values of Mo, CrN, and Mo:CrN coatings are

presented in Table 3. The Mo-doped CrN coating has the lowest thermal emittance than that of CrN coating (in the infrared range) suggesting that the addition of Mo and subsequent interactions of Mo atoms with that of the CrN lead to modify its band structures.



**Figure 4.** FTIR reflectance spectra of Mo, CrN, and Mo:CrN sputtered coatings deposited onto silicon substrates as a function of wavelength.

### 3.3.3.3 Solar selectivity results

The solar selectivity of Mo, CrN, and Mo:CrN coatings are presented in Table 3. From Table 3, it is seen that, among the three studied coatings, Mo:CrN system shows the highest selectivity. Since the band structures of Mo:CrN matrix is modified with Mo-dopant, it clearly influences the solar selective as seen from Table 3. The solar selectivity of Mo:CrN has improved from 8.5 to 9.6 due to the improvement of coating's thermal emissivity from 7.1 to 5.6. This indicates a good potential for these materials to be used in solar selective absorber applications.

**Table 3.** Solar absorptance, thermal emittance and solar selectivity values of Mo, CrN and Mo:CrN sputtered films.

Coatings name	Solar absorptance, $\alpha$ (%)	Thermal emittance, $\varepsilon$ (%)	Solar selectivity, $s = \alpha/\varepsilon$
Mo	44.7	31.5	1.4
CrN	62	7.1	8.5
Mo:CrN	53.5	5.6	9.6



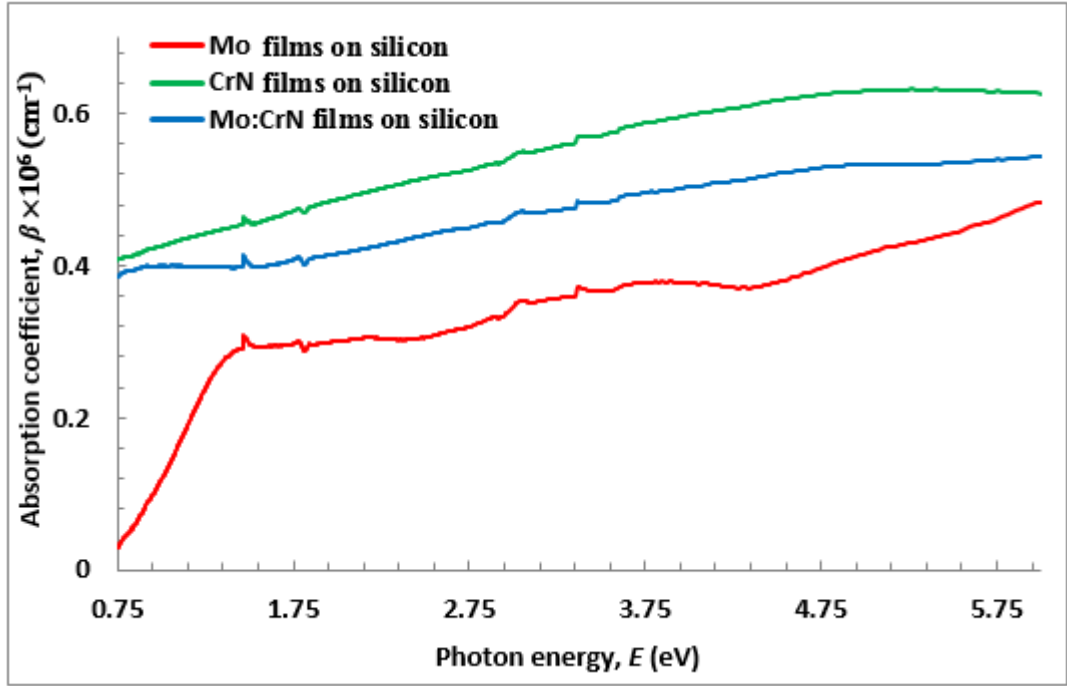
#### 3.3.3.4 *Optical band-gap analysis*

The optical characteristics of absorber materials strongly depend on the wavelength of the incident solar radiation. When solar radiation is brought onto a certain material, a portion of the incoming light is absorbed as a result of excitations of molecular and atomic motions to a specific energy level. The photon energy of visible spectrum is sufficiently high for the absorption such atoms. A linear relationship between the solar absorption coefficient and photon energy facilitates investigation of the band structure and the type of transitions involved in absorption process, and reflected in the following equation [56]:

$$\beta = 2.3026 \frac{A}{d} \quad (5)$$

where  $\beta$ ,  $A$ , and  $d$  are the absorption coefficient, optical absorbance expressed as percentage in terms of UV-Vis reflectance data (calculated as  $A = 100\% - R\%$ ), and the coating's thickness, respectively.

The absorption coefficient of as-deposited Mo, CrN, and Mo:CrN sputtered coatings as a function of incident photon energy is shown in Figure 5. Figure 5 clearly shows that CrN coatings possess the highest absorption coefficient while the absorption coefficient of Mo:CrN is intermediate between Mo and CrN coatings. The solar absorption of materials at a specific wavelength, is related with the excitation of electrons in atoms and molecules to higher energy states.

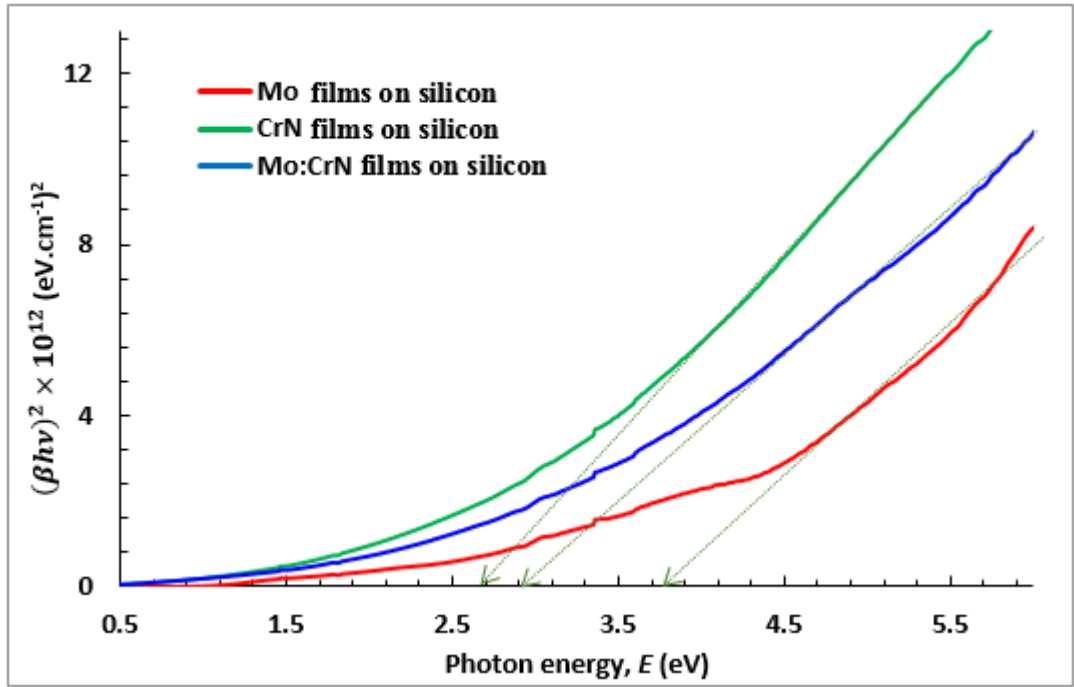


**Figure 5.** Absorption coefficient of Mo, CrN, and Mo:CrN sputtered coatings deposited onto silicon substrates as a function of photon energy.

Tauc relation is useful in studying the band structure and the type of electronic transitions involved during the absorption of solar radiation in crystalline and amorphous materials [56-58]:

$$\beta h\nu = A(h\nu - E_g)^z \quad (6)$$

where,  $\beta$  is the absorption coefficient,  $h\nu$  is the photon energy,  $h$  is Planck's constant,  $\nu$  is the frequency of the incident light,  $A$  is a constant,  $E_g$  is the band-gap energy and  $z$  is an index depending on the type of optical transitions involved in the photon absorption process.



**Figure 6.** Plots of  $(\beta hv)^2$  vs  $hv$  of Mo, CrN, and Mo:CrN sputtered coatings deposited onto silicon substrates as a function of wavelength.

Using the Tauc plots of  $(\beta hv)^2$  vs  $hv$ , for Mo, CrN and Mo:CrN coatings (see Figure 6), the energy band-gaps estimated from the intercepts of the linear portion of the curves and extrapolating them to zero along the energy axis are presented in Table 4. Energy band-gap data show that Mo coating has the highest value of 3.78 eV and the CrN coating has the lowest value for the band-gap energy. We conclude that the higher band-gap of Mo/Si coating is related to the surface oxidation of the coating (a very thin  $\text{MoO}_3$  layer) during the synthesis process. The optical band gap of CrN coating was improved from 2.67 eV to 2.88 eV when doped by Mo-metal. As discussed previously, Mo-doping on CrN coating leads to enhance the agglomeration along the preferred orientation, enlarges the grain size and thereby reduces the density of grain boundaries. All these factors eventually lead to release the trapped free electrons in the grain boundaries, when an incident photon with specific energy interacts with the coating; some portion of the incident energy is absorbed by the electrons resulting to excite them to a higher energy level if the absorbed energy is  $\geq E_g$ . The enhancement of optical band gap can also be explained through the  $(\Delta E_g^{BM})$  Burstein-Moss relation [59]:

$$\Delta E_g^{BM} = \frac{1}{2m_{vc}^*} (3\pi^2 n)^{\frac{2}{3}} \quad (7)$$

where  $m_{vc}^*$  is the electron effective mass estimated from  $m_v$  (effective electron mass in valance band) and  $m_c$  (effective electron mass in conduction band),  $n$  is the carrier concentration.

**Table 4.** Energy band-gap values of Mo, CrN and Mo:CrN sputtered films.

Coatings name	Band-gap energy, $E_g$ (eV)
Mo	3.78
CrN	2.67
Mo:CrN	2.88

### 3.3.3.5 Refractive index and extinction coefficient analysis

The refractive index,  $n$  and extinction coefficient,  $k$  of Mo, CrN and Mo:CrN coatings calculated using the UV-Vis reflectance data in the wavelength range of 190 to 2300 nm are shown in Figures 7 and 8, respectively. The complex refractive index of materials is defined by,

$$n^* = n + ik \quad (8)$$

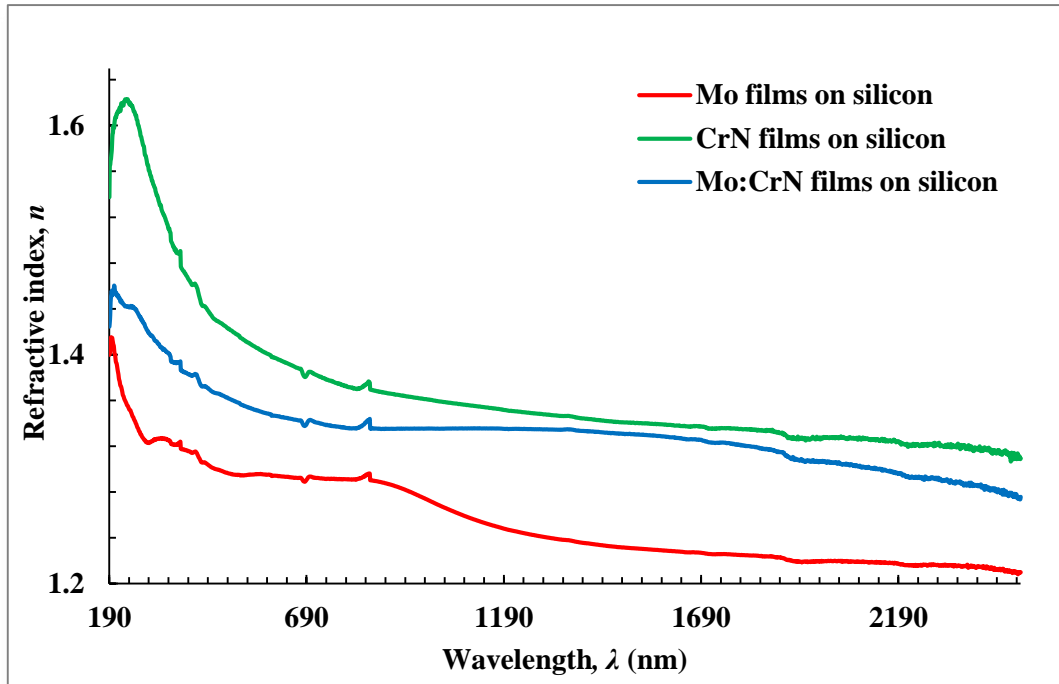
The extinction coefficient,  $k$  could be directly calculated using the absorption coefficient,  $\beta$  via following relation,

$$k = \frac{\beta\lambda}{4\pi} \quad (9)$$

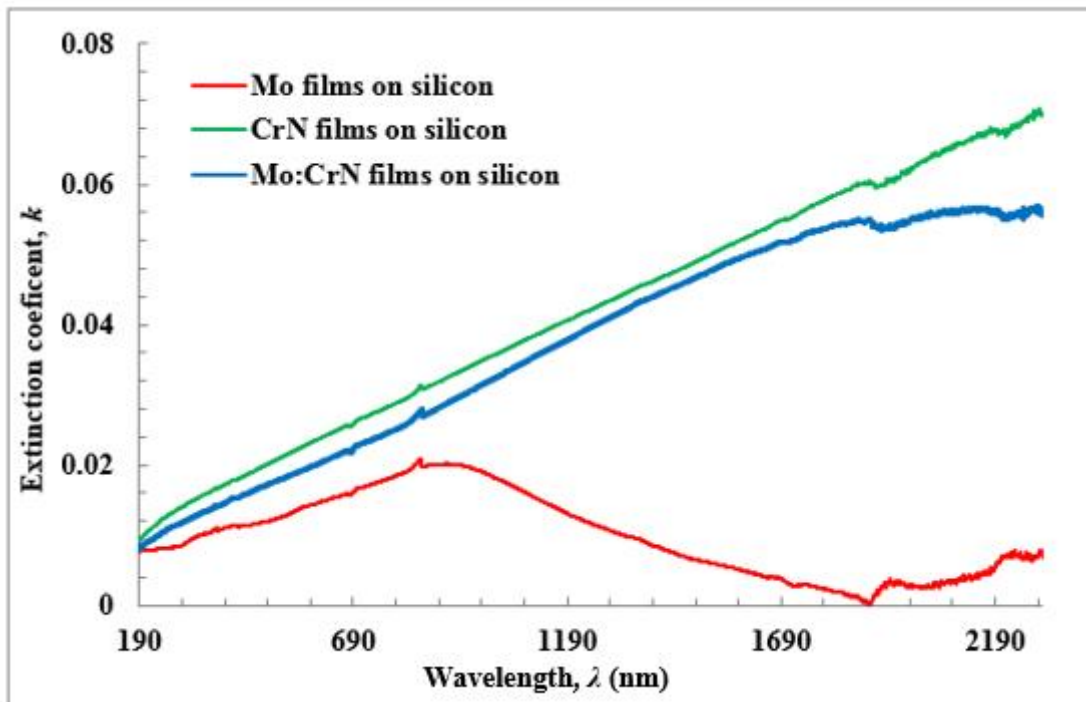
In terms of the reflectance data,  $R$  and extinction coefficient,  $k$  real part of the complex refractive index is defined using the following equation,

$$n = \left( \frac{1+R}{1-R} \right) + \sqrt{\frac{4R}{(1-R)^2} - k^2} \quad (10)$$

Figures 7 and 8 show that CrN coatings have the highest values for the refractive index and extinction coefficient within the observed wavelength range. The significant dispersion behaviors of CrN coating, which affects the  $n$  and  $k$  values, are arisen from the resonance effect between the incoming solar radiation and electronic polarizability. Our findings were consistent with earlier reported results [60]. These optical results indicate that CrN coating has better homogeneity and less porosity.



**Figure 7.** Refractive index of Mo, CrN, and Mo:CrN sputtered coatings deposited onto silicon



**Figure 8.** Extinction coefficient of Mo, CrN, and Mo:CrN sputtered coatings deposited onto silicon substrates as a function of wavelength.

### 3.3.6 Dielectric characterizations

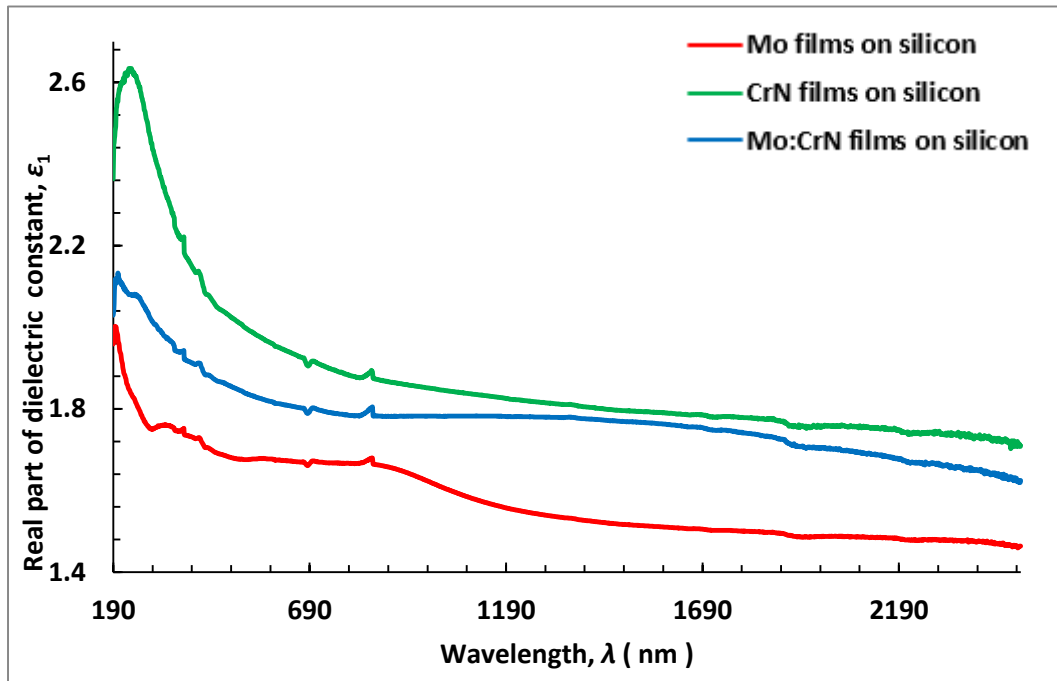
Figures 9 and 10 show the real and imaginary parts of dielectric constants, of Mo, CrN and Mo:CrN coatings, as a function of wavelength of the incident solar radiation. The frequency dependence of electron excitation spectra of a solid material can be defined in terms of complex dielectric function,

$$\varepsilon(\omega) = \varepsilon_1(\omega) + i\varepsilon_2(\omega) = (n(\omega) + ik(\omega))^2 \quad (11)$$

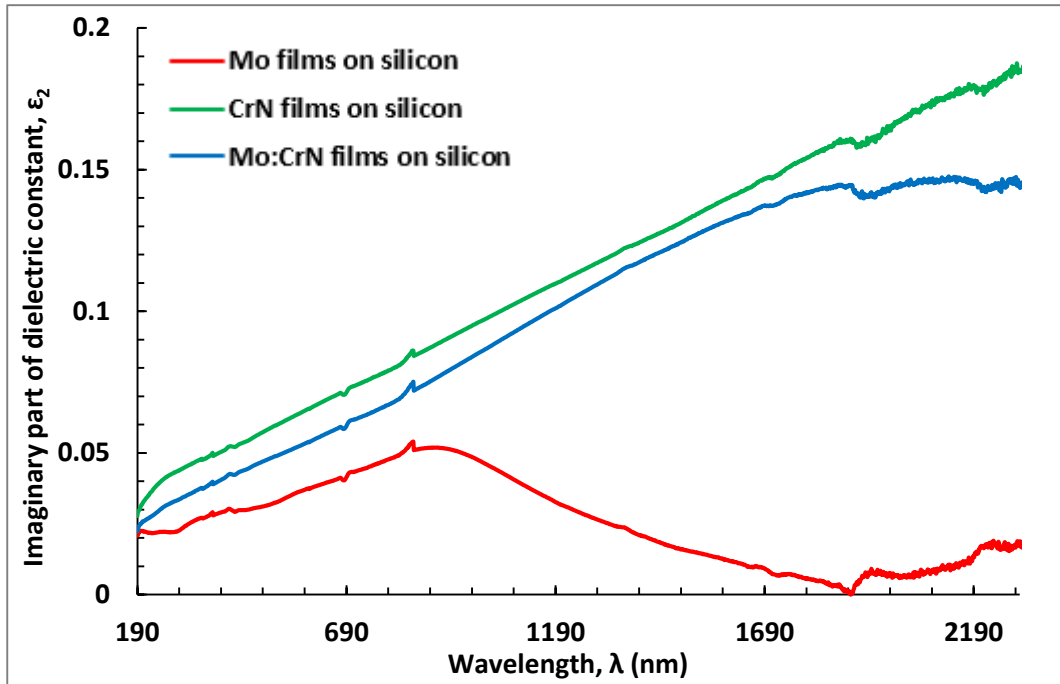
where  $\varepsilon_1$  and  $\varepsilon_2$  are the real and imaginary parts of the complex dielectric constant, respectively and are given by the following relations [61],

$$\varepsilon_1 = n^2 - k^2 \text{ and } \varepsilon_2 = 2nk \quad (12)$$

where  $\varepsilon_1$  represents the amount of polarization energy stored in dielectric medium and  $\varepsilon_2$  characterizes the energy loss of those media. The power loss in terms of heat as a loss factor, generally, produced from inelastic scattering process during the charge transfer and charge conduction mechanisms of a dielectric medium. In specified light frequency range of interest, thin film coatings having a low energy-loss nature, when they have a greater  $\varepsilon_1$  to  $\varepsilon_2$  ratio, this is due to the increase in the electron density of the films. The improvement in crystallinity of the film can decrease the degree of electron scattering and increase the free-electron density [62, 63].



**Figure 9.** Real part of dielectric constant of Mo, CrN, and Mo:CrN sputtered coatings deposited onto silicon substrates as a function of wavelength.



**Figure 10.** Imaginary part of dielectric constant of Mo, CrN, and Mo:CrN sputtered coatings deposited onto silicon substrates as a function of wavelength.

### 3.3.3.7 Energy loss analysis

The ratio of the real to imaginary part of the dielectric constants defines the power loss (loss tangent) of a material,

$$\tan\delta = \frac{\varepsilon_2}{\varepsilon_1} \quad (13)$$

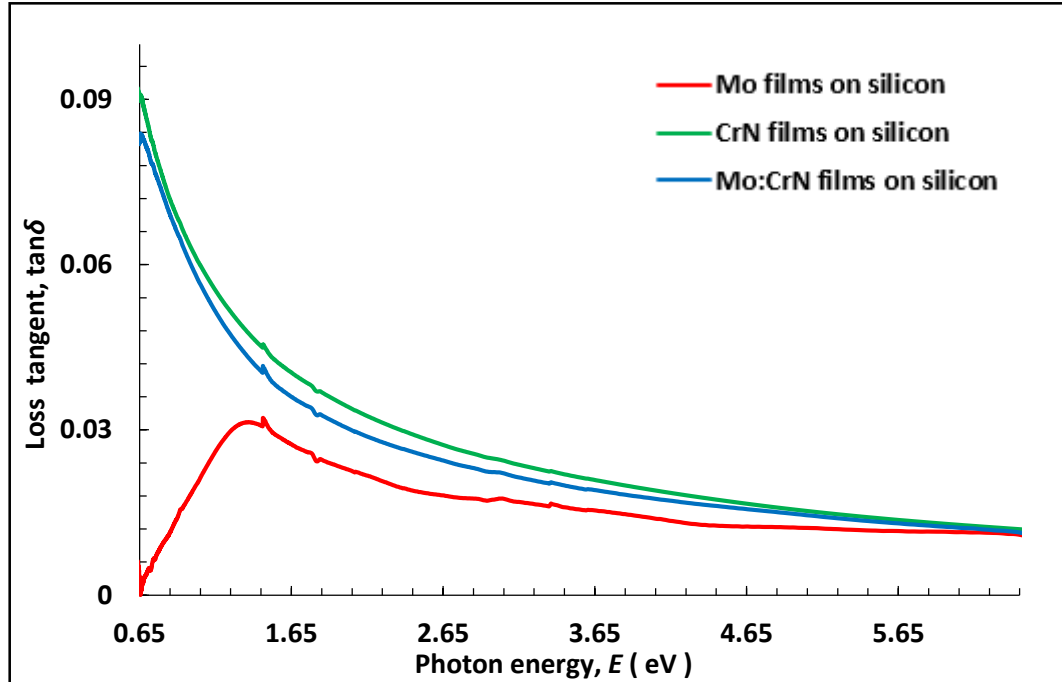
The loss tangent demonstrates the optical power loss in mechanical and oscillatory dissipative systems. Figure 11 shows the variation of  $\tan\delta$  of Mo, CrN and Mo:CrN coatings as a function of photon energy. As seen from Figure 11, it can be noted that the variation of loss tangent of these coatings resembles the same behavior of the imaginary part of the dielectric constant. It also indicates that the tangent values of these coatings are significantly low. This applauds some valuable optical qualities of these films due to lower energy losses and lower scattering of the incident solar radiation. Figure 11 also confirms the fact that energy loss has improved for the Mo-doped CrN composite.

The other energy loss functions associated with the inelastic scattering of electrons in solid thin film coatings are known as volume energy loss function,  $V_{el}$  and surface energy loss function,  $S_{el}$  [64].

$$V_{el} = \text{Im} \left( -\frac{1}{\varepsilon(\omega)} \right) = \frac{\varepsilon_2}{\varepsilon_1^2 + \varepsilon_2^2} \quad (14)$$

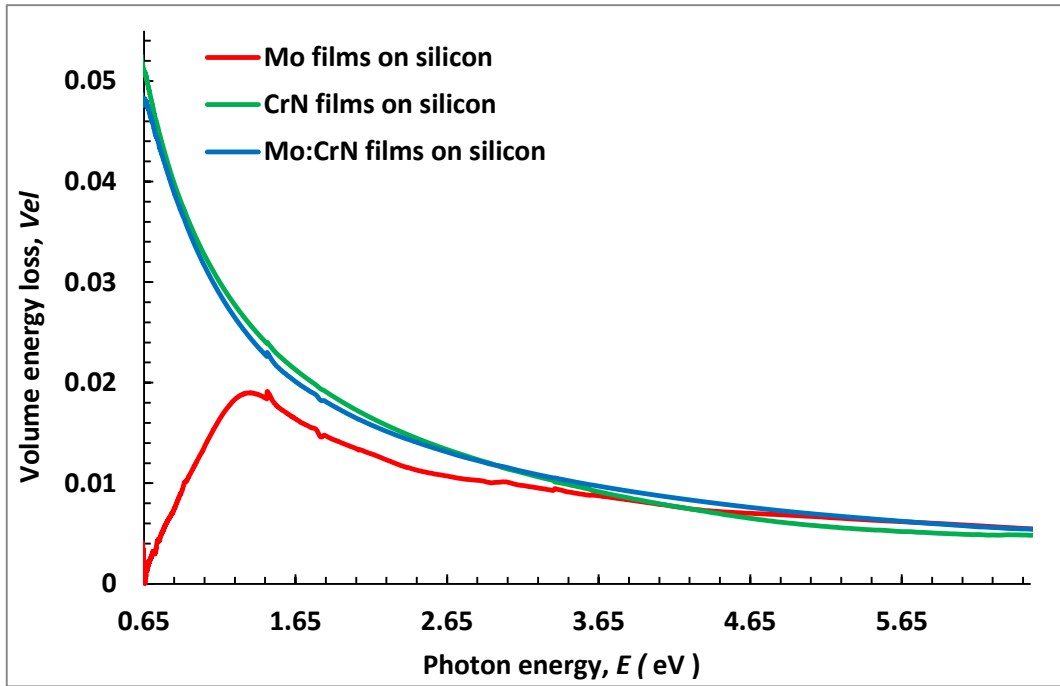
$$S_{el} = \text{Im} \left( -\frac{1}{\varepsilon(\omega) + 1} \right) = \frac{\varepsilon_2}{(1 + \varepsilon_1)^2 + \varepsilon_2^2} \quad (15)$$

The  $V_{el}$  and  $S_{el}$  values were obtained from the real and imaginary parts of the dielectric constant of the Mo, CrN and Mo:CrN coatings using equations (11) and (12). The volume and surface energy loss functions of investigated coatings, as a function of  $h\nu$ , are shown in Figures 12 and 13. As observed in these Figures, the  $V_{el}$  and  $S_{el}$  decrease rapidly with the increase in incident photon energy and no significant changes either in volume energy or surface energy losses are detected above 3.65 eV of the incident photon energies. It was also seen that as the incident photon energy reaches to above 1.65 eV, for CrN coatings, both  $V_{el}$  and  $S_{el}$  values were slightly dropped. This confirms CrN coatings are optically better than the other two coatings. Further investigation also reveal that surface energy loss of the coatings is considerably lower compared to the value of the volume energy loss functions ( $V_{el} > S_{el}$ ) for any incident photon energies. This indicates that the loss of energy of a free charge carrier when passing through the bulk of the film is much larger than that when traveling through to the exterior surface of such coatings. These findings are in good agreement with those obtained in dielectric studies of other coatings [65, 66]. It is also assumed that while passing through a medium, as a result of the excitation energy of the plasma oscillations of conduction electrons, some energies are lost by the wild moving charge carriers [67].

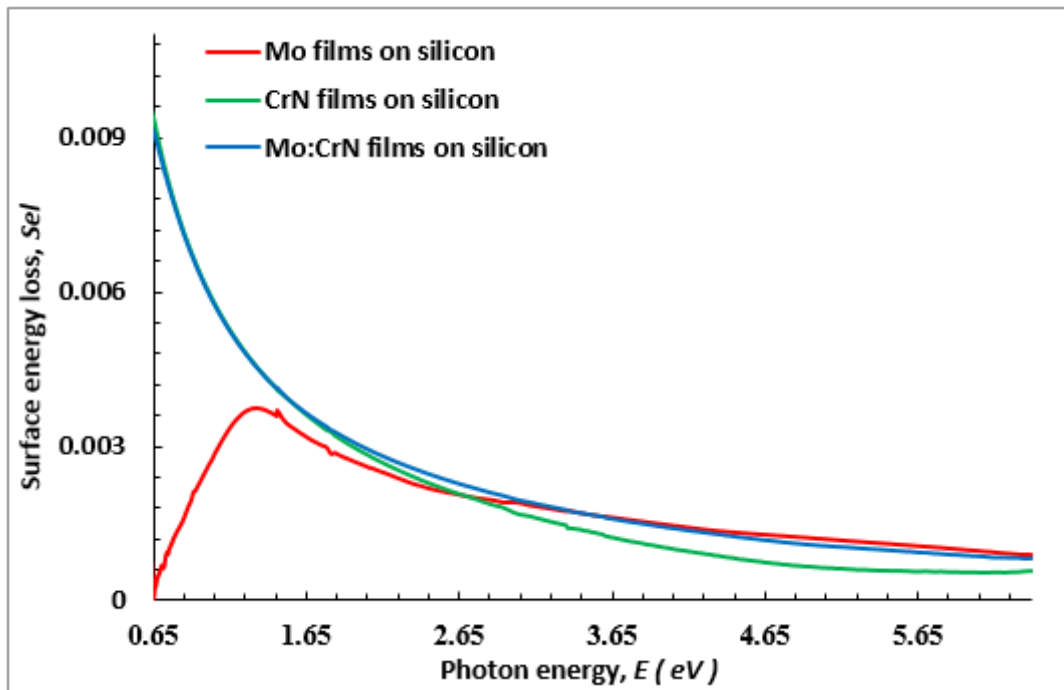


**Figure 11.** Loss tangent,  $\tan\delta$  of Mo, CrN, and Mo:CrN sputtered coatings deposited onto silicon substrates as a function of photon energy.





**Figure 12.** Volume energy loss of Mo, CrN, and Mo:CrN sputtered coatings deposited onto silicon substrates as a function of photon energy.



**Figure 13.** Surface energy loss of Mo, CrN, and Mo:CrN sputtered coatings deposited onto silicon substrates as a function of photon energy.

### 3.4 Conclusions

Mo, CrN and Mo-doped chromium nitride coatings fabricated using magnetron sputtering system were studied by means of structural, surface morphological and optical/dielectric studies in order to establish their phase forming behavior, microstructural changes and electromagnetic response upon exposure to the sunlight. XRD studies confirmed that the addition of Mo into the CrN matrix led to the formation of solid solution phases including Mo<sub>2</sub>N, CrMoN<sub>x</sub>, and Cr<sub>2</sub>N. Improvement in the film crystallinity was observed upon the Mo-doping. FESEM images showed the homogeneity of the coating's surface. The CrN films demonstrated the highest value of solar absorptance 62% while a significant reduction in the thermal emittance from 31.5% (for CrN phase) to 5.6% (for Mo:CrN phase) was observed. Consequently, the Mo:CrN films exhibited the highest solar selectivity value of 9.6. Because of higher solar absorptance value, the CrN films showed superior values for other optical parameters such as refractive index, extinction coefficient, and dielectric functions. Findings from this study would provide opportunity for future development of metal nitride-based Mo, CrN, and Mo:CrN thin film coatings for various industrial applications, especially in the area of solar selective absorbers.

### References

- [1] A.S. Korhonen, Corrosion of thin hard PVD coatings, *Vacuum*, 45 (1994) 1031-1034.
- [2] M.I. Yousaf, V.O. Pelenovich, B. Yang, C.S. Liu, D.J. Fu, Effect of bilayer period on structural and mechanical properties of nanocomposite TiAlN/MoN multilayer films synthesized by cathodic arc ion-plating, *Surface and Coatings Technology*, 282 (2015) 94-102.
- [3] B. Navinšek, P. Panjan, I. Milošev, Industrial applications of CrN (PVD) coatings, deposited at high and low temperatures, *Surface and Coatings Technology*, 97 (1997) 182-191.
- [4] X. Nie, A. Leyland, A. Matthews, Low temperature deposition of Cr(N)/TiO<sub>2</sub> coatings using a duplex process of unbalanced magnetron sputtering and micro-arc oxidation, *Surface and Coatings Technology*, 133 (2000) 331-337.
- [5] E.Y. Choi, M.C. Kang, D.H. Kwon, D.W. Shin, K.H. Kim, Comparative studies on microstructure and mechanical properties of CrN, Cr–C–N and Cr–Mo–N coatings, *Journal of Materials Processing Technology*, 187-188 (2007) 566-570.
- [6] O.V. Sobol, A.A. Postelnyk, A.A. Meylekhov, A.A. Andreev, V.A. Stolbovoy, V.F. Gorban, Structural engineering of the multilayer vacuum Arc nitride coatings based on Ti, Cr, Mo and Zr, *J. Nano. Electron. Phys.*, 9 (2017) 03003.

- [7] T. Kuznetsova, T. Zubar, S. Chizhik, A. Gilewicz, O. Lupicka, B. Warcholinski, Surface microstructure of Mo(C)N coatings investigated by AFM, *J Mater Eng Perform*, 25 (2016) 5450-5459.
- [8] L. Záborský, V. Buršíková, P. Souček, P. Vašina, J. Dugáček, P. Sřahel, J. Buršík, M. Svoboda, V. Peřina, Thermal stability of hard nanocomposite Mo-B-C coatings, *Vacuum*, 138 (2017) 199-204.
- [9] L. Zheng, F. Zhou, Z. Zhou, X. Song, G. Dong, M. Wang, X. Diao, Angular solar absorptance and thermal stability of Mo-SiO<sub>2</sub> double cermet solar selective absorber coating, *Solar Energy*, 115 (2015) 341-346.
- [10] F. Jahan, M.H. Islam, B.E. Smith, Band gap and refractive index determination of Mo-black coatings using several techniques, *Solar Energy Materials and Solar Cells*, 37 (1995) 283-293.
- [11] J. Li, L. Guo, Computer simulation on Mo/Al<sub>2</sub>O<sub>3</sub> solar energy selective absorbing coating, in: 2nd International Conference on Manufacturing Science and Engineering, ICMSE 2011, Guilin, 2011.
- [12] X.H. Gao, Z.M. Guo, Q.F. Geng, P.J. Ma, G. Liu, Microstructure and Optical Properties of SS/Mo/Al<sub>2</sub>O<sub>3</sub> Spectrally Selective Solar Absorber Coating, *J Mater Eng Perform*, 26 (2017) 161-167.
- [13] D. Xinkang, W. Cong, W. Tianmin, Z. Long, C. Buliang, R. Ning, Microstructure and spectral selectivity of Mo-Al<sub>2</sub>O<sub>3</sub> solar selective absorbing coatings after annealing, *Thin Solid Films*, 516 (2008) 3971-3977.
- [14] J. Wang, B. Wei, Q. Wei, D. Li, Optical property and thermal stability of Mo/Mo-SiO<sub>2</sub>/SiO<sub>2</sub> solar-selective coating prepared by magnetron sputtering, *Phys. Status Solidi A Appl. Mater. Sci.*, 208 (2011) 664-667.
- [15] Y. Ning, W. Wang, L. Wang, Y. Sun, P. Song, H. Man, Y. Zhang, B. Dai, J. Zhang, C. Wang, Y. Zhang, S. Zhao, E. Tomasella, A. Bousquet, J. Cellier, Optical simulation and preparation of novel Mo/ZrSiN/ZrSiON/SiO<sub>2</sub> solar selective absorbing coating, *Solar Energy Materials and Solar Cells*, 167 (2017) 178-183.
- [16] X. Gong, R.R. Chen, Y.H. Yang, Y. Wang, H.S. Ding, J.J. Guo, Y.Q. Su, H.Z. Fu, Effect of Mo on microstructure and oxidation of NiCoCrAlY coatings on high Nb containing TiAl alloys, *Applied Surface Science*, 431 (2017) 81-92.
- [17] N. Selvakumar, S. Santhoshkumar, S. Basu, A. Biswas, H.C. Barshilia, Spectrally selective CrMoN/CrON tandem absorber for mid-temperature solar thermal applications, *Solar Energy Materials and Solar Cells*, 109 (2013) 97-103.

- [18] J.A. Thornton, A.S. Penfold, J.L. Lamb, Sputter-deposited Al<sub>2</sub>O<sub>3</sub>/Mo/Al<sub>2</sub>O<sub>3</sub> selective absorber coatings, *Thin Solid Films*, 72 (1980) 101-110.
- [19] Y.H. Yang, I.W. Lyo, S.J. Park, D.S. Lim, Y.S. Oh, Tribological behavior analysis of CrMoN coating by XPS, *J. Korean Inst. Met. Mat.*, 50 (2012) 549-556.
- [20] L. Zheng, F. Gao, S. Zhao, F. Zhou, J.P. Nshimiyimana, X. Diao, Optical design and co-sputtering preparation of high performance Mo–SiO<sub>2</sub> cermet solar selective absorbing coating, *Applied Surface Science*, 280 (2013) 240-246.
- [21] D. Qi, H. Lei, T. Wang, Z. Pei, J. Gong, C. Sun, Mechanical, microstructural and tribological properties of reactive magnetron sputtered Cr–Mo–N films, *Journal of Materials Science & Technology*, 31 (2015) 55-64.
- [22] Y. Di, P. Zhang, Z. Cai, Z. Yang, Q. Li, W. Shen, Effect of Mo content on the structural and mechanical properties of CrMoN/MoS<sub>2</sub> composite coatings, *Xiyou Jinshu Cailiao Yu Gongcheng/Rare Metal Materials and Engineering*, 43 (2014) 264-268.
- [23] P. Hones, R. Sanjinés, F. Lévy, O. Shojaei, Electronic structure and mechanical properties of resistant coatings: The chromium molybdenum nitride system, *Journal of Vacuum Science & Technology A: Vacuum, Surfaces, and Films*, 17 (1999) 1024-1030.
- [24] J. Chen, C. Guo, J. Chen, J. He, Y. Ren, L. Hu, Microstructure, optical and electrical properties of CrAlN film as a novel material for high temperature solar selective absorber applications, *Materials Letters*, 133 (2014) 71-74.
- [25] L. Hong, G. Bian, S. Hu, L. Wang, H. Dacosta, Tribological Properties of CrAlN and TiN Coatings Tested in Nano- and Micro-scale Laboratory Wear Tests, *J Mater Eng Perform*, 24 (2015) 2670-2677.
- [26] S.J. Ju, G.E. Jang, Y.W. Jang, H.H. Kim, C. Lee, Growth and properties of CrN<sub>x</sub>/TiN<sub>y</sub>/Al based on N<sub>2</sub> gas flow rate for solar thermal applications, *Transactions on Electrical and Electronic Materials*, 17 (2016) 146-149.
- [27] J.Z. Kong, T.J. Hou, Q.Z. Wang, L. Yin, F. Zhou, Z.F. Zhou, L.K.Y. Li, Influence of titanium or aluminum doping on the electrochemical properties of CrN coatings in artificial seawater, *Surface and Coatings Technology*, 307 (2016) 118-124.
- [28] S.Y. Park, S.U. Han, H.H. Kim, G.E. Jang, Y.J. Lee, Growth and characteristics of Al<sub>2</sub>O<sub>3</sub>/AlCrNo/Al solar selective absorbers with gas mixtures, *Transactions on Electrical and Electronic Materials*, 16 (2015) 264-267.
- [29] C. Zou, L. Huang, J. Wang, S. Xue, Effects of antireflection layers on the optical and thermal stability properties of a spectrally selective CrAlN-CrAlON based tandem absorber, *Solar Energy Materials and Solar Cells*, 137 (2015) 243-252.

- [30] Y. Wu, B. Wang, Y. Ma, Y. Huang, N. Li, F. Zhang, Y. Chen, *Nano Res.*, 3 (2010) 661.
- [31] D. Yuelan, Z. Ping, C. Zhihai, Y. Zhen, L. Qi, S. Wei, Effect of Mo content on the structural and mechanical properties of CrMoN/MoS<sub>2</sub> composite coatings, *Rare Metal Materials and Engineering*, 43 (2014) 264-268.
- [32] B.D. Cullity, *Elements of X-ray Diffraction*, Addison-Wesley Publishing Company, Inc., CA, USA, 1967.
- [33] T. Boström, E. Wäckelgård, G. Westin, Solution-chemical derived nickel–alumina coatings for thermal solar absorbers, *Solar Energy*, 74 (2003) 497-503.
- [34] A. Millar, M.M. Rahman, Z.-T. Jiang, Review of sol-gel Derived mixed metal oxide thin film coatings with the addition of carbon materials for selective surface applications, *Journal of Advanced Physics*, 3 (2014) 179-193.
- [35] M.M. Rahman, Z.-T. Jiang, C.-Y. Yin, L.S. Chuah, H.-L. Lee, A. Amri, B.-M. Goh, B.J. Wood, C. Creagh, N. Mondinos, M. Altarawneh, B.Z. Dlugogorski, Structural thermal stability of graphene oxide-doped copper–cobalt oxide coatings as a solar selective surface, *Journal of Materials Science & Technology*, 32 (2016) 1179-1191.
- [36] M. Ashokkumar, S. Muthukumaran, Cu doping effect on optical, structural and morphological properties of Cd<sub>0.9</sub>Zn<sub>0.1</sub>S thin films, *Journal of Luminescence*, 145 (2014) 167-174.
- [37] J. Liang, Y. Huang, J. Oh, M.S.D. Kozolv, R. Baughman, Y. Ma, *Adv. Funct. Mater.*, 21 (2011) 3778.
- [38] M.M. Rahman, Z.-T. Jiang, Z.-F. Zhou, Z. Xie, C.Y. Yin, H. Kabir, M.M. Haque, A. Amri, N. Mondinos, M. Altarawneh, Effects of annealing temperatures on the morphological, mechanical, surface chemical bonding, and solar selectivity properties of sputtered TiAlSiN thin films, *Journal of Alloys and Compounds*, 671 (2016) 254-266.
- [39] X. Wang, Solar selective absorbers with foamed nanostructure prepared by hydrothermal method on stainless steel, *Solar Energy Materials & Solar Cells*, 146 (2016) 99-106.
- [40] J.A. Thornton, J.L. Lamb, Thermal stability studies of sputter-deposited multilayer selective absorber coatings, *Thin Solid Films*, 96 (1982) 175-183.
- [41] S. Jeong Heo, S.-W. Kim, I.-W. Yeo, S.-J. Park, Y.-S. Oh, Effect of bias voltage on microstructure and phase evolution of Cr–Mo–N coatings by an arc bonded sputter system, *Ceramics International*, 42 (2016) 5231-5237.

- [42] M.K. Kazmanli, M. Ürgen, A.F. Cakir, Effect of nitrogen pressure, bias voltage and substrate temperature on the phase structure of Mo–N coatings produced by cathodic arc PVD, *Surface and Coatings Technology*, 167 (2003) 77-82.
- [43] A. Gilewicz, B. Warcholinski, Deposition and characterisation of Mo<sub>2</sub>N/CrN multilayer coatings prepared by cathodic arc evaporation, *Surface and Coatings Technology*, 279 (2015) 126-133.
- [44] M. Čekada, P. Panjan, M. Maček, P. Šmíd, Comparison of structural and chemical properties of Cr-based hard coatings, *Surface and Coatings Technology*, 151–152 (2002) 31-35.
- [45] A. Öztürk, K.V. Ezirmik, K. Kazmanlı, M. Ürgen, O.L. Eryılmaz, A. Erdemir, Comparative tribological behaviors of TiN, CrN and MoNCu nanocomposite coatings, *Tribology International*, 41 (2008) 49-59.
- [46] O. Knotek, R. Elsing, G. Krämer, F. Jungblut, On the origin of compressive stress in PVD coatings — an explicative model, *Surface and Coatings Technology*, 46 (1991) 265-274.
- [47] H.K.D.H. Bhadeshia, Developments in martensitic and bainitic steels: role of the shape deformation, *Materials Science and Engineering: A*, 378 (2004) 34-39.
- [48] J.A. Thornton, D.W. Hoffman, Stress-related effects in thin films, *Thin Solid Films*, 171 (1989) 5-31.
- [49] P.H. Mayrhofer, M. Geier, C. Löcker, L. Chen, Influence of deposition conditions on texture development and mechanical properties of TiN coatings, *International Journal of Materials Research*, 100 (2009) 1052-1058.
- [50] M.I. Yousaf, V.O. Pelenovich, B. Yang, C.S. Liu, D.J. Fu, Influence of substrate rotation speed on the structure and mechanical properties of nanocrystalline AlTiN/MoN coatings synthesized by cathodic arc ion-plating, *Surface and Coatings Technology*, 265 (2015) 117-124.
- [51] E. Mohammadpour, Z.-T. Jiang, M. Altarawneh, N. Mondinos, M.M. Rahman, H.N. Lim, N.M. Huang, Z. Xie, Z.-F. Zhou, B.Z. Dlugogorski, Experimental and predicted mechanical properties of Cr<sub>1-x</sub>Al<sub>x</sub>N thin films, at high temperatures, incorporating in situ synchrotron radiation X-ray diffraction and computational modelling, *RSC Adv.*, 7 (2017) 22094-22104.
- [52] C. Zou, L. Huang, J. Wang, S. Xue, Effects of antireflection layers on the optical and thermal stability properties of a spectrally selective CrAlN–CrAlON based tandem absorber, *Solar Energy Materials and Solar Cells*, 137 (2015) 243-252.

- [53] J.H. Kang, K.J. Kim, Structural, optical, and electronic properties of cubic  $TiN_x$  compounds, *Journal of Applied Physics*, 86 (1999) 346-350.
- [54] H.A. Miran, M.M. Rahman, Z.-T. Jiang, M. Altarawneh, L.S. Chuah, H.-L. Lee, E. Mohammedpur, A. Amri, N. Mondinos, B.Z. Dlugogorski, Structural and optical characterizations of pre- and post-annealed sol-gel derived CoCu-oxide coatings, *Journal of Alloys and Compounds*, 701 (2017) 222-235.
- [55] M. Asadi, S.M. Rozati, Optical and structural properties of nanostructured copper oxide thin films as solar selective coating prepared by spray pyrolysis method, *Materials Science-Poland*, 35 (2017) 355-361.
- [56] Z.-T. Jiang, A study of Cr-Al oxide for single layer halftone phase-shifting masks for deep-ultraviolet region photolithography, *Japanese Journal of Applied Physics*, 37 (1998) 4008-4013.
- [57] H. Kabir, M.M. Rahman, T.S. Roy, A. Bhuiyan, Structural and optical properties of plasma polymerized pyromucic aldehyde thin films, *International Journal of Mechanical & Mechatronics Engineering*, 12 (2012) 30-34.
- [58] M.M. Rahman, Z.-T. Jiang, P. Munroe, L.S. Chuah, Z.-F. Zhou, Z. Xie, C.Y. Yin, K. Ibrahim, A. Amri, H. Kabir, M.M. Haque, N. Mondinos, M. Altarawneh, B.Z. Dlugogorski, Chemical bonding states and solar selective characteristics of unbalanced magnetron sputtered  $Ti_xM_{1-x-y}N_y$  films, *RSC Advances*, 6 (2016) 36373-36383.
- [59] P.A. Wolff, Theory of the Band Structure of Very Degenerate Semiconductors, *Physical Review*, 126 (1962) 405-412.
- [60] M.M. Rahman, H.A. Miran, Z.-T. Jiang, M. Altarawneh, L.S. Chuah, H.-L. Lee, A. Amri, N. Mondinos, B.Z. Dlugogorski, Investigation of the post-annealing electromagnetic response of Cu-Co oxide coatings *via* optical measurement and computational modelling, *RSC Advances*, 7 (2017) 16826-16835.
- [61] B. Barış, H.G. Özdemir, N. Tuğluoğlu, S. Karadeniz, Ö.F. Yüksel, Z. Kişnişci, Optical dispersion and dielectric properties of rubrene organic semiconductor thin film, *Journal of Materials Science: Materials in Electronics*, 25 (2014) 3586-3593.
- [62] C. Fournier, O. Bamiduro, H. Mustafa, R. Mundle, R.B. Konda, F. Williams, A.K. Pradhan, Effects of substrate temperature on the optical and electrical properties of Al:ZnO films, *Semiconductor Science and Technology*, 23 (2008) 085019.
- [63] Y. Kim, J.Y. Leem, Influence of annealing temperature on photoluminescence properties and optical constants of N-doped ZnO thin films grown on muscovite mica substrates, *Physica B: Condensed Matter*, 476 (2015) 71-76.

- [64] M.M. El-Nahass, A.A.M. Farag, Structural, optical and dispersion characteristics of nanocrystalline GaN films prepared by MOVPE, *Optics & Laser Technology*, 44 (2012) 497-503.
- [65] H.E. Atyia, N.A. Hegab, Determination and analysis of optical constants for Ge<sub>15</sub>Se<sub>60</sub>Bi<sub>25</sub> thin films, *Physica B: Condensed Matter*, 454 (2014) 189-196.
- [66] C.S.M. K.R. Rajesh, Estimation of the refractive index and dielectric constants of magnesium phthalocyanine thin films from its optical studies, *Materials Letters*, 53 (2002) 329– 332.
- [67] D.P. D.Bohm, A collective description of electron interactions III. Coulomb interactions in a degenerate electron gas, *Physical Review*, 92 (1953) 609.



## CHAPTER FOUR

---

### **Paper III: Annealing Impacts on Microstructural, Optical and Mechanical Studies of Sputtered CrN Thin Film Coatings: Experimental Studies and FEM Modeling**

---

#### **Abstract**

Chromium nitride (CrN) coatings were deposited by magnetron sputtering onto Si(100) substrates. The coatings were then annealed at different temperatures (500-800 °C in steps of 100 °C) in air for 1 hour. X-ray diffraction (XRD), field emission scanning electron microscopy (FESEM), X-ray photoelectron spectroscopy (XPS), UV-Vis spectroscopy, nanoindentation tests and finite element modeling (FEM) were conducted in order to investigate their structural, morphological, optical and mechanical properties. XRD patterns show that the crystallinity of the CrN phase increases with the rise in annealing temperatures together with its preferred orientations along (111) and (200) diffraction planes. The lattice constants were slightly reduced from 4.19 to 4.11 nm at 800 °C. The lattice microstrains and residual stresses were also reduced as the annealing temperatures rose as a result of reduced defects, dislocations and vacancies. Smooth grain-like surfaces with grain sizes ranging between ~50 - 250 nm were confirmed by FESEM micrographs. XPS studies indicated the existence of Cr and N on the coating systems. The solar absorptance of CrN coatings is increased from 61% to 89% until an annealing temperature of 800 °C, and slightly decreased at 800 °C. However, the optical band-gap was gradually dropped from 2.62 to 1.38 eV as the annealing progresses and then slightly increased to 1.48 eV at 800 °C due to the formation of Cr<sub>2</sub>O<sub>3</sub> at the films' surface. A gradual increase of dielectric constants of CrN films were realized with the subsequent annealing progression. Nanoindentation results indicated that as the annealing progresses, the hardness and elastic modulus values are lowered.

#### **4.1 Introduction**

Physical vapour deposited (PVD) binary CrN coatings are considered to be very useful candidates in many industrial applications because of their thermal stability, good coating-to-substrate adhesion, abrasion resistance, excellent wear resistance, low friction coefficient, oxidation resistance, and ideal hardness and elastic modulus values [1-4]. CrN coatings also show higher oxidation resistance and exceptional corrosion resistance under deleterious environmental exposures such as high temperatures and high pressure [5]. In

comparison to other transition metal nitride coatings (*e.g.*, TiN, and TiCN), CrN coatings offer superior thermal stability, corrosion resistance and better tribological performance. Consequently, CrN coatings have been widely used as protective coatings in drawing dies, cutting tools, moulds, grinding tools, piston rings, and various moving parts in mechanical equipment [6-9]. The effect of heat treatment on the mechanical properties and microstructural features of CrN/AlN thin film based coatings have been studied by Tien *et al.* [10]. CrN thin film coatings have been studied for many years because of their excellent mechanical performance, thermal properties and anti-oxidation behaviour [11].

The chemical composition, chemical bonding states, roughening kinetics, and mechanical properties of Al-doped TiN coatings which had been prepared by magnetron sputtering in an (Ar+N<sub>2</sub>) gas mixture were studied *via* XPS, AFM and nanoindentation measurements [12]. Increased Al-dopants from 10 to 50 at.% reduces the grain size and surface roughness due to the nucleation process, but the mechanical properties of the TiN structure were improved due to a reduced grain size, which indicates a high density of grain boundaries [12]. A linear relationship between residual stress and hardness of single-phase thin film coating materials such as TiN [13], and CrN [14] synthesized by physical vapour deposition methods have been reported in earlier studies. The strengthening effect of transition metal nitride based films such as TiN and CrN with decreasing grain size, generally, follows the Hall–Petch relationship as described in [15].

The absorption of solar energy by a thin film coating is dependent on its electronic configuration, wavelength of light, and the surface topographies of the coatings such as pits, pores, and/or peaks. Absorption of light may also be responsible for the excitation of electrons to higher energy states, the vibrational and rotational motions of bonds, the chemical reaction and restructuring/breaking of the chemical bonds, and the ionisation of atoms or molecules [16]. The optical properties and thermal stability of a spectrally selective CrAlN–CrAlON thin film based absorbing coatings have been investigated in [17]. To date, various types of absorbing surfaces such as interference-type, cermet coating, and absorber–reflector tandem have been successfully developed in order to improve their solar absorption [18-23]. Magnetron sputtering derived HfO<sub>x</sub>/Mo/HfO<sub>2</sub> thin film coatings exhibited extraordinary solar absorptance up to 0.923 [24]. High temperature solar absorption together with good thermal stability and oxidation resistance of CrAlN films have been reported in an earlier study [19].

The enhancement of the tribological and mechanical properties of magnetron sputtered Ti/TiN, Cr/CrN and TiCr/TiCrN thin film coatings have been reported by Ezazi *et al.* [25]. In their study, the authors described combining TiN and CrN phases into a single film and presented a solution for the damage mechanisms that degrade material properties. The elastic hardness of CrN, CrAlN, CrTiN, and CrAlTiN sputtered coatings were evaluated by their grain sizes [26]. An average hardness of 14.5 GPa was reported for the CrN phase while CrTiAlN coating with the most compact morphological features demonstrated the highest hardness of 22.0 GPa [26]. Among the existing transition metal nitrides, CrN thin film coatings have been extensively studied with respect to their structural features, morphological information, thermal and mechanical properties which are the key requirements for high-temperature applications [10, 15, 27-30].

Many studies have been undertaken which examine the structural, morphological, spectral selective, local electronic bonding states, optical, mechanical and tribological properties of CrN-based thin film coatings [31-37]. However, a comprehensive study investigating the impact of annealing temperatures on structural, morphological, and optical properties and providing a detailed mechanical analysis *via* experimental procedure and finite element modeling in one paper is still lacking. Therefore, in this paper, paramount attention has been paid to understanding the impact of annealing temperatures on structural, optical, dielectric, and mechanical properties of sputtered CrN thin film coatings. The nanoindentation method was used to probe the mechanical parameters of CrN coatings. The intrinsic hardness was estimated *via* experiment and by modeling the substrate effect and was related to the microstructural features of the coatings. Accordingly, the correlation between their mechanical properties, residual stress level, adhesive strength, and levels of load induced stress induced at the coating-substrate interface, was also examined.

## **4.2 Experimental Technique**

### **4.2.1 Film Preparation Technique**

The UDP650 closed field unbalanced magnetron sputtering (Teer Coatings Ltd, UK) system was used to prepare CrN thin film coatings onto Si (100) substrates. Two vertically mounted pure Cr targets (purity 99.9 %, size 345 mm × 145 mm × 8 mm) surrounded by a rotating substrate holder provides a uniform exposure for growing the coatings. Prior to coating, a background pressure of  $0.4 \times 10^{-4}$  Pa and the working gas pressure (during sputtering) of 0.4 Pa was maintained throughout the process. Ar (99.999 %) was used as the working gas

for sputtering with a fixed flow rate at 50 sccm, and N<sub>2</sub> (99.999 %) was used as a reactive gas to form nitrides while the optical emission monitor (OEM) was used to control dynamically. The nitrogen reactive gas was injected near the substrate holder. The entire synthesis process was carried out without any external heating and keeping the target to a substrate distance of 17 cm. Advanced Energy Pinnacle Plus power supply, at a frequency of 250 kHz was used to control the bias voltage while a DC power supply (current mode) was used to control the target current supply. To coat the CrN films, 0.2 μm chromium adhesive layers were applied to promote the coating adhesion with a bias voltage of -80 V [38, 39]. The total thicknesses of these coatings were  $d = 1.8 \mu\text{m}$ . Finally, the obtained sputtered CrN coatings were annealed from 500 to 800 °C in steps of 100 °C in air for 1 hour. Elaborate details on the sample deposition parameters are outlined in Table 1.

**Table 1.** CrN thin film coating deposition conditions.

Experimental Conditions	Name/Values
Substrate	Si(100) wafer
Target materials	Pure Cr (99.9 %)
Gases	Ar is working gas, N <sub>2</sub> is reactive gas
Substrate thickness (mm)	0.40
Target to substrate distance (mm)	170
Substrate temperature (°C)	500
Substrate DC bias voltage (V)	-55
Substrate holder rotation frequency (rpm)	10
Ar flow rate (sccm)	50
N <sub>2</sub> flow rate (%)	Controlled by optical emission monitor, OEM = 35
Ar partial pressure (Pa)	0.17
N <sub>2</sub> partial pressure (Pa)	0.13
(Ar + N <sub>2</sub> ) pressure (Pa)	0.40
Base/ultimate pressure (Pa)	$4 \times 10^{-4}$
Cr target power (kW)	2
Cr target current (DC)	6.0 A
Deposition rate (nm/min)	20
Deposition time (min)	90
Thickness of the coating (μm)	~1.8
Annealing temperature (°C)	500-800 in steps of 100

#### 4.2.2 XRD Experiments

The XRD measurements of the samples were carried out using a Bruker AXS D8 Advance (Germany) with Cu-K<sub>α</sub> radiation ( $\lambda = 1.54 \text{ \AA}$ ). The XRD machine was operated at 40 kV

and 40 mA coupled with a Lynx-eyed detector. The XRD patterns were collected in a  $2\theta$  (degree) geometry = 30– 70 with a step size of  $0.01^\circ$ .

#### **4.2.3 FESEM Experiments**

The morphological features of as-deposited and annealed CrN thin film coatings were analysed using a field-emission scanning electron microscope manufactured by Zeiss Neon 40EsB FIBSEM, an Oxford Instruments Inca X-act SDD X-ray detector.

#### **4.2.4 XPS Experiments**

Elemental compositions of the CrN films were estimated *via* XPS measurements around the outermost 5 nm surface. The XPS data of CrN films before and after annealing were collected using a Kratos Axis Ultra XPS spectrometer (Manchester, UK) operated with an Al- $K_\alpha$  monochromatic radiation (photon energy = 1486.6 eV) source at a power of ~10 mA and ~15 kV. The XPS machine was equipped with a cold stage, and an Ar ion gun for etching the coatings. The analysis chamber was set at a uniform pressure of  $2.9 \times 10^{-9}$  Torr. The XPS survey spectra were analysed using CASA 2.3.1.5 XPS software.

#### **4.2.5 UV-Vis Experiments**

The UV–Vis reflectance data of the coatings collected, in the wavelength range of 190 to 2300 nm, were used to study various optical parameters of CrN films before and after annealing. A UV–Vis double beam spectrophotometer with 60 mm integrating sphere (JASCO UV-670, USA) was used to acquire the reflectance spectra in the ultraviolet to visible range of the solar spectra. For a given wavelength range, the solar absorptance,  $\beta$  of these coatings was calculated using the Beckman-Duffie method [40, 41]. The UV-Vis reflectance data were used to calculate the optical constants such as solar absorptance, band-gap, refractive index, dielectric constants and energy loss functions for as-deposited and post annealed of CrN coatings.

#### **4.2.6 Nanoindentation Experiments**

Nanoindentation experiments were carried out in order to study the mechanical properties of the samples, and using an Ultra-Micro Indentation System 2000 workstation (CSIRO, Sydney, Australia), equipped with a diamond Berkovich indenter. A standard fused silica specimen was used to calibrate the area function of the indenter tip. The load control method was used with different maximum loadings of 5 mN, taking into account the fact that the

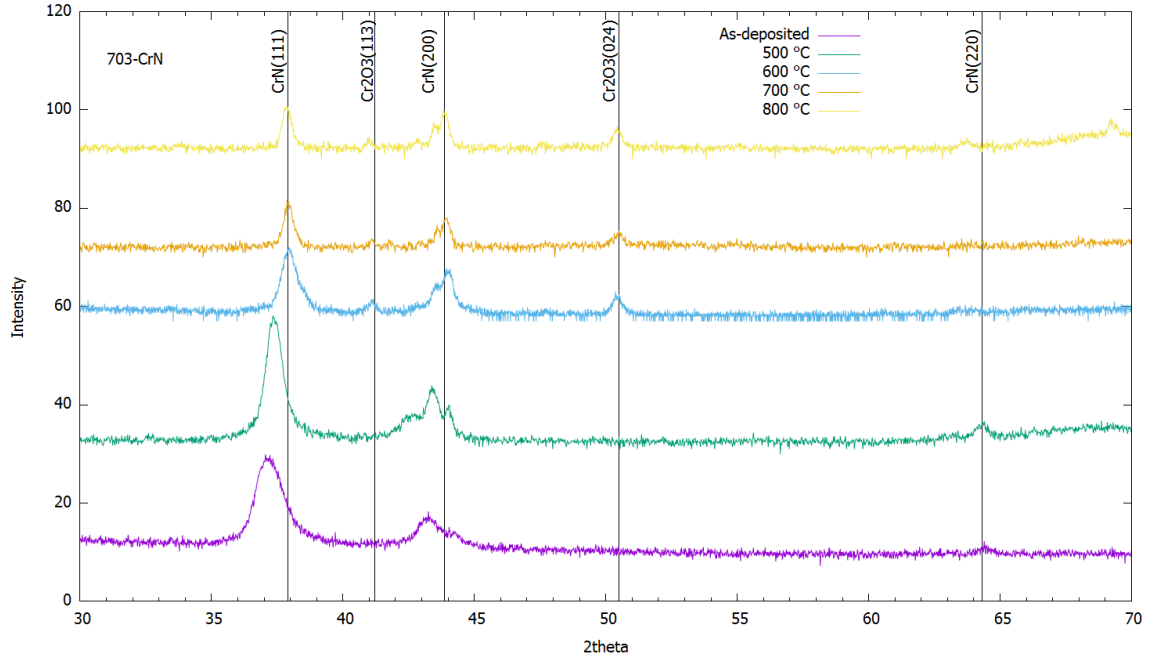
CrN coating thickness was 1.4  $\mu\text{m}$ . This was based on the consideration that the maximum displacement during indentation should be no higher than 10% of the coating thickness, and that high loading may result in micro-cracks in the coating which is thought to be relatively brittle, compared with metal coatings. To obtain better resolutions, the number of measuring points have been increase to 15 during loading, and 20 during unloading, respectively. Finite element modeling (FEM) was used in this work, aimed at a detailed understanding of the load induced stress intensity and distribution within different coatings materials and configurations. Input parameters consisted of both structural and mechanical properties of the coating systems obtained from experiments. A two-dimensional (2D) axial symmetry model was adapted, with a spherical indenter (5  $\mu\text{m}$  radius) at the top of a coating layer supported by substrate with the loading direction along the axial z-axis, using COMSOL Metaphysics software [42, 43].

### 4.3 Results and Discussion

#### 4.3.1 XRD Analysis of as-deposited and Annealed CrN Films

The XRD patterns of CrN films before and after annealing, between 500 to 800  $^{\circ}\text{C}$  in 100  $^{\circ}\text{C}$  increments in air for 1 hour, are shown in Figure 1. The diffraction patterns confirmed the deposition of a face-centered-cubic CrN structure with space group; Fm-3m (ICDD 11-0065). CrN peaks (111), (200), and (220) were identified at  $\sim 37^{\circ}$ ,  $\sim 43^{\circ}$  and  $\sim 63^{\circ}$  diffraction angles, respectively [44-46]. In this coating, oxidation of CrN at high temperatures is believed to occur through outward diffusion of Cr and nitrogen while oxygen diffuses inwardly and forms oxides inside coating layers. The  $\text{Cr}_2\text{O}_3$  phase was detected above 600  $^{\circ}\text{C}$  annealing at  $41.4^{\circ}$  (113), and  $51.3^{\circ}$  (024), according to  $\text{Cr}_2\text{O}_3$  (ICDD 38-01479) [47-49]. Hexagonal  $\text{Cr}_2\text{N}$  phase was not identified due to the absence of any noticeable diffraction lines expected for  $\text{Cr}_2\text{N}$  (ICDD 35-0803) [45, 46, 50], at  $40.19^{\circ}$  (002),  $42.6^{\circ}$  (111), and  $56.01^{\circ}$  (112). Diffraction peaks of  $\text{Cr}_2\text{N}$  phase were not detected due to the presence of intensive  $40.19^{\circ}$  (002),  $42.61^{\circ}$  (111), and  $56.01^{\circ}$  (112) reflection lines that might overlap the potential CrN phase [45, 50]. Furthermore, the absence of a  $\text{Cr}_2\text{N}$  phase could be due to its amorphous nature (very weak crystallites or no peaks) [45, 49, 50]. The formation of  $\text{Cr}_2\text{O}_3$  during annealing in air was discussed by Mohammadpour *et al.* [51], and Qi *et al.* [52]. There are broadening in the main diffraction peaks of crystal planes of (111), and (200). The XRD patterns also demonstrate that with a rise in annealing temperatures, the degree of crystallinity of the CrN phase increases, and preferred orientations along (111) and (200) reflection planes increase with some peak sharpening [52]. It is implied that the

peak sharpening behaviour could possibly originate from the grain growth and the release of residual stress induced in the crystal matrix.

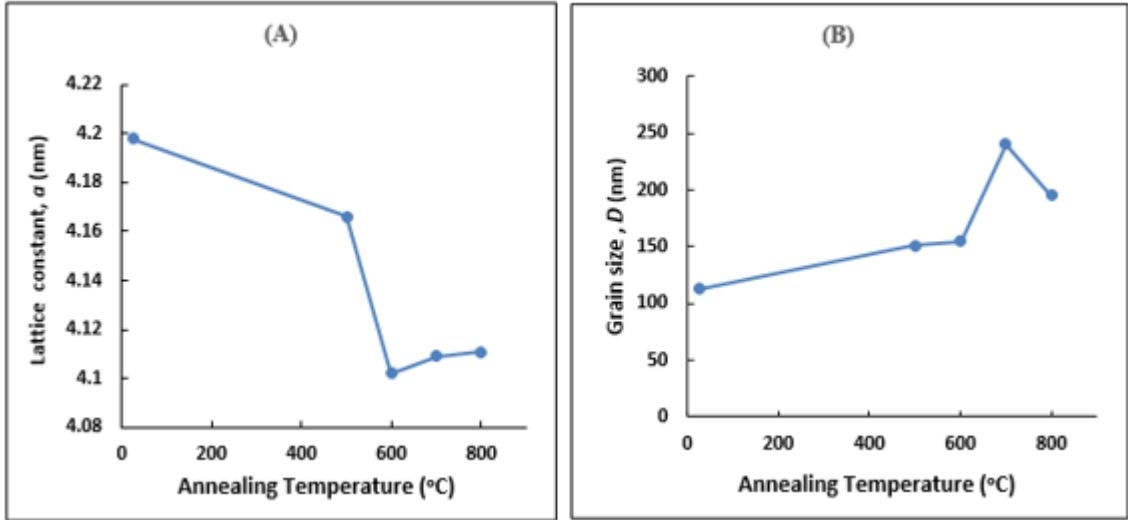


**Figure 1.** The X-ray patterns of CrN films as deposited on silicon substrate and after annealed for 1hr at 500, 600, 700, and 800 °C.

The as-deposited lattice constant slightly decreased from 4.19 nm to 4.11 nm at 800 °C as shown in Figure 2. This might have resulted from the discharge of compressive residual stress created by the sputtering process and crystal structure refinements through the annealing route [44, 50]. The Debye Scherrer formula of Eq. 1, was employed to estimate the grain size of the coatings.

$$D = \frac{K \lambda}{\gamma \cos \theta} \quad (1)$$

where  $K$  is a dimensionless quantity known as the crystallite-shape factor ( $K = 0.94$ ),  $\lambda$  is the X-ray wavelength of Cu- $K_{\alpha}$  radiation ( $\lambda = 0.154$  nm),  $\gamma$  is the line broadening at half the maximum intensity (FWHM) measured in radians, and  $\theta$  is the Bragg angle [53]. The crystallite size increased with increasing annealing temperatures (up to 700 °C) and then abruptly decreased to at 800 °C. It is clear from the above tabulated results (see Table 2), that crystal sizes of the 700 °C annealed CrN coatings were mostly greater than that of the as deposited one (Figure 2 (B)) due to faster grain growth at high temperatures [54].



**Figure 2.** Temperature dependent (A) lattice constants and (B) grain size of sputtered CrN films before and after annealing.

The microstrain and residual stress developed within the film coatings was estimated by evaluating the  $d$ -spacing of the CrN(111) using diffraction results [55]:

$$\varepsilon = \frac{d-d_0}{d_0} \quad (2)$$

where  $\varepsilon$  is the component of microstrain normal to the surface, and  $d$  and  $d_0$  are the measured and strain free  $d$ -spacing values, respectively. The internal residual stress,  $\sigma_x$  induced in the coating was calculated using the following equation,

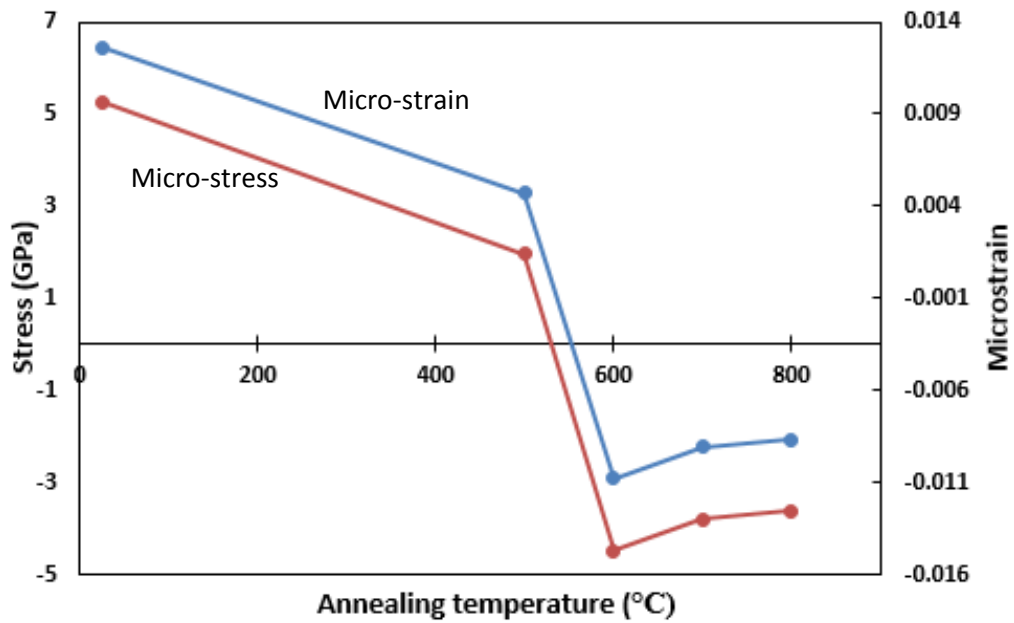
$$\sigma_x = \frac{E}{(1-\nu)} \times \frac{d-d_0}{d_0} \quad (3)$$

where  $d$  and  $d_0$  are obtained from the experimental diffraction patterns and JCPDS card of CrN phase, respectively, using the elastic properties of the CrN phase as obtained from our nanoindentation results. The Poisson's ratio value of  $\nu = 0.28$  was used from Ref. [55].



**Table 2.** Variation of crystallite size, lattice parameters, residual stress, and macrostrain of CrN coatings with different annealing temperatures along (111) plane.

Annealing temperature (°C)	Crystallite size, $D_g$ (nm)	Lattice constant, $a$ (nm)	Bragg angle, $2\theta^\circ$	Microstrain, $\epsilon$	Stress, $\sigma_x$ (Gpa)
Room temperature	112.7	4.19	37.5	0.0126	5.25
500	150.8	4.16	37.3	-0.0047	1.88
600	154.4	4.10	37.9	-0.0108	-4.31
700	239.9	4.09	37.9	-0.0091	-3.5
800	195.3	4.11	37.9	-0.0087	-2.7



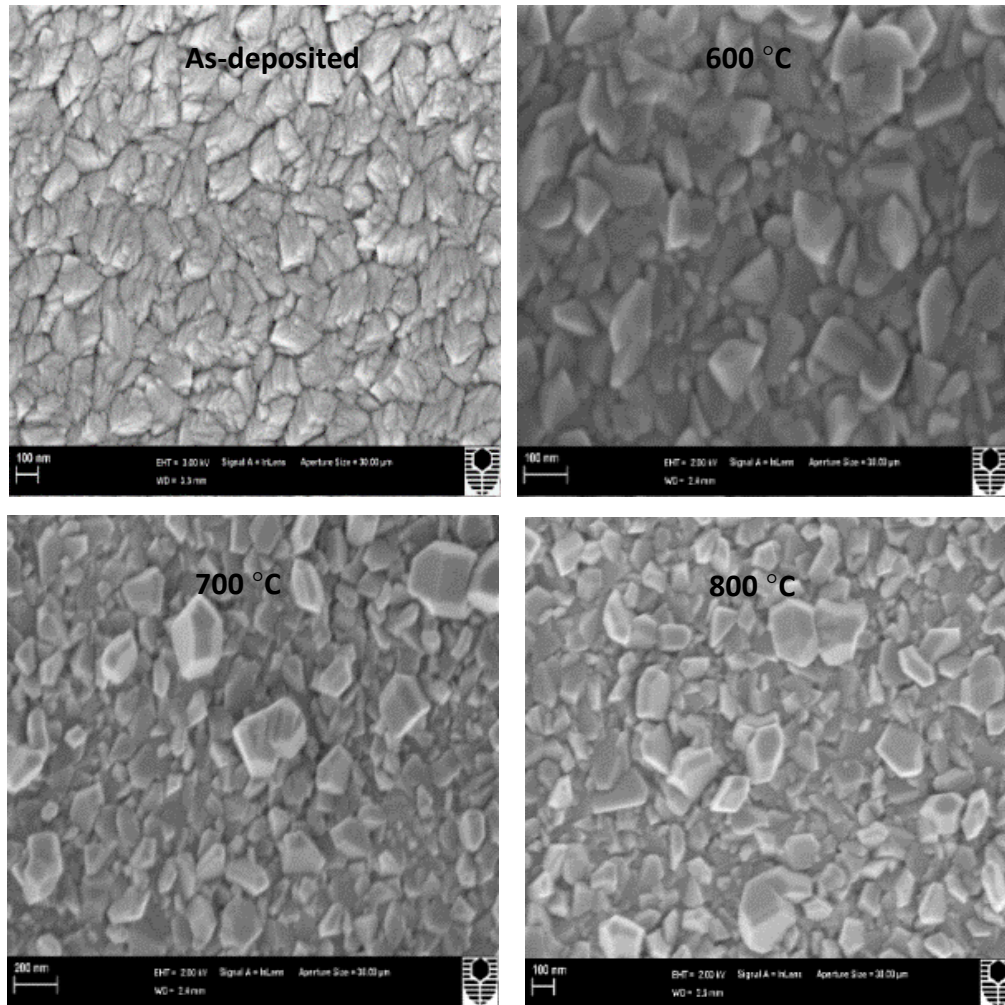
**Figure 3.** Micros stress ( $\sigma_x$ ) and microstrain ( $\epsilon$ ) of sputtered CrN films before annealing and after annealing.

In Figure 3 and Table 2, it can be observed that in CrN structures, residual stresses are released until 600 °C and then promptly increase steeply through 700 and 800 °C temperatures. The development of residual stress in these coatings can be seen in two mechanisms: the thermal residual stress generated due to the difference in thermal expansion coefficient between coatings and substrates, and/or, the buildup of defects such as vacancies, cavities, and dislocations. The release of internal residual stress in the CrN phase may be associated to the absorption and extinction of sputtering defects during annealing. The heating procedure may result in diffusing the defects through the CrN lattice and absorbing defects in grain boundaries and dislocation cores. Our observations are consistent with the findings reported by Mohammadpour *et al.* [56]. In this study it was seen

that the lattice microstrain and residual stresses are reduced as the annealing temperatures rise. This reflects the fact that the release of internal crystallite residual stresses in thin film coatings is the consequence of a reduction in defects, such as dislocations and vacancies. Our experimental results of crystal dimensions, lattice microstrains, and residual stress change trends were in good agreement with the Fourier analysis simulation conducted by Cunha *et al.* [57].

#### **4.3.2 Morphological Features of CrN Films *via* FESEM Studies**

Figure 4 illustrates the FESEM images of CrN thin film coatings before and after annealing at 500 to 800 °C in steps of 100 °C in air for 1 hour. The FESEM images show a smooth grain-like surface with grain sizes ranging between 50 - 250 nm. The morphologies observed were a mixture of irregular grains, with reasonably small aspect ratios. Similar surface features were observed with the CrN samples annealed above 600 °C which were investigated *via* FESEB technique [52]. The grain-like uniform crystal forming surface features were originated from mixed grains with a size ranging between 82.6 and 198 nm. It is interesting to note that after annealing, the CrN surface morphologies change from as-deposited taper and triangular compacted structures to granular and face-centered structures. Furthermore, the Cr<sub>2</sub>O<sub>3</sub> grains appeared in the coating top layer. Above 600 °C, the film grain sizes being enlarged with the increase in annealing temperatures [52]. This is due to the increased grain size of Cr<sub>2</sub>O<sub>3</sub> structures which developed after 600 °C and which were detected to be as large as ~0.500 μm at 700 °C due to the grain coalescence effect. Thus, the major changes in microstructure of the CrN phase occurred at temperature above 600 °C.



**Figure 4.** The FESEM morphological features of sputtered CrN thin films in as deposited state and after being annealed at various temperatures.

#### 4.3.3 *X-ray Photoelectron Spectroscopy (XPS) Characterizations of CrN Films before and after Annealing*

XPS analysis of CrN thin film coatings in the binding energy range of 0-1200 eV, before and after annealing, were carried out to estimate their elemental compositions are listed in Table 3. From Table 3, it is evident that annealing has a protruding effect on the atomic composition of these coatings. The atomic percentages of Cr and N were reduced with the rise in annealing temperature until 600 °C, while the oxygen contents were enhanced. This indicates that the occurrence of surface oxidation around the coatings as the temperature rises. At higher annealing temperatures, the higher oxygen content gives rise to the thicker and predominant oxygen layer around the surfaces.

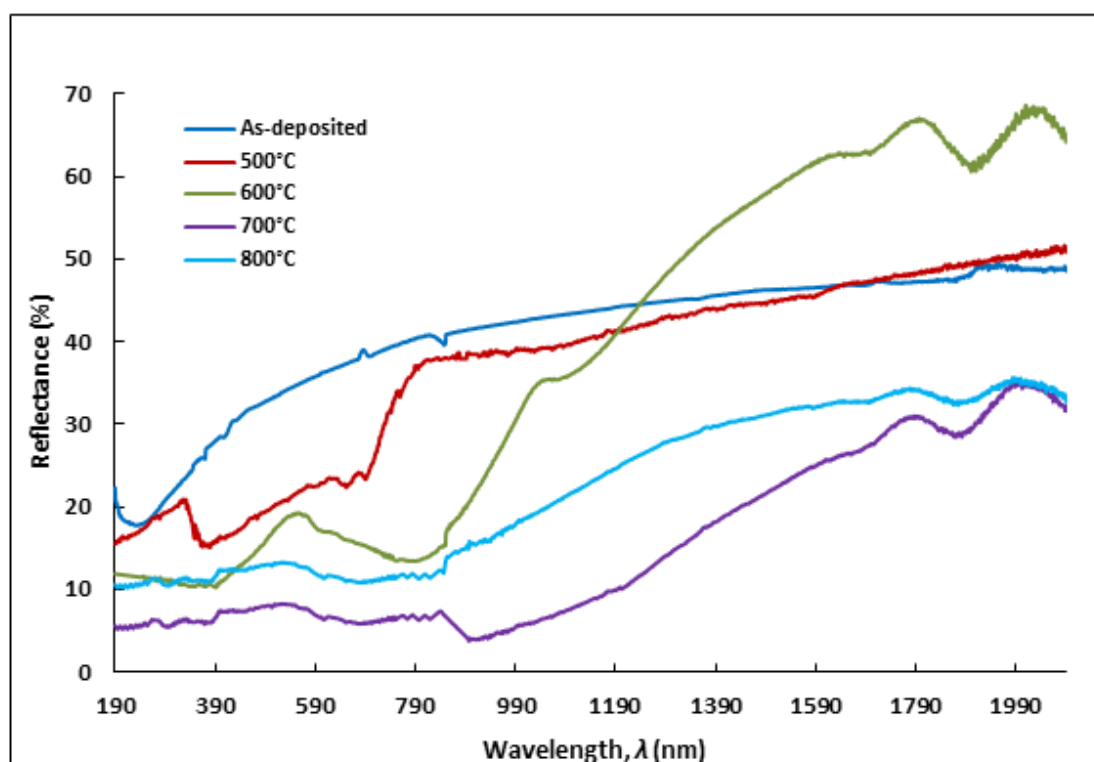
**Table 3.** XPS results of sputtered CrN films in as-deposited and at various annealing states.

Annealing temperatures (°C)	Atomic percentages (%) of elements		
	Cr	N	O
As deposited	36.92	37.87	25.21
500	28.40	11.97	59.63
600	32.35	4.55	63.10
700	32.60	3.03	64.37
800	36.78	2.68	60.54

#### 4.3.4 Optical Characterizations of CrN Films before and after Annealing

##### 4.3.4.1 UV-Vis Characterizations

Table 4 charts the solar absorptance,  $\beta$  values of the sputtered CrN films which were estimated using the ultraviolet visible reflectance data collected in the wavelength range of 190-2300 nm (see Figure 5), as described in [58, 59]. Low spectral reflectance indicates high spectral absorptance and vice versa. From this study, it is shown that the annealing temperature of the absorber coating layer influences the final absorptance of the CrN matrix. Clear absorption edges of these coatings were noticed at the shorter wavelength range of spectra. Other scholars also reported a similar phenomenon [60-65].



**Figure 5.** UV-Vis reflectance spectra of CrN sputtered films deposited onto silicon substrates as a function of wavelength

Generally, the absorption edges shift towards the longer wavelength sides with the rise of annealing temperatures. As a result, higher absorptance values are recorded at high annealing temperatures. However, in order to obtain optimized spectra with selective solar absorption, the position of the reflectance value in the cut-off area (at ~2300 nm) has to be of a relatively high reflectance value. The absorption edge of CrN coatings annealed at 700 °C detected at 900 nm showed a relatively lower interference peak comparing to the other spectra.

**Table 4.** Solar absorptance values of CrN coatings before and after annealing at different temperatures in air for 1 h.

Sample annealing condition (°C)	Solar absorptance, $\beta$ (%)
As-deposited	0.61
500	0.66
600	0.68
700	0.89
800	0.83

This indicates that the absorptance value of the coating annealed at 700 °C is the highest (89%). Even though its reflectance position in the cut-off area is relatively lower than the other coatings, 700 °C annealed coatings can be considered as optimal due to its highest absorptance. The absorptance value of 89% appears to be very promising in their applications for harvesting solar energy in selective absorber systems. We may summarize that the crystallized nanosized grain-like particles that grown and become more to be as a solid solution (as seen in FESEM studies) are capable of providing a conducive surface for the absorption of solar radiation due to the multiple reflections that occur inside the pores [66]. As a result, the solar absorptance value is enhanced due to the interaction and relaxation mechanisms in absorber and resonant scattering in the pores [64, 67].

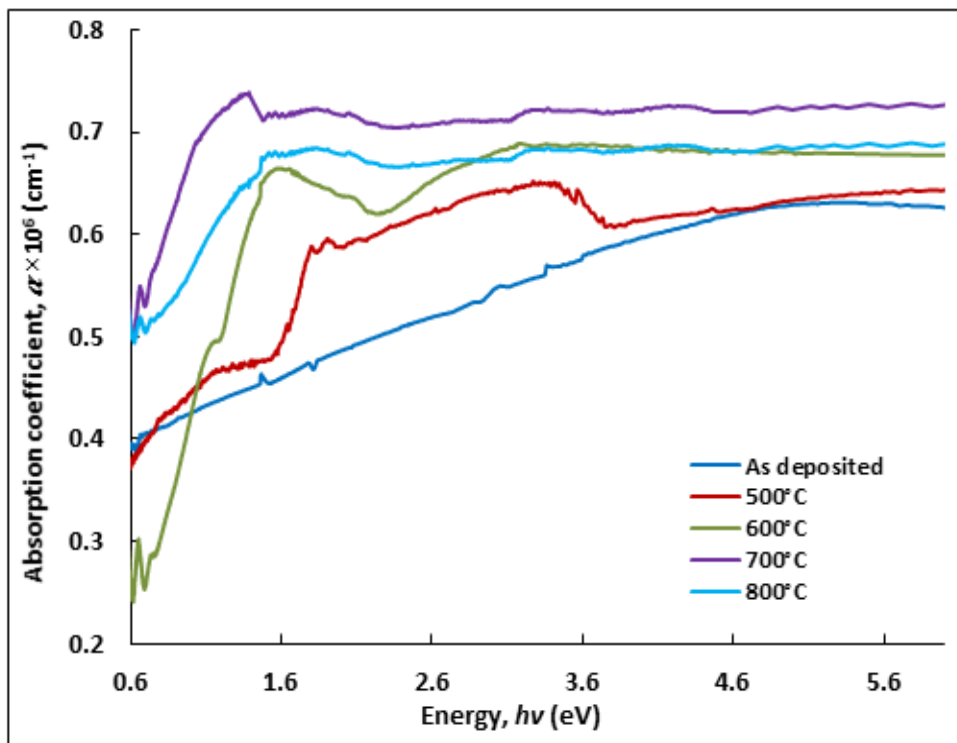
#### 4.3.4.2 Optical Band-gap Analysis

The linear absorption coefficient can be determined by using the reflectance spectra of the films using the following relation,

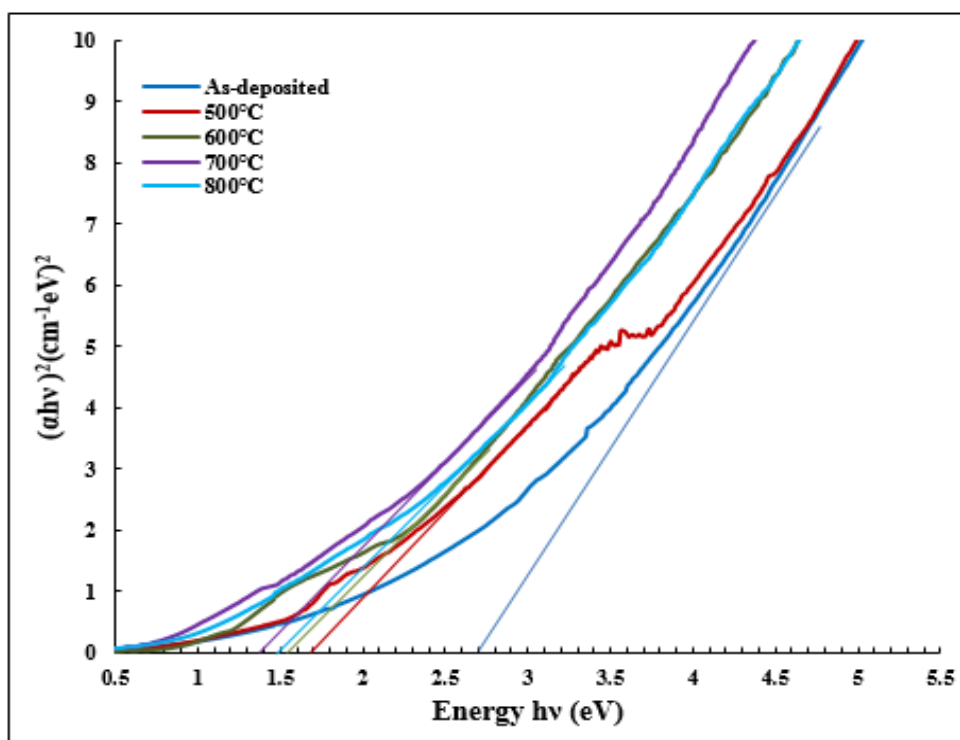
$$\alpha = 2.3026 \frac{A}{d} \quad (4)$$

where  $\alpha$  is the absorption coefficient,  $A$  is the solar absorptance (in terms of %) as estimated from the UV-Vis reflectance data, and  $d$  is the coating's thickness [68]. Solar absorption of UV-Vis light is related to excitation of electrons in both atoms and molecules. The spectral dependence of  $\alpha$  helps to study the band structure and the type of electronic transitions

involved in the absorption process. The energy dependence of the absorption coefficient of CrN systems before and after annealing is displayed in the following Figure 6. Crystalline and amorphous materials obey the Tauc relation during the photon absorption process which can be used for CrN coating band-gap calculations [40, 69-71]. Tauc plots of photon energy against  $(\alpha h\nu)^2$  for CrN coatings before and after annealing are shown in Figure 7.



**Figure 6.** Energy dependence of the absorption coefficient of sputtered CrN films before and after annealing.



**Figure 7.** Tauc plots of  $(\alpha h\nu)^2$  VS photon energy( $h\nu$ ) of CrN coatings before and after annealing. Estimation of band-gaps of thin films in direct method.

The energy band-gap values of CrN coatings before and after annealing as estimated *via* the interception of linear portion of the curves extrapolated to zero in the photon energy axis are tabulated in Table 5. The values of as-deposited and annealed coatings energy gaps lie between 1.38 and 2.62 eV. It is found that the energy band-gap values are dramatically reduced with the rise in annealing temperature of the Cr-nitride systems. The energy band-gap values are linearly decreased with the rise in annealing temperature up to 700 °C, then increased to 1.48 eV at 800 °C. The subsequent drop in materials energy band-gap values represent a very important aspect in improving the photon absorption capability of these coatings. The spectral absorption of solar surfaces strongly depends on the presence of localized states around the forbidden energy band-gap. The absorption contours offer valuable information on these localized states and highlight the occurrence of disorderness in the films [72]. The energy band-gaps of CrN coatings was changed from 2.62 to 1.38 eV, as the annealing progresses from room temperature to 700 °C. With the gradual increase in annealing temperature, the degree of crystallinity of CrN coatings is increased together with the monotonic increase in their grain sizes and thereby the energy band-gaps are decreased. It is also assumed that the energy band-gap is associated with the change in carrier concentration and can be seen in the Burstein-Moss shift [73]. The BM shift in band-gaps

arises because conduction the bands lower energy states are obstructed by the presence of higher carrier concentrations. The BM shift or band-gap narrowing is also related to several many-body interactions between the carriers in the conduction bands and valence bands. As a result, the energy band-gap values are dwindled. Our results were found to concur with previous reports [74, 75]. Thus, the band-gap studies, of CrN systems are well-consistent with our XRD and FESEM results.

**Table 5.** Energy band-gaps of CrN coatings before and after annealing at different temperatures.

Sample annealing condition (°C)	Energy band-gap, $E_g$ (eV)
As-deposited	2.62
500	1.68
600	1.54
700	1.38
800	1.48

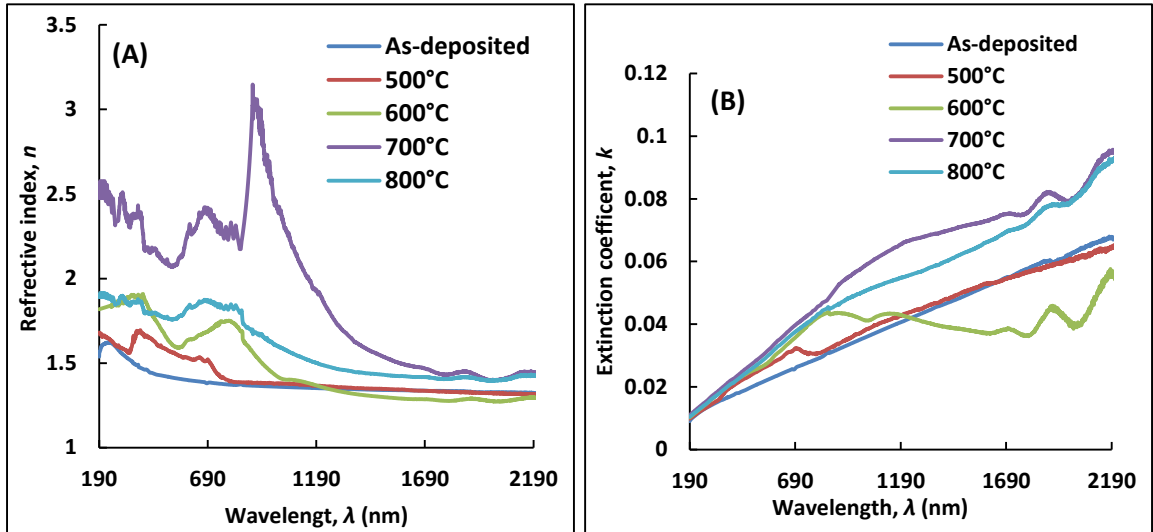
#### 4.3.4.3 *Refractive Index and Extinction Coefficient Analysis*

The refractive index and extinction coefficient are two key parameters in realizing various optical and dielectric properties of coating based materials. UV-Vis reflectance spectra collected in the wavelength range of 190–2200 nm were used to calculate the refractive index,  $n$  and the extinction coefficient,  $k$  of the coatings from the coming relation,

$$n^* = n + ik \quad (5)$$

Elaborate explanations of refractive index,  $n$  and extinction coefficient,  $k$  are available elsewhere [40]. The wavelength dependence of the refractive index, and extinction coefficient parameters of CrN coatings before and after annealing are delineated in Figure 8.





**Figure 8.** (A) Refractive index, and (B) Extinction coefficient of CrN sputtered films deposited onto silicon substrates as a function of wavelength before and after annealing.

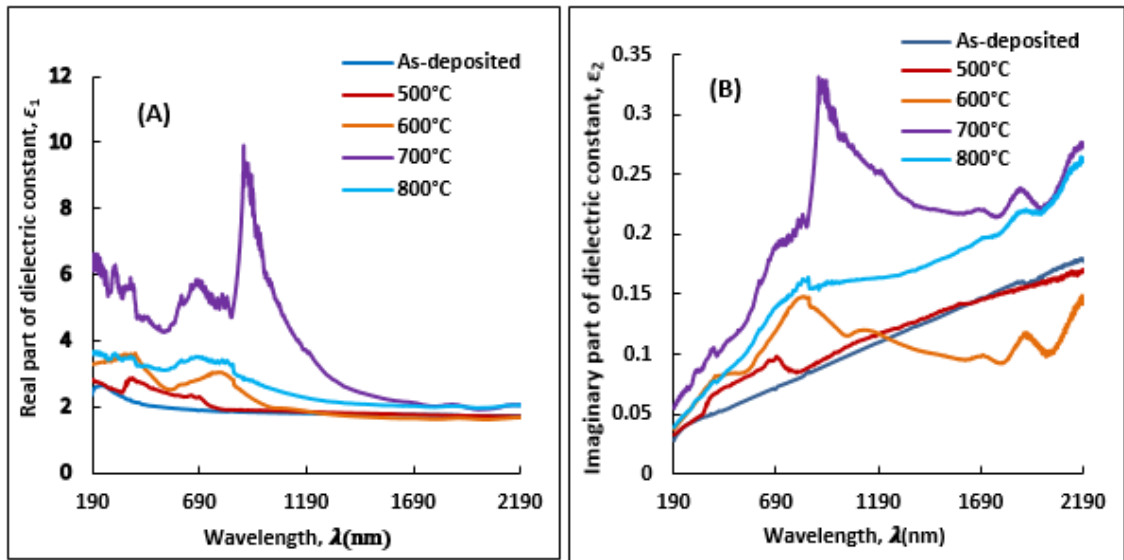
Both  $n$  and  $k$  have increased dramatically with the increasing of annealing temperatures. This may confirm the enhancement of the films crystallinity. Further investigations also reveal that in the lower wavelength region of up to around 850 nm,  $n$  refractive index is linearly increased and reached to a maximum value and then it sharply dropped with the increase in wavelength. Similarly, the  $k$  values increase with the increase in wavelengths. These features indicate that  $n$  shows asymmetrical dispersions in the lower wavelength regions and normal dispersion in the higher wavelength sides whereas the reverse phenomena were identified for the  $k$ . The dispersion of the refractive index explores a peak at 850 nm corresponding to  $\pi$ - $\pi^*$  transitions of the UV oscillator. On the other hand, the abnormal nature arises due to the resonance effects between incoming solar radiation and electronic polarizability. This occurs due to the coupling of electrons and oscillating electric fields of the incident electromagnetic radiation [75-78]. The refractive index is strongly associated with the electronic polarizability of ions and local field of the CrN coatings. A complete understanding of the refractive index of these coatings is very important for their applications in integrated optical devices, such as solar absorber systems for different functions, solar heating and solar electrical generating systems in medium and warm environmental fields. The refractive index represent a key parameter for the design of such devices.

#### 4.3.4.4 Dielectric Characterizations

Dielectric parameters play an important role in identifying the characteristics of solar selective absorbing coatings. It is well-known that the optical band-gap probes the optical properties near the band edges of a material. In particular, localized states near the conduction or the valence band have a strong effect on the optical absorption and thus decline the band-gap energy [68, 79]. The frequency dependence of the electron excitation spectra of thin film based materials can be defined in terms of complex dielectric constant,

$$\varepsilon(\omega) = \varepsilon_1(\omega) + \varepsilon_2(\omega) = ((n(\omega) + ik(\omega))^2 \quad (6)$$

where  $\varepsilon_1$  and  $\varepsilon_2$  are the real and imaginary parts of the dielectric function, respectively. Figure 9 shows the real and imaginary parts of dielectric constant of CrN coatings, as a function of wavelength, before annealing and after being annealed at different temperatures.



**Figure 9.** (A) Real and (B) imaginary part of dielectric constant of CrN sputtered films deposited onto silicon substrates as a function of wavelength before and after annealing.

In the visible and UV-region, the  $\varepsilon_1$  and  $\varepsilon_2$  values increase with the rise in annealing temperatures. The real part of the dielectric constant, of CrN sputtered films, as the function of wavelength resembles the same trend as that of the reflective index because these two quantities are directly proportional to each other. It is also known that the real part of the dielectric constant ( $\varepsilon_1$ ) is associated to the polarization and anomalous dispersion of the medium, while  $\varepsilon_2$  is related to the exponential decay of the electric field *i.e.*, the power dissipation into the medium. In the visible and UV-region, the  $\varepsilon_1$  and  $\varepsilon_2$  values increase with the rise in annealing temperatures. A greater value of  $\varepsilon_1/\varepsilon_2$  indicates that the CrN thin film coatings have a good low-loss dielectric nature, which may be due to the increased electron density functions of the coatings. It is also assumed that the improvement in crystallinity of

the coatings can decrease the degree of electron scattering and increase the free-electron density [78, 80]. The essential electron excitation spectrum of the thin film coatings was inferred from the frequency dependence of the complex dielectric constant. Thin film's frequency response of the dielectric constant shows that the interactions of the photons and electrons in the film originates within the observed wavelength range. In thin film materials, the power loss factor generally arises from the inelastic scattering process during the charge conduction and charge transfer mechanisms. The amount of energy represented by  $\epsilon_1$  and  $\epsilon_2$  as stored in dielectrics are termed as polarization energy and loss energy, respectively [78].

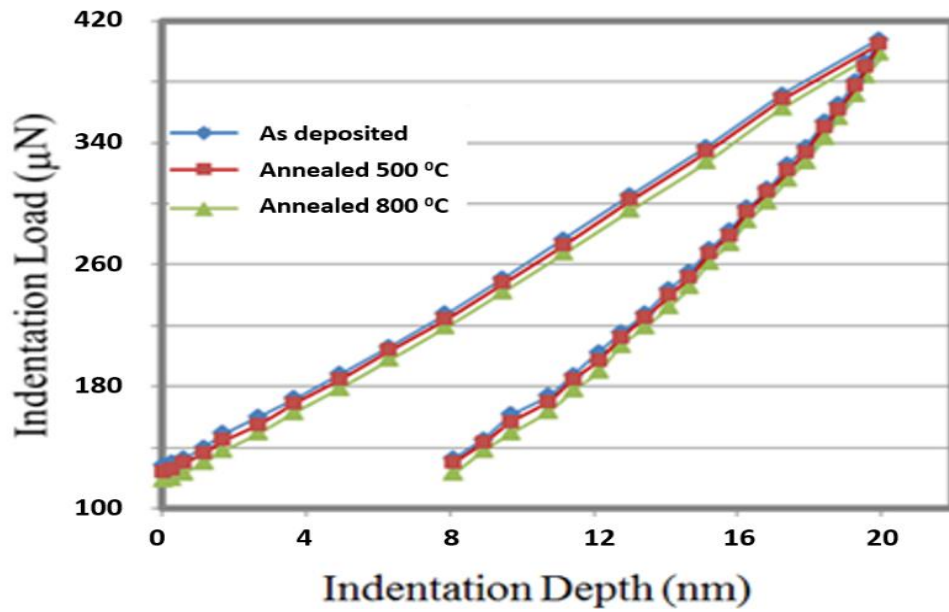
#### **4.3.5 Mechanical Characterizations of CrN Films: Nanoindentation and FEM Modeling**

##### **4.3.5.1 Nanoindentation Results**

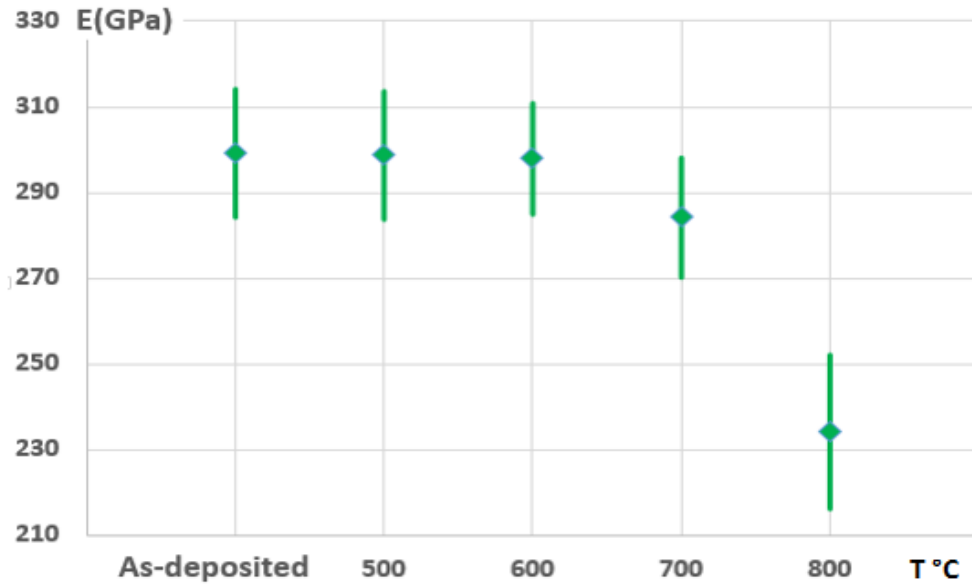
Generally speaking loading-displacement curves are shown in Figure 10, while the experimental results of Young's modulus  $E$  and hardness  $H$  are given in Figures 11 and 12. The elastic modulus  $E$  of the as-deposited film is 299 GPa (see Table 6). After annealing it changes within the range 215-315 GPa (taking into account the error margin). A general trend may be identified, namely that the Young's modulus decreases with the increasing annealing temperature. This is in general agreement with previous studies [82]. Within the error margin, no significant change in the modulus was observed in all the three samples after annealing at a temperature of 600 °C (see Figure 11). However, after annealing at 700 and 800 °C, significant change in the elastic modulus was observed, with a ~22% drop after annealing at 800 °C. The hardness value  $H$  of the as-deposited film was measured as 18.5 GPa. After the films were annealed at 600-800 °C, a 3 to 8% decrease of hardness values was observed. Similar effects, *i.e.*, the lowering of  $E$  and  $H$  values after annealing have been reported for different coatings. For example, it was reported that annealing has a negative impact on ITO thin films [54, 83].

The Hall-Petch relationship [84] can be used to elucidate the correlation between the hardness with grain size data of CrN coatings. The H-P relationship predicts that as the grain size of a material is decreased, the yield strength (hardness/elastic constant) is increased and vice versa. Nanoindentation results of the CrN phase at different annealing temperatures displayed in Table 6 revealed that, from room temperature to 800 °C, the elastic modulus and hardness values of CrN structure is gradually reduced from  $299.3 \pm 15$  and  $18 \pm 0.5$  GPa to  $234.1 \pm 10$ , and  $17 \pm 0.5$  GPa, respectively. According to the Hall-Petch phenomenon, the hardness of materials is inversely proportional to the square root of the

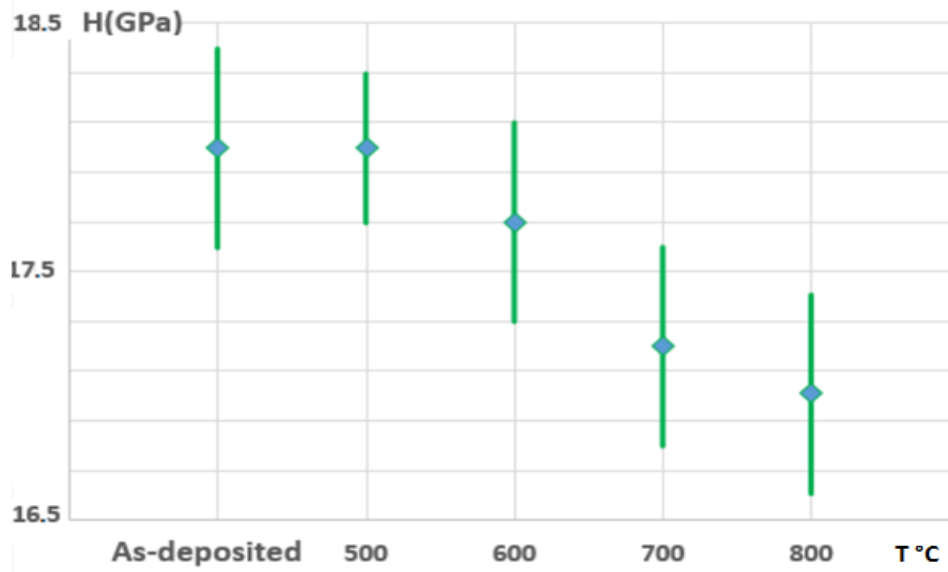
grain sizes [85]. Thus, the grain size, yield strength and nanoindentation results presented in Table 2 and Table 6 are consistent with each other and obey the H-P effect.



**Figure 10.** Typical loading-displacement curves.



**Figure 11.** Elastic modulus plot for the CrN samples, as deposited, and annealed at 500, 600, 700, and 800 °C, respectively.



**Figure 12.** Hardness plots for the CrN sputtered films as deposited, and annealed at 500, 600, 700, and 800 °C, respectively.

**Table 6.** Elastic modulus derived from the indentation data.

Annealing temperature (°C)	Elastic modulus, $E$ (GPa)	Hardness, $H$ (GPa)
As deposited	$299.3 \pm 15$	$18 \pm 0.5$
500	$298.8 \pm 15$	$18 \pm 0.5$
600	$298.0 \pm 13$	$17.7 \pm 0.4$
700	$284.2 \pm 14$	$17.2 \pm 0.5$
800	$234.1 \pm 10$	$17 \pm 0.5$

To understand the impact of annealing on the mechanical properties, we need to identify the factors affecting these mechanical properties. It has been reported that the hardness of the coatings produced using the PVD method can be enhanced by the level of residual compressive macrostresses, as well as high levels of defects and associated microstresses [86]. The coatings prepared by physical vapor deposition methods such as sputtering usually accumulate a considerable amount of residual stress in the coatings [87], which helps with enhancing hardness. However after annealing, the absolute stress within the CrN film will be reduced to only about half of that before annealing (Figure 3), and this had a detrimental effect on the hardness of the film. Furthermore, the elastic modulus of a material has been found to be directly proportional to the square root of the hardness of the same material [88], which explained the lowered  $E$  value after the CrN film has been annealed. The microstructure and impurity could also modify the mechanical properties. For example, the increase of the grain size after annealing, coupled with the formation of  $\text{Cr}_2\text{O}_3$  phase at

higher temperature, also contributes to the decrease of the hardness, which is consistent with previous studies on the same and similar materials [52, 54, 56, 87, 89].

#### 4.3.5.2 FEM Modeling

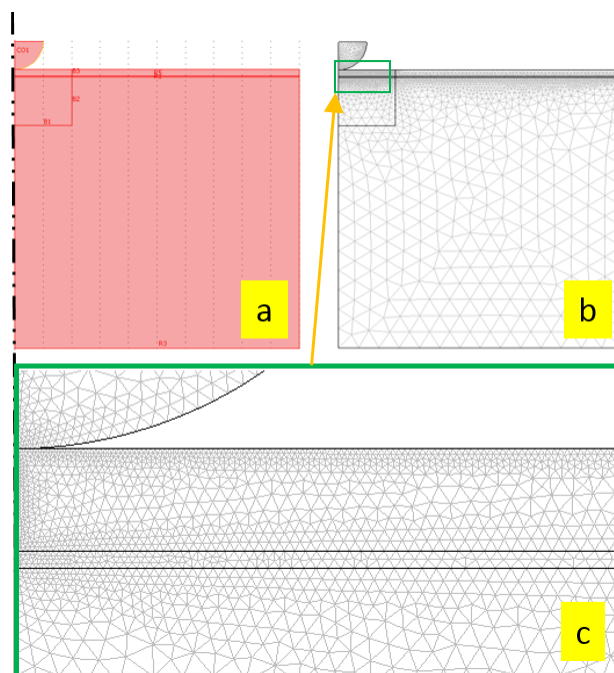
Finite element modeling was used in this work, and aimed at a detailed understanding of the load induced stress intensity and distribution within different coating materials and configurations. Comsol Multiphysics software was used as the simulation tool. A 2D axial symmetry model was adapted, with a spherical indenter (5  $\mu\text{m}$  radius) at the top of a 1.2  $\mu\text{m}$  CrN coating layer supported by three different substrates: silica, silicon (111) and steel. For comparison purposes, an interlayer was inserted between the coating and substrate, with a thickness of 0.2  $\mu\text{m}$ , which was typical for our samples. A software pre-defined contact pair was created between the indenter and the surface of the film, which completely defined the boundary condition of the contact. The diamond indenter, which has a higher stiffness in the normal direction, was selected as the master boundary, and the surface of the film, the slave boundary. The friction in the shear direction was not modeled. For the purpose of modeling calibration, a standard fused silica sample (Young's modulus 71.7 GPa) was experimentally tested using a spherical indenter of 10  $\mu\text{m}$ , and loaded with a different loading. The indentation depth at different loadings are recorded. This experiment setup was then built into a FEM model and tested. Using the same indentation depth the modeling results of the loadings agree well with the experimental data, within an error margin of 3%. Further details of modeling have been given in our previous work [90]. The elastic moduli obtained from our nanoindentation measurements (Table 6) were used for the coating layer. Modeling parameters for the interlayer, substrate and the indenter, are given in Table 7 [90].

**Table 7.** Modeling parameters of substrate, indenter and interlayer [90].

Samples name	Young's modulus, E (GPa)	Poisson's ratio	Yield strength (GPa)	BH (GPa)
Steel	200	0.30	675	1.7
Silicon (111)	200	0.25	-	-
Silica	80	0.25	-	-
Cr	200	0.30	700	1.7
Indenter (diamond)	1141	0.07	-	-

Interactive meshing was applied in order to optimize the modeling process. Typical geometrical model and meshing are presented in Figure 13. The elastic modulus used in the modeling work are those obtained from the indentation data, which are listed in Table 6.

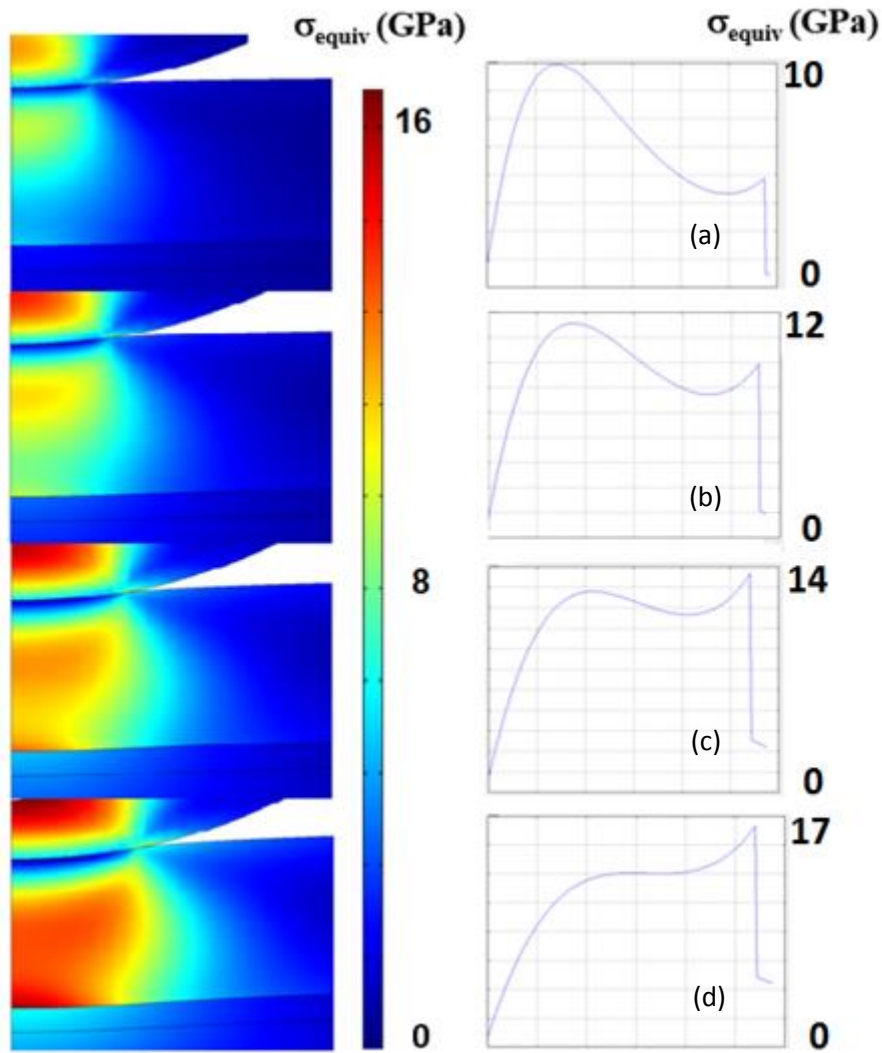
Details of load induced stress distribution within the coating layer plays an important part in determining the integrity of the coatings under loading conditions. Firstly, the focus is on the load induced von Mises stress, also known as equivalent stress and is labelled as  $\sigma_{\text{equiv}}$ . This is a measure of the ‘severity’ of the potential damage to the integrity of the coating. Our modeling results indicate that, there are two primary locations in the coating layer with high load induced stress concentrations: one is close to the indenter, and the other is at the interface between the coating and the interlayer or substrate. At shallow indentation depth, the stress maximum is close to the coating surface. When the indentation depth increases, the stress maximum moves downwards, and the stress maximum shifts towards the interface between the coating and the substrate (see Figure 14). With small loadings, when the stress maximum is close to the coating surface, the load induced stress is primarily compressive in nature, which is less detrimental to the integrity of the coating. However, with the increase of the loading, the stress maximum will move towards the interface, while it becomes tensile in the horizontal direction, when intensity of shear stress also increased. These are the primary cause of lateral crack and delamination [91].



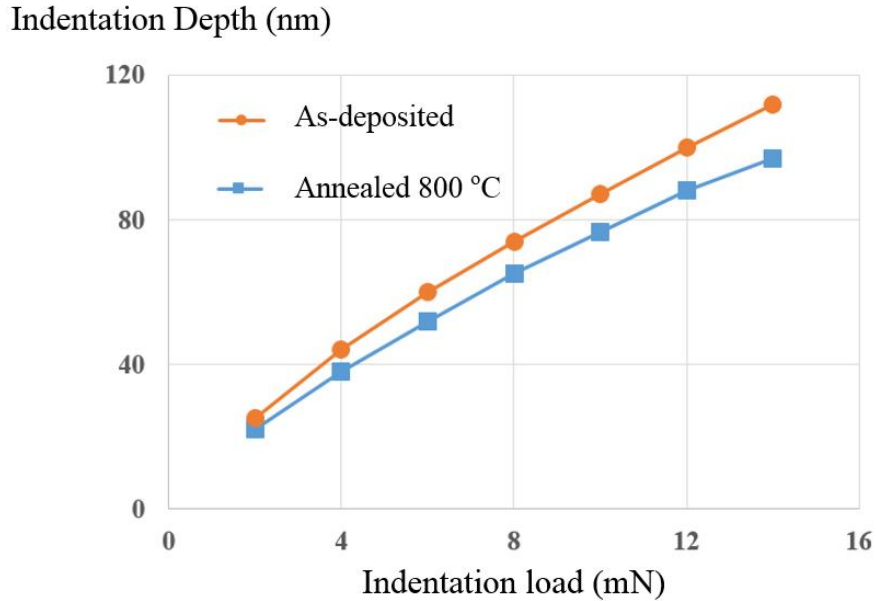
**Figure 13.** Geometry and the meshing of the indentation model used in this work. (a) The diagrammatic sketch of FEM model, with a diamond indenter of 5  $\mu\text{m}$  in radius on the top of a CrN coating layer of 1.2  $\mu\text{m}$  thick. The coating is setting on an interlay of 0.2  $\mu\text{m}$ , and then the substrate represented by a square of 50  $\mu\text{m}$ . Note that this model is ‘axial symmetric’ so that it represents a cylinder formed by rotating the schematics about the dashed line (b) FEM mesh generated using interactive method, so that denser meshing points are located in the areas of interest, and (c) Magnified meshing details around the contact between the indenter and the film.

Here we observed that, after annealing above 600 °C, the films become softer with lower elastic moduli (Table 6). The change in elastic modulus will, in turn, result in a change in the load induced stress level and distributions in the film. In Figure 15 we show the FEM results of a comparison of the indentation depth and as a function of the maximum (load induced) stress level within two different films – as-deposited and annealed. It is clearly demonstrated that, in order to induce the same stress level, a greater indentation depth is required for the as-deposited film. In other words, even assuming that the yield strength remains the same after the film is annealed, a smaller indentation depth is required to result in yielding within the film. As discussed in Section 3.6.1, the hardness of the film would have been already reduced after annealing, due to the reduced residual stress, formation of Cr<sub>2</sub>O<sub>3</sub>, *etc.* Generally speaking, the yield strength of a material is positively correlated to its hardness [92, 93]. Taking into account of all these factors, our FEM modeling results predict a negative impact of annealing upon the mechanical integrity of the CrN film, *i.e.*, much lower indentation depth will result in the yielding of the film.





**Figure 14.** Modeling results of load induced stress distribution in the as-deposited CrN coating on a silica substrate, at different indentation depth. The Young's moduli adopted are 299.3 GPa for the CrN film (Table 6), and 80 GPa for the substrate (Table 7), respectively. (a) indentation depth 0.1  $\mu\text{m}$ , (b) indentation depth 0.16  $\mu\text{m}$ , (c) indentation depth 0.22  $\mu\text{m}$ , and (d) indentation depth 0.28  $\mu\text{m}$ . The right-hand side column presents the stress distribution along the centre symmetrical axis at corresponding indentation displacement, with the horizontal axis being the depth from the coating surface, 0-2  $\mu\text{m}$ .

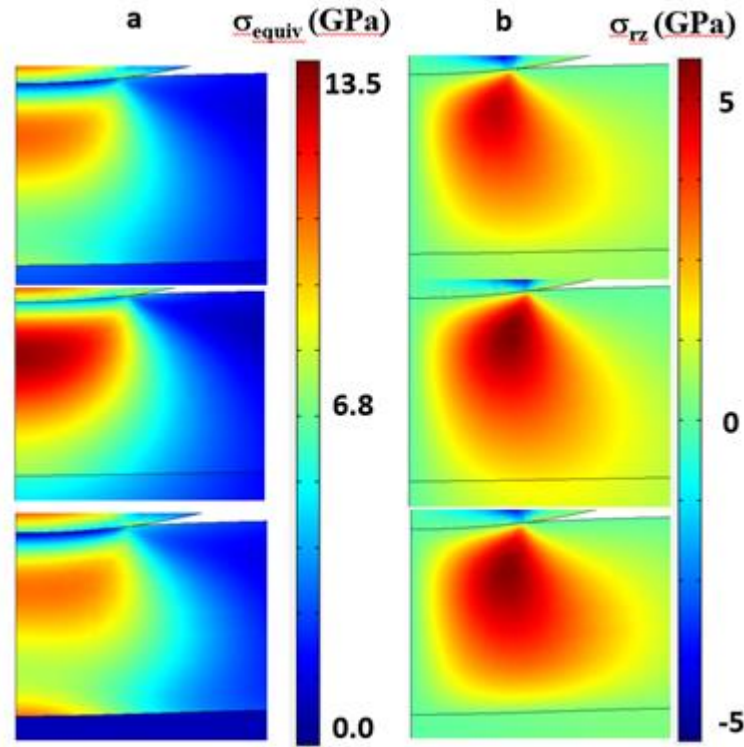


**Figure 15.** The modelling results of indentation depth as a function of the indentation loading, for the as-deposited and annealed (800 °C) CrN films.

The thickness of the interlayer, as well as the material matching between the interlayer and substrate, also plays a very important role which has an impact on the level of load induced stress level in the coating layer. For example, our modeling results indicate that, when a thin Cr interlayer (~100 nm) is added between the CrN coating and the substrate, there will be a (20–30%) increase in the stress level. It should also be noted that, after annealing the hardness and the strength of the coating materials are also decreased, so the lowering of the stress level does not mean the damage tolerance of the coating becomes greater.

A comparison for CrN different substrate materials is shown in Figure 16. Importantly, the maximum load induced stress level within the coating layer will vary for different substrate materials. Of the three different type of substrates modeled in this work, *i.e.*, silicon, steel, and silica, the later has the lowest elastic modulus, so at the same indentation depth the lowest stress level will be induced in it. In contrast, silicon and steel substrates have higher elastic modulus, so both the equivalent and shear stress concentrations occupy a larger volume. At the same time, the equivalent stress concentration is shifted down towards the interface. Generally speaking, for materials with higher elastic modulus delamination are more likely to occur under heavy loadings. It is also interesting to note that, although silicon and steel substrate have about the same Young’s modulus, the load induced stress level is much lower within the latter. This is due to the elasto-plastic property of the interlayer,

which tends to have higher deformation once the load induced stress level exceeds its yielding strength, resulting in larger localized deformation. As a result, the stress tends to concentrate at the interface between the coating and the substrate.



**Figure 16.** Finite element modeling results of (a) equivalent stress and (b) shear stress distribution within sample CrN at an indentation depth of 0.12  $\mu\text{m}$ . Top to bottom: silica substrate, silicon substrate, steel substrate.

In summary, the hardness and elastic modulus of the as-deposited coatings are calculated as 18.5 GPa and 299 GPa from indentation results. Annealing at a temperature below 500 °C does not affect  $H$  and  $E$  values, but 800 °C annealing reduces the  $H$  and  $E$  by 8% and 22%, respectively. From FEM modeling it has been seen that the load induced stress levels are reduced after the coatings are annealed, particularly at higher temperatures. The load induced stress level will also change when using different types of substrates, and in materials of high elastic modulus, a higher level of stress will be induced at the interface between the coating and the substrate, which is detrimental to the coating integrity and results in delamination. Finally, introducing a metal interlayer will increase the stress level at the interface.

#### 4.4 Conclusions

This study aims at understanding the structural evolution, optical, dielectric, and mechanical studies and finite element modeling of as-deposited and annealed CrN thin film coatings. The existence of a face-centered cubic CrN phase was confirmed *via* XRD studies but the presence of a Cr<sub>2</sub>N phase hexagonal was not detected. The gradual increase of grain size and the gradual decrease in lattice parameters with the rise in annealing temperatures was observed. The atomic compositions of CrN coatings before and after annealing were also confirmed using the XPS studies. A consistency between the solar absorptance and energy band-gap studies of these coatings were revealed in the UV-Vis reflectometry studies. The mechanical properties studied by nanoindentation showed that hardness and elastic modulus are dependent on the microstructure, grain refinement and residual stress. It is known that greater hardness corresponds with the smaller crystallite size of thin film coatings. The hardness of CrN coatings was governed by the composite structure formed by the nanocrystallites and amorphous structures after the heat treatment. As a result, the coatings hardness didn't reach to the superhardness level. It is believed that the post annealing amorphous layers formed around the grain boundaries substantially degrades the strength and hardness of the CrN coatings. However, a thick amorphous layer could essentially improve the oxidation resistance and stability of the CrN coatings by hindering atomic disseminations at high temperature exposures.

#### References

- [1] X. Nie, A. Leyland, A. Matthews, *Surface and Coatings Technology*, 133-134 (2000) 331-337.
- [2] G. Li, P. Deshpande, J.H. Li, R.Y. Lin, *Tsinghua Science and Technology*, 10 (2005) 690-698.
- [3] A. Kumar, H.L. Chan, J.J. Weimer, L. Sanderson, *Thin Solid Films*, 308-309 (1997) 406-409.
- [4] E. Zalnezhad, A.A.D.M. Sarhan, M. Hamdi, *International Journal of Precision Engineering and Manufacturing*, 14 (2013) 467-473.
- [5] B. Navinšek, P. Panjan, I. Milošev, *Surface and Coatings Technology*, 97 (1997) 182-191.
- [6] R. Cremer, D. Neuschütz, *Surface and Coatings Technology*, 146-147 (2001) 229-236.
- [7] S. PalDey, S.C. Deevi, *Materials Science and Engineering A*, 342 (2003) 58-79.
- [8] T. Polcar, N.M.G. Parreira, R. Novák, *Surface and Coatings Technology*, 201 (2007) 5228-5235.

- [9] S.K. Pradhan, C. Nouveau, A. Vasin, M.A. Djouadi, *Surface and Coatings Technology*, 200 (2005) 141-145.
- [10] S.-K. Tien, J.-G. Duh, *Thin Solid Films*, 494 (2006) 173-178.
- [11] J.N. Tu, J.G. Duh, S.Y. Tsai, *Surface and Coatings Technology*, 133-134 (2000) 181-185.
- [12] P.W. Shum, Z.F. Zhou, K.Y. Li, Y.G. Shen, *XPS, Materials Science and Engineering: B*, 100 (2003) 204-213.
- [13] P.H. Mayrhofer, F. Kunc, J. Musil, C. Mitterer, *Thin Solid Films*, 415 (2002) 151-159.
- [14] P.H. Mayrhofer, G. Tischler, C. Mitterer, *Surface and Coatings Technology*, 142-144 (2001) 78-84.
- [15] P.H. Mayrhofer, C. Mitterer, L. Hultman, H. Clemens, *Progress in Materials Science*, 51 (2006) 1032-1114.
- [16] P.W. Atkins, *The Elements of Physical Chemistry*, Oxford University Press, Oxford, UK, 1992.
- [17] C. Zou, L. Huang, J. Wang, S. Xue, *Solar Energy Materials and Solar Cells*, 137 (2015) 243-252.
- [18] A. Avila-García, U. Morales-Ortiz, *Solar Energy Materials and Solar Cells*, 90 (2006) 2556-2568.
- [19] J. Chen, C. Guo, J. Chen, J. He, Y. Ren, L. Hu, *Materials Letters*, 133 (2014) 71-74.
- [20] H. Sai, H. Yugami, Y. Kanamori, K. Hane, *Solar Energy Materials and Solar Cells*, 79 (2003) 35-49.
- [21] N. Selvakumar, H.C. Barshilia, K.S. Rajam, A. Biswas, *Solar Energy Materials and Solar Cells*, 94 (2010) 1412-1420.
- [22] Q.C. Zhang, D.R. Mills, *Solar Energy Materials and Solar Cells*, 27 (1992) 273-290.
- [23] S. Zhao, E. Wäckelgård, *Solar Energy Materials and Solar Cells*, 90 (2006) 1861-1874.
- [24] N. Selvakumar, H.C. Barshilia, *Solar Energy Materials and Solar Cells*, 98 (2012) 1-23.
- [25] M.A. Ezazi, M.M. Quazi, E. Zalnezhad, A.A.D. Sarhan, *Ceramics International*, 40 (2014) 15603-15615.
- [26] Q. Wang, F. Zhou, J. Yan, *Surface and Coatings Technology*, 285 (2016) 203-213.
- [27] H.C. Barshilia, N. Selvakumar, B. Deepthi, K.S. Rajam, *Surface and Coatings Technology*, 201 (2006) 2193-2201.
- [28] P.H. Mayrhofer, F. Rovere, M. Moser, C. Strondl, R. Tietema, *Scripta Materialia*, 57 (2007) 249-252.

- [29] G. Beshkov, G.P. Vassilev, M.R. Elizalde, T. Gomez-Acebo, *Materials Chemistry and Physics*, 82 (2003) 452-457.
- [30] L. Hultman, *Vacuum*, 57 (2000) 1-30.
- [31] M. Akbarzadeh, A. Shafyei, H.R. Salimijazi, *International Journal of Engineering, Transactions A: Basics*, 27 (2014) 1127-1132.
- [32] S.Y. Lee, G.S. Kim, J.H. Hahn, *Surface and Coatings Technology*, 177-178 (2004) 426-433.
- [33] J.C. Sánchez-López, A. Contreras, S. Domínguez-Meister, A. García-Luis, M. Brizuela, *Thin Solid Films*, 550 (2014) 413-420.
- [34] M. Mahbubur Rahman, A. Duan, Z.-T. Jiang, Z. Xie, A. Wu, A. Amri, B. Cowie, C.-Y. Yin, *Journal of Alloys and Compounds*, 578 (2013) 362-368.
- [35] M.M. Rahman, Z.-T. Jiang, Z. Xie, X. Duan, Z.F. Zhou, P.C. Wo, C.Y. Yin, N. Mondinos, Q. Gu, H. Widjaja, K. Jack, A. Yago, A. Amri, *Journal of Physical Chemistry C*, 118 (2014) 18573-18579.
- [36] M.M. Rahman, Z.-T. Jiang, X. Duan, Z. Xie, A. Tadich, Z.-f. Zhou, N. Mondinos, C.-Y. Yin, M. Altarawneh, B.Z. Dlugogorski, *Journal of Alloys and Compounds*, 661 (2016) 268-273.
- [37] K. Ibrahim, Hatem Taha, M. Mahbubur Rahman, Humayun Kabir, Zhong-Tao Jiang, *Journal of Optics*, 20 (2018) 033001.
- [38] Y. Wu, B. Wang, Y. Ma, Y. Huang, N. Li, F. Zhang, Y. Chen, *Nano Res.*, 3 (2010) 661.
- [39] D. Yuelan, Z. Ping, C. Zhihai, Y. Zhen, L. Qi, S. Wei, *Rare Metal Materials and Engineering*, 43 (2014) 264-268.
- [40] K. Ibrahim, M. Mahbubur Rahman, H. Taha, E. Mohammadpour, Z. Zhou, C.-Y. Yin, A. Nikoloski, Z.-T. Jiang, *Applied Surface Science*, 440 (2018) 1001-1010.
- [41] A. Millar, M.M. Rahman, Z.-T. Jiang, *Journal of Advanced Physics*, 3 (2014) 179-193.
- [42] A. Amri, Z.-T. Jiang, X. Zhao, Z. Xie, C.-Y. Yin, N. Ali, N. Mondinos, M.M. Rahman, D. Habibi, *Surface and Coatings Technology*, 239 (2014) 212-221.
- [43] Z. Li, P. Munroe, Z.T. Jiang, X. Zhao, J. Xu, Z.F. Zhou, J.Q. Jiang, F. Fang, Z.H. Xie, *Acta Materialia*, 60 (2012) 5735-5744.
- [44] S. Jeong Heo, S.-W. Kim, I.-W. Yeo, S.-J. Park, Y.-S. Oh, *Ceramics International*, 42 (2016) 5231-5237.
- [45] A. Gilewicz, B. Warcholinski, *Surface and Coatings Technology*, 279 (2015) 126-133.
- [46] D. Qi, H. Lei, T. Wang, Z. Pei, J. Gong, C. Sun, *Journal of Materials Science & Technology*, 31 (2015) 55-64.

- [47] T.K. Tsai, Y.H. Li, J.S. Fang, *Thin Solid Films*, 615 (2016) 91-96.
- [48] C. Zou, L. Huang, J. Wang, S. Xue, *Solar Energy Materials and Solar Cells*, 137 (2015) 243-252.
- [49] L. Wang, X. Nie, *Journal of Materials Engineering and Performance*, 23 (2013) 560-571.
- [50] E.Y. Choi, M.C. Kang, D.H. Kwon, D.W. Shin, K.H. Kim, *Journal of Materials Processing Technology*, 187-188 (2007) 566-570.
- [51] E. Mohammadpour, Z.-T. Jiang, M. Altarawneh, Z. Xie, Z.-f. Zhou, N. Mondinos, J. Kimpton, B.Z. Dlugogorski, *Thin Solid Films*, 599 (2016) 98-103.
- [52] Z.B. Qi, B. Liu, Z.T. Wu, F.P. Zhu, Z.C. Wang, C.H. Wu, *Thin Solid Films*, 544 (2013) 515-520.
- [53] A.L. Patterson, *Physical Review*, 56 (1939) 978-982.
- [54] L. Wang, X. Nie, Effect of annealing temperature on tribological properties and material transfer phenomena of CrN and CrAlN coatings, *J Mater Eng Perform*, 23 (2014) 560-571.
- [55] I.C. Noyan, J.B. Cohen, *Residual stress: measurement by diffraction and interpretation*, Springer-Verlag New York, USA, 1987.
- [56] E. Mohammadpour, Z.-T. Jiang, M. Altarawneh, N. Mondinos, M.M. Rahman, H.N. Lim, N.M. Huang, Z. Xie, Z.-f. Zhou, B.Z. Dlugogorski, *RSC Advances*, 7 (2017) 22094-22104.
- [57] L. Cunha, L. Rebouta, F. Vaz, M. Staszuk, S. Malara, J. Barbosa, P. Carvalho, E. Alves, E. Le Bourhis, P. Goudeau, J.P. Rivière, *Vacuum*, 82 (2008) 1428-1432.
- [58] M.M. Rahman, Z.-T. Jiang, Z.-f. Zhou, Z. Xie, C.Y. Yin, H. Kabir, M.M. Haque, A. Amri, N. Mondinos, M. Altarawneh, *Journal of Alloys and Compounds*, 671 (2016) 254-266.
- [59] H.A. Miran, M.M. Rahman, Z.-T. Jiang, M. Altarawneh, L.S. Chuah, H.-L. Lee, E. Mohammedpur, A. Amri, N. Mondinos, B.Z. Dlugogorski, *Journal of Alloys and Compounds*, 701 (2017) 222-235.
- [60] R. Bayón, G. San Vicente, C. Maffiotte, A. Morales, *Solar Energy Materials and Solar Cells*, 92 (2008) 1211-1216.
- [61] R. Bayón, G. San Vicente, C. Maffiotte, A. Morales, *Renewable Energy*, 33 (2008) 348-353.
- [62] T. Boström, E. Wäckelgård, G. Westin, *Solar Energy*, 74 (2003) 497-503.
- [63] C.J. Brinker, G.C. Frye, A.J. Hurd, C.S. Ashley, *Thin Solid Films*, 201 (1991) 97-108.

- [64] W. Piskorz, F. Zasada, P. Stelmachowski, A. Kotarba, Z. Sojka, *Catalysis Today*, 137 (2008) 418-422.
- [65] A. Amri, X. Duan, C.Y. Yin, Z.T. Jiang, M.M. Rahman, T. Pryor, *Applied Surface Science*, 275 (2013) 127-135.
- [66] E. Ienei, L. Isac, C. Cazan, A. Duta, *Solid State Sciences*, 12 (2010) 1894-1897.
- [67] M.E. Rincón, J.D. Molina, M. Sánchez, C. Arancibia, E. García, *Solar Energy Materials and Solar Cells*, 91 (2007) 1421-1425.
- [68] A.A.M. Farag, M. Fadel, *Optics and Laser Technology*, 45 (2013) 356-363.
- [69] M.S. Hossain, H. Kabir, M.M. Rahman, K. Hasan, M.S. Bashar, M. Rahman, M.A. Gafur, S. Islam, A. Amri, Z.-T. Jiang, M. Altarawneh, B.Z. Dlugogorski, *Applied Surface Science*, 392 (2017) 854-862.
- [70] M.M. Rahman, Z.T. Jiang, P. Munroe, L.S. Chuah, Z.F. Zhou, Z. Xie, C.Y. Yin, K. Ibrahim, A. Amri, H. Kabir, M.M. Haque, N. Mondinos, M. Altarawneh, B.Z. Dlugogorski, *RSC Advances*, 6 (2016) 36373-36383.
- [71] H. Kabir, M.M. Rahman, T.S. Roy, A.H. Bhuiyan, *International Journal of Mechanical and Mechatronics Engineering*, 12 (2012) 30-34.
- [72] M.M. Rahman, H.A. Miran, Z.-T. Jiang, M. Altarawneh, L.S. Chuah, H.-L. Lee, A. Amri, N. Mondinos, B.Z. Dlugogorski, *RSC Adv.*, 7 (2017) 16826-16835.
- [73] J.W. Jeon, D.W. Jeon, T. Sahoo, M. Kim, J.H. Baek, J.L. Hoffman, N.S. Kim, I.H. Lee, *Journal of Alloys and Compounds*, 509 (2011) 10062-10065.
- [74] B. Kumar, H. Gong, R. Akkipeddi, *Journal of Applied Physics*, 97 (2005) 063706.
- [75] A. Jain, P. Sagar, R.M. Mehra, *Solid-State Electronics*, 50 (2006) 1420-1424.
- [76] S.W. Xue, X.T. Zu, W.L. Zhou, H.X. Deng, X. Xiang, L. Zhang, H. Deng, *Journal of Alloys and Compounds*, 448 (2008) 21-26.
- [77] S. Sarkar, N.S. Das, K.K. Chattopadhyay, *Solid State Sciences*, 33 (2014) 58-66.
- [78] Y. Kim, J.Y. Leem, *Physica B: Condensed Matter*, 476 (2015) 71-76.
- [79] S.H. Wemple, M. DiDomenico Jr, *Physical Review B*, 1 (1970) 193-202.
- [80] C. Fournier, O. Bamiduro, H. Mustafa, R. Mundle, R.B. Konda, F. Williams, A.K. Pradhan, *Semiconductor Science and Technology*, 23 (2008) 085019.
- [81] B. Barış, H.G. Özdemir, N. Tuğluoğlu, S. Karadeniz, O.F. Yüksel, Z. Kişnişi, *Journal of Materials Science: Materials in Electronics*, 25 (2014) 3586-3593.
- [82] J. Almer, M. Odén, G. Håkansson, *Philosophical Magazine*, 84 (2004) 611-630.
- [83] C.Y. Yen, S.R. Jian, G.J. Chen, C.M. Lin, H.Y. Lee, W.C. Ke, Y.Y. Liao, P.F. Yang, C.T. Wang, Y.S. Lai, J.S.C. Jang, J.Y. Juang, *Applied Surface Science*, 257 (2011) 7900-7905.



- [84] D.F. Arias, A. Gómez, J.M. Vélez, R.M. Souza, J.J. Olaya, *Materials Chemistry and Physics*, 160 (2015) 131-140.
- [85] Z.T. Wu, Z.B. Qi, D.F. Zhang, B.B. Wei, Z.C. Wang, *Surface and Coatings Technology*, 289 (2016) 45-51.
- [86] J. Almer, M. Odén, G. Håkansson, *Thin Solid Films*, 385 (2001) 190-197.
- [87] H. Oettel, R. Wiedemann, S. Preißler, *Surface and Coatings Technology*, 74-75 (1995) 273-278.
- [88] Y.W. Bao, W. Wang, Y.C. Zhou, *Acta Materialia*, 52 (2004) 5397-5404.
- [89] E.Y. Choi, M.C. Kang, D.H. Kwon, D.W. Shin, K.H. Kim, *Journal of Materials Processing Technology*, 187-188 (2007) 566-570.
- [90] X. Zhao, Z. Xie, P. Munroe, *Materials Science and Engineering: A*, 528 (2011) 1111-1116.
- [91] Z.H. Xie, R. Singh, A. Bendavid, P.J. Martin, P.R. Munroe, M. Hoffman, *Thin Solid Films*, 515 (2007) 3196-3201.
- [92] J.J. Gilman, *Journal of Applied Physics*, 46 (1975) 1435-1436.
- [93] E.J. Pavlina, C.J. Van Tyne, *J. Mater. Eng. Perform.*, 17 (2008) 888-893.

## CHAPTER FIVE

---

### **Paper IV: Tailoring the Annealing Impacts on Structural, Morphological, Opto-dielectric and Mechanical Behaviors of Mo:CrN Coatings: Experimental Studies and Finite Element Modeling**

---

#### **Abstract**

In the present study, molybdenum doped chromium nitride coatings deposited onto silicon substrates *via* unbalanced magnetron sputtering, in as-deposited condition and annealed at 500 – 800 °C in steps of 100 °C were studied to reveal their temperature dependent structural, morphological, optical and mechanical behaviors. An analysis of these features was carried out using X-ray diffraction (XRD), field emission scanning electron microscopy (FESEM), UV-Vis spectroscopy, nanoindentation and finite element modeling (FEM) techniques. XRD results exhibited a significant improvement in the crystallinity of the Mo-doped CrN coatings along (111) and (200) diffraction planes, as the annealing temperatures increased. The lattice parameters were gradually decreased as the temperature increased and it reached the lowest value of 4.125 nm at 800 °C. The same tendency was also observed for lattice micorstrains and residual stresses. Smooth grain-like surfaces were observed by FESEM imaging techniques. At an annealing temperature of 700 °C, the spectral absorptance of Mo:CrN films attained its peak value (86%), whereas the energy band-gaps were reduced from 2.48 to 1.14 eV. The other optical parameters such as complex dielectric constants, Urbach energy values, and steepness parameters of these coatings were also discussed. Nanoindentation experiments and finite element modeling (FEM) results indicated that at higher annealing temperatures, both the mechanical hardness ( $H$ ) and the elastic modulus ( $E$ ) of Mo:CrN coatings dwindled.

#### **5.1 Introduction**

Metal nitride coatings such as titanium nitrides and chromium nitrides have attractive physico-chemical, optical, electronic, mechanical and thermal characteristics which make them suitable and scalable in a wide range of technological and industrial applications [1-6]. Due to their high hardness, good adhesion to substrate, excellent wear resistance, low friction coefficient, high corrosion and oxidation resistance, attractive elastic modulus values, high melting point and superior chemical stabilities, these coatings have been widely used in high-speed cutting and machining [7], moulding dies and cold forming [8], combustion engine moving parts and rocket nozzles [9]. CrN-based coatings proposed to show significant superiority over TiN-based coatings in terms of corrosion and wear resistance, and anti-oxidant behaviours at high

operating temperatures [10, 11]. For these reasons, metal nitride coatings based materials have been widely investigated to improve their structural, mechanical, optical, and chemical characteristics.

The sputtering deposition technique is considered as a favourable method for fabricating ceramic-based CrN coatings with high quality structure, good mechanical and tribological properties [8, 9]. The majority of these studies have been focused on doping the binary CrN by other elements, *e.g.*, Ti [12], Si [13, 14], Al [15], Cu [16], V [17], Nb [18], and Mo [19]. It has been reported that the dopants either substitute the host atoms on their sites or distribute their atoms around the amorphous grain boundaries at the columnar nanocrystalline structure of CrN coatings. The Mo has been extensively used as a dopant for CrN coatings because of its potential to improve the hardness [19], wear, and friction resistance, and corrosion and oxidation resistances [20-22]. It is considered as a dopant to the CrN structure due to its ability to form a molybdenum oxide layer on the surface of the coating which suppresses the diffusion of oxygen into the upper surface of coatings [20, 23]. Ezazi *et al.* have reported that the Mo-dopant significantly affects the preferred orientation of CrN coatings [24]. The incorporation of Mo also induces the compressive residual stress in the lattice structure of CrN. Moreover, the mechanical properties such as hardness, elastic strain and plastic deformation resistance of Mo-doped CrN coatings were remarkably enriched [19, 20]. All these eventually confirm the vital role of Mo-doping in manipulating the hardness and damage resistance of CrN coatings.

The CrN, and Mo-doped CrN sputtered thin film coatings were investigated to comprehend their structural, spectral selective, and mechanical features in both as deposited and annealed at various temperatures [25, 26]. Various optical coefficients such as optical absorption coefficient, optical band-gaps, complex refractive index, dielectric constants, and energy loss functions of these coatings were thoroughly inspected. The nanoindentation and finite element modeling results indicated that the hardness and elastic modulus values of CrN coatings are significantly reduced with the annealing progression. In view of these facts, in this study the evolution of Mo-doped CrN coatings as a function of annealing temperatures in the range of 500–800 °C in steps of 100 °C has been extensively examined. Nano-indentation experiments and finite element stimulations (FEM) were also carried out to reveal their mechanical characteristics. It is also aimed at attaining a control methodology to develop a novel solar absorptive coating with desired physico-chemical, optical, dielectric, and mechanical properties for mid to high temperature applications.

## 5.2 Experimental Section

### 5.2.1 Film preparation methodology

An unbalanced magnetron sputtering ion plating (UDP650, Teer Coatings Ltd, UK) system was used to fabricate Mo:CrN films onto Si (100) substrates. Two Cr and one Mo targets (99.9% purity; 345 × 145 × 8 mm size) were used in the system to coat the films. Elaborate details of specimen preparation methodology has been described elsewhere [26]. Finally, the obtained Mo:CrN thin film coatings were annealed at 500–800 °C in steps of 100 °C in air for 1 hour.

### 5.2.2 XRD analysis

XRD measurements were conducted using a Bruker AXS D8 Advance X-ray diffractometer (Cu- $K_{\alpha}$  radiation of wavelength,  $\lambda = 1.54 \text{ \AA}$ ), operated at 40 kV and 40 mA integrated with a Lynx-eyed detector. The scan parameters used were:  $2\theta$  scan range (degree) 30 – 65; step size (degree): 0.01, time/step 0.15 s and total scan time/sample was ~15 minutes. Phase identification of the films was confirmed by matching the diffraction peaks with those of the JCPDS database. The lattice parameters of the defined structures were estimated from the XRD peaks using Debye-Scherrer formula.

### 5.2.3 FESEM Imaging

The structural morphologies of as-deposited and annealed Mo:CrN thin film coatings were analysed *via* Philips XL 20 SEM provided with an electron dispersive X-ray (EDX) analysis column and a Zeiss Neon 40EsB Field Emission Scanning Electron Microscopy (FESEM). The samples were fixed onto the holder using carbon tape prior to coating with platinum in order to minimize the charging effects.

### 5.2.4 UV-Vis Studies

A JASCO UV-670, USA double beam spectrophotometer was used to record the reflectance spectra of Mo:CrN coatings in the wavelength range of 190 to 2300 nm. The solar absorptance of Mo:CrN coatings were estimated using Beckman-Duffie method described in [27, 28],

$$\alpha = \frac{\int_{0.19}^{2.3} I_{sol}(\lambda)(1-R(\lambda))d\lambda}{\int_{0.19}^{2.3} I_{sol}(\lambda)d\lambda} \quad (1)$$

The other optical constants such as solar absorptance, optical band-gap, and dielectric parameters of as-deposited and post annealed of Mo:CrN sputtered coatings were computed from the UV-Vis reflectance data.

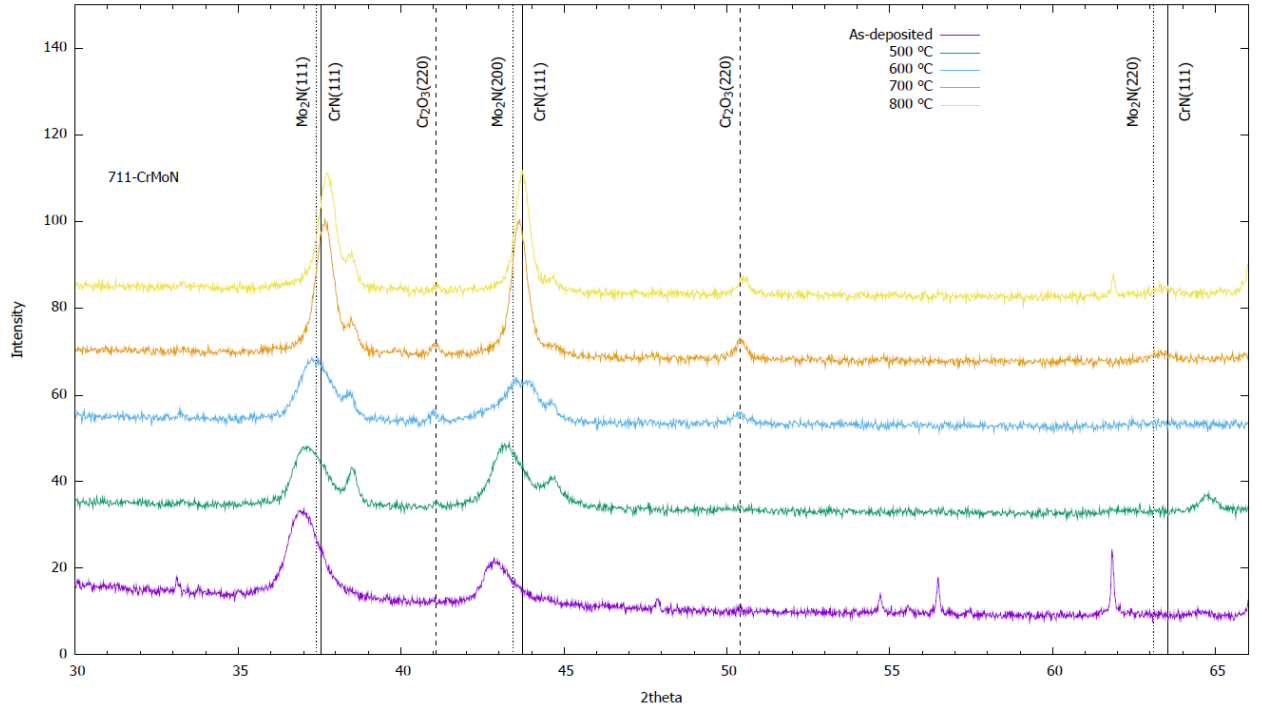
### 5.2.5 *Nanoindentation and Finite Element Modelling FEM Tests*

In this study, experimental nanoindentation has been carried out to investigate the mechanical properties of Mo:CrN thin film coating, *via* Ultra-Micro Indentation System 2000 workstation (CSIRO, Sydney, Australia). This nanoindentation machine is equipped with a diamond Berkovich indenter. Calibration of the indenter was performed using a standard fused silica specimen. In the experiments we used load control method with a maximum loading of 5 mN, taking into account that the CrMoN coating thickness is 1.4  $\mu\text{m}$ , and that the maximum indentation depth during indentation should be no higher than 10% of the coating thickness. This is because a high loading may result in micro-cracks in the relatively brittle coating layers. The number of measuring points was set to 15 during loading, and 20 during unloading, respectively. COMSOL Multiphysics software has been used as the modeling tool (FEM) to simulate the intensity and distribution of loading induced stress within different coatings materials and configurations. A 2D axial symmetry model was constructed, with a spherical indenter (5  $\mu\text{m}$  radius) at the top of Mo:CrN coating layers with different thicknesses. Its objective is to evaluate the magnitude and distribution of the stress within the film, as well as the influence of the film thickness and type of the substrate on the integrity of the film-substrate system. The coating layers with different thicknesses were modeled and were built on four different types of substrates: silica, silicon 100, silicon 110, and steel, which are the typical scenarios of real industrial applications [29, 30].

## 5.3 **Results and Discussion**

### 5.3.1 *XRD Analysis of the as-deposited and Annealed Mo:CrN Coatings*

The XRD patterns of as-deposited and annealed Mo:CrN thin film coatings are shown in Fig. 1. The XRD results confirm the presence of face-centered-cubic CrN structures with a space group: Fm-3m (ICDD 11-0065). The Bragg peaks featured at  $2\theta$  ( $= 37^\circ$ ,  $43^\circ$  and  $63^\circ$ ) are assigned to (111), (200), and (220) reflection lines, respectively [19, 22, 31]. The main diffraction peaks of the (111), and (200) reflection lines were broadened due to overlap the peaks of CrN and Mo<sub>2</sub>N phases. This is consistent with results reported in Ref. [31].



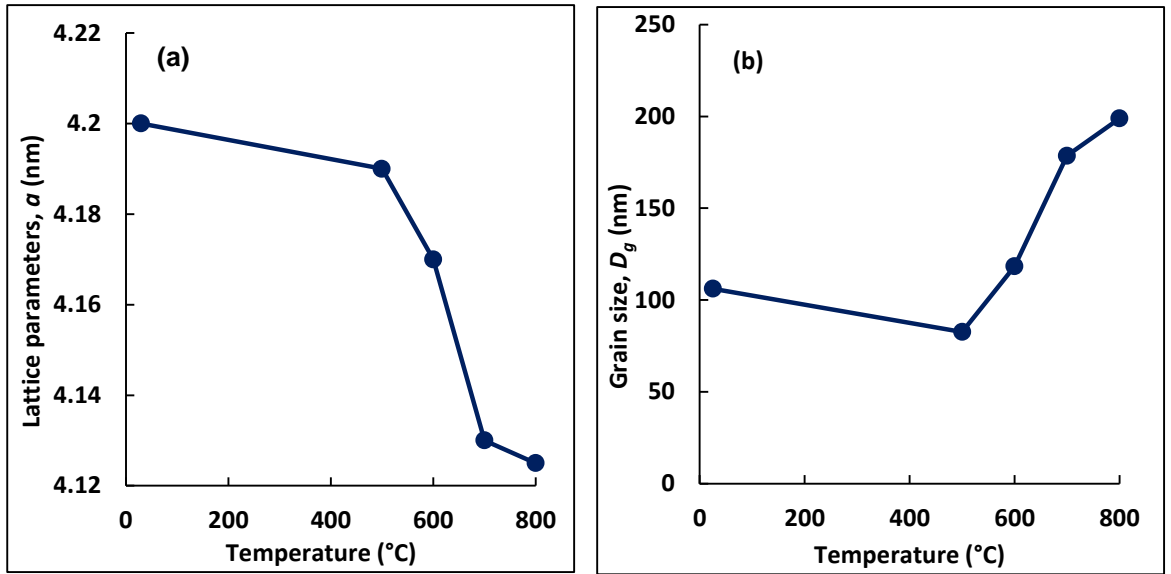
**Figure 1.** The X-ray patterns of Mo:CrN films as deposited on silicon substrate and after annealed for 1hr at 500, 600, 700, and 800 °C.

Moreover, the crystalline structures of both CrN and Mo<sub>2</sub>N phases improved with increasing annealing temperature due to enhancement of the grain growth and release of residual stress in the lattice structures [23]. A new phase of Cr<sub>2</sub>O<sub>3</sub> was observed at 32.5°, 41.4° and 51.3° referring to (104), (113) and (024) reflection planes, respectively (ICDD 38-01479) for the coatings annealed at 600 °C [32-34]. It is believed that in Mo-doped CrN coatings, the CrN phases are oxidized at higher annealing temperatures due to the external dissemination of chromium and nitrogen. However, the surface oxygen molecules are dispersed inwardly to form metal oxides around the coating surfaces.

The lattice constant of as-deposited Mo:CrN coatings was calculated to be 4.20 Å, and it slightly decreased to ~ 4.125 Å when the film annealed at 800 °C (See Table 1 and Fig. 2), indicating a shrinkage and distortion in the lattice structures. This is also attributed to the release of residual stress resulting from sputtering deposition and/or the structural changes during the heat treatment cycles [20, 22]. The Debye method was used to calculate the crystallite size of Mo:CrN films.

$$D = \frac{K \lambda}{\beta \cos \theta} \quad (2)$$

where  $K$  is the crystallite-shape factor ( $K = 0.9$ ),  $\lambda$  is the X-ray wavelength,  $\beta$  is the full line width at half maximum intensity (FWHM, in radians), and  $\theta$  is the Bragg angle [35].



**Figure 2.** Temperature dependent (a) lattice constants and (b) grain size of sputtered Mo:CrN films before and after annealing.

**Table 1.** Variation of crystallite size, lattice parameters, residual stress, and microstrains of Mo:CrN coatings with different annealing temperatures along (111) plane.

Annealing temperature ( $^{\circ}\text{C}$ )	Crystallite size, $D_g$ (nm)	Lattice constant, $a$ (nm)	Bragg angle, $2\theta^{\circ}$	Microstrains, $\varepsilon$	Stress, $\sigma_x$ (Gpa)
Room temperature	106.18	4.20	37.02	0.01303	5.43
500	82.64	4.19	37.12	0.01052	4.38
600	118.41	4.17	37.26	0.0068	2.821
700	178.58	4.13	37.66	-0.0033	-1.36
800	198.93	4.12	37.72	-0.0049	-2.05

From Table 1, the calculated crystallite size of as-deposited Mo:CrN coatings were 106.18 nm, and it was sharply decreased to 82.64 nm as the films were annealed at 500  $^{\circ}\text{C}$ . Then it started to increase with the increase in annealing temperatures reaching to the maximum value of 198.93 nm for the film annealed at 800  $^{\circ}\text{C}$ . This is based on the fact that high temperature annealing enhances the agglomeration of the coating particles, and thereby larger grains were grown [34, 36].

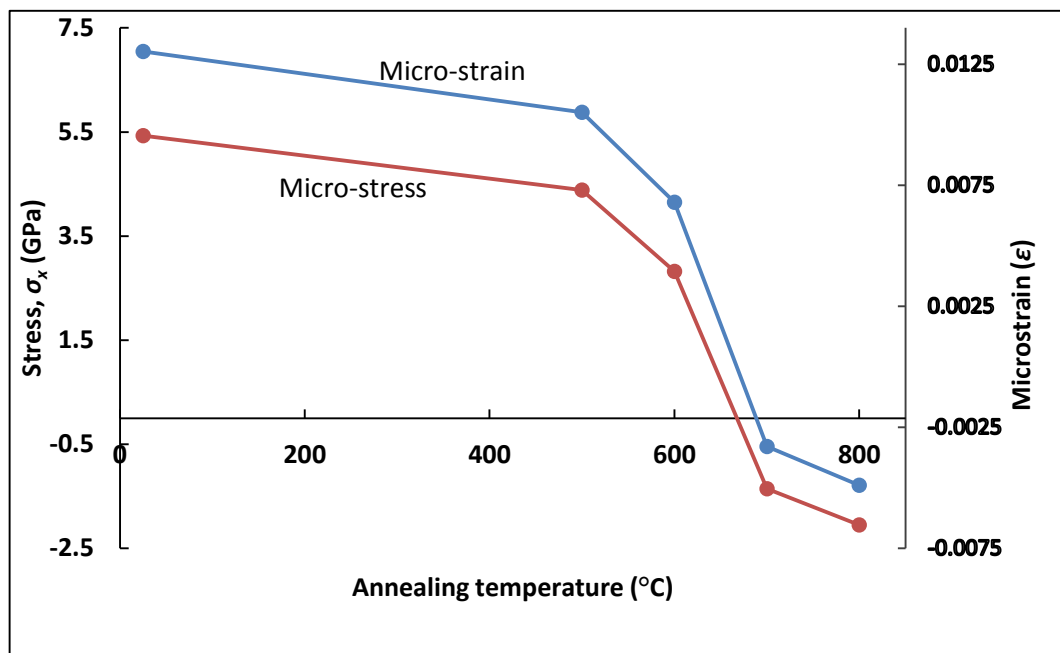
The microstrain developed within the coatings was calculated by assessing the  $d$ -spacing of CrN(111) phase using the following relation [37],

$$\varepsilon = \frac{d-d_0}{d_0} \quad (3)$$

where  $\varepsilon$  is the microstrain component, and  $d$  and  $d_0$  are the experimental and usual  $d$ -separation values, respectively. The internal residual stress,  $\sigma_x$  values were calculated using,

$$\sigma_x = \frac{E}{(1-\nu)} \times \frac{d-d_0}{d_0} \quad (4)$$

Experimentally measured values of elastic modulus and Poisson's ratios were used to estimate the internal residual stress values.



**Figure 3.** Micros stress ( $\sigma_x$ ) and microstrain ( $\varepsilon$ ) of sputtered Mo:CrN films before annealing and after annealing.

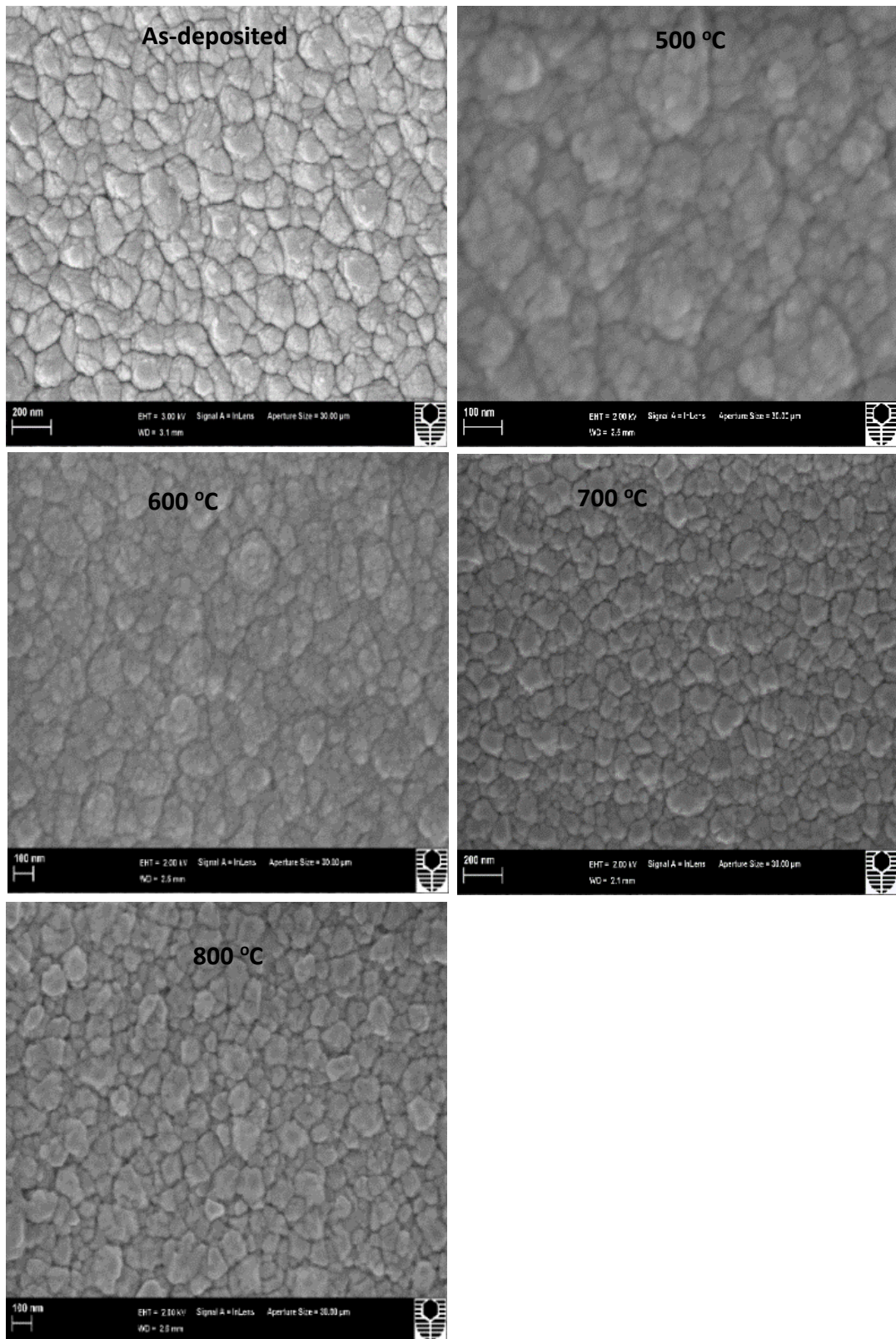
Referring to Fig. 3 and Table 1, it is seen that the microstrain in Mo:CrN structure releases gradually and smoothly, while in CrN coatings microstrains were steadily released until 600 °C and then increased abruptly at 700 and 800 °C [26]. The growth of residual stress in Mo:CrN films is associated with two mechanisms: (i) the difference in the thermal expansion coefficients between the coatings and the substrates, and (ii) the occurrence of various defects (e.g., vacancies, cracks, and disorders) around the coating surfaces. The internal stress release is also believed to be related to the absorption and annihilation of sputtering imperfections during the heat treatment cycles. Thermal treatment also results to spread the deficiencies in the Mo:CrN phase, and these defects are absorbed in the grain



boundaries. Our results are in good agreement with an earlier report [36]. The lattice microstrains and compressive residual stresses, in Mo:CrN coatings, are slightly higher than those of CrN coatings, and decreased for both coatings as the annealing progresses (see Table 1 and Fig. 3). These trends of changing the lattice constants, lattice microstrains and compressive residual stresses of Mo:CrN coatings with respect to the annealing process are consistent with the Fourier analysis diffraction peak studies reported in Ref. [38].

### **5.3.2 Morphological Features of Mo:CrN Films via FESEM Studies**

The surface morphologies of as deposited and annealed Mo:CrN coatings are shown in Fig. 4. The Mo:CrN coating showed a plane grain-like surface along with a combination together with a mixture of asymmetrical grains and insignificant aspect ratios. The grain sizes of Mo:CrN structures were estimated to fall in the range of 45 and 237 nm. These observations were consistent with an earlier FESEM measurements [39, 40]. By way of contrast, the surface features observed from the Mo:CrN coatings were different in size and shape. With the subsequent annealing procedures, the Mo:CrN surface features were transformed from as-deposited narrow and trilateral condensed assemblies to coarse and face-centered morphologies. The Cr<sub>2</sub>O<sub>3</sub> phases were seen at top coatings' layers and beyond 600 °C, the crystallite sizes were subsequently enlarged [40]. In summary, we say that key deviations in microstructural features of Mo:CrN coatings transpired at annealing beyond 600 °C [39-42].

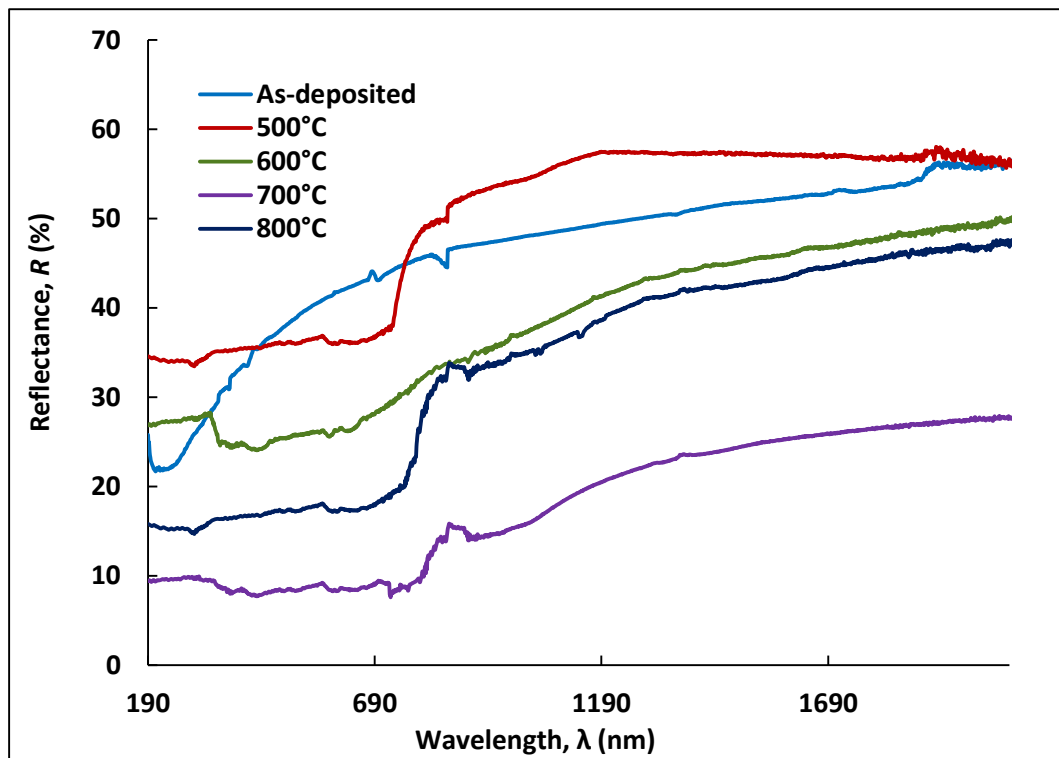


**Figure 4.** The FESEM morphological features of sputtered Mo:CrN thin films in as deposited state and after being annealed at various temperatures.

### 5.3.3 Opto-dielectric Characterizations of Mo:CrN Films

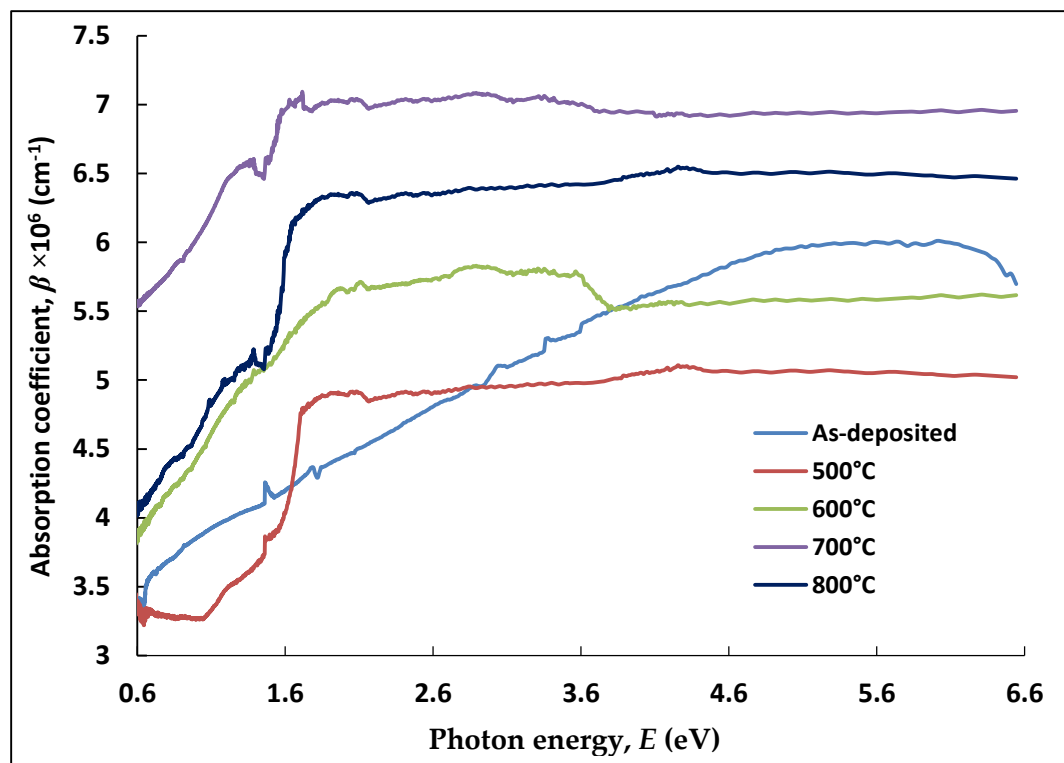
#### 5.3.3.1 UV-Vis Investigations

The reflectance data, measured in the UV-Vis range of 190-2300 nm, has been used to calculate the solar absorptance of Mo:CrN thin film coatings using Duffie-Beckman method [43-45]. Fig. 5 shows the reflectance spectra of as-deposited and annealed Mo-doped CrN thin film coatings. We have selected only four annealing steps, since they afford an optimized reflective system compared to other annealing cycles [46]. As seen in Fig. 5, in a general, the absorption edges shift towards the longer wavelength sides with the rise in annealing temperatures. Fig. 6 shows the dependence of the absorption coefficient of fabricated Mo-doped CrN coatings on annealing temperature. It is clear from Fig. 6 that, all coatings show an increase in the absorption coefficient in the visible region with increasing annealing temperature, except the film annealed at 500 °C. The maximum absorption coefficient was observed for the film annealed at 700 °C [47]. In general, it has been proposed that the reflectance behaviours of Mo-doped CrN coatings in the NIR region is governed by three factors: (i) coating thickness, (ii) the fundamental properties of coating's materials and (iii) the reflectivity of the substrate due to annealing [48, 49].



**Figure 5.** UV-Vis reflectance spectra of Mo:CrN sputtered films deposited onto silicon substrates as a function of wavelength before and after annealing.

The absorption edge of the film coated with Mo:CrN, annealed to 800 °C reaches a reasonably long wavelength at 1500 nm with lower interference peak and absorption edge than the other spectrum for annealed and as-deposited Mo:CrN coatings. These reduce the absorption value of the film coating annealed at 800 °C. The highest absorptance among the other four spectra is 86% for the film annealed at 700 °C (see Table 2). The coating annealed at 700 °C may be assumed to attain the optimum state because of its highest solar absorptance (86%) which is very encouraging comparing to the rest of the coating systems. Consequently, these coatings have a great potential of using as selective surfaces in solar energy collecting devices. We believe that the nano-grains grown during the high temperature annealing induces the formation of solid solutions (see the FESEM images). These solid solutions successfully provide with a favourable surface for incoming solar radiation to be absorbed *via* manifold reflections [50]. As such, this improves the solar absorption as a result of the interaction and relaxation mechanism in the absorber as well as multiple reflections and resonant scattering phenomena occurring around the pore/aggregate [43, 51].



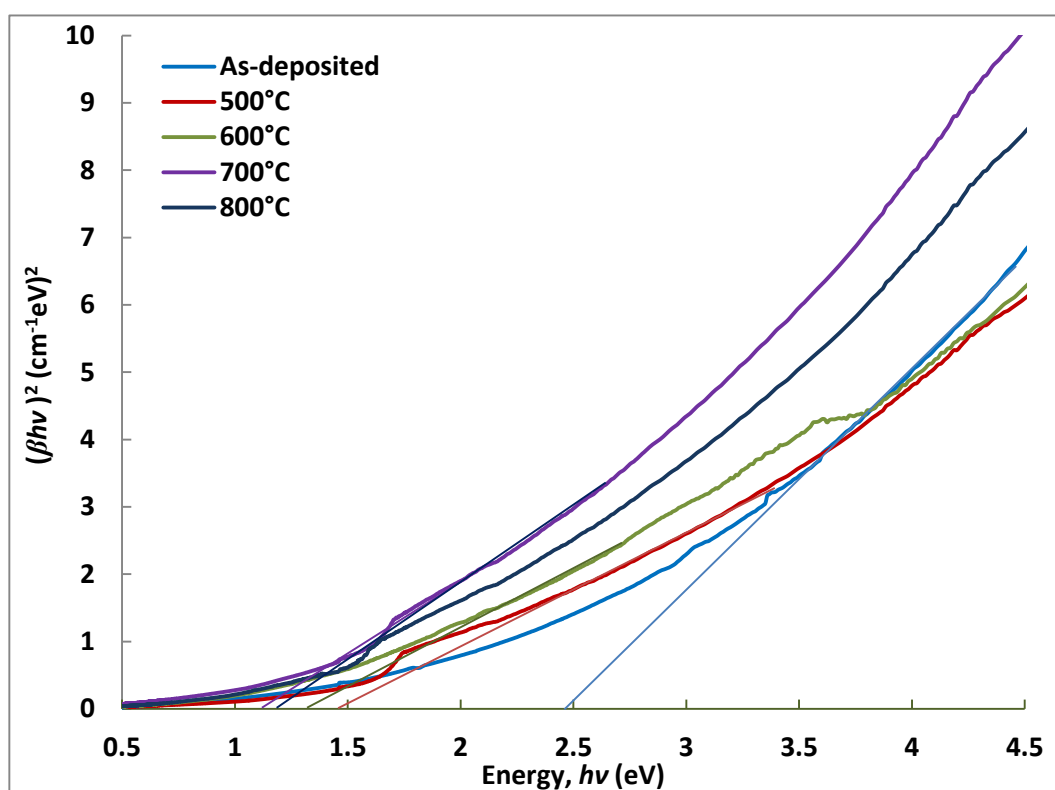
**Figure 6.** Energy dependence of the absorption coefficient of sputtered Mo:CrN films before and after annealing.

**Table 2.** Solar absorbance values of Mo:CrN coatings before and after annealing at different temperatures in air for 1 h.

Sample annealing condition (°C)	Solar absorbance, $a$ (%)
Prior-annealing	0.55
500	0.59
600	0.67
700	0.86
800	0.72

### 5.3.3.2 Optical Band-gap Analysis

The energy band-gaps of the fabricated coatings were calculated *via* Tauc plots using the following relation [44, 52-55]. Tauc plots of  $(\beta h\nu)^2$  vs  $h\nu$  of Mo:CrN coatings are shown in Fig. 7 and the corresponding energy band-gap values are tabulated in Table 3.



**Figure 7.** Tauc plots of  $(\beta h\nu)^2$  vs photon energy( $h\nu$ ) of Mo:CrN coatings before and after annealing.

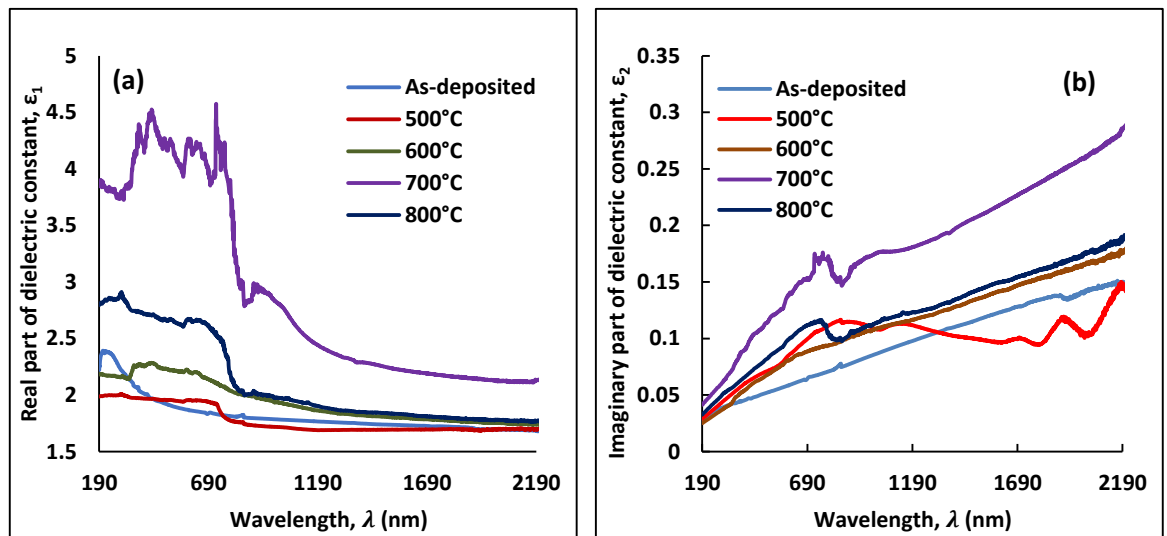
**Table 3.** Energy band-gaps of Mo:CrN coatings before and after annealing at different temperatures.

Sample annealing condition (°C)	Energy band-gap, $E_g$ (eV)
Prior-annealing	2.48
500	1.38
600	1.36
700	1.14
800	1.22

The energy band gap values of as-deposited and annealed coatings lie between 1.22 and 2.48 eV. It was found that the energy band-gap values of Mo:CrN coatings systematically decreased with increasing annealing temperatures. This band-gap study is consistent with the lattice parameter values of these coatings. The lowest value of  $E_g$  was assigned to be 1.14 eV for the films prepared at 700 °C, and it increased to 1.22 eV as the annealing increased to 800 °C. This could be related to the improvement of crystallite in the annealed coating compared to the as-deposited one. This decrease in the band-gap values is useful in enhancing the selective spectral absorption ability of Mo:CrN films. It is known that the spectral absorption of selective surfaces sturdily related to the existence of localized states in the vicinity of forbidden energy-gaps. The absorption curves provide us with the significant evidence on these localized states by indicating the existence of irregularities around the coating's surface [56].

### 5.3.3.3 Dielectric Characterizations

Figs. 8 (a) and (b) show the real and imaginary parts of the dielectric constant of Mo:CrN coatings before and after annealing.



**Figure 8.** (a) Refractive index, and (b) Extinction coefficient of Mo:CrN sputtered films deposited onto silicon substrates as a function of wavelength before and after annealing.

It is observed that in the visible and UV regions, both the real and imaginary parts of the dielectric constant values increase with increasing annealing temperatures. This may be attributed to the increase of electron density in the Mo-doped CrN thin film coatings due to Mo doping. Additionally, the improvement in the crystallinity of these coatings due to the enhancement of annealing temperature could possibly decrease both the electron scattering and the density of grain boundaries in the coatings structures, hence the trapped electrons result in increasing the density of the free-electrons [57-59]. In general, the power loss factor mainly arises from inelastic scattering routes during the charge conduction and charge transmission procedures of a dielectric medium. From Eq. 6 and Fig. 8 it can be seen that, annealing will result in an increase in both the energy loss and the energy stored in the media, which in turn will cause an increase in the absorption within the media. This is consistent with the experimental results shown in Fig. 6.

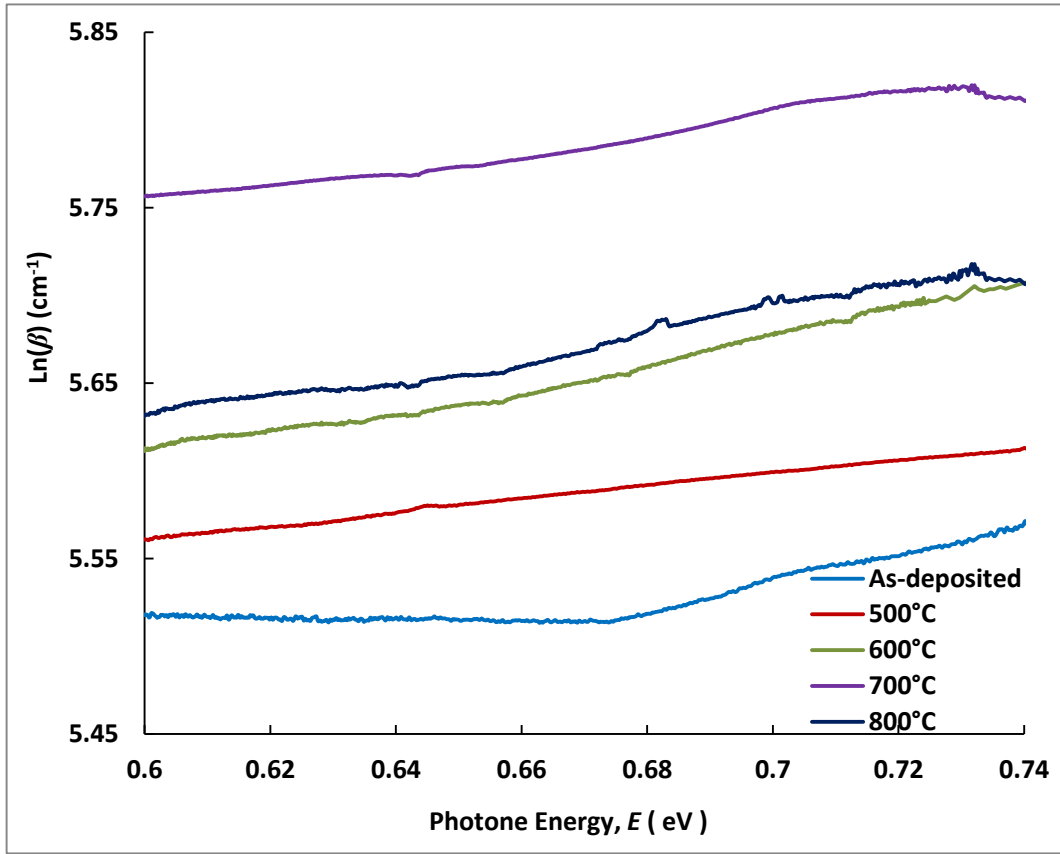
#### **5.3.3.4 Urbach Energy and Steepness Parameters**

The spectral absorption coefficient,  $\beta$  strongly depends on the photon energy,  $h\nu$  on the presence of localized states around the band gap. The relationship between  $\beta$  and  $h\nu$  is known as Urbach empirical rule. According to Tauc's theory the density of these states fall off exponentially with the photon energy by the following relation [56, 60]:

$$\beta = \beta_o \exp\left(\frac{h\nu}{E_U}\right) \quad (5)$$

$$\ln \beta = \ln \beta_o + \left(\frac{h\nu}{E_U}\right) \quad (6)$$

where  $\beta_o$  is a constant,  $h\nu$  is the incident photon energy and  $E_U$  is the Urbach energy. The behaviour of  $\ln\beta$  as a function of photon energy near the absorption edge of Mo:CrN coatings before and after annealing is outlined in Fig. 9. The slope of the tangent straight lines leads to determine the Urbach energy,  $E_U$  of CrMoN films. Fig. 10 illustrates the variations of Urbach energy of CrMoN before and after annealing, and the corresponding values are recorded in Table 4.



**Figure 9.** Photon energy dependence of  $\ln(\beta)$  of Mo:CrN sputtered films before and after annealing.

From Fig. 10, it is observed that  $E_U$  values are deliberately decreased with the increase in annealing temperatures. This is in accordance with the previous results reported by Rahman *et al.* and Xue *et al.* [56, 61]. The reduction of Urbach energy values is associated with a few factors: reduction of the localized density of states around the tails of the absorption edges, and increase in degree of crystallinity of these coatings, and coatings quality enhancements. Urbach band tail studies of these coatings is also found to be -consistent with the energy band-gap studies, where  $E_g$  values were also dwindled with the gradual rise annealing temperatures.

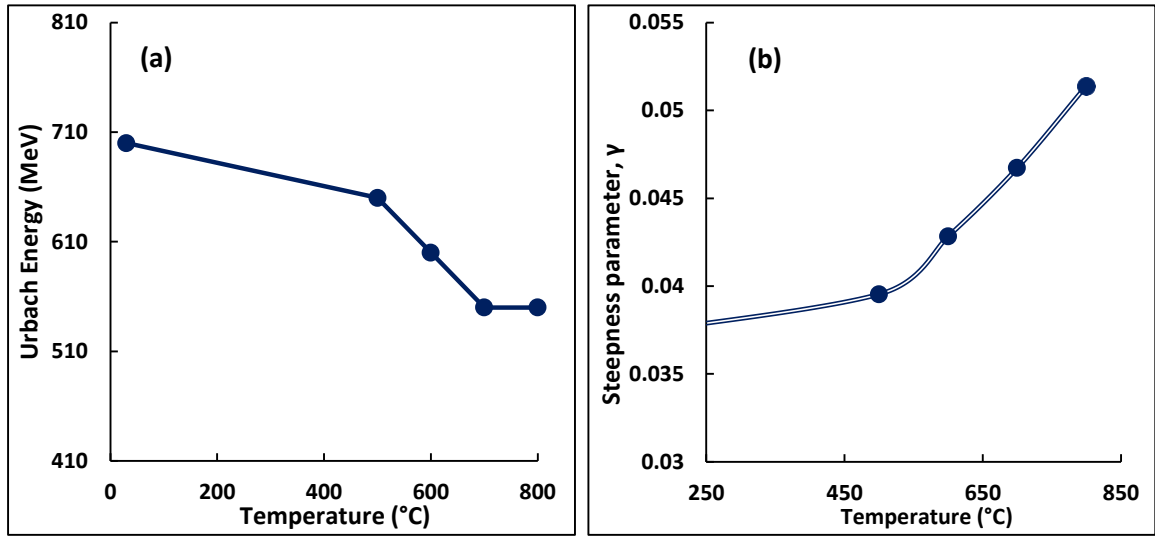
According to Tauc's theory, absorption density of these states related exponentially with the photon energy by the following relation,

$$\beta = \beta_o \exp\left(\frac{\gamma h\nu}{K_B T}\right) \quad (7)$$

where  $\gamma$  is a constant known as the steepness parameter. Combing Eqs. (8) and (10), the steepness parameter,  $\gamma$  can be expressed as,



$$\gamma = \frac{K_B T}{h\nu} \quad (8)$$



**Figure 10.** Annealing temperature dependence of (a) Urbach energy, and (b) steepness parameter of Mo:CrN sputtered films on silicon substrates before and after annealing.

Using above relation, the steepness parameters,  $\gamma$  of Mo:CrN coatings were estimated and tabulated in Table 4. From the steepness parameter plots, of Mo:CrN coatings, before and after annealing it could be observed that the steepness of the Urbach tails behave in an opposite manner to the Urbach energy dependence of annealing temperatures. The steepness parameter of Mo:CrN coatings is gradually increased with the increase of annealing temperatures.

**Table 4.** Urbach energy values and steepness parameters of Mo:CrN coatings before annealing and at different annealing temperatures.

Annealing temperature (°C)	Urbach energy, $E_U$ (meV)	Steepness parameter, $\gamma$
As-deposited	700	0.0367
500	650	0.0395
600	600	0.0428
700	550	0.0467
800	550	0.0514

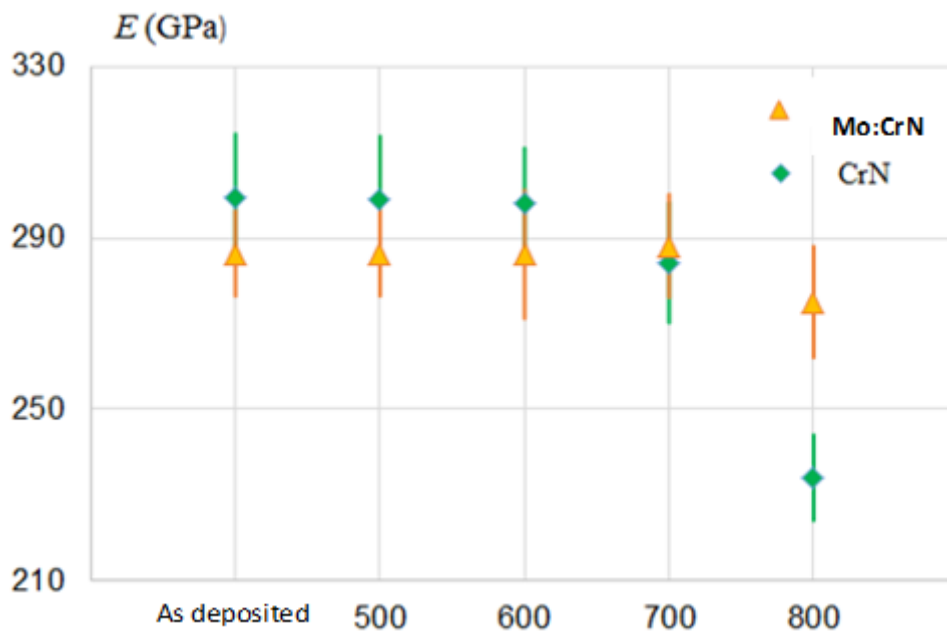
As a result, the degree of crystallinity of Mo:CrN coatings is enhanced. Steepness parameters are also found to be in consistent with other results such as energy band-gaps, and Urbach energy. Generally, the optical band structure and optical transition s are strongly affected by the width of the localized states around the band gaps of the coatings [56, 60]. Referring to Tauc's theory (Eq. 5), the coefficient of absorption around the absorption edge

exponentially depends on  $h\nu$  and follow's the Urbach law. Interactions between lattice vibrations and localized states in tail of the coatings band-gap have significant impacts on the optical properties of these coatings.

### 5.3.4 Mechanical Characterizations of Mo:CrN Films: Nanoindentation and Finite Element Modeling

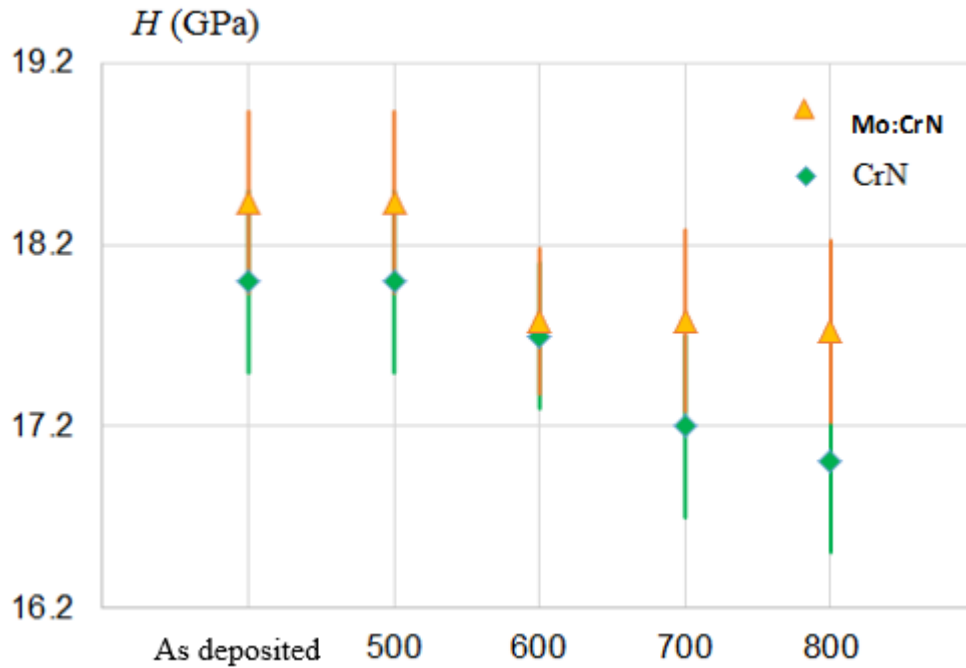
#### 5.3.4.1 Nanoindentation Results

The indentation results of Young's modulus  $E$  and hardness  $H$  are shown in Fig. 11 and Fig. 12, respectively. The elastic modulus  $E$  varied within a narrow range of 275-290 GPa. No significant changes were identified for the Mo:CrN coatings before and after annealing up to 700 °C, while a drop in  $E$  about 5% was observed for the sample annealed at 800 °C.



**Figure 11.** Elastic modulus plots for the Mo:CrN samples, as deposited, and annealed at 500, 600, 700, and 800 °C, respectively. The CrN data from our previous work [27] is also included for comparison purpose.

As such, annealing has less influence on the Young's modulus of the Mo:CrN samples, compared to that on the  $E$  value of the CrN sample which had a 22% drop after 800 °C heat treatment [26]. Variation of the hardness  $H$  of Mo:CrN film with annealing temperature is within the range of 17.7 – 18.5 GPa, as indicated in Fig. 12, showing a ~4% decrease after annealing. This is compared to an 8% decrease for the CrN sample. This trend, *i.e.*, both  $E$  and  $H$  will decrease after annealing, is consistent with previous studies for different samples [26, 62, 63].



**Figure 12.** Hardness plots for the Mo:CrN sputtered films as-deposited, and annealed at 500, 600, 700, and 800 °C, respectively. The CrN data from our previous work [27] is also included for comparison purpose.

#### 5.3.4.2 Finite Element Modeling (FEM)

In this work, Comsol Multiphysics software was used as the modeling tool to simulate the intensity and distribution of load induced stress within different coatings materials and configurations. Note that in the following sections the phrase “load induced stress” is adapted in order to differentiate from “residual stress”, the former referring the stress gained during the sputtering process, while the latter is induced by an artificial load during modelling process to evaluate the load carrying capability of the coating layer. A 2D axial symmetry model was constructed, with a spherical indenter (5  $\mu\text{m}$  radius) at the top of Mo:CrN coating layers with different thicknesses. The objective is to evaluate the magnitude and distribution of the load induced stress within the film, as well as the influence of the film thickness and the type of substrate on the integrity of the film-substrate system. The coating layers with different thickness were modeled, and they were built on four different types of substrate: silica, silicon 100, silicon 110, and steel, which are the typical scenarios of real industrial applications. Further details of modeling, including geometry and meshing generation *etc.*, have been given in our previous works [26, 30].

The elastic moduli obtained from our nanoindentation work were used for the coating layer. Parameters for films obtained from the nanoindentation results, as well as the parameters of

substrate and the indenter, are given in Table 5. Note that the steel substrate is modelled as linear plasto-elastic material, with yield strength of 0.675 GPa, and an isotropic tangent modulus of 1.7 GPa [30].

Frequently the load carrying capability of the films is assessed by the equivalent stress, or von Mises stress, labelled as  $\sigma_{equiv}$ . This is a measure of the “severity” of the of load induced stress, or an assessment of the potential damage it could cause, and can be expressed by,

$$\sigma_{equiv} = \left\{ 0.5 \left[ (\sigma_{xx} - \sigma_{yy})^2 + (\sigma_{yy} - \sigma_{zz})^2 + (\sigma_{zz} - \sigma_{xx})^2 + (\sigma_{xy} + \sigma_{yz} + \sigma_{zx})^2 \right] \right\}^{1/2} \quad (9)$$

where  $\sigma_{xx}$ ,  $\sigma_{yy}$ ,  $\sigma_{zz}$ ,  $\sigma_{xy}$ ,  $\sigma_{yz}$ ,  $\sigma_{zx}$  are the corresponding stress tensor components, respectively.

**Table 5.** Modeling parameters of substrate, indenter and interlayer [20].

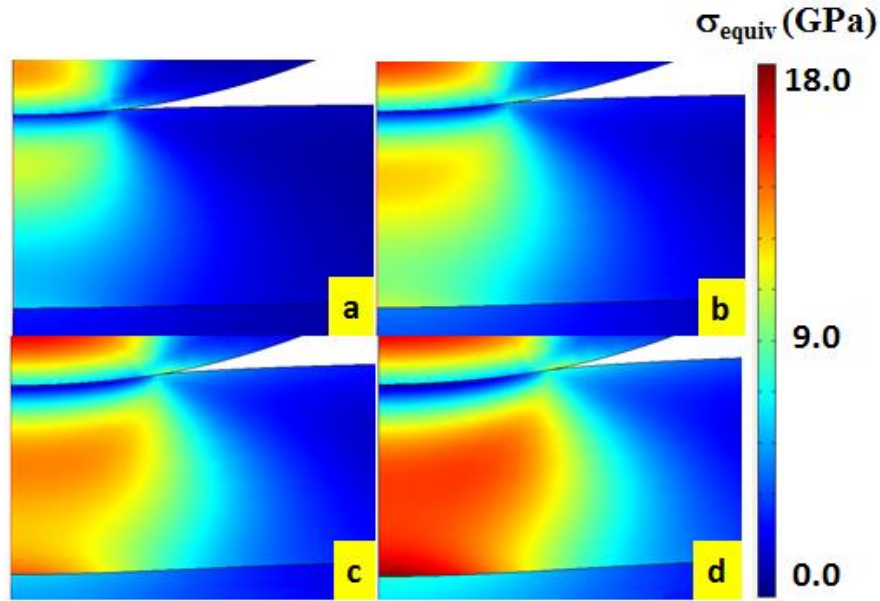
Samples name	Young's modulus, E (GPa)	Poisson's ratio	Yield strength (GPa)	BH (GPa)
Steel	200	0.3	675	1.7
Silicon (111)	200	0.25	-	-
Silica	80	0.25	-	-
Cr	200	0.3	700	1.7
Indenter (diamond)	1141	0.07	-	-

Frequently the load carrying capability of the films is assessed by the equivalent stress, or von Mises stress, labelled as  $\sigma_{equiv}$ . This is a measure of the “severity” of the stress, or an assessment of the potential damage it could cause, and can be expressed by,

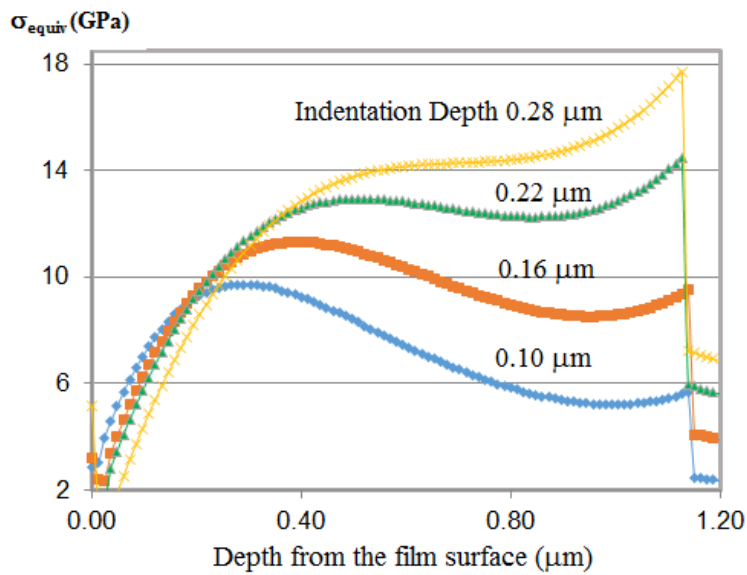
$$\sigma_{equiv} = \left\{ 0.5 \left[ (\sigma_{xx} - \sigma_{yy})^2 + (\sigma_{yy} - \sigma_{zz})^2 + (\sigma_{zz} - \sigma_{xx})^2 + (\sigma_{xy} + \sigma_{yz} + \sigma_{zx})^2 \right] \right\}^{1/2} \quad (16)$$

where  $\sigma_{xx}$ ,  $\sigma_{yy}$ ,  $\sigma_{zz}$ ,  $\sigma_{xy}$ ,  $\sigma_{yz}$ ,  $\sigma_{zx}$  are the corresponding stress tensor components, respectively.

Similar to our previous results on the CrN films [26], two primary high stress concentrations in the coating layer were identified, one is close to the indenter, and the other is at the interface between the coating and the substrate. With the increase in indentation depth, the stress maximum moves downwards towards the interface between the coating and the substrate (See Figs. 13 and 14). Furthermore, during this process the intensity of shear stress also increased. These may be considered as a primary cause of lateral delamination and cracks [64].

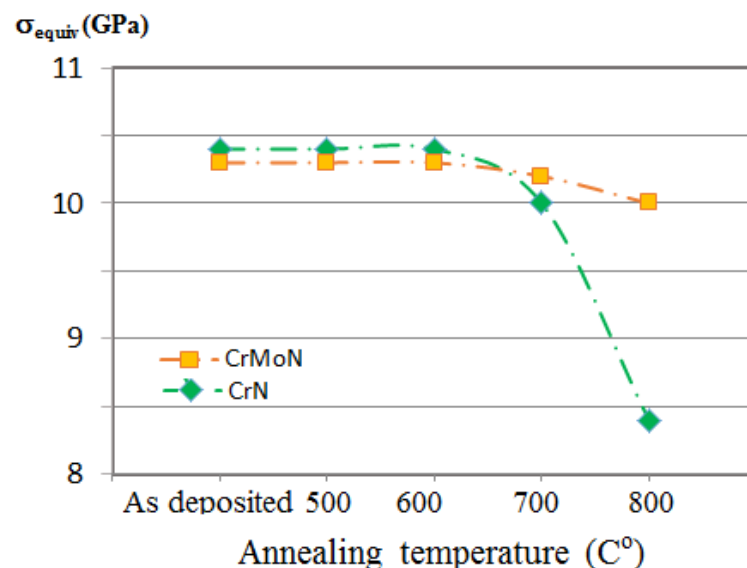


**Figure 13.** FE modeling results of equivalent stress distribution in the as-deposited Mo:CrN film (1.2  $\mu\text{m}$ ) on silica substrate, at different indentation depth. (a) indentation depth 0.1  $\mu\text{m}$ , (b) indentation depth 0.16  $\mu\text{m}$ , (c) indentation depth 0.22  $\mu\text{m}$ , and (d) indentation depth 0.28  $\mu\text{m}$ .



**Figure 14.** FE modeling results of equivalent stress distribution within 1.2  $\mu\text{m}$  Mo:CrN film on silica substrate, at different indentation depth. The stress is plotted along the symmetrical axis which is the straight vertical line through the indenter-film contact point, and starting from the surface of the film downwards.

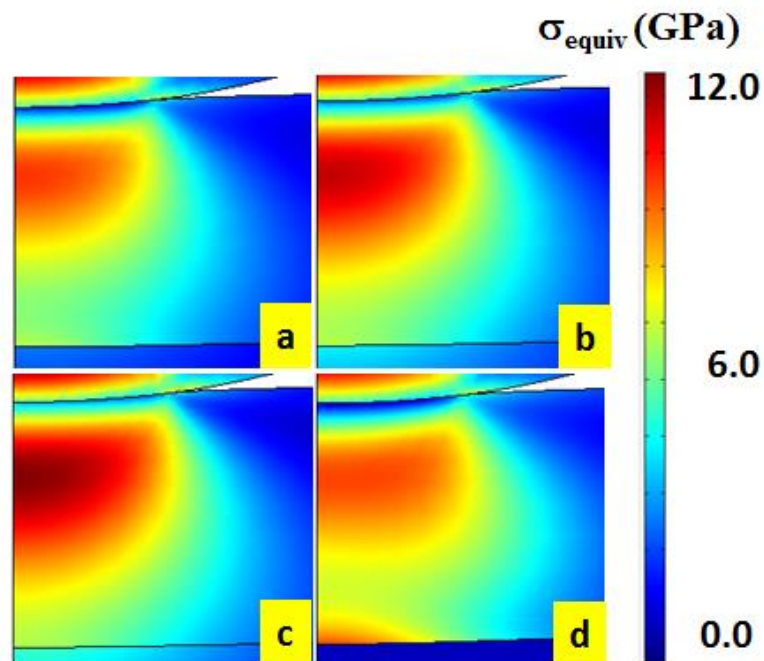
Fig. 15 shows a comparison of the maximum equivalent stress in the as-deposited and annealed Mo:CrN coatings. As expected, at the same indentation depth, higher stress levels will be induced within “harder” materials, or materials with a higher Young’s modulus. After samples are annealed, the modulus will normally decrease hence the stress level will also decrease. Compared to CrN films, less reduction in the stress level is seen in the Mo:CrN, due to the fact that, after annealing the decrease in the modulus within the latter is smaller. In this report the influence of the different substrate materials, as well as the film thickness, on the stress distributions within the film is also analysed through FEM modeling works. Figs. 16 and 17 show a comparison of stress distribution within the CrMoN film when it is deposited onto different substrate materials. From the results two important points could be noted. Firstly, softer substrate materials help alleviate the stress level within the films– at the same indentation depth lower stress levels are observed in the film on silica substrate, which has a small Young’s modulus. High stress levels are seen in the Si(100) and Si(110), which have higher Young’s moduli [65]. Secondly, within a film deposited onto a plasto-elastic substrate (such as most metals), stress tends to concentrate towards the interface between the film and the substrate, which has a detrimental effect on the integrity of the coating.



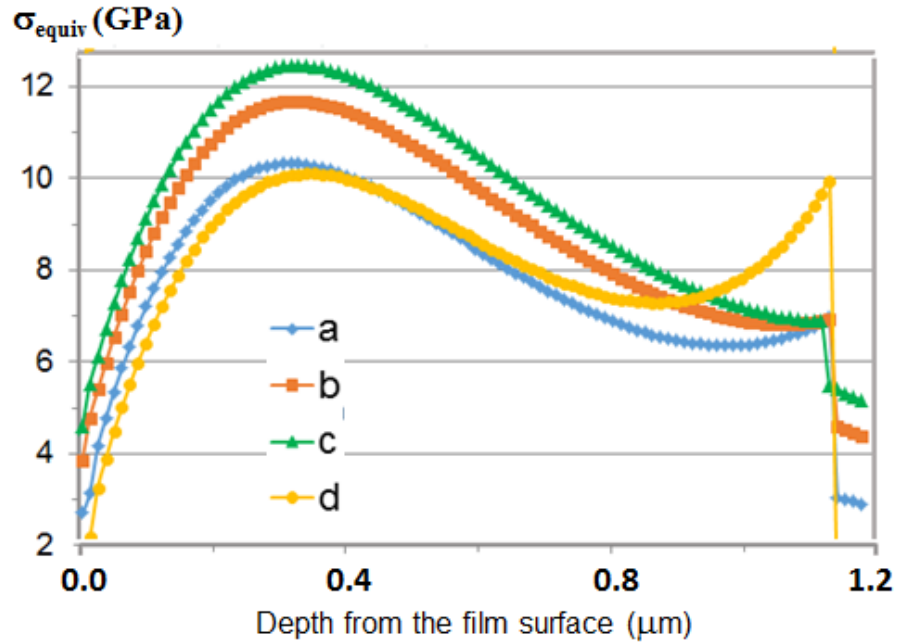
**Figure 15.** The modeling results of maximum equivalent stress within the 1.2 μm Mo:CrN coating on silicon substrate, at an indentation depth of 0.12 μm, before and after annealing at 500, 600, 700, and 800 °C, respectively.

The distributions of load induced stress in films with different thickness are shown in Figs. 18 and 19. The loading depth  $d$  modelled here is 0.3 μm, and the thickness of the films,  $t$ ,

varies between 1 ~ 2  $\mu\text{m}$ . So the ratio  $d/t$  % varies from 30% - 15%. Within a thin film of 1.0  $\mu\text{m}$  the highest stress, ~ 20 GPa, appear at the interface between the film and the substrate. With the increase of the film thickness the stress level decreases, and the maximum moves upwards away from the interface. For the 1.4  $\mu\text{m}$  film, the maximum stress level reduced to ~ 15 GPa. Further increase of the film thickness will completely remove the stress concentration at the interface (Figs. 18 and 19). Stress concentration near the interface is the primary cause for the damage at the film-substrate interface, resulting in delamination, or lateral crack [30, 64]. Under the same loading, stress concentration tends to move away from the interface, reducing the possibility of delamination.



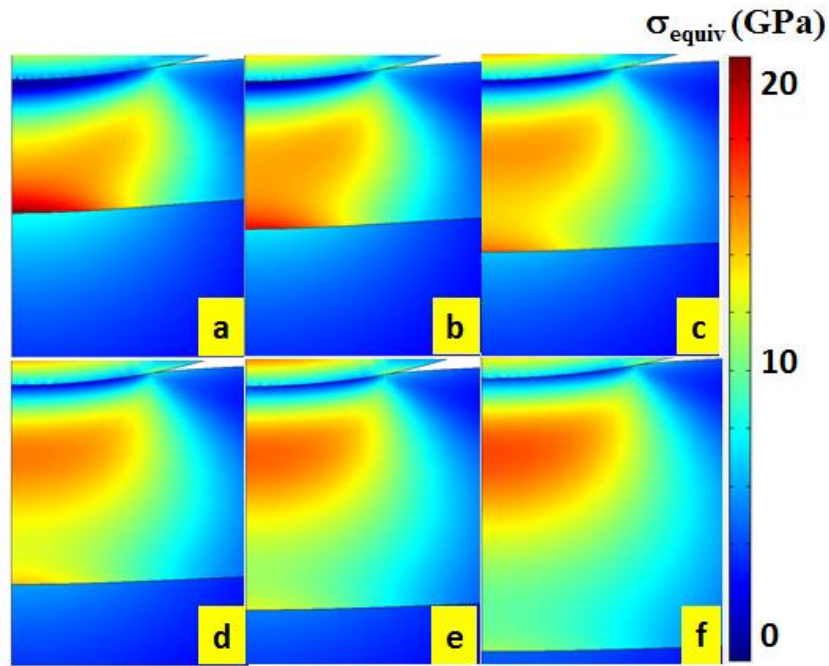
**Figure 16.** Finite element modeling results of equivalent stress distribution within 1.2  $\mu\text{m}$  Mo:CrN films at an indentation depth of 0.12  $\mu\text{m}$ . (a) silica substrate, (b) silicon (100) substrate, (c) silicon (110) substrate, and (d) steel substrate.



**Figure 17.** FE modeling results of equivalent stress distribution within 1.2  $\mu\text{m}$  Mo:CrN film on different type of substrate. The stress is plotted along the symmetrical axis which is the straight vertical line through the indenter-film contact point, and starting from the surface of the film downwards: (a) silica substrate, (b) silicon (100) substrate, (c) silicon (110) substrate, and (d) steel substrate.

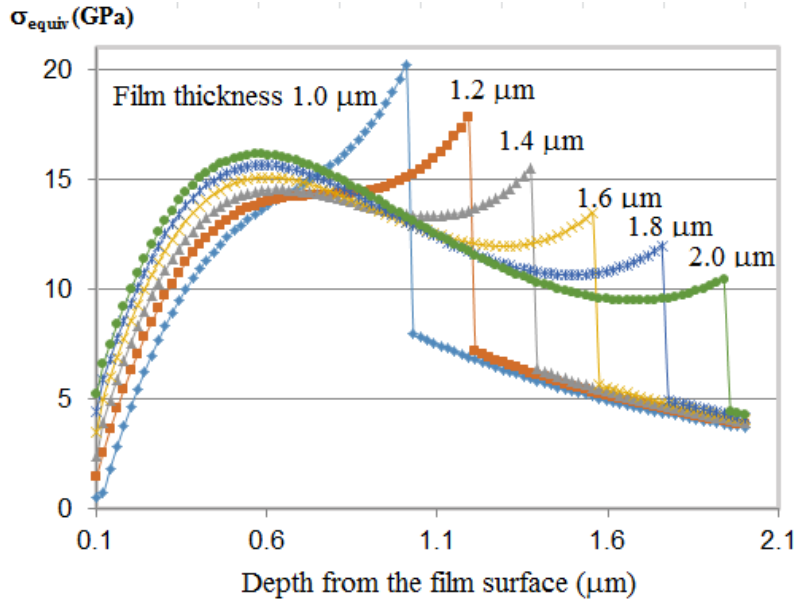
The distributions of load induced stress in films with different thickness are shown in Figs. 18 and 19. The loading depth  $d$  modelled here is 0.3  $\mu\text{m}$ , and the thickness of the films,  $t$ , varies between 1 ~ 2  $\mu\text{m}$ . So the ratio  $d/t$  % varies from 30% - 15%. Within a thin film of 1.0  $\mu\text{m}$  the highest stress, ~ 20 GPa, appear at the interface between the film and the substrate. With the increase of the film thickness the stress level decreases, and the maximum moves upwards away from the interface. For the 1.4  $\mu\text{m}$  film, the maximum stress level reduced to ~ 15 GPa. Further increase of the film thickness will completely remove the stress concentration at the interface (Figs. 18 and 19). Stress concentration near the interface is the primary cause for the damage at the film-substrate interface, resulting in delamination, or lateral crack [30, 64]. Under the same loading, stress concentration tends to move away from the interface, reducing the possibility of delamination.





**Figure 18.** Modeling results of equivalent stress distribution within Mo:CrN coating of different thickness and on Si 100 substrate. The indenter depth is set to 0.3  $\mu\text{m}$ : (a) 1.0  $\mu\text{m}$ , (b) 1.2  $\mu\text{m}$ , (c) 1.4  $\mu\text{m}$ , (d) 1.6  $\mu\text{m}$ , (e) 1.8  $\mu\text{m}$ , and (f) 2.0  $\mu\text{m}$ .

As a short summary, the hardness and elastic modulus of the as-deposited Mo:CrN film were evaluated as 18.4 GPa and 287 GPa, respectively, from the indentation results (see Table 6). Annealing at a temperature below 600  $^{\circ}\text{C}$  does not affect  $H$  and  $E$ , but 800  $^{\circ}\text{C}$  annealing reduces both the  $H$  and  $E$  values by  $\sim 4\%$ . Compared to those of CrN films, the mechanical properties of Mo:CrN films show better resistance to heat treatment [26]. Dongli Qi *et al.* [19] have reported that *via* nano-indentation measurements, CrMoN film coatings hardness  $H$  and effective elastic modulus  $E^*$  have increased gradually with the increasing of sputtering temperature  $T_s$  from 100 to 300  $^{\circ}\text{C}$ .



**Fig. 19.** FE modeling results of equivalent stress distribution within Mo:CrN films with different thickness and on silica substrate. The stress is plotted along the symmetrical axis from the surface of the film downwards, the indenter depth is set to 0.3  $\mu\text{m}$ .

**Table 6.** Elastic modulus of the Mo:CrN films, derived from the indentation data [23].

Annealing temperature ( $^{\circ}\text{C}$ )	Elastic modulus, $E$ (GPa)	Hardness, $H$ (GPa)
As-deposited	287	18.4
500	287	18.4
600	284	17.7
700	288	17.7
800	274	17.5

Under the same loadings, the stress levels will be reduced after the films are annealed. Stress level and distribution will change when different type of substrate is used. Substrate with higher elastic modulus will induce higher level of stress within the coatings. Using metal substrate with plasto-elastic properties could increase the possibility of delamination under loading, due to heavy local deformation immediately underneath the interface between the film and the substrate. On the other hand, increasing the thickness of the film will reduce or even remove the stress concentration at the interface, which help reduce the possibility of delamination, and keep the integrity of the coating layer.

## 5.4 Conclusions

An investigation of the structural evolution, morphological studies, optical analysis, and mechanical properties of as-deposited and annealed Mo:CrN thin film coatings were conducted. Face-centered cubic CrN structure was established *via* XRD studies. A steady

decrease in lattice constants was noticed, while there was gradual increase in crystallite sizes with the rise in annealing temperatures. UV-Vis analysis has established a good consistency between the spectral absorptance features, optical band-gaps, Urbach energy and steepness parameter results of these coatings both before and after annealing. Experimental results showed that as the annealing temperature increased up to 700 °C, there were an increase in the solar absorptance, and a decrease in the optical band-gap in the Mo:CrN film. The nanoindentation studies shown that the film's hardness, and the elastic modulus values also strongly depends on the microstructural features, grain modification, and compressive residual stress of these coatings. The inverse relationship between the films' hardness and grain size of thin film materials were also confirmed. It is suggested that the formation of nanograins and amorphous phases after the heat treatment has governed thin film hardness and elastic modulus values. However, we were unable to achieve the super-hardness with these films. The amorphous layers generated at the grain boundaries, during the high temperature annealing, noticeably reduces the mechanical strength and physical hardness of Mo:CrN thin film coatings. The amorphous layers formed are basically believed to develop films stability by impeding the atomic distributions during the high temperature applications. Finite element modeling suggested that softer substrate materials help alleviate the stress level within the films– at the same indentation depth lower load induced stress levels are observed in the film on a silica substrate. It is also believed that within a coating deposited onto a metal substrate, load induced stress tends to concentrate towards the interface between the coatings and the substrate.

## References

- [1] X. Nie, A. Leyland, A. Matthews, *Surface and Coatings Technology*, 133–134 (2000) 331-337.
- [2] G. Li, P. Deshpande, J.H. Li, R.Y. Lin, *Tsinghua Science and Technology*, 10 (2005) 690-698.
- [3] A. Kumar, H.L. Chan, J.J. Weimer, L. Sanderson, *Thin Solid Films*, 308-309 (1997) 406-409.
- [4] E. Zalnezhad, A.A.D.M. Sarhan, M. Hamdi, *International Journal of Precision Engineering and Manufacturing*, 14 (2013) 467-473.
- [5] S. PalDey, S.C. Deevi, *Materials Science and Engineering A*, 342 (2003) 58-79.
- [6] G. Abadias, *Surface and Coatings Technology*, 202 (2008) 2223-2235.
- [7] J.Y. Cheong, X.Z. Ding, B.K. Tay, X.T. Zeng, *Key Engineering Materials*, 2010, pp. 725-729.

- [8] S.R. Pulugurtha, D.G. Bhat, M.H. Gordon, J. Shultz, M. Staia, S.V. Joshi, S. Govindarajan, *Surface and Coatings Technology*, 202 (2007) 1160-1166.
- [9] J. Musil, Hard nanocomposite coatings: Thermal stability, oxidation resistance and toughness, *Surface and Coatings Technology*, 207 (2012) 50-65.
- [10] X. Guan, Y. Wang, G. Zhang, J. Xin, L. Wang, Q. Xue, *RSC Advances*, 6 (2016) 87003-87012.
- [11] P.Z. Shi, J. Wang, C.X. Tian, Z.G. Li, G.D. Zhang, D.J. Fu, B. Yang, *Surface and Coatings Technology*, 228 (2013) S534-S537.
- [12] L. Lu, Q.M. Wang, B.Z. Chen, Y.C. Ao, D.H. Yu, C.Y. Wang, S.H. Wu, K.H. Kim, *Transactions of Nonferrous Metals Society of China (English Edition)*, 24 (2014) 1800-1806.
- [13] H.N. Shah, R. Jayaganthan, A.C. Pandey, *Materials and Design*, 32 (2011) 2628-2634.
- [14] Z. Wu, F. Zhou, Q. Ma, Q. Wang, Z. Zhou, L. Kwok-Yan Li, *RSC Advances*, 6 (2016) 76724-76735.
- [15] N. Bagcivan, K. Bobzin, S. Theiß, *Thin Solid Films*, 528 (2013) 180-186.
- [16] S. Tan, X. Zhang, X. Wu, F. Fang, J. Jiang, *Applied Surface Science*, 257 (2011) 5595-5600.
- [17] P. Panjan, A. Drnovšek, J. Kovač, P. Gselman, T. Bončina, S. Paskvale, M. Čekada, D. Kek Merl, M. Panjan, *Thin Solid Films*, 591 (2015) 323-329.
- [18] E. Bemporad, C. Pecchio, S. De Rossi, F. Carassiti, *Surface and Coatings Technology*, 188-189 (2004) 319-330.
- [19] D. Qi, H. Lei, T. Wang, Z. Pei, J. Gong, C. Sun, *Journal of Materials Science & Technology*, 31 (2015) 55-64.
- [20] E.Y. Choi, M.C. Kang, D.H. Kwon, D.W. Shin, K.H. Kim, *Journal of Materials Processing Technology*, 187-188 (2007) 566-570.
- [21] Y. Benlatreche, C. Nouveau, I. Rahil, R. Marchai, L. Chekour, *Plasma Processes and Polymers*, 6 (2009) S135-S140.
- [22] S. Jeong Heo, S.-W. Kim, I.-W. Yeo, S.-J. Park, Y.-S. Oh, *Ceramics International*, 42 (2016) 5231-5237.
- [23] Z.B. Qi, B. Liu, Z.T. Wu, F.P. Zhu, Z.C. Wang, C.H. Wu, *Thin Solid Films*, 544 (2013) 515-520.
- [24] K. Ho Kim, E. Young Choi, S. Gyun Hong, B. Gyu Park, J. Hong Yoon, J. Hae Yong, *Surface and Coatings Technology*, 201 (2006) 4068-4072.
- [25] K. Ibrahim, M. Mahbubur Rahman, H. Taha, E. Mohammadpour, Z. Zhou, C.-Y. Yin, A. Nikoloski, Z.-T. Jiang, *Applied Surface Science*, 440 (2018) 1001-1010.

- [26] K. Ibrahim, M.M. Rahman, X. Zhao, J.-P. Veder, Z.-f. Zhou, E. Mohammadpour, R.H. Majeed, A.N. Nikoloski, Z.-T. Jiang, *Journal of Alloys and Compounds*, 750 (2018) 451-464.
- [27] T. Boström, E. Wäckelgård, G. Westin, *Solar Energy*, 74 (2003) 497-503.
- [28] J. Liang, Y. Huang, J. Oh, M.S.D. Kozolv, R. Baughman, Y. Ma, *Adv. Funct. Mater.*, 21 (2011) 3778.
- [29] Z. Li, P. Munroe, Z.T. Jiang, X. Zhao, J. Xu, Z.F. Zhou, J.Q. Jiang, F. Fang, Z.H. Xie, *Acta Materialia*, 60 (2012) 5735-5744.
- [30] X. Zhao, Z. Xie, P. Munroe, *Materials Science and Engineering: A*, 528 (2011) 1111-1116.
- [31] A. Gilewicz, B. Warcholinski, *Surface and Coatings Technology*, 279 (2015) 126-133.
- [32] T.K. Tsai, Y.H. Li, J.S. Fang, *Thin Solid Films*, 615 (2016) 91-96.
- [33] C. Zou, L. Huang, J. Wang, S. Xue, *Solar Energy Materials and Solar Cells*, 137 (2015) 243-252.
- [34] L. Wang, X. Nie, *Journal of Materials Engineering and Performance*, 23 (2013) 560-571.
- [35] A.L. Patterson, *Physical Review*, 56 (1939) 978-982.
- [36] E. Mohammadpour, Z.-T. Jiang, M. Altarawneh, N. Mondinos, M.M. Rahman, H.N. Lim, N.M. Huang, Z. Xie, Z.-f. Zhou, B.Z. Dlugogorski, *RSC Advances*, 7 (2017) 22094-22104.
- [37] J.B. Cohen, I.C. Noyan, *Residual Stresses: Measurement by Diffraction and Interpretation*, Springer Verlag New York, USA, 1987.
- [38] L. Cunha, L. Rebouta, F. Vaz, M. Staszuk, S. Malara, J. Barbosa, P. Carvalho, E. Alves, E. Le Bourhis, P. Goudeau, J.P. Rivière, *Vacuum*, 82 (2008) 1428-1432.
- [39] D. Yuelan, Z. Ping, C. Zhihai, Y. Zhen, L. Qi, S. Wei, *Rare Metal Materials and Engineering*, 43 (2014) 264-268.
- [40] J. Mougín, T. Le Bihan, G. Lucazeau, *Journal of Physics and Chemistry of Solids*, 62 (2001) 553-563.
- [41] F.H. Lu, H.Y. Chen, C.H. Hung, *Surfaces and Films*, 21 (2003) 671-675.
- [42] H.Y. Chen, F.H. Lu, *Thin Solid Films*, 515 (2006) 2179-2184.
- [43] W. Piskorz, F. Zasada, P. Stelmachowski, A. Kotarba, Z. Sojka, *Catalysis Today*, 137 (2008) 418-422.
- [44] M.M. Rahman, Z.-T. Jiang, Z.-f. Zhou, Z. Xie, C.Y. Yin, H. Kabir, M.M. Haque, A. Amri, N. Mondinos, M. Altarawneh, *Journal of Alloys and Compounds*, 671 (2016) 254-266.

- [45] H.A. Miran, M.M. Rahman, Z.-T. Jiang, M. Altarawneh, L.S. Chuah, H.-L. Lee, E. Mohammedpur, A. Amri, N. Mondinos, B.Z. Dlugogorski, *Journal of Alloys and Compounds*, 701 (2017) 222-235.
- [46] A. Amri, X. Duan, C.-Y. Yin, Z.-T. Jiang, M.M. Rahman, T. Pryor, *Applied Surface Science*, 275 (2013) 127-135.
- [47] M.M. Rahman, Z.-T. Jiang, P. Munroe, L.S. Chuah, Z.-f. Zhou, Z. Xie, C.Y. Yin, K. Ibrahim, A. Amri, H. Kabir, M.M. Haque, N. Mondinos, M. Altarawneh, B.Z. Dlugogorski, *RSC Advances*, 6 (2016) 36373-36383.
- [48] A. Amri, Z.T. Jiang, T. Pryor, C.Y. Yin, Z. Xie, N. Mondinos, *Surface and Coatings Technology*, 207 (2012) 367-374.
- [49] P.W. De Oliveira, C. Becker-Willinger, M.H. Jilavi, *Advanced Engineering Materials*, 12 (2010) 349-351.
- [50] E. Ienei, L. Isac, C. Cazan, A. Duta, *Solid State Sciences*, 12 (2010) 1894-1897.
- [51] M.E. Rincón, J.D. Molina, M. Sánchez, C. Arancibia, E. García, *Solar Energy Mater Solar Cells*, 91 (2007) 1421-1425.
- [52] M.S. Hossain, H. Kabir, M.M. Rahman, K. Hasan, M.S. Bashar, M. Rahman, M.A. Gafur, S. Islam, A. Amri, Z.-T. Jiang, M. Altarawneh, B.Z. Dlugogorski, *Applied Surface Science*, 392 (2017) 854-862.
- [53] H. Kabir, M.M. Rahman, T.S. Roy, A.H. Bhuiyan, *International Journal of Mechanical and Mechatronics Engineering*, 12 (2012) 30-34.
- [54] A. Millar, M.M. Rahman, Z.-T. Jiang, *Journal of Advanced Physics*, 3 (2014) 179-193.
- [55] M.M. Rahman, Z.-T. Jiang, C.-Y. Yin, L.S. Chuah, H.-L. Lee, A. Amri, B.-M. Goh, B.J. Wood, C. Creagh, N. Mondinos, M. Altarawneh, B.Z. Dlugogorski, *Journal of Materials Science & Technology*, 32 (2016) 1179-1191.
- [56] M.M. Rahman, H.A. Miran, Z.-T. Jiang, M. Altarawneh, L.S. Chuah, H.-L. Lee, A. Amri, N. Mondinos, B.Z. Dlugogorski, *RSC Advances*, 7 (2017) 16826-16835.
- [57] Y. Kim, J.Y. Leem, *Physica B: Condensed Matter*, 476 (2015) 71-76.
- [58] C. Fournier, O. Bamiduro, H. Mustafa, R. Mundle, R.B. Konda, F. Williams, A.K. Pradhan, *Semiconductor Science and Technology*, 23 (2008) 085019.
- [59] A.S. Hassanien, *Journal of Alloys and Compounds*, 671 (2016) 566-578.
- [60] A.S. Hassanien, A.A. Akl, *Journal of Alloys and Compounds*, 648 (2015) 280-290.
- [61] S.W. Xue, X.T. Zu, W.L. Zhou, H.X. Deng, X. Xiang, L. Zhang, H. Deng, *Journal of Alloys and Compounds*, 448 (2008) 21-26.
- [62] A. Amri, Z.-T. Jiang, X. Zhao, Z. Xie, C.-Y. Yin, N. Ali, N. Mondinos, M.M. Rahman, D. Habibi, *Surface and Coatings Technology*, 239 (2014) 212-221.

- [63] C.Y. Yen, S.R. Jian, G.J. Chen, C.M. Lin, H.Y. Lee, W.C. Ke, Y.Y. Liao, P.F. Yang, C.T. Wang, Y.S. Lai, J.S.C. Jang, J.Y. Juang, *Applied Surface Science*, 257 (2011) 7900-7905.
- [64] Z.H. Xie, R. Singh, A. Bendavid, P.J. Martin, P.R. Munroe, M. Hoffman, *Thin Solid Films*, 515 (2007) 3196-3201.
- [65] M.A. Hopcroft, W.D. Nix, T.W. Kenny, *Journal of Microelectromechanical Systems*, 19 (2010) 229-238.

## CHAPTER SIX

---

### **Paper V: Understanding the Electronic Structural and Optical Properties of CrN and Mo:CrN Clusters: A DFT based First Principle Study**

---

#### **Abstract**

CrN, one of the most investigated transition metal nitrides, is prominent for its wear, corrosion and oxidation resistance and many other superior properties. In the present study, we carried out density functional theory (DFT) analysis to probe the structural, electronic and optical properties of pristine and Mo-doped CrN structures in non-crystalline phases with different combinations by replacing one or two Cr and/or N atoms. Throughout the studies, it was found that the Cr<sub>4</sub>Mo<sub>2</sub>N<sub>2</sub> structure to be chemically and energetically the most stable species among six clusters (Cr<sub>4</sub>N<sub>4</sub>, Cr<sub>3</sub>Mo<sub>2</sub>N<sub>3</sub>, Cr<sub>4</sub>Mo<sub>2</sub>N<sub>2</sub>, Cr<sub>3</sub>MoN<sub>4</sub>, Cr<sub>4</sub>MoN<sub>3</sub>, and Cr<sub>2</sub>Mo<sub>2</sub>N<sub>4</sub>). The DFT derived electronic structure predicts that the clusters Cr<sub>4</sub>MoN<sub>3</sub> and Cr<sub>3</sub>Mo<sub>2</sub>N<sub>3</sub> possess magnetic susceptibility. The DFT based infrared (IR), Raman and ultraviolet-visible (UV-Vis) analyses indicated that the clusters formed by Cr<sub>4</sub>N<sub>4</sub> and Cr<sub>4</sub>Mo<sub>2</sub>N<sub>2</sub> are naturally stable and able to function as light harnessing materials to be used in solar selective surfaces.

#### **6.1 Introduction**

Over the years research interests on metal nitrides have received widespread attention owing to a good combination of numerous properties such as large band-gap, corrosion-, erosion-, wear resistance, oxidation resistance, superior physical, chemical and thermal stability, and physical strength [1-14]. Due to these properties, they have secured applications in many technological devices such as, non-volatile storage devices [8-10], superhard coatings [15-17], microelectronic devices [13], electronic and photonic devices [4, 5, 14], high-temperature structural materials [18], anti-reflective coatings [19-22], solar absorbing and solar selective surfaces [23, 24], and optical storage devices [3]. Investigations on refinement of their properties and researching new materials with superior properties are always the key focus [25]. For example, the introduction of an appropriate dopant can successfully enhance the properties by inducing defects such as vacancy, atom substitution, and cluster formation and deformation [7]. Carbon doping on CrAlN matrix was carried out to realize the dopant's effect on electromagnetic properties [7]. It was shown



that C-doped dispersed CrAlN clusters demonstrate higher resistivity at low frequency. However, too much carbon doping enhances disorderly characteristics which in turn reduces the magnetic coupling [7].

Structural, optical and electrical properties of Mn- and Cr-doped GaN diluted magnetic semiconductors are widely investigated due to their potential applications in electronic and spin-dependent photonic devices [4, 6, 14]. The electronic structure of AlN, CrN and Cr-doped AlN matrices were studied *via* XPS and soft X-ray emission spectroscopy at the near K-edge and results were compared with that of density function models [2]. Due to large band-gap (6.2 eV), high acoustic velocity, and higher thermal and physical toughness, AlN is used in the semiconductor industry as high-temperature optoelectronic devices [2]. Due to their improved functional and mechanical properties such as superelasticity and shape memory effects, Ti-Ni materials are widely used in the design of instruments, aerospace technologies and medical science [26-28]. Numerous reported findings exhibited the correlation between the electronic structure and phase stability of metal nitride-based materials [29-32]. It has been established that Al-doped CrN presents better mechanical and oxidation resistance performances at higher temperatures in comparison with the conventional binary CrN matrix [33].

Among various metal nitride complexes, CrN has emerged as a very potent material for protective and wear-resistant materials due to its distinguished hardness, higher melting point and wide applicability in various industries [34, 35]. Thus, research focus, both theoretically and experimentally, is given to CrN systems to investigate their different properties and stability [36, 37]. Wear resistance for compressive stress and oxidation resistance behaviour at high temperature exposure of CrN coatings were experimentally established by research groups led by Navinsek and Mayrhofer [38, 39]. Theoretical investigations of the CrN system, by using a modified local spin-density approximation (LSDA+U) method has been well-known as a Mott insulator [40]. Brik and co-researchers [41] provided an explanation on the hardness of a series of transition metal nitrides (TMNs, where TM=Sc, Y, Ti, Zr, Hf, V, Nb, Ta, Mo, W) by generalized gradient approximation (GGA) theory. They also investigated the electronic structures of various TMNs. In a theoretical study, Zhou and co-researchers [42] elucidated the alloying effects on various TM (TM = Sc, Y, Ti, Zr, Hf, V, Nb, Ta, Mo, W) within the CrN system by using the density functional theory (DFT) and they predicted that alloying with V, Nb, Ta, Mo, and W can improve the ductility of the CrN matrix. In another report, the same group presented the

thermodynamic and structural stability of the CrN system by using modified density functional theory (DFT + U) [37]. More recently, they also explored the structural and mechanical properties of Cr-Mo-N and Cr-W-N both theoretically and experimentally, Mo and W were used to replace Cr and N atoms in the CrN matrix [43]. First principle and experimental studies on structural, microstructural, electronic, interface, thermodynamic, and magnetic properties of various types of nitride based materials have been reported elsewhere [44-47].

In recent years, MoCrN complexes are being as potential substitutes for CrN as they tend to exhibit structural evolution and superior hardness within the range of 28–31 GPa due to the Cr-doping [48]. Klimashin and co-researchers performed theoretical and experimental analysis on MoCrN and MoCrAlN matrices and found their mechanical hardness to be more pronounced than that of CrN matrix [48, 49]. It is evidently seen that chromium can enhance the properties of MoN and subsequently molybdenum is also able to enhance the properties of CrN. It was indicated that the intensive theoretical calculations on CrN or/and CrMoN systems in crystal phases have been previously reported. However, to our knowledge, the effect of Mo-doped CrN system in a non-crystalline phase has yet to be studied. In view of this, we have therefore carried out structural, electronic, and optical properties of CrN phase and different Mo:CrN complexes in a non-crystalline phase using DFT. We have found that, in general, the addition of Mo in CrN increases its electrical conductivity by lowering the energy gaps while Mo:CrN complexes are chemically more favourable than the pristine CrN system. From Infrared (IR) spectra analysis, it was seen that apart from CrN cluster, at least two Mo:CrN clusters are more likely to be formed naturally. The overall analysis was conducted *via* structural optimization of the clusters through density of states (DOS) studies, IR analysis, Raman analysis, and ultraviolet-visible (UV-Vis) spectra simulations for CrN and Mo:CrN phases.

## 6.2 Computational Details

Initially, we considered a simple CrN cluster of eight atoms (4 Cr and 4 N atoms) to form a Cr<sub>4</sub>N<sub>4</sub> structure. Subsequently, the Cr and/or N atoms were replaced from the Cr<sub>4</sub>N<sub>4</sub> cluster with the Mo atoms to form five different clusters, namely, Cr<sub>3</sub>Mo<sub>2</sub>N<sub>3</sub>, Cr<sub>4</sub>Mo<sub>2</sub>N<sub>2</sub>, Cr<sub>2</sub>Mo<sub>2</sub>N<sub>4</sub>, Cr<sub>4</sub>MoN<sub>3</sub>, and Cr<sub>3</sub>MoN<sub>4</sub>. The maximum force and RMS force threshold were set to 0.000450 a.u and 0.000300 a.u. for convergence. The minimum energy was determined corresponding to the value of the force upon which the convergence occurred. All these clusters were geometrically optimized *via* DFT integrated with the B3LYP hybrid

functional using LANL2DZ basis sets [50]. The IR and Raman simulations of the clusters were performed with same level of theory along with the imaginary frequencies. If imaginary frequencies are present in a vibrational spectra of a cluster, it is very unlikely of finding this structure in a stable form in the nature [51]. Gaussian 09 program was used to conduct the DFT based simulations [52].

Chemical potential ( $\mu$ ) of the clusters was calculated using the following relation [53],

$$\mu = -\frac{(E_{Homo}+E_{Lumo})}{2} \quad (1)$$

where,  $E_{Homo}$  and  $E_{Lumo}$  indicate the energy associated with the highest occupied molecular orbital (HOMO) and the lowest unoccupied molecular orbital (LUMO). The energy gap between HOMO and LUMO known as band-gap ( $E_g$ ) is related to the electrical conductivity and is defined by the following equation [53],

$$E_g = E_{Lumo} - E_{Homo} \quad (2)$$

Chemical hardness ( $\eta$ ) and softness ( $S$ ) are derived from Koopman's theorem and are defined by the subsequent equations [54, 55],

$$\eta = \frac{(E_{Lumo}-E_{Homo})}{2} \quad (3)$$

$$S = \frac{1}{2\eta} \quad (4)$$

The concept of electrophilicity introduced by Parr *et al.* is defined as [54],

$$\omega = \frac{\mu^2}{2\eta} \quad (5)$$

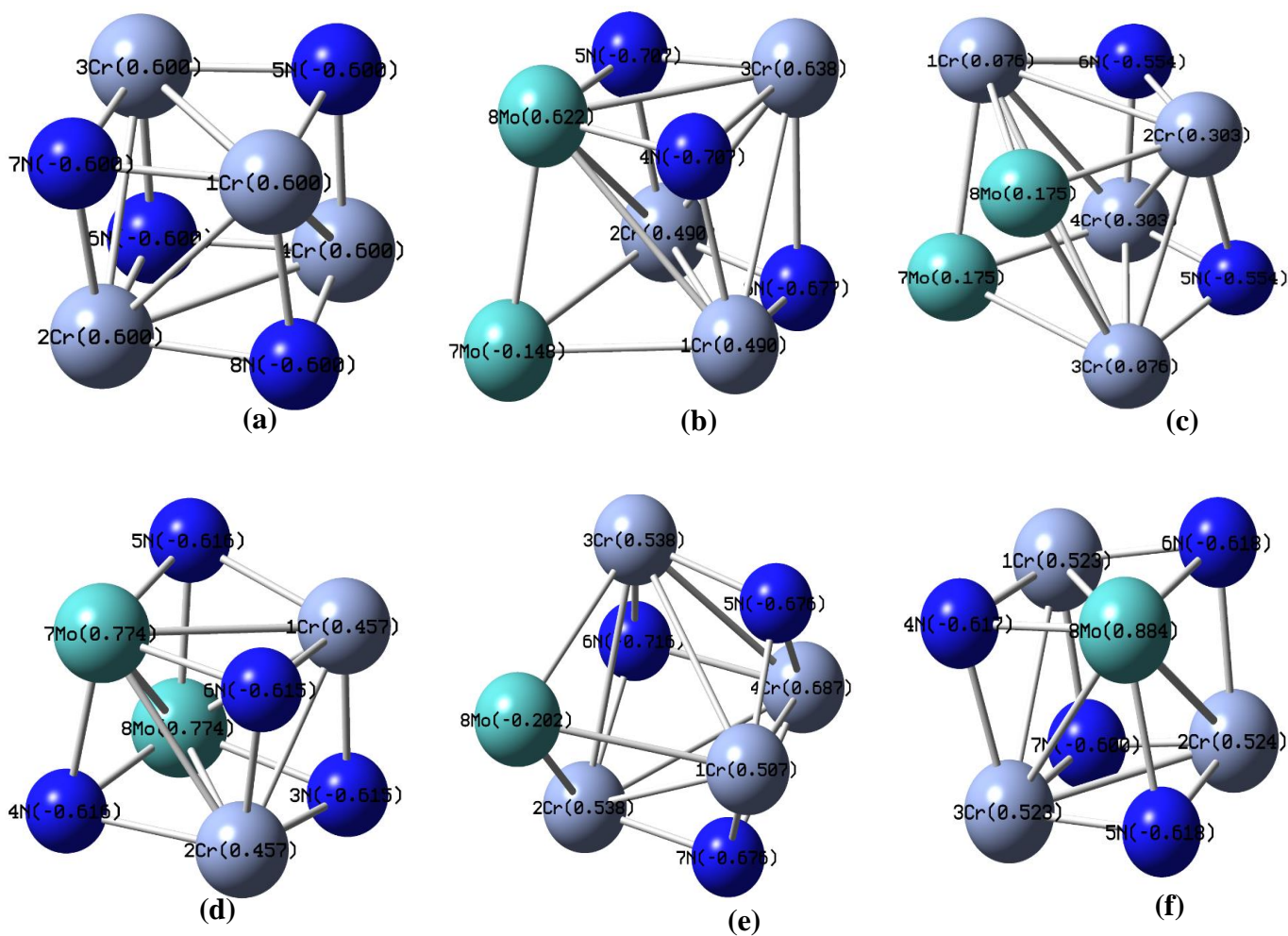
Dipole moments arise in molecules if the electrons of the molecules are distributed in a non-uniform way inside the molecule. It occurs due to the difference of electronegativity of the atoms within the molecule. Mulliken charge analysis were automatically done by the Gaussian 09 program during the geometry optimization operation. The optical properties of the clusters were investigated using the ultraviolet-visible (UV-Vis) spectra analysis with time dependent DFT (TD-DFT) using B3LYP hybrid potential and LANL2DZ basis set [51]. The UV-Vis spectra of molecular systems are graphical descriptions of their behaviour under the influence of ultraviolet through visible to near infrared solar spectra. These spectra also provide a theoretical approximation about the optical band gap of the molecules or clusters. Using the optimized molecular geometries of considered clusters, the fundamental vibrational wave numbers along with their corresponding infra-red (IR) intensities, and Raman activities of these clusters were computed at the B3LYP/ LANL2DZ basis sets using

the Gaussian 09 program package. The unscaled B3LYP/LANL2DZ vibrational frequencies are, normally, slightly larger than the experimental standards.

## **6.3 Results and Discussion**

### **6.3.1 Structural simulations**

Figure 1 illustrates the Mulliken charge distribution of the  $\text{Cr}_4\text{N}_4$  cluster and other five clusters formed from the Mo-doped CrN system. From the Mulliken charge distribution of  $\text{Cr}_4\text{N}_4$  cluster, it is seen that Cr atoms act as electron donors (positively charged) and N atoms act as electron acceptors (negatively charged). This occurs mainly due to the higher electronegativity of N (3.04) compared to Cr (1.66) and remains unchanged in other clusters. As a result, nitrogen atoms attract electrons from chromium atoms. However, the electronegativity of Mo (2.16) is in between Cr and N and thereby in  $\text{Cr}_3\text{MoN}_4$ ,  $\text{Cr}_2\text{Mo}_2\text{N}_4$  and  $\text{Cr}_4\text{Mo}_2\text{N}_2$ , Mo atoms have a net positive charge as the electrons are drawn away by the neighbouring nitrogen atoms. However, in  $\text{Cr}_4\text{MoN}_3$  and  $\text{Cr}_3\text{Mo}_2\text{N}_3$ , one Mo atom has a net negative charge due to the excess electrons that are drained from neighbouring chromium atoms due to its lower electronegativity. The atomic distances of the Cr-Cr, Cr-N, Cr-Mo, Mo-N, Mo-Mo, of CrN and Mo:CrN clusters are shown in Table 1.



**Figure 1.** Mulliken charge distribution of: (a)  $\text{Cr}_4\text{N}_4$ , (b)  $\text{Cr}_3\text{Mo}_2\text{N}_3$ , (c)  $\text{Cr}_4\text{Mo}_2\text{N}_2$ , (d)  $\text{Cr}_2\text{Mo}_2\text{N}_4$ , (e)  $\text{Cr}_4\text{MoN}_3$ , and (f)  $\text{Cr}_3\text{MoN}_4$  clusters.

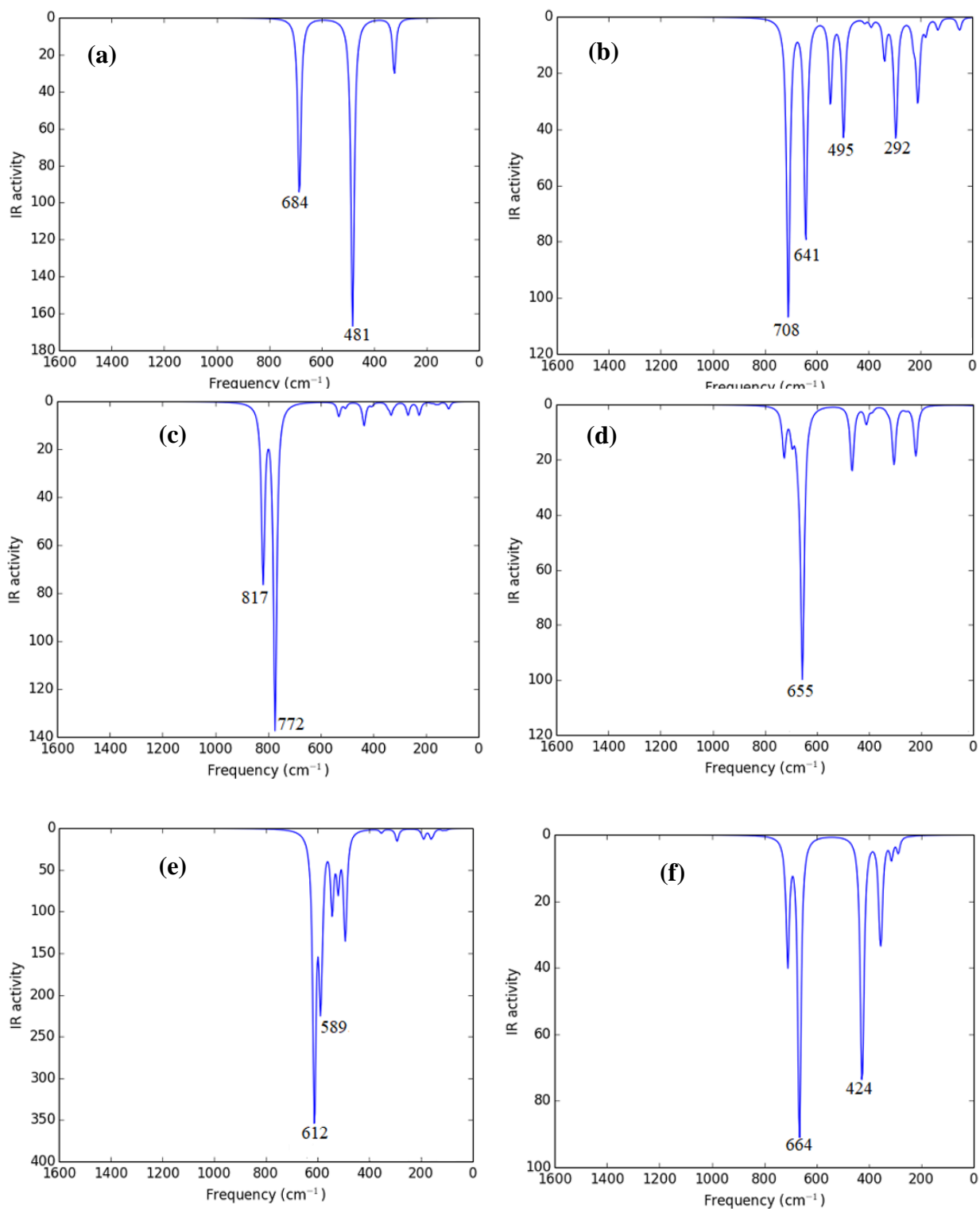
**Table 1.** Atomic distances of CrN and Mo:CrN clusters.

System	Cr-Cr (Å)	Cr-N (Å)	Cr-Mo (Å)	N-Mo (Å)	Mo-Mo (Å)
Cr <sub>4</sub> N <sub>4</sub>	2.52	1.86	-	-	-
Cr <sub>3</sub> Mo <sub>2</sub> N <sub>3</sub>	2.82	1.95	2.64	1.89	2.40
Cr <sub>4</sub> Mo <sub>2</sub> N <sub>2</sub>	2.70	1.86	2.45	3.07	2.67
Cr <sub>2</sub> Mo <sub>2</sub> N <sub>4</sub>	2.47	1.95	2.56	1.98	2.66
Cr <sub>4</sub> MoN <sub>3</sub>	2.77	1.85	2.65	3.23	-
Cr <sub>3</sub> MoN <sub>4</sub>	2.50	1.88	2.59	1.96	-

Dipole moment, a measure of polarity and symmetry of charge distribution [56] of the clusters are listed in Table 2. In the cluster of Cr<sub>4</sub>N<sub>4</sub>, the charge distribution is completely symmetrical and hence it possesses no dipole moment since the other clusters possess an uneven charge distribution and own net dipole moment. Thus, we conclude that the introduction of Mo in CrN system increases its polarity as all the Mo:CrN clusters have non-zero dipole moments (Table 2). The zero point energies (ZPE) of these six metal nitride clusters are also tabulated in Table 2. From Table 2, it is seen that the Cr<sub>2</sub>Mo<sub>2</sub>N<sub>4</sub> cluster has the highest ZPE of -526.5 Hartree while Cr<sub>4</sub>Mo<sub>2</sub>N<sub>2</sub> has the lowest ZPE of -589.5 Hartree which suggest that the replacement of nitrogen atoms by molybdenum atoms results to drop the ZPE of these clusters. The reverse phenomenon occurs when chromium atoms are substituted by molybdenum atoms. The Cr<sub>4</sub>N<sub>4</sub>, Cr<sub>4</sub>Mo<sub>2</sub>N<sub>2</sub> and Cr<sub>3</sub>MoN<sub>4</sub> clusters do not possess any imaginary frequencies in their IR spectra indicating that these clusters have a probability of forming naturally in a stable form [57]. On the other hand, the three rest clusters have at least one imaginary frequency in their IR spectra, thus, it is very unlikely that these clusters can naturally exist in a stable ailment. The strongest IR peak of Cr<sub>4</sub>N<sub>4</sub> at 481 cm<sup>-1</sup> (see Fig. 2) is believed to be due to the vibration of bending mode of nitrogen atoms around the chromium atoms. Though the frequency of absorption varies from one cluster to another, it basically depends on the position and composition of molybdenum atoms. This vibrational mode of bending of nitrogen atoms remains invariant for all other clusters.

**Table 2.** Zero point energy (ZPE), dipole moment and number of imaginary frequency of the Cr<sub>4</sub>N<sub>4</sub> and Mo:CrN clusters as calculated using DFT.

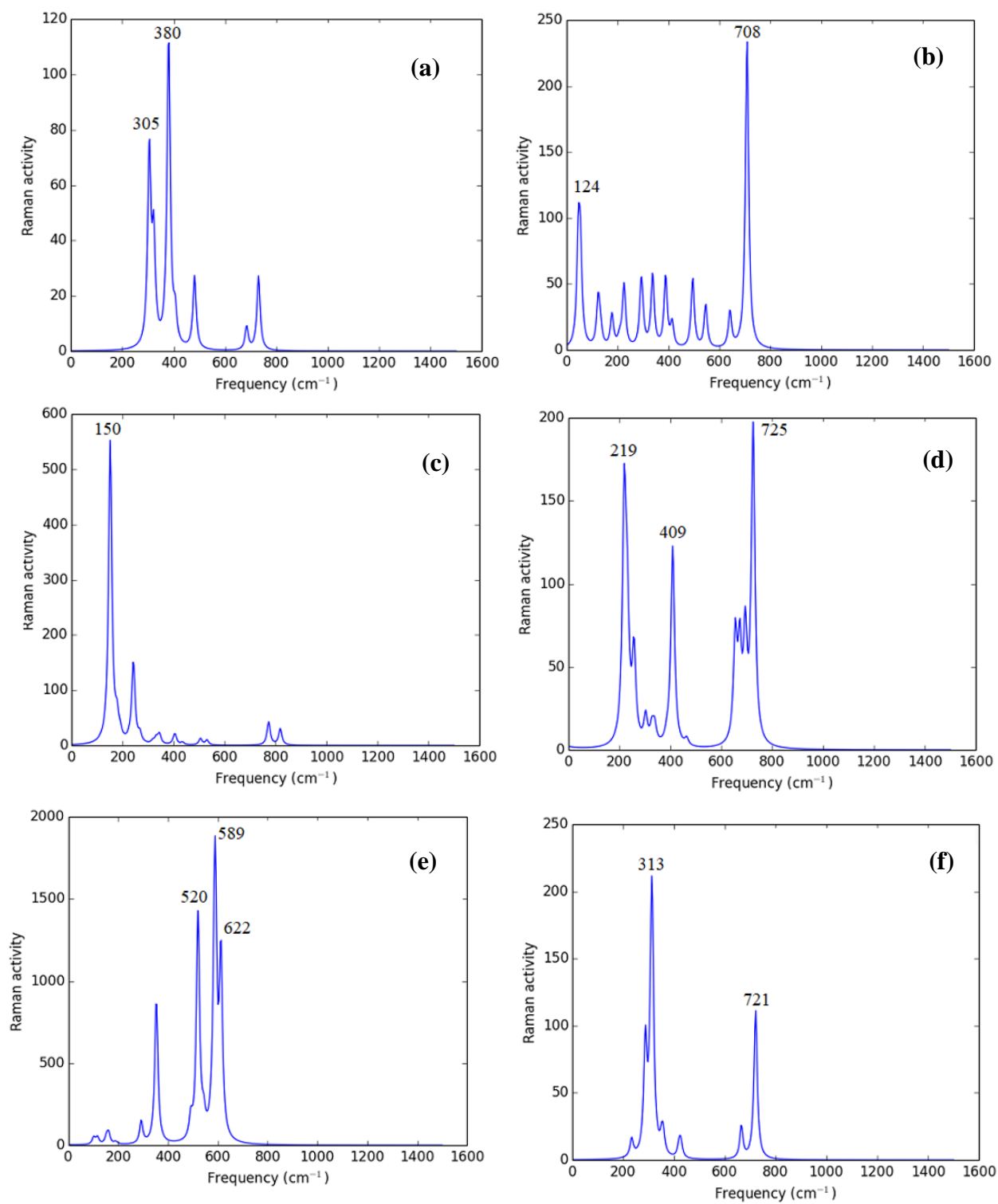
System	Zero point energy	Dipole moment $\mu_D$ (Debye)	Number of imaginary frequency $N_i$
	<i>ZPE</i> (Hartree)		
Cr <sub>4</sub> N <sub>4</sub>	-564.0	0	0
Cr <sub>3</sub> Mo <sub>2</sub> N <sub>3</sub>	-558.2	1.61	1
Cr <sub>4</sub> Mo <sub>2</sub> N <sub>2</sub>	-589.5	3.39	0
Cr <sub>2</sub> Mo <sub>2</sub> N <sub>4</sub>	-526.5	0.54	3
Cr <sub>4</sub> MoN <sub>3</sub>	-576.9	0.68	2
Cr <sub>3</sub> MoN <sub>4</sub>	-545.3	0.52	0



**Figure 2.** Infrared (IR) spectra of: (a)  $\text{Cr}_4\text{N}_4$ , (b)  $\text{Cr}_3\text{Mo}_2\text{N}_3$ , (c)  $\text{Cr}_4\text{Mo}_2\text{N}_2$ , (d)  $\text{Cr}_2\text{Mo}_2\text{N}_4$ , (e)  $\text{Cr}_4\text{MoN}_3$ , and (f)  $\text{Cr}_3\text{MoN}_4$  clusters.



The simulated Raman spectra of the  $\text{Cr}_4\text{N}_4$  and five Mo:CrN clusters are displayed in Figure 3. Similar to IR studies, the Raman spectra also provided with similar but complementary information about vibrational modes of a system [58]. The frequencies  $292\text{ cm}^{-1}$ ,  $392\text{ cm}^{-1}$ ,  $684\text{ cm}^{-1}$ , and  $730\text{ cm}^{-1}$  in  $\text{Cr}_4\text{N}_4$  are most likely to be Fermi resonance pairs [58]. This is because these pairs are present in almost equal separation as assigned in  $\text{Cr}_4\text{N}_4$  cluster, although other overtones and combinational bands are present [59]. Other vibrational modes of the clusters above  $1600\text{ cm}^{-1}$  may also exist. However, these calculations were not taken into account for the sake of brevity.



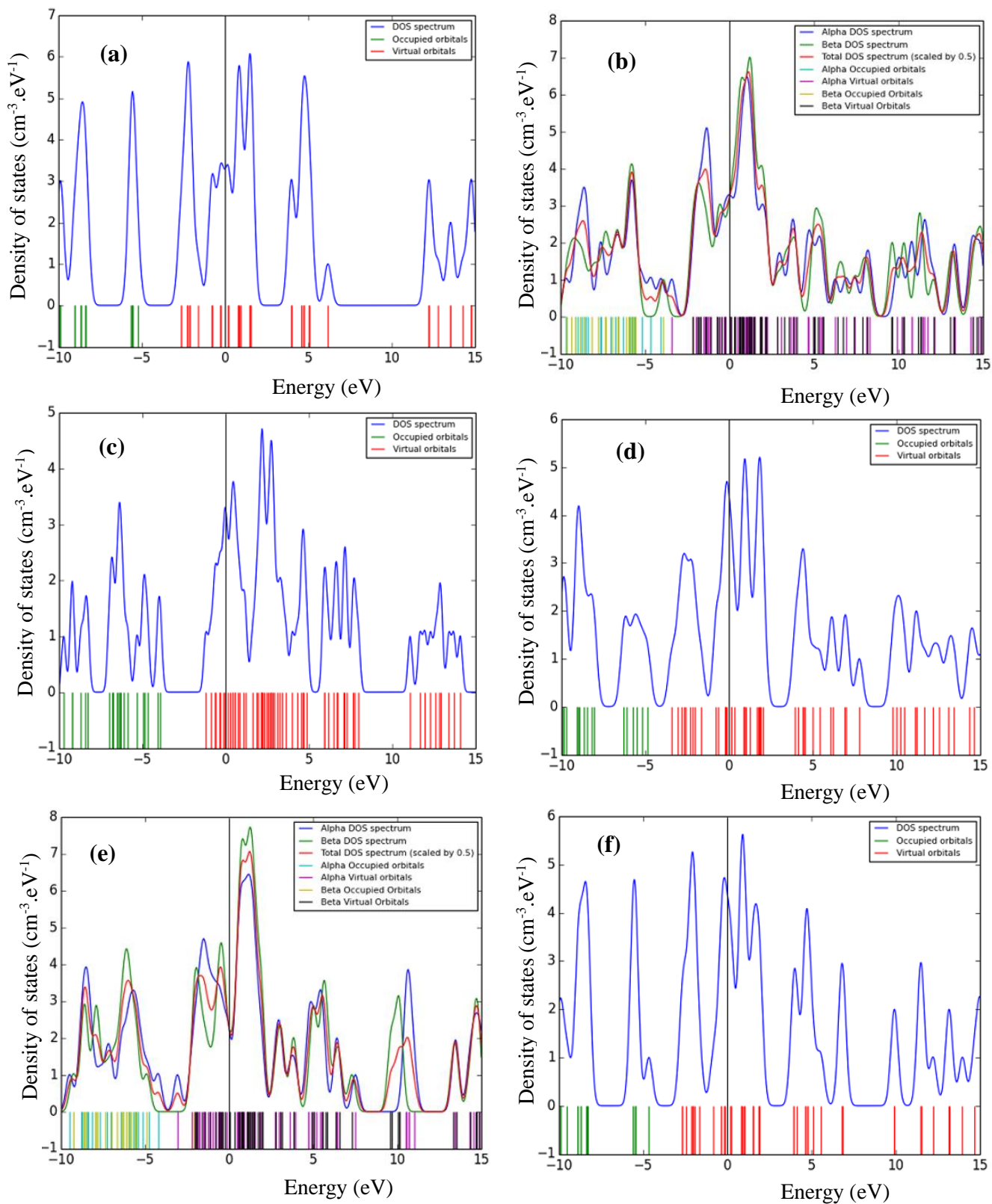
**Figure 3.** Raman spectra of: (a)  $\text{Cr}_4\text{N}_4$ , (b)  $\text{Cr}_3\text{Mo}_2\text{N}_3$ , (c)  $\text{Cr}_4\text{Mo}_2\text{N}_2$ , (d)  $\text{Cr}_2\text{Mo}_2\text{N}_4$ , (e)  $\text{Cr}_4\text{MoN}_3$ , and (f)  $\text{Cr}_3\text{MoN}_4$  clusters.

### 6.3.2 Electronic Properties

HOMO and LUMO of the  $\text{Cr}_4\text{N}_4$  and five Mo:CrN clusters were calculated by using the DOS spectra obtained from DFT analysis (see Figure 4). DOS spectra show the graphical representations of the occupied and unoccupied molecular orbitals (MO) of these clusters. The green bars and red bars indicate the occupied and unoccupied MOs of the clusters, respectively. DOS spectra facilitate estimation of the energy band-gap values,  $E_g$  in a graphical manner which are quantitatively discussed in the subsequent section. HOMO/LUMO gap is generally known as the energy band-gap,  $E_g$ . The energy band-gap,  $E_g$  of the  $\text{Cr}_4\text{N}_4$  cluster is found to be 2.61 eV (see Table 3). This result is in good agreement with that of the experimental studies [60]. The energy band-gap values of the rest of the clusters except  $\text{Cr}_4\text{Mo}_2\text{N}_2$  ( $E_g = 2.72$  eV) decreased. This reveals that the  $\text{Cr}_4\text{Mo}_2\text{N}_2$  cluster is the most stable among these six clusters which is in congruous with the results obtained from ZPE [61]. For  $\text{Cr}_3\text{Mo}_2\text{N}_3$ ,  $\text{Cr}_2\text{Mo}_2\text{N}_4$ ,  $\text{Cr}_4\text{MoN}_3$  and  $\text{Cr}_3\text{MoN}_4$ , the  $E_g$  values estimated are: 1.99 eV, 1.94 eV, 1.62 eV and 1.99 eV respectively. Thus, these four clusters are less stable than  $\text{Cr}_4\text{N}_4$  but are more conductive; they may be used in solar energy harvesting devices as solar selective surfaces. Furthermore, DOS spectra analysis of  $\text{Cr}_3\text{Mo}_2\text{N}_3$  and  $\text{Cr}_4\text{MoN}_3$  clusters indicated their magnetic susceptibility as their MOs are split into alpha and beta MOs which may also be used in spintronic devices [62].

Chemical potential ( $\mu$ ), a measure of chemical stability of the clusters [63], was estimated using DFT analysis for the  $\text{Cr}_4\text{N}_4$  and five Mo:CrN clusters are presented in Table 3. From the chemical potential data, we see that except for  $\text{Cr}_4\text{Mo}_2\text{N}_2$  cluster ( $E_g = 2.72$  eV), the rest of the clusters have nearly equal chemical potential ranges from 3.53 to -3.94 eV. This suggests that the  $\text{Cr}_4\text{Mo}_2\text{N}_2$  cluster is chemically the most stable while the other clusters exhibit similar chemical stabilities.

The electrophilicity,  $\omega$  having vacant orbitals that are attracted to an electron rich region, of  $\text{Cr}_4\text{N}_4$  and five other clusters was also calculated *via* DFT analysis and delineated in Table 3. For the  $\text{Cr}_4\text{N}_4$  cluster, the calculated value of  $\omega$  was found to be 5.95 eV. For all clusters except  $\text{Cr}_4\text{Mo}_2\text{N}_2$ , the values of  $\omega$  significantly increased compared to that of  $\text{Cr}_4\text{N}_4$  cluster. An increase in  $\omega$  implies the increase of its chemical reactivity and *vice versa* [54]. Thus, we summarize that the  $\text{Cr}_4\text{Mo}_2\text{N}_2$  cluster is the least chemically reactive among the six clusters considered in this study.



**Figure 4.** Density of state (DOS) spectra of: (a)  $\text{Cr}_4\text{N}_4$ , (b)  $\text{Cr}_3\text{Mo}_2\text{N}_3$ , (c)  $\text{Cr}_4\text{Mo}_2\text{N}_2$ , (d)  $\text{Cr}_2\text{Mo}_2\text{N}_4$ , (e)  $\text{Cr}_4\text{MoN}_3$ , and (f)  $\text{Cr}_3\text{MoN}_4$  clusters.

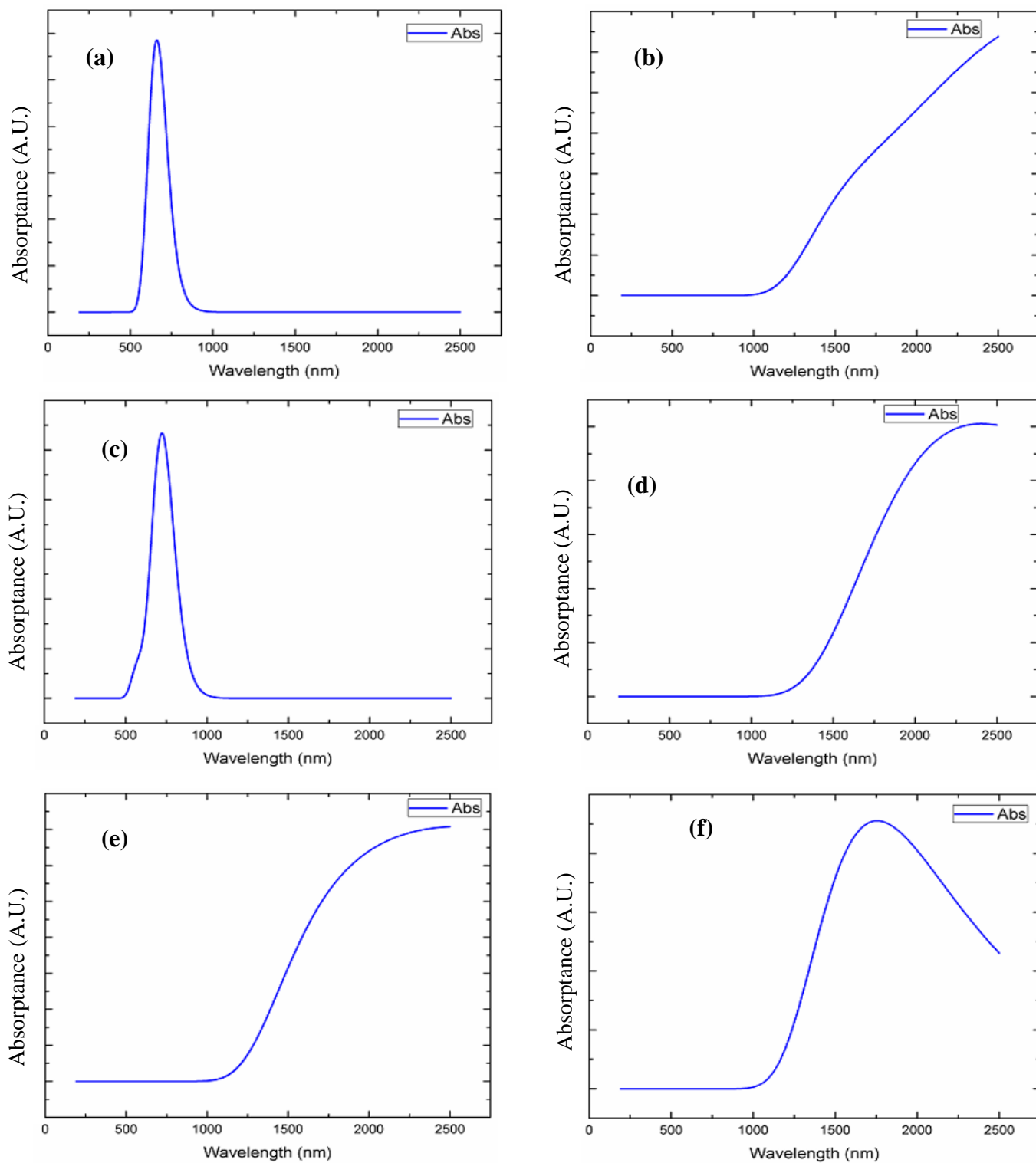
**Table 3.** HOMO and LUMO energies, HOMO-LUMO gap, chemical hardness, softness, electrophilicity and chemical potential of the Cr-Mo-N clusters as calculated using DFT.

System	HOMO energy $E_{\text{Homo}}$ (eV)	LUMO energy $E_{\text{Lumo}}$ (eV)	Energy band-gap, $E_g$ (eV)	Chemical hardness, $\eta$ (eV)	Chemical softness, $S$ (eV <sup>-1</sup> )	Electrophilicity, $\omega$ (eV)	Chemical potential, $\mu$ (eV)
Cr <sub>4</sub> N <sub>4</sub>	-5.25	-2.64	2.61	1.30	0.65	5.95	3.94
Cr <sub>3</sub> Mo <sub>2</sub> N <sub>3</sub>	-4.52	-2.53	1.99	0.99	0.50	6.26	3.53
Cr <sub>4</sub> Mo <sub>2</sub> N <sub>2</sub>	-3.91	-1.19	2.72	1.36	0.37	2.39	2.55
Cr <sub>2</sub> Mo <sub>2</sub> N <sub>4</sub>	-4.70	-2.76	1.94	0.97	0.51	7.17	3.73
Cr <sub>4</sub> MoN <sub>3</sub>	-4.68	-3.06	1.62	0.81	0.62	9.22	3.87
Cr <sub>3</sub> MoN <sub>4</sub>	-4.65	-2.66	1.99	0.99	0.50	6.72	3.66

The chemical hardness and the chemical softness of Cr<sub>4</sub>N<sub>4</sub> and five other clusters calculated *via* DFT analysis are presented in Table 3. These two key parameters of a material carry the same information in the reciprocal nature *i.e.*, they are reciprocal to each other. An increase of chemical hardness of a material results in the increase of its chemical stability and conductivity [55]. As seen from Table 3, the Cr<sub>4</sub>N<sub>4</sub> cluster has a chemical hardness of 1.30 eV. It is clearly found that the chemical hardness values of rest of the clusters except Cr<sub>4</sub>Mo<sub>2</sub>N<sub>2</sub> ( $\eta = 1.36$  eV) cluster were monotonically decreased. A similar trend was recorded for the chemical softness values of all these structures. Consequently, this designates that the Cr<sub>4</sub>Mo<sub>2</sub>N<sub>2</sub> cluster chemically achieves the most stable form while the other five structures possess comparable chemical stabilities. The findings on the chemical hardness and softness of these clusters were found to be consistent with energy band-gap, chemical potential, and electrophilicity findings as discussed in the aforementioned sections.

### 6.3.3 Optical Properties

The UV-Vis spectrum simulations, of Cr<sub>4</sub>N<sub>4</sub> and five Mo:CrN clusters such as Cr<sub>3</sub>Mo<sub>2</sub>N<sub>3</sub>, Cr<sub>4</sub>Mo<sub>2</sub>N<sub>2</sub>, Cr<sub>2</sub>Mo<sub>2</sub>N<sub>4</sub>, Cr<sub>4</sub>MoN<sub>3</sub>, Cr<sub>3</sub>MoN<sub>4</sub>, in the wavelength range of 190 to 2500 nm performed *via* DFT analysis are presented in Figure 5. These UV-Vis spectra of molecular systems afford us with the graphical descriptions of their behaviour under the influence of electromagnetic radiation from ultraviolet to visible, and then to near infrared range of the



**Figure 5.** Ultraviolet-visible (UV-Vis) spectra of: (a)  $\text{Cr}_4\text{N}_4$ , (b)  $\text{Cr}_3\text{Mo}_2\text{N}_3$ , (c)  $\text{Cr}_4\text{Mo}_2\text{N}_2$ , (d)  $\text{Cr}_2\text{Mo}_2\text{N}_4$ , (e)  $\text{Cr}_4\text{MoN}_3$ , and (f)  $\text{Cr}_3\text{MoN}_4$  clusters.

solar spectrum. A broad and intense peak for the  $\text{Cr}_4\text{N}_4$  cluster was assigned at 510 – 900 nm, and a similar peak was also observed for  $\text{Cr}_4\text{Mo}_2\text{N}_2$  cluster around 480 – 1000 nm. This is consistent with our previous simulations and analyses. As these two structures have the largest energy band-gap values, highest chemical potentials, highest chemical hardness, and highest values for the electrophilicity. From these studies, we realize that these two clusters can absorb a large amount of electromagnetic radiation of the visible range and can be potentially used in solar energy harvesting devices as the solar absorber material [64]. However, the other four clusters do not exhibit much tendency to absorb electromagnetic radiation in the ultraviolet and visible range of the solar spectrum. They absorb energy in near the infrared range from 1200 nm and above. This absorption behaviour in the near infrared range of the solar spectrum suggests that they may have potential applications in telecommunication devices.

#### 6.4 Conclusions

In this work, we have systematically studied the CrN and Mo:CrN clusters in a non-crystalline phase using DFT. From the investigations of structural and electronic properties of the clusters, we have seen that the  $\text{Cr}_4\text{Mo}_2\text{N}_2$  cluster is the most stable physically and chemically. The clusters  $\text{Cr}_3\text{Mo}_2\text{N}_3$ ,  $\text{Cr}_2\text{Mo}_2\text{N}_4$ ,  $\text{Cr}_4\text{MoN}_3$  and  $\text{Cr}_3\text{MoN}_4$  are comparatively less stable but more conductive than  $\text{Cr}_4\text{N}_4$  cluster. DOS analysis shows that  $\text{Cr}_3\text{Mo}_2\text{N}_3$  and  $\text{Cr}_4\text{MoN}_3$  have magnetic susceptibilities due to their odd number of electrons and unbalanced spins. Furthermore, due to the unbalanced spins, the molecular orbitals are split into alpha and beta orbitals depending on the spin orientations and have a net magnetic susceptibility. Thus, these materials might have great potentials to be used in spintronic devices. The IR analysis confirmed that the  $\text{Cr}_4\text{N}_4$ ,  $\text{Cr}_4\text{Mo}_2\text{N}_2$  and  $\text{Cr}_3\text{MoN}_4$  clusters have a possibility to form naturally. From the UV-Vis analysis, it is revealed that  $\text{Cr}_4\text{N}_4$  and  $\text{Cr}_4\text{Mo}_2\text{N}_2$  clusters are smart candidates that are capable of absorbing large amount of visible radiation and thereby can be used in solar energy collecting devices as the solar selective surface. However,  $\text{Cr}_3\text{Mo}_2\text{N}_3$ ,  $\text{Cr}_2\text{Mo}_2\text{N}_4$ ,  $\text{Cr}_4\text{MoN}_3$  and  $\text{Cr}_3\text{MoN}_4$  clusters tend to absorb solar radiation in the near infrared range and could be used in telecommunication purposes.

#### References

- [1] J.L. Endrino, S. Palacín, A. Gutiérrez, F. Schäffers, J.E. Krzanowski, , *Journal of Materials Science*, 42 (2007) 7607-7610.
- [2] B.J. Arnold, S. Krishnamurthy, B. Kennedy, D. Cockburn, D. McNally, J.G. Lunney, R. Gunning, M. Venkatesan, J. Alaria, J. Michael, D. Coey, C. McGuinnessy, J.H. Guo, , *e- Journal of Surface Science and Nanotechnology*, 7 (2009) 497-502.

- [3] H. Morkoc, S. Strite, G.S. Gao, M.E. Lin, B. Sverdlov, M. Burns, M.L. Reed, N.A. El-Masry, H.H. Stadelmaier, M.K. Ritums, M.J. Reed, C.A. Parker, J.C. Roberts, S.M. Bedair, *J. Appl. Phys*, 73 (1994) 3473-3475.
- [4] M.L. Reed, N.A. El-Masry, H.H. Stadelmaier, M.K. Ritums, M.J. Reed, C.A. Parker, J.C. Roberts, S.M. Bedair, *Applied Physics Letters*, 79 (2001) 3473-3475.
- [5] M.S. Kim, Y.K. Zhou, M. Funakoshi, S. Emura, S. Hasegawa, H. Asahi, S. Kimura, S. Emura, K. Tokuda, Y.K. Zhou, S. Hasegawa, H. Asahi, *Appl. Phys. Lett*, 89 (2006) 232511-232048.
- [6] S. Kimura, S. Emura, K. Tokuda, Y.K. Zhou, S. Hasegawa, H. Asahi, *Journal of Crystal Growth*, 311 (2009) 2046-2048.
- [7] F. Zeng, C. Chen, B. Fan, Y.C. Yang, P.Y. Yang, J.T. Luo, F. Pan, W.S. Yan, *Journal of Alloys and Compounds*, 509 (2011) 440-446.
- [8] A. Mycielski, L. Kowalczyk, R.R. Gałazka, R. Sobolewski, D. Wang, A. Burger, M. Sowińska, M. Groza, P. Siffert, A. Szadkowski, B. Witkowska, W. Kaliszek, *Journal of Alloys and Compounds*, 423 (2006) 163-168.
- [9] F. Pan, C. Song, X.J. Liu, Y.C. Yang, F. Zeng, *Materials Science and Engineering R: Reports*, 62 (2008) 1-35.
- [10] Y.C. Yang, F. Pan, Q. Liu, M. Liu, F. Zeng, *Nano Letters*, 9 (2009) 1636-1643.
- [11] P. Zeman, J. Musil, *Applied Surface Science*, 252 (2006) 8319-8325.
- [12] J.H. Edgar, *Properties of Group III Nitrides*, INSPEC, Exeter, UK, 1994.
- [13] B.D. Beake, V.M. Vishnyakov, R. Valizadeh, J.S. Colligon, *Journal of Physics D: Applied Physics*, 39 (2006) 1392-1397.
- [14] M. Hashimoto, Y.-K. Zhou, M. Kanamura, H. Asahi, *Solid State Communications*, 122 (2002) 37-39.
- [15] M. Mahbubur Rahman, A. Duan, Z.-T. Jiang, Z. Xie, A. Wu, A. Amri, B. Cowie, C.-Y. Yin, *Journal of Alloys and Compounds*, 578 (2013) 362-368.
- [16] M.M. Rahman, Z.-T. Jiang, X. Duan, Z. Xie, A. Tadich, Z.-f. Zhou, N. Mondinos, C.-Y. Yin, M. Altarawneh, B.Z. Dlugogorski, *Journal of Alloys and Compounds*, 661 (2016) 268-273.
- [17] M.M. Rahman, Z.-T. Jiang, Z. Xie, X. Duan, Z.-f. Zhou, P.C. Wo, C.-Y. Yin, N. Mondinos, Q. Gu, H. Widjaja, K. Jack, A. Yago, A. Amri, *The Journal of Physical Chemistry C*, 118 (2014) 18573-18579.
- [18] G. Petzow, M. Herrmann, *Silicon Nitride Ceramics*, in: M. Jansen (Ed.) *High Performance Non-Oxide Ceramics II*, Springer Berlin Heidelberg 2002, pp. 47-167.



- [19] D. Barbier, X. Orignac, X.M. Du, R.M. Almeida, X. Orignac, D. Barbier, X.M. Du, R.M. Almeida, Proc. of Topical Symp. VII on Advanced Materials in Optics, Electro-Optics and Communication Technologies, 69 (1995) 33-897.
- [20] X. Orignac, D. Barbier, X.M. Du, R.M. Almeida, Applied Physics Letters, 69 (1996) 895-897.
- [21] R.M. Almeida, X. Orignac, D. Barbier, Journal of Sol-Gel Science and Technology, 2 (1994) 465-467.
- [22] Y. Sorek, R. Reisfeld, I. Finkelstein, S. Ruschin, Applied Physics Letters, 63 (1993) 3256-3258.
- [23] M.M. Rahman, Z.-T. Jiang, P. Munroe, L.S. Chuah, Z.-f. Zhou, Z. Xie, C.Y. Yin, K. Ibrahim, A. Amri, H. Kabir, M.M. Haque, N. Mondinos, M. Altarawneh, B.Z. Dlugogorski, RSC Advances, 6 (2016) 36373-36383.
- [24] M.M. Rahman, Z.-T. Jiang, Z.-f. Zhou, Z. Xie, C.Y. Yin, H. Kabir, M.M. Haque, A. Amri, N. Mondinos, M. Altarawneh, Journal of Alloys and Compounds, 671 (2016) 254-266.
- [25] P. Dev, Y. Xue, P. Zhang, M. Hirai, Y. Ueno, T. Suzuki, W. Jiang, C. Grigoriu, K. Yatsui, Phys. Rev. Lett., 100 (2008) 1052-1055.
- [26] K. Otsuka, C. Wayman, K. Otsuka, C. Wayman, Shape Memory Materials, Cambridge University Press, Cambridge, UK, 1998.
- [27] K. Otsuka, X. Ren, Progress in Materials Science, 50 (2005) 511-678.
- [28] V.G. Pushin, A.I. Lotkov, Y.R. Kolobov, R.Z. Valiev, E.F. Dudarev, N.N. Kuranova, A.P. Dyupin, D.V. Gunderov, G.P. Bakach, Phys. Metals Metallogr., 106 (2008) 520-530.
- [29] S. Shabalovskaya, A. Narmonev, O. Ivanova, A. Dementjev, Physical Review B, 48 (1993) 13296-13311.
- [30] G.L. Zhao, T.C. Leung, B.N. Harmon, M. Keil, M. Müllner, W. Weber, Physical Review B, 40 (1989) 7999-8001.
- [31] N. Hatcher, O.Y. Kontsevoi, A.J. Freeman, Physical Review B, 79 (2009) 020202.
- [32] J. Cai, D.S. Wang, S.J. Liu, S.Q. Duan, B.K. Ma, Physical Review B - Condensed Matter and Materials Physics, 60 (1999) 15691-15698.
- [33] R. Sanjinés, O. Banakh, C. Rojas, P.E. Schmid, F. Lévy, Thin Solid Films, 420-421 (2002) 312-317.
- [34] L. Cunha, M. Andritschky, K. Pischow, Z. Wang, Thin Solid Films, 355-356 (1999) 465-471.
- [35] C. Nouveau, M.A. Djouadi, O. Banakh, R. Sanjinés, F. Lévy, Thin Solid Films, 398-399 (2001) 490-495.

- [36] G. Berg, C. Friedrich, E. Broszeit, C. Berger, *Surface and Coatings Technology*, 86-87 (1996) 184-191.
- [37] L. Zhou, F. Körmann, D. Holec, M. Bartosik, B. Grabowski, J. Neugebauer, P.H. Mayrhofer, *Physical Review B*, 90 (2014) 184102.
- [38] P.H. Mayrhofer, H. Willmann, C. Mitterer, *Surface and Coatings Technology*, 146-147 (2001) 222-228.
- [39] B. Navinšek, P. Panjan, I. Milošev, *Surface and Coatings Technology*, 97 (1997) 182-191.
- [40] A. Herwadkar, W.R.L. Lambrecht, *Physical Review B*, 79 (2009) 035125.
- [41] M.G. Brik, C.G. Ma, *Computational Materials Science*, 51 (2012) 380-388.
- [42] L. Zhou, D. Holec, P.H. Mayrhofer, *Journal of Physics D: Applied Physics*, 46 (2013) 365301.
- [43] L. Zhou, F.F. Klimashin, D. Holec, P.H. Mayrhofer, *Scripta Materialia*, 123 (2016) 34-37.
- [44] C.-M. Shi, T.-G. Wang, Z.-L. Pei, J. Gong, C. Sun, *Journal of Materials Science & Technology*, 30 (2014) 1193-1201.
- [45] J.C.M. Sung, B.R. Wu, S.L. Lee, M.F. Tai, *Materials Chemistry and Physics*, 72 (2001) 136-140.
- [46] T. Guo, G. Xu, S. Tan, N. Liu, J. Zhang, X. Zeng, J. Liang, *Materials Research Bulletin*, 95 (2017) 354-360.
- [47] S.A. Khan, S. Azam, *Materials Research Bulletin*, 70 (2015) 436-441.
- [48] F.F. Klimashin, H. Riedl, D. Primetzhofer, J. Paulitsch, P.H. Mayrhofer, *Journal of Applied Physics*, 118 (2015) 025305.
- [49] F.F. Klimashin, P.H. Mayrhofer, *Scripta Materialia*, 140 (2017) 27-30.
- [50] A.D. Becke, *The Journal of Chemical Physics*, 98 (1993) 1372-1377.
- [51] E. Runge, E.K.U. Gross, *Physical Review Letters*, 52 (1984) 997-1000.
- [52] M.J. Frisch et al., *Gaussian 09*, Revision D.01, in: I. Gaussian (Ed.), Wallingford, CT, USA, 2009.
- [53] A.S. Rad, S.S. Shabestari, S.A. Jafari, M.R. Zardoost, A. Mirabi, *Molecular Physics*, 114 (2016) 1756-1762.
- [54] R.G. Parr, L.v. Szentpály, S. Liu, *Journal of the American Chemical Society*, 121 (1999) 1922-1924.
- [55] R.G. Pearson, *Journal of Chemical Sciences*, 117 (2005) 369-377.
- [56] P. Atkins', J.D. Paula, *Physical Chemistry*, Oxford University Press, Oxford, UK, 2014.

- [57] P. Souvatzis, O. Eriksson, M.I. Katsnelson, S.P. Rudin, *Physical Review Letters*, 100 (2008) 095901.
- [58] K. Nakamoto, *Infrared and Raman Spectra of Inorganic and Coordination Compounds: Part B: Applications in Coordination, Organometallic, and Bioinorganic Chemistry*, John Wiley & Sons, Inc., Hoboken, New Jersey, USA, 2009.
- [59] J. Clarkson, W. Ewen Smith, *Journal of Molecular Structure*, 655 (2003) 413-422.
- [60] Khalil Ibrahim, M Mahbubur Rahman, Hatem Taha, Z. Ehsan Mohammadpour, Hifeng Zhou, Chun-Yang Yin, Aleksandar Nikoloski, Z.-T. Jiang, *Applied Surface Science*, 440 (2018) 1001-1010.
- [61] A.S. Rad, N. Nasimi, M. Jafari, D.S. Shabestari, E. Gerami, *Sensors and Actuators B: Chemical*, 220 (2015) 641-651.
- [62] A.K. Srivastava, N. Misra, *Computational and Theoretical Chemistry*, 1047 (2014) 1-5.
- [63] R.G. Pearson, *Inorganic Chemistry*, 27 (1988) 734-740.
- [64] S. Sarkar, K. Bhattacharjee, G.C. Das, K.K. Chattopadhyay, *CrystEngComm.*, 16 (2014) 2634-2644.

## CHAPTER SEVEN

---

### Conclusions

---

In this study, we have considered spectral selective behaviours, mechanical characteristics of novel Mo, CrN and Mo-doped CrN thin film coatings in crystalline and noncrystalline phases in order to find their potential applications as solar selective surfaces, and mechanical and industrial purposes such as cutting tools, in dry cutting, bearing spindles, metal forming, stamping dies, other mechanical machineries along with automotive and aerospace applications. The structural, morphological, optical, surface chemical composition, and mechanical properties of these materials were investigated *via* XRD, FESEM, XPS and EDX, UV-Vis and FTIR, and nanoindentation, finite element modeling (FEM), and density function theory (DFT) analysis techniques.

XRD studies of Mo, CrN and Mo:CrN sputtered thin film coatings showed that Mo-doping into the CrN phase leads to the formation of Mo<sub>2</sub>N, CrMoN<sub>x</sub>, and Cr<sub>2</sub>N solid solution phases together with a significant enhancement of their degree of crystallinity. The Mo coating showed a uniform, fine, smooth, dense and compact surface structure which appeared to be different from those of the CrN and Mo:CrN phases. Moreover, the grain sizes of Mo coatings were also relatively smaller than the other two coatings. Uniform larger grains and loose structures in CrN, and Mo:CrN coatings were believed to be caused by a non-reactive nucleation process. Additionally, the morphological features of Mo:CrN system were more refined edged and slightly increased in comparison to the other two phases. Consequently, it is assumed that the Mo atoms were diffused around the CrN structure during the synthesis processes, and the stimulated grain growth eventually acted as the nucleation site for lattice distortions. Even though the CrN coatings demonstrated the highest solar absorptance of 62% in the visible range of the solar spectrum, the highest solar selectivity value of 9.6 was attained by the Mo:CrN structure. But due to the higher solar absorptance of the CrN phase in the UV-Vis range, superior values of other optical parameters e.g., the refractive index, extinction coefficient, and dielectric functions were also achieved by the CrN phase.

In the next step of our studies, the exploration stage, an extensive understanding of the structural evolution, optical parameters, dielectric function, and mechanical studies and finite element modeling magnetron sputtered CrN coatings was attempted in as-deposited

and various annealed states. The face-centered-cubic CrN(111) phase with space group: Fm-3m was confirmed *via* XRD studies. The degree of crystallinity of the CrN phase was gradually increased, preferred orientations along (111) and (200) reflection planes and some peak sharpening was observed, with the subsequent rise in annealing temperatures. The existence of the Cr<sub>2</sub>O<sub>3</sub> phase was detected above 600 °C annealing. But the presence of the Cr<sub>2</sub>N phase was not seen either due to its amorphous nature or very weak crystallite sizes. It was also observed that up to 600 °C the CrN structure releases the residual stress, this being affected by two mechanisms: the thermal residual stress generated due to the difference in thermal expansion coefficient between coatings and substrates, and/or, the buildup of defects such as vacancies, cavities, and dislocations. The release of internal residual stresses may be also related to the absorption and extinction of sputtering defects initiated during the heat treatment process of the coatings. The gradual increase of grain size and the gradual decrease in lattice parameters with the rise in annealing temperatures was observed. The solar absorptance of the CrN phase was gradually increased from 61% to 89% as the annealing reaches to 700 °C while energy band-gap values were subsequently reduced from 2.62 eV to 1.38 eV. As a result, a good consistency between the structural features and optical studies of CrN coatings, before and after annealing, was confirmed. The nanoindentation studies showed that the hardness and the elastic modulus are dependent on the microstructure, grain refinement and internal residual stress of the CrN phase. The higher hardness values corresponded to the smaller crystallite size of CrN coatings and was governed by the combined nano-crystallites and amorphous phases formed after the annealing process. FEM studies revealed that the load induced stress levels is reduced after the coatings were annealed, particularly at higher temperatures. The load induced stress level also depends on the types of substrates used, and in materials of high elastic modulus, the higher level of stress will be induced around the coating and the substrate interface. However, the introduction of a suitable metal interlayer may enhance the stress level at the interface between the coating and substrate.

Temperature dependent structural evolution, surface morphological features, optical, dielectric, and mechanical features sputtered Mo:CrN coatings were carried out via XRD, FESEM, UV-vis, nanoindentation and finite element modeling techniques. Formation of CrN and Cr<sub>2</sub>N phases were identified at (111) and (200) reflection planes. In addition to CrN(111) and Cr<sub>2</sub>N(200) phases, multiple Cr<sub>2</sub>O<sub>3</sub> phases were also detected at different reflection planes. The crystalline behaviours of these phases were enhanced with the

gradual increase in annealing temperatures due to the enhanced grain growth and the release of residual stresses in the lattice structures. From the results of XRD studies, lattice parameters, induced residual stress values were gradually decreased while crystallite sizes were monotonically increased with the linear rise in annealing temperatures. An average grain size of 80-200 nm was estimated via FESEM studies. After the Mo:CrN coatings were annealed, the surface morphologies changed from triangular compacted structures to granular and faced structures and Cr<sub>2</sub>O<sub>3</sub> grains were detected at the top layer of these coatings. Furthermore, as the annealing temperature rise above 600 °C, the grain sizes were linearly increased. The temperature dependent solar absorptance, energy band-gap values, Urbach energy and steepness parameter studies of Mo:CrN coatings were correlated with each other. The optical studies of Mo:CrN coatings before and after annealing were in good agreement with the structural results obtained from the XRD analysis. The nanoindentation results also show that the hardness and the elastic modulus values are very closely related to the microstructural features, grain refinement and residual stresses of Mo:CrN coatings. Higher values of hardness associated with the smaller grain sizes and the formation of nano-crystallites and amorphous structures during the heat treatment process also strongly affect the film's hardness and elastic modulus parameters. The post annealing amorphous layers such as the Cr<sub>2</sub>O<sub>3</sub> phase formed at the grain boundaries may lead to a reduction in the strength and hardness of these coatings. But it is also considered that, the formed amorphous layer may improve stability of the coatings by obstructing the atomic movements in high temperature applications. FEM studies suggests that with the increase of the film thickness, the stress level decreases, and the peak position moves upwards away from the coating-substrate interface. For example, for a 1.4 μm thick film, the maximum value of the induced stress level reduced to ~ 15 GPa and a further increase of the film thickness completely eliminates the stress concentration. It was established that the stress concentration at the interface results in damage to the film-substrate interface and a delamination, or lateral crack is introduced on the coatings surface. Under the same loading, stress concentration tends to move away from the interface and thereby the possibility of film damage is reduced.

In the final step of our current studies, we have conducted DFT based computational studies on pristine and Mo-doped CrN clusters in a non-crystalline phase to reveal structural, electronic and optical properties for their potential solar selective surface applications. Among the six considered clusters, the Cr<sub>4</sub>Mo<sub>2</sub>N<sub>2</sub> cluster shown the highest stability both physically and chemically. The four other clusters Cr<sub>3</sub>Mo<sub>2</sub>N<sub>3</sub>, Cr<sub>2</sub>Mo<sub>2</sub>N<sub>4</sub>,

$\text{Cr}_4\text{MoN}_3$  and  $\text{Cr}_3\text{MoN}_4$  were comparatively less stable but more conductive than  $\text{Cr}_4\text{N}_4$  cluster. Density of states (DOS) studies indicated that  $\text{Cr}_3\text{Mo}_2\text{N}_3$  and  $\text{Cr}_4\text{MoN}_3$  clusters possess magnetic susceptibilities due to the presence of odd numbered electrons and unbalanced spins. Consequently, the molecular orbitals were split into  $\alpha$ - and  $\beta$ - orbitals based on the spin orientations and had a net magnetic susceptibility. Hence,  $\text{Cr}_3\text{Mo}_2\text{N}_3$  and  $\text{Cr}_4\text{MoN}_3$  clusters carry great potential to be used in spintronic devices. On the other hand, the UV-V showed that  $\text{Cr}_4\text{N}_4$  and  $\text{Cr}_4\text{Mo}_2\text{N}_2$  clusters are capable of absorbing the visible solar radiation and can be used in solar energy harvesting devices as the solar selective surface. Furthermore investigations demonstrated that the  $\text{Cr}_3\text{Mo}_2\text{N}_3$ ,  $\text{Cr}_2\text{Mo}_2\text{N}_4$ ,  $\text{Cr}_4\text{MoN}_3$  and  $\text{Cr}_3\text{MoN}_4$  clusters are good absorbers of the near infrared solar radiation and can be used in telecommunication fields.

Due to the combination of a large number of extraordinary properties such as superior optical properties, good wear resistance, wonderful thermal and corrosion resistance, good adhesion, high-temperature oxidation resistance, and a high level of hardness, metal nitride based materials are widely used in optical, protective, and decorative coatings, solar selective surfaces and mechanical devices. Despite their technological importance, so far, there have few investigations of solar selectivity features in the presence of various dopants. Optical responses of metal nitride based thin film coatings greatly vary from one application to the other. Nevertheless, thorough research is still needed to further increase their mechanical properties, thermal and chemical stability and the oxidation resistance behaviours of these materials before their place in the commercial market for industrial production is confirmed.

These materials show increasing roles to play in energy related applications, such as cost-effective, sustainable and environmental friendly solar selective surfaces. The solar selectivity values of these materials depends on the right choice of a material having maximum solar absorptance in the visible range and minimum thermal emittance in the infrared range of the solar spectrum, coatings structure, band-gaps, surface roughness, chemical bonding states, and particle morphology. Higher values of spectral absorption can also be achieved with a multilayer thin film coating. Using a multilayer coating, superior solar selectivity is achieved by either intrinsic absorption by the individual layers or absorption due to the interference between the constructed layers. A better solar selective feature can also be attained by using multilayer selective absorbers consisting of an absorbing layer placed between the anti-reflecting layer and a metallic substrate. An

anti-reflection (AR) layer is used to minimize the reflection of the incident radiation, thereby increasing the spectral absorption. This type of multi-layer coating allows the solar radiation easily pass through the surface of the material, the reflected waves from different optical interfaces create destructive interference and the solar absorption is enhanced. Thus, in future there are enormous opportunities to developing metal nitride and/or metal oxynitride based multilayer coatings with optimized synthesis conditions to achieve higher solar selectivity. The addition of an AR layer also improves the solar absorptance and reduces the thermal emittance values of such coatings. Thus, our findings will also facilitate engineering designs of metal nitride-based Mo, CrN, and Mo:CrN sputtered coatings for various industrial applications, especially in the area of solar selective absorbers. That will open a new avenue for the designation of high performance solar, thermal, optical, and mechanical devices with superior thermal stability, and good solar selectivity for different industrial applications in a mid and high temperature working environments.



## APPENDIX 1

---

### Sample Preparation Methodology

---

Sputtering is a physical vapour deposition (PVD) technique to prepare the thin film coatings. The sputtering process involves ejecting atoms from a 'target' material that is a source onto a 'substrate' such as steel, aluminium, and silicon. In the magnetron sputtering system magnets arranged behind the target that generates magnetic trap for the charged particles such as argon gas in front of the target. As soon as power is supplied to the magnetrons, the target is biased with a negative voltage normally at  $-300$  V or higher. During the coating synthesis process, the target material is bombarded by energetic glowing ions produced by a discharge plasma placed in front of the cathode plate. As a result, atoms released from target materials moved towards the substrate region and condense to yield a thin film coating. Simultaneously, the secondary electrons ejected out of the target's surface helps to sustain the hot plasma. This is the fundamental principle of a conventional sputtering system. However, a conventional sputtering system has some limitations such as low plasma ionization efficiencies, high substrate heating effects, and a low deposition rate of the coatings. For this reason, an unbalanced magnetron sputtering system is utilized to avoid these restrictions. The unbalanced magnetron sputtering technique has substantial impacts in the following areas: hard and superhard coatings, coatings with specific optical, wear resistant coatings, low friction coatings, corrosion-resistant coatings, decorative coatings with superior electrical and mechanical properties, and solar selective coatings.

A close-field unbalanced magnetron sputtering technique was used to synthesize the Mo, CrN, Mo:CrN coatings onto Si(100) substrates. The UDP650 closed field unbalanced magnetron sputtering (Teer Coatings Ltd, UK) system installed at the City University of Hong Kong was used to sputter these coatings. The coating preparation procedure includes the substrates preparation, and coatings deposition. This sputtering system offers excellent coating adhesion to the work substrates and a wide range of properties which have been tailored to suit various engineering applications. It is a powerful and flexible system which can be used to coat solid metal or alloys and a variety of compounds. A brief description about the sputtering process to deposit the Mo, CrN and Mo:CrN coatings together with the deposition parameters have been described in the following sections.

Silicon, Si(100) substrates were ultrasonically cleaned in a warm (nearly 40° C) acetone and methanol solution for 20 minutes, and then dried with nitrogen gas, before placing them into the sputtering chamber. A background pressure of  $4 \times 10^{-4}$  Pa was accomplished in the chamber before the deposition process. In order to achieve a homogeneous film thickness, the substrates were rotated at a speed of 10 rpm throughout the synthesis process. The nitride films were prepared in a mixture of Ar and N<sub>2</sub> gas atmosphere. Prior to any measurements, all the samples were mechanically cleaned in ultra-high vacuum *via* a diamond needle file and tungsten-wire brush. Details about the deposition parameters of Mo, CrN, Mo:CrN unbalanced magnetron sputtered coatings are delineated in the following Table 1.

**Table 1.** Details of the deposition conditions of the Mo, CrN, Mo:CrN unbalanced magnetron sputtered coatings.

Experimental Conditions	Mo/Si	Mo:CrN/Si
Substrate	Si	Si
Target materials	Mo target only	Two Cr and one Mo targets
Reaction gas	Ar is working gas, only	Ar is working gas, N <sub>2</sub> is reactive gas
Substrate thickness (mm)	1.5	1.5
Target to substrate distance (mm)	17	17
Substrate DC bias voltage (V)	-80	-80
Substrate holder rotation frequency (rpm)	10	10
Ar flow rate (sccm)	50	50
N <sub>2</sub> flow rate (%)	--	OEM = 30
Ar partial pressure (Pa)	0.133	0.133
Background pressure prior to coating (Pa)	4×10 <sup>-4</sup>	4×10 <sup>-4</sup>
Working gas pressure during sputtering (Pa)	0.15	0.15
Mo target power (VA)	294×4	-
Cr target power (VA)	-	-
Cr + Mo targets power (VA)	-	330× 3
Deposition time (min)	25	70
Coating thickness (µm)	1.2	1.2
Interlayer thickness (µm)	-	0.2

OEM = Controlled by optical emission monitor for nitrogen flow rate measurements  
sccm = standard cubic centimetre per minute (a unit of flow measurements)

## APPENDIX 2

---

### Experimental Theory and Techniques

---

#### 1. General Introduction

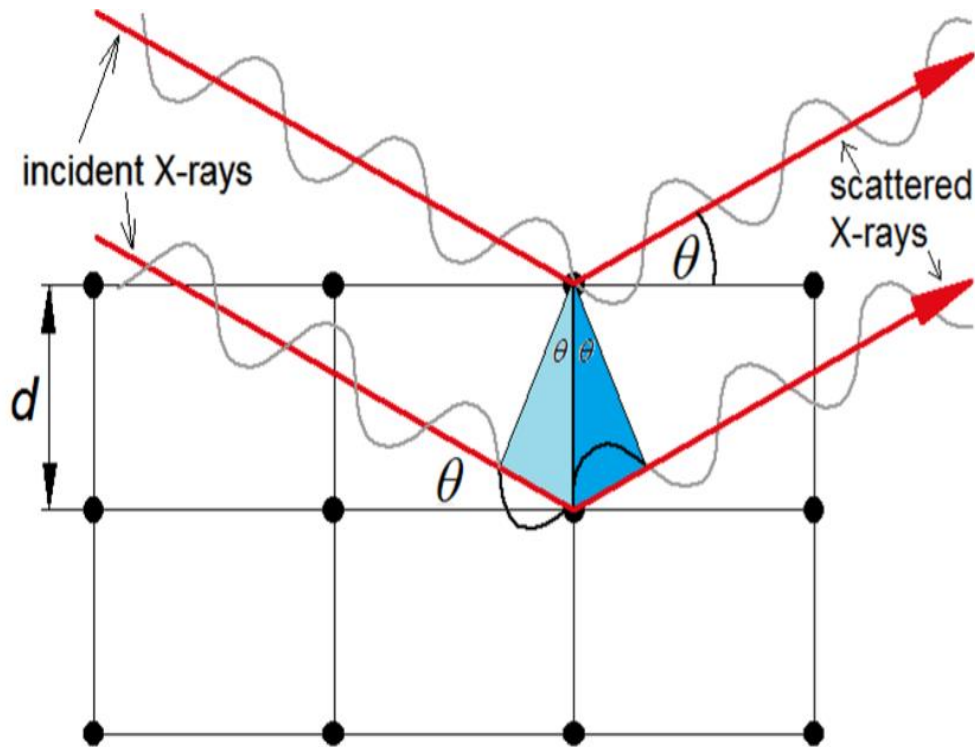
This section of the thesis deals with a brief theoretical background and experimental methodologies used to characterize the coated sputtered thin film coatings for their structural, morphological, optical, mechanical, and other properties. The theories and techniques to be discussed are XRD, field emission scanning electron microscopy (FESEM), ultraviolet visible (UV-Vis) spectroscopy, Fourier transform infra-red (FTIR) spectroscopy, energy dispersive X-ray spectroscopy (EDX), and X-ray photoelectron spectroscopy (XPS), nanoindentation, finite element modeling (FEM) techniques. Some of the experimental set-up, instrumental images and measuring techniques are also presented in the subsequent sections.

#### 2. X-ray Diffraction Measurements

The non-destructive XRD method has been utilised to determine crystalline phase and structural information of metal nitride thin film coatings. The X-rays interaction with a periodic crystal lattice forms a diffraction pattern due to the X-ray wavelength being almost of the same order of the unit cell constant. For a certain diffraction angle, the diffracted beams from the coatings surface atoms interfere constructively and appear as intensity peaks. This beam diffraction is related directly to the arrangement of crystal atomic which is described by Bragg's law [1]:

$$n\lambda = 2d\sin\theta \quad (1)$$

where  $n$  is an integer,  $\lambda$  the X-rays wavelength,  $d$  the distance between parallel consecutive atomic planes, and  $\theta$  the angle between these planes and the incident beam. Different crystalline phases, elements, or compounds are then identified by analysing the  $d$  values that are the characteristic for a particular crystal structure. Figure 1 illustrates the incident and scattered X-rays make an angle of  $\theta$  symmetric to the normal of crystal plane in XRD analysis [2].



**Figure 1.** Incident and scattered X-rays make an angle of  $\theta$  symmetric to the normal of crystal plane in XRD analysis [2].

XRD measurements for all Mo, CrN, and Mo: CrN thin films coatings were conducted using a Bruker AXS D8 Advance (Germany) with Cu- $K_{\alpha}$  radiation ( $\lambda = 1.54 \text{ \AA}$ ). More details on the XRD experimental measurement procedures and experimental conditions are described in the experimental techniques of Chapters 3, 4, and 5. Figure 2 shows the Bruker AXS D8 Advance XRD machine.



**Figure 2.** Powder diffraction X-ray diffraction (XRD), Bruker AXS D8 Advance.

### **2.1 Analyzing the X-ray Diffraction Data**

XRD data were used to identify crystalline phases of materials, to calculate unit cell dimensions, grain sizes, lattice microstrains, and residual stress. For crystalline materials, X-rays scattered by the electrons results in maximum and minimum of the XRD patterns. The maximum intensity peaks follow the Bragg's law, for each  $d$ -spacing. The plots of XRD peak intensities as a function of diffraction angles  $\theta$  represents the characteristics of the crystallographic structure and the atomic composition of a material. The phase identification can be accomplished by comparing the Bragg peaks and its  $2\theta$  positions.

In crystalline films, lattice parameters can be identified using the relationship between  $d$ -spacing and its Miller indices. For a cubic crystal system having a reflection plane of (110) in an XRD pattern the lattice parameter can be estimated from the following relationship,

$$d_{hkl} = \left( \frac{1}{a_0^2} (h^2 + k^2 + l^2) \right)^{1/2} \quad (2)$$

where  $\lambda = 0.154$  nm for Cu- $K\alpha$  radiation. This equation estimates the lattice parameter,  $a_0$  within an error of  $\pm 0.00001$  nm.

The grain size or crystallite size,  $D$  of a crystal phase at a particular reflection plane can be determined from its full width at half maximum (FWHM) values using the Debye Scherrer equation [3]:

$$D = \frac{K \lambda}{\beta \cos \theta} \quad (3)$$

where  $\beta$  is the full width at half maximum (FWHM) in radians which is identified *via* peak fitting using Lorentzian curve. The constant of proportionality,  $K$  (Scherrer constant = 0.89) depends on the shape of the crystal, the size distribution of the crystal and how the width is determined. Thus, the Debye-Scherrer relationship yields to,

$$D = \frac{0.89\lambda}{\beta \cos \theta} \quad (4)$$

The lattice microstrain and residual stress developed within the coatings can be estimated by evaluating the  $d$ -spacing of a crystalline phase [4]:

$$\varepsilon = \frac{d-d_0}{d_0} \quad (5)$$

where,  $\varepsilon$  is the component of microstrain normal to the surface, and  $d$  and  $d_0$  are the measured and strain free  $d$ -spacing values, respectively. The internal stress,  $\sigma_x$  induced in the coating was calculated using the following equation,

$$\sigma_x = \frac{E}{(1-\nu)} \times \frac{d-d_0}{d_0} \quad (6)$$

where  $d$  and  $d_0$  are obtained from the experimental diffraction patterns and JCPDS cards, respectively. The elastic properties of studied phase (for example:  $E$ , the elastic modulus = 300 GPa and  $\nu$  is Poisson's ratio = 0.28) [4] were used to carry out these calculations for various samples.

### 3. Emission Scanning Electron Microscopy (FESEM) and Energy Dispersive X-ray (EDX) Experiments

Field emission scanning electron microscopy (FESEM), is a type of microscopic methodology in which thin films microstructure and its morphology can be revealed using well-focused beam of high energy electrons. The primary intense electron beams generated from the electron gun interacts with the electrons released from sample during

the bombardment process. This interaction produces number of signals such as, secondary and back-scattered electrons accompanying with X-rays [5]. These signals detected by a photomultiplier detector that produces the films surface morphology of the particular scanned area. The field-emission cathode equipped with the electron gun also liberates electrons. These cathodic electrons are accelerated by the electric field. In a high vacuum level these electrons are focused and deflected by electronic lenses to produce a narrow scan beam that bombards the sample. As a result, the secondary electrons emitted from the coating's surface, the angle and velocity of the ejected electrons collectively resemble to the surface structure of the coating. FESEM provides improved spatial resolution and minimum sample charging and sample damage compared to SEM imaging process [6]. The X-rays released as result of the electron beam interactions with atoms in the coating surface are the characteristics of the elements present in the sample's surface. The X-rays released energy is dependent on the atomic structure of the coating and every atom reveals a specific X-ray emission spectrum. The X-rays generated can be separated in an energy spectrum to estimate the elemental/atomic compositions of the coating. This process is known as the energy dispersive X-ray spectroscopy (EDX).

In this work, the morphological features and EDX analysis of the thin film coatings were tested using Zeiss Neon 40EsB FESM with extra high tension EHT voltage field emission gun of 30 kV, an Oxford Instruments Inca X-act SDD X-ray detector (see Figure 3). In EDX experiments, the spectrum range of interest used was 0.1 to 20 keV which allowed a comparatively shorter period of time 10-100 seconds to complete the EDS analysis of a sample.





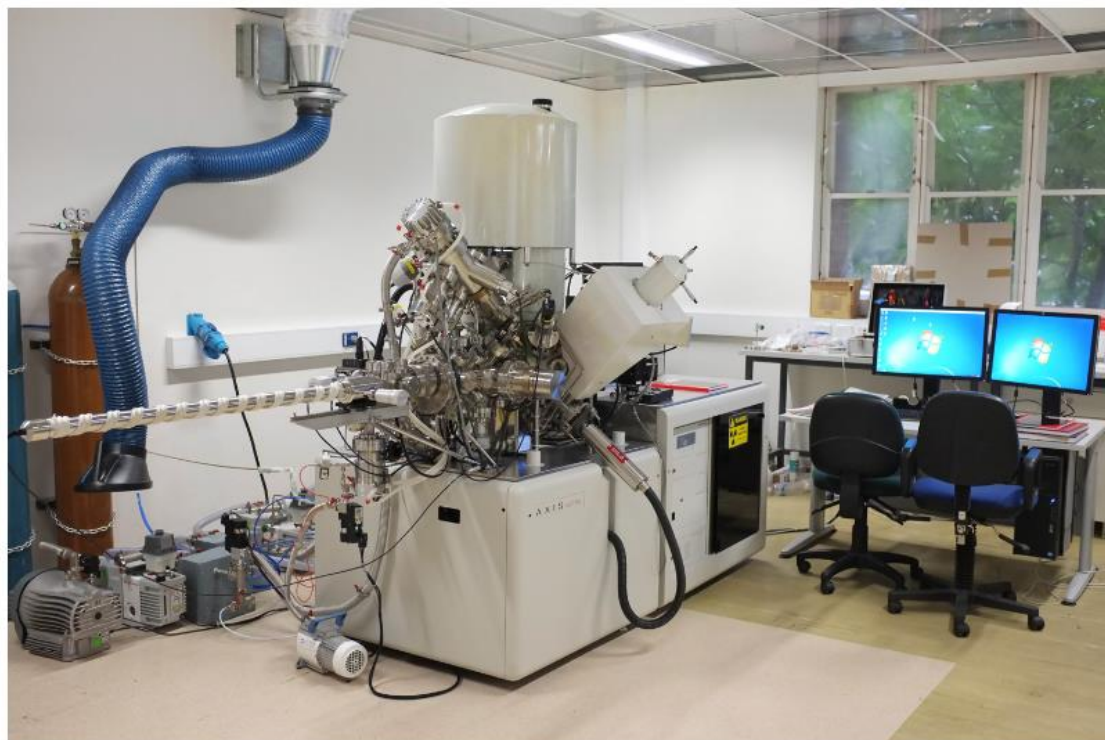
**Figure 3.** FESEM machine.

#### **4. X-ray Photoelectron Spectroscopy (XPS) Measurements**

X-ray photoelectron spectroscopy (XPS) is used to identify the chemical compositions, surface chemical bonding states and surfaces electronic structure of solid state materials. During the XPS tests, samples are placed horizontally in an ultrahigh vacuum chamber and exposed to a monochromatic X-ray source. In XPS process, the core level photoelectrons are emitted from the atomic shells of the elements present on the surface, as result of X-ray induced excitations of the samples surfaces. The ejected electrons binding energies are the characteristics of the elements from which they are emitted. The XPS spectra is obtained by counting the number of electrons as a function of their binding energies. The amount of chemical elements present in the specimen is a measured by the area under peaks of an XPS spectrum, its shape, and position of each element. The XPS is known as a surface sensitive technique because the photoelectrons are emitted from near the surface only and become available for detections.

In this work, the XPS study was performed using Kratos Axis Ultra DLD XPS spectrometer (Manchester, UK) operated with an Al- $K_{\alpha}$  monochromatic radiation Al (photon energy = 1486.6 eV) source. The XPS machine was operated at a power of ~10 mA and ~15 kV. The XPS machine equipped with a cold stage, and an Ar ion gun for etching the coatings is shown in the following Figure 4. The X-rays irradiate the sample at an incidence angle of about 45°. The analysis chamber was set at a uniform pressure of

$2.9 \times 10^{-9}$  Torr. The collected XPS spectra were analysed using CASA 2.3.1.5 XPS software.

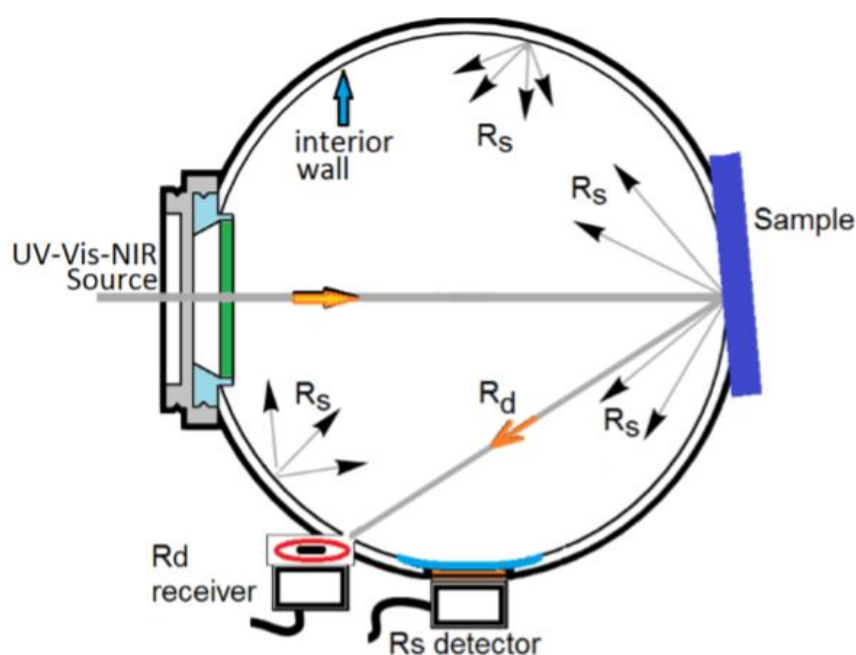


**Figure 4.** X-ray photoelectron spectroscopy system (Kratos Axis Ultra DLD XPS spectrometer).

##### **5. Optical Characterisations via UV-Vis-NIR and FTIR Reflectance Spectra**

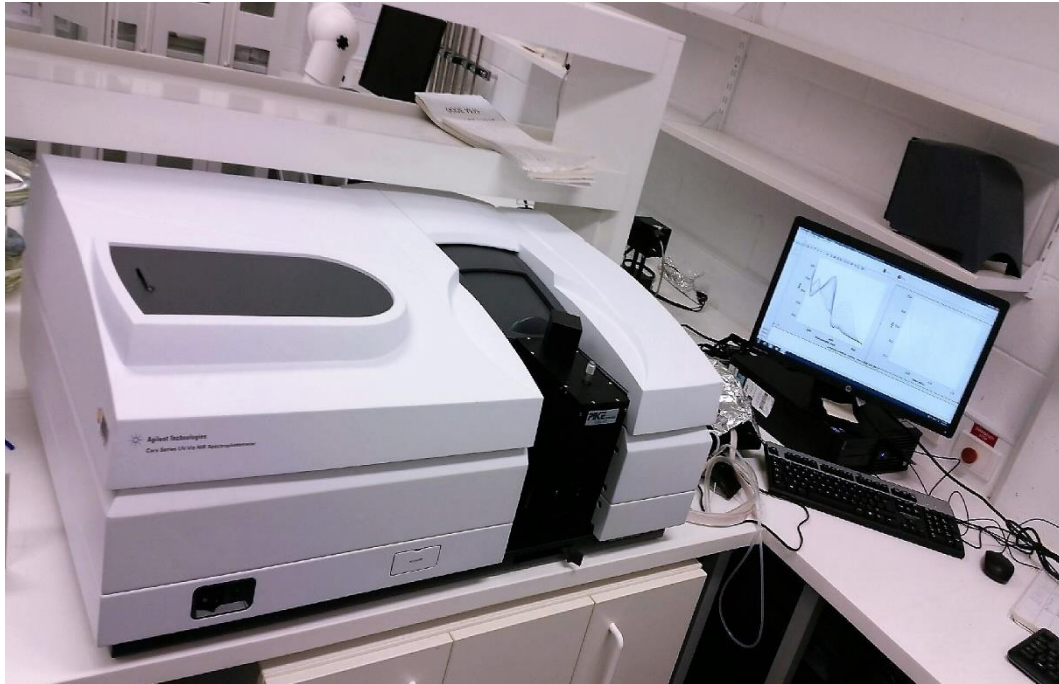
The optical performance of metal nitride thin films based solar absorbers can be studied through UV-Vis and FTIR studies. The UV-Vis reflectance data of the metal nitride coatings were collected in wavelength range of  $0.19 \mu\text{m}$  –  $2.5 \mu\text{m}$  while the FTIR reflectance spectra were acquired at  $2.5 \mu\text{m}$  and above. The Beckman-Duffie method was employed to estimate the solar absorptance in the visible range and thermal emittance in the infrared range of the solar spectra [7-9]. The UV-Vis-NIR spectrophotometer consists of a light source, sample holder, diffraction grating in monochromator or a prism to separate the different wavelengths of light, and a detector. The spectrophotometer uses a tungsten filament ( $0.3\text{-}2.5 \mu\text{m}$ ) as a source of radiation. The detector used in this system is a photodiode and photomultiplier tubes accompanied with scanning monochromators, which filter the light that only light of a single wavelength reaches the detector at a time. The diffraction grating is moved to the ‘step through’ each wavelength by the scanning monochromator, so that its intensity can be measured as a function of wavelengths.

The optical response of an opaque surface are of two types: specular reflectance and diffuse reflectance. In specular reflectance ( $R_s$ ), the incoming irradiation angle is equal to the reflected polar angle. Generally, a nicely polished surface works as the specular reflectance and a rough surface reflects diffusely. In most cases, samples produce a combination of specular and diffuse reflectance, and the measurements of these two reflectance is quite difficult. Consequently, the total or overall reflection is measured using an integrating sphere of highly reflecting interior wall, which shows the combination of  $R_s$  and  $R_d$  (see Figure 5).



**Figure 5.** Specular reflectance ( $R_s$ ) and diffuse reflectance ( $R_d$ ) in a reflectance mode of integrated sphere. Adapted from Refs. [10, 11].

In this work, the UV-Vis-NIR, Cary 5000 double beam spectrophotometer with 60 mm integrating sphere, was used to record the solar reflectance data of near normal hemispherical spectrum from 0.19 to 2.3  $\mu\text{m}$ , using a Deuterium (300 to 350 nm) and Halogen (330 to 2700 nm) lamps as shown in Figure 6.



**Figure 6.** Cary 5000 UV-Vis-NIR spectrophotometer.

Optical properties materials are strongly affected while light passing through them due to the changes of intensity of the propagation vector. For example, the refractive index,  $n$  and the extinction coefficient,  $k$ : the two most important optical properties, which are generically called optical constants; can be determined by studying the reflectances as a function of wavelength through a thin film material. Different experimental techniques are available for measuring  $n$  and  $k$  values, Simmons and Potter have been summarized some of them [12].

In an optical or dielectric medium, the refractive index,  $n$  is defined as the ratio of the velocity of light,  $c$  in vacuum to its velocity,  $v$  in the medium;  $n = c/v$ . Maxwell's formula for the refractive index of a substance can be obtained using this definition and can be expressed as [13],

$$n = \sqrt{\epsilon_r \mu_r} \quad (7)$$

where,  $\epsilon_r$  is the static dielectric constant or relative permittivity and  $\mu_r$  is the relative permeability. When a plane monochromatic electromagnetic wave propagates in a non-scattering homogeneous material experiences attenuation due to various loss mechanisms such as the generation of phonons (lattice waves), photogenerations, free carrier absorptions, and scattering. In such a medium, the refractive index becomes a complex

optical constant;  $n^* = n + ik$ , where  $n^*$  complex refractive index, with the real part  $n$ , and the imaginary part  $k$  (extinction coefficient).

The refractive index,  $n$  and extinction coefficient,  $k$  may also be determined using Swanepoel's method [14, 15]. In case of a uniform thickness  $d$ , the interference effects give rise to the spectrum showing the transmission curve in a maximum and minimum. These interference fringes could be used to investigate the optical constants of metal nitride based materials *via* following relationships [16-18]. In a transparent medium, the refractive index,  $n$  is given by:

$$n = [M + (M^2 + n_s^2)^{1/2}]^{1/2} \quad (8)$$

where,

$$M = \frac{2n_s}{T_{min}} - \frac{n_s^2}{2} \quad (9)$$

In the case of a weak and medium absorption coatings, the refractive index,  $n$  is given by,

$$n = [n^* + (n^{*2} + n_s^2)^{1/2}]^{1/2} \quad (10)$$

where,

$$n^* = \frac{T_{max} - T_{min}}{T_{min}T_{max}} - \frac{n_s^2 + 1}{2} \quad (11)$$

Extinction coefficient,  $k$  may be calculated using the absorbance  $x$  that given in terms of the interference extremes using the following:

$$x = \frac{E_M - [E_M^2 - (n^2 - 1)^3 (n^2 - n_s^2)]^{1/2}}{(n-1)^3 (n - n_s^2)} \quad (12)$$

where

$$E_M = \frac{8n^2 n_s}{T_{max}} + (n^2 - 1)(n^2 - n_s^2) \quad (13)$$

and

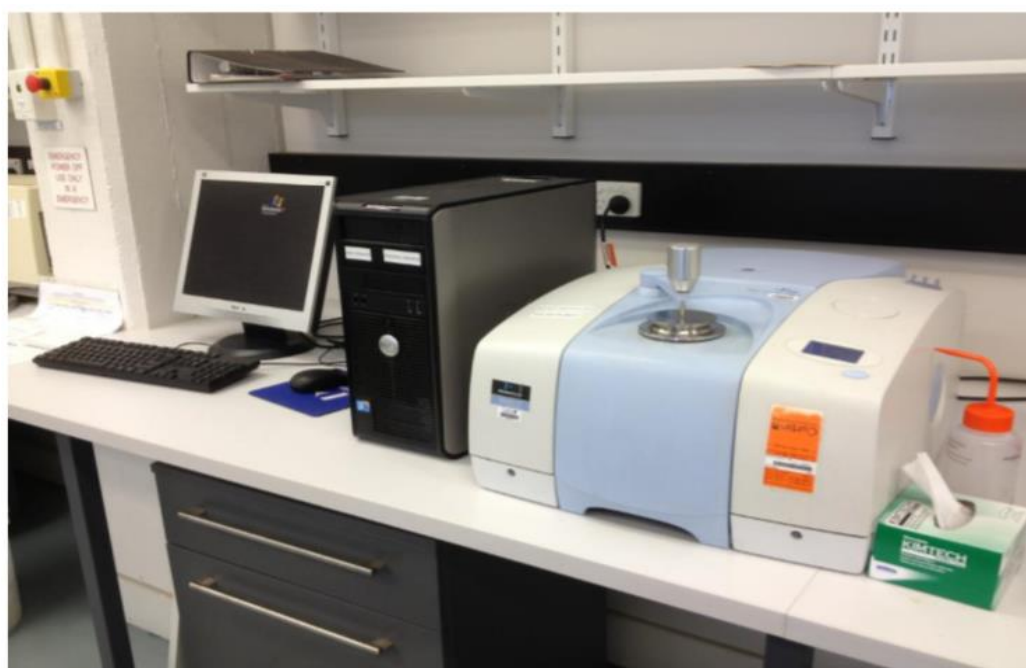
$$x = \exp\left(\frac{-4\pi kd}{\lambda}\right) \quad (14)$$

In the present study, the UV-Vis reflectance spectra were used to investigate the linear absorption coefficient ( $\alpha$ ), optical band-gap analysis, dielectric characterizations, the loss tangent ( $\tan\delta$ ), volume and surface energy loss functions, optical dispersion energy parameters, Urbach energy values, and steepness parameters of CrN and Mo:CrN coatings in as-deposited and various annealing states that are extensively described in Chapters 3, 4, and 5 in this dissertation.

The FTIR machine consists of an infrared source, interferometer, sample compartments and a detector. Basically, the energy of IR spectra is emitted from a glowing black-body source, and its beam passes through an aperture that controls the amount of energy presented, after that, this beam enters the interferometer where the spectral encoding

occurs. The resulting beam exits from interferometer is transmitted through or reflected off the sample surface (depend on the device type used) *via* entering the sample compartment. The beams finally, will passes through detector for final measurement, which digitised and sent to the computer in which the Fourier transformation processed.

The thermal emittance values of our metals nitride thin film coatings, in the infrared range of the spectra, was measured from the FTIR reflectance data. For this purpose, the FTIR reflectance spectra collected in the range of 2.5 to 15.4  $\mu\text{m}$  (in a range of 4000 to 650  $\text{cm}^{-1}$ ), using a reflected off type of Perkin Elmer Spectrum 100 FTIR Spectrometer (see Figure 7 for the machine diagram).



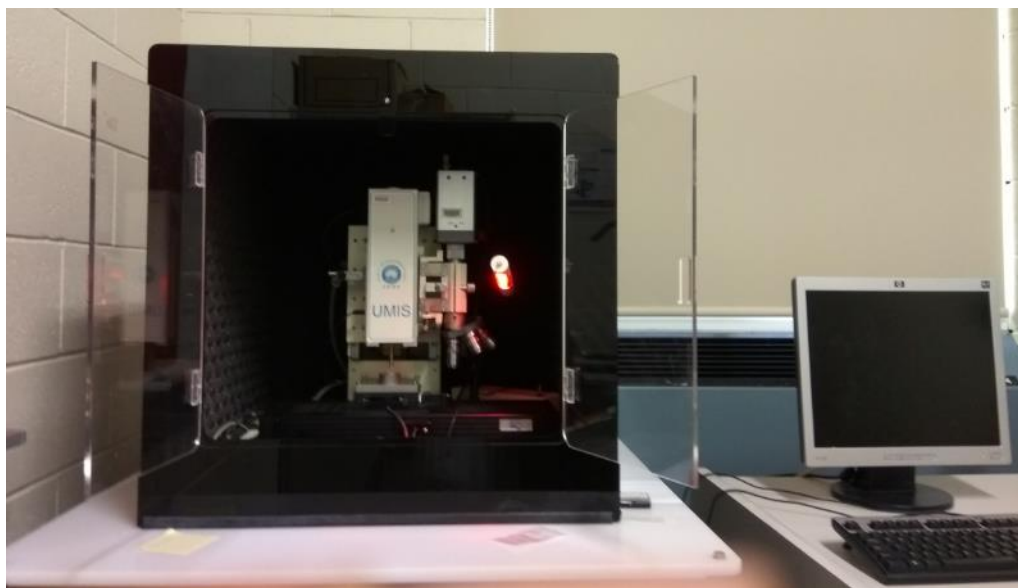
**Figure 7.** Perkin Elmer Spectrum 100 FTIR spectrometer.

The sample of thin film coating surface placed on the crystal surface area and pressed to a force of around 80 N using a pressure arm in order to maintain the coating surface touching evenly onto the diamond surface. The final reflectance spectrum was obtained after several times of scanning with resolution of 2  $\text{cm}^{-1}$ . For each scanning spectrum a background correction was performed.

## 6. Mechanical Properties of Thin Film Coatings: Nanoindentation and Finite Element Modeling (FEM) Studies

### 6.1 Nanoindentation Measurements

The mechanical properties of thin film coating based materials are remarkably important in many practical devices such as data storage technologies, integrated circuits and microprocessors. The elastic modulus/Young's modulus ( $E$ ) and hardness ( $H$ ) are the key mechanical properties for any materials. Using Oliver and Pharris method, the hardness and elastic modulus values of a material can be estimated from a set of  $P-h$  (load-displacement) nanoindentation data during loading and unloading cycle [19]. Typically, the depth of penetration is measured using either an inductance or capacitance displacement sensor, and indenter is the key component of nanoindentation, which should have high precision in geometry to facilitate indentation contact area. The indenters may be spherical ball-end, flat-ended cylindrical, or sharp and commonly made from diamond. The preferred indenter shape for nano- and microscale measurements, is the sharp shape including Berkovich, Vickers and cube corner especially in the characterisation of the mechanical properties of thin film based samples. The mechanical properties of our thin film coatings have been investigated *via* the nanoindentation workstation (Ultra-Micro Indentation System 2000, CSIRO, Sydney, Australia) equipped with a Berkovich indenter of 5  $\mu\text{m}$  in radius. The method proposed by Oliver and Pharr was used to determine the mechanical properties of our thin films [19-21]. The nanoindentation machine is shown in the following Figure 8.



**Figure 8:** Nanoindentation machine.

In nanoindentation measurements, a controlled load ( $P$ ) is applied through a diamond tip which is in contact with the surface of the material. The load and penetration depth,  $h$  are monitored during the loading unloading contact cycle. The penetration depth,  $h$  is recorded as a function of the applied load,  $p$  to generate the  $P-h$  data set. Using the  $P-h$  data set, the Young's modulus, hardness, fracture toughness and residual stress of the thin film coatings can be calculated. The hardness of a solid materials is defined by the following relation,

$$H = \frac{P_{max}}{A} \quad (15)$$

where  $P_{max}$  is the maximum load and  $A$  is the area of the indenter in contact with the material's surface. Using the following  $P-h$  diagram [19] shown in Figure 9, the maximum load ( $P_{max}$ ), maximum displacement ( $h_{max}$ ), and the stiffness ( $S$ ) parameters of a material can be calculated. The elastic/Young's modulus ( $E$ ) is defined as the stiffness of a material in the elastic region where Hooke's law is satisfied. The Young's modulus can be measured via  $P-h$  curve (Figure 7) from the following equation,

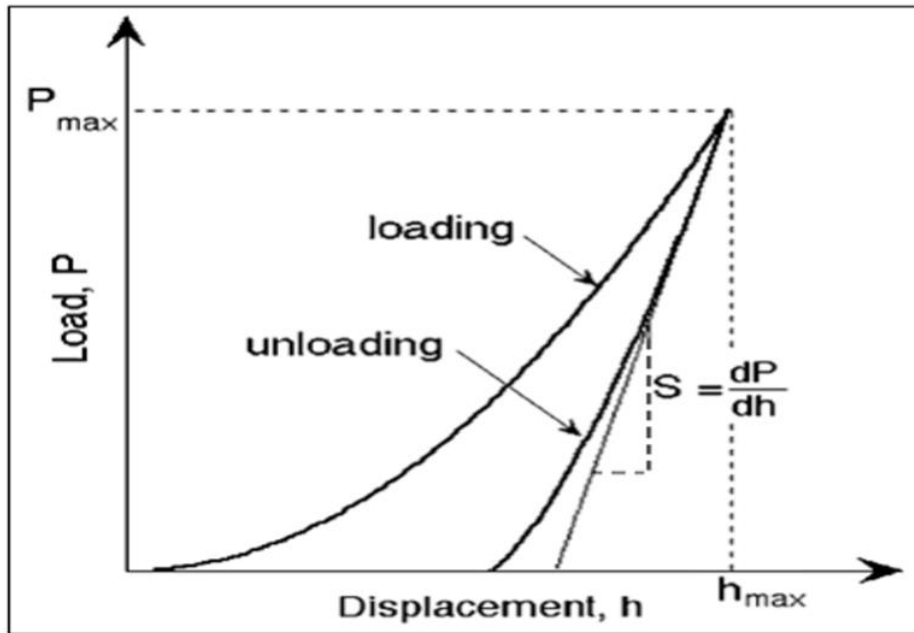
$$S = \beta \frac{2}{\sqrt{\pi}} E_{eff} \sqrt{A} \quad (15)$$

where  $\beta$  is a dimensionless constant taken as unity and  $E_{eff}$  can be measured through,

$$\frac{1}{E_{eff}} = \left( \frac{1 - \nu^2}{E} + \frac{1 - \nu_1^2}{E_i} \right) \quad (16)$$

where  $E$  elastic modulus and  $\nu$  refer the Poisson's ratio of the indenter and  $E_i$  and  $\nu_i$  are represent the elastic modulus and Poisson's ratio of the indented material, respectively [20, 21].





**Figure 9.** Typical loading-unloading curve from a nanoindentation experiment with maximum load ( $P_{\max}$ ) and depth of penetration ( $h_{\max}$ ) [19].

## 6.2 Finite Element Modeling (FEM)

In order to assess the mechanical response of the coating system to external loading and to realize the stress distribution within the coating and the substrate under spherical-tip indentation, finite element modeling (FEM) has been conducted. The nanoindentation data were used as input parameters. COMSOL Multiphysics® Ver. 3.5a software has been used to perform the FEM simulations. The simulation mode used is a two dimensional (2D) axisymmetric model constructed in the loading direction along the  $z$ -axis. The details of the model set-up are briefly described in the following section.

The working mode consists of a coating ( $1.2 \mu\text{m}$  thick) on top of silicon substrate (around  $1.00 \text{ mm}$  thick), under a radius of  $5 \mu\text{m}$  spherical tipped indenter loading. In order to keep simplicity, a rectangular simulation block of dimensions  $50 \times 50 \mu\text{m}$  was considered. Furthermore, time-dependent deformation behaviours such as creep, surface roughness, and contamination were also ignored for the simulation procedures. The indenter contacting area with the sample was assumed to be frictionless together with a perfect bonding between the substrate and coating. The following boundary conditions were considered: the bottom ( $z = 50 \mu\text{m}$ ) was fixed along  $z$ -axis, the right edge of the block ( $x = 50 \mu\text{m}$ ) was fixed along the  $x$ -axis. On the left edge of the simulation block ( $x = 0$ ), the axisymmetric axis was placed to create the 3D effects. The indenter tip was located at  $z =$

0  $\mu\text{m}$ . The indentation loading process was simulated as downward movements in successive steps of 0.01  $\mu\text{m}$  each, between 0 to 0.12  $\mu\text{m}$ .

The finite element modeling simulation subdivides an object into very small finite sized elements, and the physics behind each element can be defined by a finite number of degrees of freedoms. In FEM simulation process, each such element is assigned a set of characteristic equations (giving physical behaviours, boundary conditions, and applied forces) that are then solved as a set of simultaneous equations to reveal the object's characteristics. According to Hooke's law, the stress-strain relationship is given by,

$$\sigma_s = B \varepsilon_s \quad (17)$$

where  $B$  is the elasticity matrix definition, and the stress,  $\sigma_s$  and strain components,  $\varepsilon_s$  are presented in matrix form with the six stress and strain components:

$$\sigma_s = \begin{bmatrix} \sigma_s \\ \sigma_s \\ \sigma_s \\ \tau_{xy} \\ \tau_{yz} \\ \tau_{xz} \end{bmatrix}, \quad \varepsilon_s = \begin{bmatrix} \varepsilon_s \\ \varepsilon_s \\ \varepsilon_s \\ \gamma_{xy} \\ \gamma_{yz} \\ \gamma_{xz} \end{bmatrix} \quad (18)$$

where the  $\sigma_s$ ,  $\tau$ ,  $\varepsilon_s$ , and  $\gamma$  are the normal stress, shear stress, normal strain and shear strain respectively, along  $x$ -,  $y$ -, and  $z$ -axis. The deformation components  $-(u, v, w)$  in 3D and their derivatives, can be described in tensor forms:  $\varepsilon_{xy}$ ,  $\varepsilon_{yz}$ ,  $\varepsilon_{xz}$  or in engineering forms:  $\gamma_{xy}$ ,  $\gamma_{yz}$ ,  $\gamma_{xz}$  in the following way,

$$\varepsilon_x = \frac{\partial u}{\partial x}; \quad \varepsilon_y = \frac{\partial v}{\partial y}; \quad \varepsilon_z = \frac{\partial w}{\partial z} \quad (19)$$

$$\varepsilon_{xy} = \frac{\gamma_{xy}}{2} = \frac{1}{2} \left( \frac{\partial u}{\partial y} + \frac{\partial v}{\partial x} \right); \quad \varepsilon_{yz} = \frac{\gamma_{yz}}{2} = \frac{1}{2} \left( \frac{\partial v}{\partial z} + \frac{\partial w}{\partial y} \right); \quad \varepsilon_{xz} = \frac{\gamma_{xz}}{2} = \frac{1}{2} \left( \frac{\partial u}{\partial z} + \frac{\partial w}{\partial x} \right) \quad (20)$$

The inverse elasticity matrix ( $B^{-1}$ ), in case of isotropic materials, which is also known as the flexibility or compliance matrix, can be described as:

$$B^{-1} = \frac{1}{E} \begin{bmatrix} 1 & -\nu & -\nu & 0 & 0 & 0 \\ -\nu & 1 & -\nu & 0 & 0 & 0 \\ -\nu & -\nu & 1 & 0 & 0 & 0 \\ 0 & 0 & 0 & 2(1+\nu) & 0 & 0 \\ 0 & 0 & 0 & 0 & 2(1+\nu) & 0 \\ 0 & 0 & 0 & 0 & 0 & 2(1+\nu) \end{bmatrix} \quad (21)$$

where  $E$  is the modulus of elasticity and  $\nu$  is Poisson's ratio. To find  $B$ ,  $B^{-1}$  should be inverted to give:

$$B = \frac{E}{(1+\nu)(1-2\nu)} \begin{bmatrix} 1-\nu & \nu & \nu & 0 & 0 & 0 \\ \nu & 1-\nu & \nu & 0 & 0 & 0 \\ \nu & \nu & 1-\nu & 0 & 0 & 0 \\ 0 & 0 & 0 & \frac{1-2\nu}{2} & 0 & 0 \\ 0 & 0 & 0 & 0 & \frac{1-2\nu}{2} & 0 \\ 0 & 0 & 0 & 0 & 0 & \frac{1-2\nu}{2} \end{bmatrix} \quad (22)$$

Using the nanoindentation results of the coatings as the input parameters, the stress distributions around the coatings surface can be visualized using computational modeling process.

## 7. Density Function Theory

The density functional theory (DFT) is one of the most successful and one of the most promising approaches to simulate the structural, magnetic, optical, and electronic structure of various materials. Density function theory based simulations are widely used for atoms, molecules, solids to nuclei, and in classical and quantum fluids. DFT can provide the ground state properties of a system, and the electron density plays a key role. Using the DFT we can predict a large variety of molecular properties such as molecular structures, enthalpy, vibrational frequencies, thermodynamic potentials, ionization potentials, chemical potentials, ionization energies, electric and magnetic dipole moments, reaction paths, atomic and molecular distances, Bohr magnetons etc. The original purpose of DFT has been devoted to study the spin polarized systems, molecular dynamics,

multicomponent systems such as nuclei and electron hole droplets, superconductors, relativistic electronic systems, time-dependent phenomena, bosons, fermions and so on. In this study, the geometrical clusters of the considered systems were optimized *via* DFT integrated with the B3LYP hybrid functional using LANL2DZ basis sets [22]. Gaussian 09 program was used to conduct the DTF based simulations [23]. Chemical potential ( $\mu$ ) of the clusters was calculated using the following relation [24],

$$\mu = -\frac{(E_{Homo}+E_{Lumo})}{2} \quad (23)$$

where,  $E_{Homo}$  and  $E_{Lumo}$  indicate the energy associated with the highest occupied molecular orbital (HOMO) and the lowest unoccupied molecular orbital (LUMO). The energy gap between HOMO and LUMO known as band-gap ( $E_g$ ) is related to the electrical conductivity and is defined by the following equation [24],

$$E_g = E_{Lumo} - E_{Homo} \quad (24)$$

Chemical hardness ( $\eta$ ) and softness ( $S$ ) are derived from Koopman's theorem and are defined by the subsequent equations [25, 26],

$$\eta = \frac{(E_{Lumo}-E_{Homo})}{2} \quad (25)$$

$$S = \frac{1}{2\eta} \quad (26)$$

The concept of electrophilicity introduced by Parr *et al.* is defined as [25],

$$\omega = \frac{\mu^2}{2\eta} \quad (27)$$

Mulliken charge analysis were automatically done by the Gaussian 09 program during the geometry optimization operation. The optical properties of the clusters were investigated using the ultraviolet-visible (UV-Vis) spectroscopy. Using the optimized molecular geometries of considered clusters, the fundamental vibrational wave numbers along with their corresponding infra-red (IR) intensities, and Raman activities of these clusters were computed at the B3LYP/ LANL2DZ basis sets using the Gaussian 09 program package.

## References

- [1] A. Guinier, Diffraction of X-rays by Crystals, in X-ray Diffraction in Crystals, 1994.
- [2] B.B. He, Two-dimensional X-ray Diffraction, Wiley, A John Wiley & Sons Inc. Publication, Hoboken, New Jersey, USA, 2009.
- [3] B. Borie, X-Ray Diffraction in Crystals, Imperfect Crystals, and Amorphous Bodies, Journal of the American Chemical Society, 87 (1965) 140-141.
- [4] I.C. Noyan, J.B. Cohen, Residual stress: measurement by diffraction and interpretation, Springer-Verlag New York, USA, 1987.

- [5] R.F. Egerton, *Physical principles of electron microscopy: An Introduction to TEM, SEM and AEM*, Springer, USA, 2005.
- [6] J.B. Pawley, *Biological Low-Voltage Scanning Electron Microscopy*, Springer, USA, 2008.
- [7] J.A. Duffie, W.A. Beckman, *Solar Engineering of Thermal Processes*, John Wiley & Sons, USA, 2006.
- [8] A. Millar, M.M. Rahman, Z.-T. Jiang, *Journal of Advanced Physics*, 3 (2014) 179-193.
- [9] M.M. Rahman, Z.-T. Jiang, Z.-f. Zhou, Z. Xie, C.Y. Yin, H. Kabir, M.M. Haque, A. Amri, N. Mondinos, M. Altarawneh, *Journal of Alloys and Compounds*, 671 (2016) 254-266.
- [10] A. Roos, *Use of an integrating sphere in solar energy research*, *Solar Energy Materials and Solar Cells*, 30 (1993) 77-94.
- [11] T. Tesfamichael, *Acta Universitatis Upsaliensis*, Sweden, 2000.
- [12] H. Wang, Q. Le-Van, A. Aassime, X.L. Roux, F. Charra, N. Chauvin, A. Degiron, *Advanced Optical Materials*, 6 (2018) 1870009.
- [13] J. Singh, *Optical-Properties-of-Condensed-Matter-and-Applications*, Wiley, A John Wiley & Sons Inc. Publication, Hoboken, New Jersey, USA, 2006.
- [14] N. Segmane, D. Abdelkader, A. Amara, A. Drici, F.C. Akkari, N. Khemiri, M. Bououdina, M. Kanzari, J. Bernède, *Optical Materials*, 75 (2018) 686-694.
- [15] R. Swanepoel, *Journal of Physics E: Scientific Instruments*, 16 (1983) 1214-1222.
- [16] H.E. Atyia, N. Hegab, *The European Physical Journal-Applied Physics*, 63 (2013).
- [17] H. Atyia, N. Hegab, *Physica B: Condensed Matter*, 454 (2014) 189-196.
- [18] S. El-Sayed, *Materials chemistry and physics*, 78 (2003) 262-270.
- [19] A. Prasitthipayong, S. Vachhani, S. Tumey, A. Minor, P. Hosemann, *Acta Materialia*, 144 (2018) 896-904.
- [20] D. Belov, I. Blinkov, V. Sergevnin, N. Smirnov, A. Volkhonskii, A. Bondarev, T. Lobova, *Surface and Coatings Technology*, 338 (2018) 1-13.
- [21] M.S. Kabir, P. Munroe, Z. Zhou, Z. Xie, *Ceramics International*, in Press (2018).  
<https://doi.org/10.1016/j.ceramint.2018.01.199>
- [22] A.D. Becke, *The Journal of Chemical Physics*, 98 (1993) 1372-1377.
- [23] M.J. Frisch et al., *Gaussian 09, Revision D.01*, in: I. Gaussian (Ed.), Wallingford, CT, USA, 2009.
- [24] A.S. Rad, S.S. Shabestari, S.A. Jafari, M.R. Zardoost, A. Mirabi, *Molecular Physics*, 114 (2016) 1756-1762.

[25] R.G. Parr, L.v. Szentpály, S. Liu, *Journal of the American Chemical Society*, 121 (1999) 1922-1924.

[26] R.G. Pearson, *Journal of Chemical Sciences*, 117 (2005) 369–377.